Advanced Metrology

for the Development of Nature-Inspired

Polymer Electrolyte Fuel Cells

Viswanath Sasank Bethapudi

A thesis submitted for the award of the degree of

Doctor of Philosophy (PhD)

Centre for Nature Inspired Engineering

&

Electrochemical Innovation Lab

Department of Chemical Engineering

University College London (UCL)

Torrington Place, London, WC1E 7JE, United Kingdom

January 2021

Declaration

I, Viswanath Sasank Bethapudi, confirm that the work presented in this thesis is my own. Where information has been derived from other sources, I confirm that this has been indicated in the thesis.

Signature:

Date: 7th January 2021

Acknowledgements

- I would like to thank Prof Marc-Olivier Coppens for agreeing to be my PhD supervisor, providing the right guidance and support throughout this program, and helped me in becoming an independent researcher. Working with Prof Coppens over the years has had a significant influence on my ability to comprehend engineering.
- My next thanks would go to Prof Dan Brett, my supervisor, who has been the architect of my PhD program. His constant encouragement and motivation have been crucial factors for the successful completion of my studies.
- I would like to thank Dr. Gareth Hinds from NPL (UK) for his constant support, and the opportunities given to present my work at industrial meetings.
- I extend my heartfelt thanks to the members of Centre for Nature Inspired Engineering (CNIE) and Electrochemical Innovation Lab (EIL) groups for their academic and technical support.
- Many thanks to the staff at chemical engineering department for the timely help and assistance provided during this program.
- I feel fortunate for the blessings of my teachers.
- Finally, I share and dedicate all the achievements to my family.

I. Abstract

The cathode flow-field is an important component in polymer electrolyte membrane fuel cells (PEMFCs) that influences the cell's performance significantly. An effective cathodic flow-field design is necessary for efficient transport and removal of reactants and products from its respective electrode. Fractal flow-fields, inspired by the flow mechanism of air inside the lungs, are identified to provide homogeneous, scalable and uniform distribution of reactants to polymer PEMFC electrodes. In this thesis, the design and development of lung-inspired fractal flow-fields, developed from layered planar printed circuit board (PCB) plates, is presented for cathodic reactant transport. The PCB-based approach makes the fractal flow-field cost-effective, easy to manufacture, scalable and lightweight, compared to laser sintered stainless steel fractal flow-fields, developed in previous work in the Centre for Nature-Inspired Engineering.

Furthermore, advanced metrology techniques are utilised to characterise the lung-inspired fuel cells with a view to optimise their design and performance. Uniformity and alignment between individual PCB layers producing a fractal hierarchy of flow channels have been characterised using X-ray computed tomography (X-ray CT). Performance polarisations, current-voltage degradations and cell temperatures indicate that fractal PEMFCs perform better than conventional, single-serpentine PEMFCs. Standard electrochemical characterisations confirm the basis for the observed performance enhancement when using a fractal flow-field.

Acoustic emission (AE) analysis, a first of its kind non-invasive and non-destructive hydration diagnostics tool, is utilised as a water management technique that identifies the presence of liquid water in flow channels and

correlates its removal and generation with the level of cell performance. In addition, electro-thermal mapping, which reflects the surface distribution of current and temperature generated inside the cell, is performed to evaluate the influence of reactant and water distribution conditions inside the cells on its localised and overall cell performance.

II. Impact Statement

Fuel cells involve a complex interplay of physical and electrochemical processes. They are an important technology in the context of renewable energy and sustainability. Development of advanced metrology tools is essential to understand, monitor and improve their operation, and to support improved fuel cell designs. Performance improvements have been demonstrated by taking a nature-inspired approach to flow plate design, leading to easy scalability and higher efficiency. In this thesis, the use of advanced diagnostic techniques is presented to understand water management in lung-inspired, polymer electrolyte membrane (PEM) fuel cells, which take hydrogen as a fuel and produce water, with a view to optimise their design and performance.

The research work has been primarily conducted in the EPSRC “Frontier Engineering” Centre for Nature Inspired Engineering (CNIE) and the Electrochemical Innovation Lab (EIL) at UCL. CNIE is a multidisciplinary research centre having expertise in understanding the physicochemical features of natural systems and applying them in developing innovative solutions to grand challenges in energy, chemical manufacturing, water, healthcare, space technology, the built environment, etc. EIL is one of the most advanced electrochemical science and engineering research centres, with innovation, technology and enterprise as its core values.

The work presented in this thesis has been published in peer-reviewed journals like Energy Conversion and Management (impact factor 8.2), Electrochemistry Communications (impact factor 4.3) and ECS that allowed to disseminate the research to a wider audience. Besides, this work has been presented and discussed with academics and industry through international conferences (ECS,

2019 and PRiME, 2020). The author has also presented this research at the Industrial Advisory Group (IAG) meetings held at the National Physical Laboratory (UK), which partly sponsored this research work.

III. Table of Contents

IV. List of Figures

V. List of Tables

VI. List of publications

- **V.S. Bethapudi,** G. Hinds, P.R. Shearing, D.J.L. Brett, M.-O. Coppens, Acoustic emission analysis of polymer electrolyte membrane fuel cells, 2020 ECS Trans. (98) 177.
- **V.S. Bethapudi**, J. Hack, P. Trogadas, G. Hinds, P.R. Shearing, D.J.L. Brett and M.-O Coppens, Hydration state diagnosis in fractal flow-field based polymer electrolyte membrane fuel cells using acoustic emission analysis, Energy Convers. Manag. 2020; 220:113083.
- **V.S. Bethapudi**, M. Maier, G. Hinds, P.R. Shearing, D.J.L. Brett, M.O. Coppens, Acoustic emission as a function of polarisation: Diagnosis of polymer electrolyte fuel cell hydration state, Electrochem. Commun. 2019; 109: 106582.
- **V.S. Bethapudi,** J. Hack, P. Trogadas, J.I.S. Cho, L. Rasha, G. Hinds, P.R. Shearing, D.J.L. Brett, M.-O.Coppens, A lung-inspired printed circuit board polymer electrolyte fuel cell, Energy Convers. Manag. 2019; 202 :112198.
- Trogadas, P; Cho, JIS; **Bethapudi, VS**; Shearing, P; Brett, DJL; Coppens, MO, Nature-Inspired Flow-Fields and Water Management for PEM Fuel Cells. 2020 ECS Trans. (98) 145.

1. Introduction

1.1. Polymer electrolyte membrane fuel cells (PEMFCs)

1.1.1. Introduction to PEMFCs

Uncontrolled use of fossil fuels causing environmental damage [1] is forcing researchers to seek renewable energy sources that can, to an extent, suffice the global energy needs while being less detrimental on the environment. Energy derived from hydrogen can be an alternative to fossil fuel energy while being efficient, sustainable and clean at use [2]. Polymer electrolyte membrane fuel cells (PEMFC) that use hydrogen as a fuel for generating electrical power are an efficient option to utilise the energy potential contained in hydrogen as an energy vector. PEMFCs are largely considered as an ideal candidate for a wide range of power applications, both stationary and portable, for the built environment, transport sector, and to satisfy a range of other energy needs. Besides, PEMFCs can deliver power at low temperature, with low emissions, high power density, and start up quickly [3–5].

PEMFCs are electrochemical devices that convert chemical energy into electrical energy. They use ion-exchange polymers as electrolytes for the electrochemical reaction. These electrolytes have the ability to conduct protons and are good insulators for electron conduction. Besides, a PEMFC consists of a cathode and an anode, where the electrochemical half-reactions occur, and flow-field (bi-polar) plates for the supply of reactants to the respective electrodes. The PEMFC working schematic is presented in Fig. 1 [6] and the overall electrochemical reaction occurring is given in equations (1-3) [7].

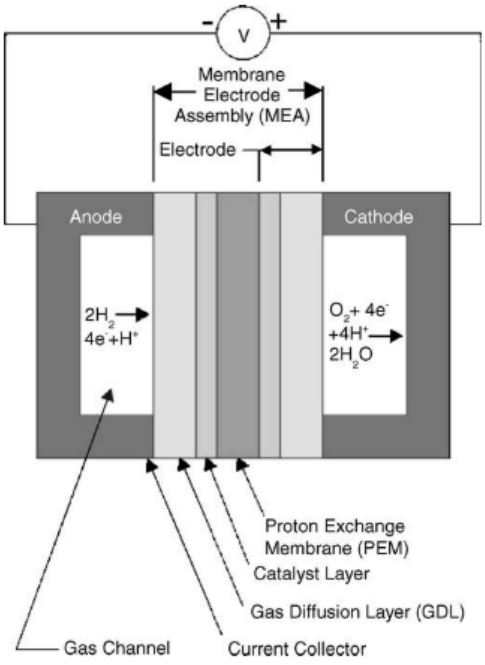

Figure 1: Schematic of a polymer electrolyte membrane fuel cell (PEMFC) operation outline. Figure adapted from [6].

The anodic and cathodic half-reactions are given in equations (1) and (2), respectively, and the overall reaction in equation (3). In addition, the PEMFC electrochemical reaction produces electrical energy with water (H_2O) and heat (Δ) generated as the only by-products.

$$H_2 \rightarrow 2H^+ + 2e^- \quad (1)$$

$$\frac{1}{2}O_2 + 2H^+ + 2e^- \rightarrow H_2O \quad (2)$$

$$H_2 + \frac{1}{2}O_2 \rightarrow H_2O + \Delta \quad (3)$$

A PEMFC consists of several assembled components, like the membrane electrode assembly (MEA), gaskets, flow-field plates, and end plates, and these components are pivotal in the efficient generation of electrical power. Of these, the flow-fields play a critical role in the supply, removal, and regulation of

reactants and water produced inside the cell. Furthermore, their designs can significantly influence the functioning, performance and durability of a PEMFC [8,9].

1.1.2. Flow-field(s) and its impact on PEMFC performance

Flow-field plates are essential components for PEMFCs; they provide the necessary mechanical compression to hold individual components of the cell together, provide electrical conductivity between the cells, and introduce oxidant (oxygen in air) and fuel (hydrogen) to the respective electrodes [8,9]. A wide range of flow-fields has been developed for PEMFCs. Some conventional ones include serpentine, parallel, interdigitated, pin, mesh, cascade, perforated and biomimetic designs [10–18]. A major operational issue that could be impacted by the structure of the flow-field is the accumulation of water in the channels and under the land areas, especially at the cathode region [10,19–21]. Inefficient removal of accumulated water from the flow-field channels by reactant gases results in cell flooding. Flooding leads to a non-uniform reactant distribution on the electrode surface, resulting in a heterogeneous current density distribution that can hinder cell operating performance, and accelerate the degradation of cell performance and cell components, respectively [11,22,23].

Serpentine flow channels are widely acknowledged as having operational advantages compared to other conventional flow-fields in terms of uniform reactant distribution, water and heat management, effective utilisation of electrocatalysts, improved reactant flow at the electrode surface, uniform stack compression and water and thermal management [8,10,24–28]. There are several configurations of serpentine design based flow-fields, like single-serpentine, multiple-serpentine and serpentine in combination with other conventional flow-field designs. However, the serpentine flow-field has a long

reactant flow path that often results in a concentration gradient and pressure drop along the reactant flow path [29]. In addition, stagnation of liquid water

along the serpentine flow paths results in mass transfer related issues, like channel flooding and reactant starvation that reduce the overall cell performance [30,31]. The flow-field design needs to be improved to overcome issues such as the decrease in fuel cell performance at low current density under low temperature and low relative humidity conditions [32]; a significant decrease in reactant concentration from inlet to outlet of the fuel cell [33]; uneven reactant consumption and current density distribution [34]; cathode water accumulation during higher humidity operation [19,35]; and high pressure drop at large scale (> 10 cm^2 area of the flow-field) [36].

1.2. Nature-inspired chemical engineering (NICE) solutions for fuel cells

1.2.1. Overview of bio/nature-inspired mechanisms and methodology

Through evolution, nature has developed mechanisms and systems with efficient distribution and the right balance between flow dynamics and energy transformation [37,38]. For instance, respiratory organs, the vascular network [39] and trees [40] are exemplary for efficient reactant transport and distribution with optimised thermodynamic balance [41]. The networks inside organs and trees follow a branched, hierarchical, fractal architecture between macroscopic and microscopic length scales [42]. Such a fractal structure allows for efficient transport and uniform distribution of materials inside them, maintaining a constant functionality through scale-up [43].

Some of the flow mechanisms and principles observed in nature have been studied and implemented in developing flow-fields for fuel cells that eventually enhanced the cell's performance [12–14,44,45]. Asadzade et al. [44] identified lung-shaped microfluidic flow patterns in bipolar plates as a means of maximising power density. Kloess et al. [12] established, via simulations and experimental studies, that serpentine and interdigitated flow-fields, when integrated with lung and leaf flow patterns, delivered enhanced performance. Guo et al. [14] mimicked the hierarchical structures of leaf veins, with three hierarchical generations, by incorporating them into serpentine and interdigitated flow-fields, leading to improved performance over conventional flow-fields. Through numerical modelling and simulation, Arvay et al. [13] reviewed CFD simulations applied to nature-inspired flow-fields. They concluded that the efficacy of these designs increases when used in

conjunction with standard interdigitated flow-field designs. Collectively, these studies show that decreased pressure drop, uniform flow distribution, higher oxygen delivery and homogeneous reactant distribution can be achieved by using bio/nature-inspired flow-field designs. However, the primary purpose of these studies is to provide improved gas distribution at the GDL level by either imitating or mimicking mechanisms from nature, without precisely analysing the physiochemical formulations and phenomena responsible for the improvements, and thus fuel cell performance. Furthermore, a common concern identified in all these studies is the cost and complexity involved in developing such bio/nature-inspired flow-field patterns, thus hindering scalability of such designs into large-area fuel cells and stacks.

1.2.2. NICE mechanism based PEMFC flow-fields

Mechanisms occurring in nature have inspired solutions to several issues faced by synthetic processes. Some critical mechanisms include: (a) hierarchical networks to bridge scales, minimise transport limitations and provide efficiently scalable solutions, (b) balancing of forces to achieve superior performance, and (c) use of dynamics as an organising mechanism [38,46,47]. Fundamentally, a nature-inspired approach differs from replication and mimicking [48–50], as inspiration considers the mechanistic and physiochemical features behind the processes [51]. Such an approach finds application in, e.g. architecture [52], biological applications, catalysis and reactor engineering [53–55], fuel cells and electrochemical engineering [36,56,57].

Coppens [38,43], for the first time, developed a systematic and thematic nature-inspired chemical engineering (NICE) methodology that leverages fundamental mechanisms underpinning desirable properties in natural systems, such as scalability, efficiency and robustness, in designs that address similar challenges in engineering, for a range of applications. NICE designs adopt the natural mechanisms, but adapt them to the different context of the technological application, recognising that nature and technology operate under different constraints [38].

Applied to fuel cell design, Kjelstrup, Coppens et al. [58] formulated the design and mathematical procedure for developing a fractal based, lung-inspired distribution system with catalytic layers for fuel cells, as shown in Fig. 2, which resulted in reduced entropy generation and enhanced fuel cell performance.

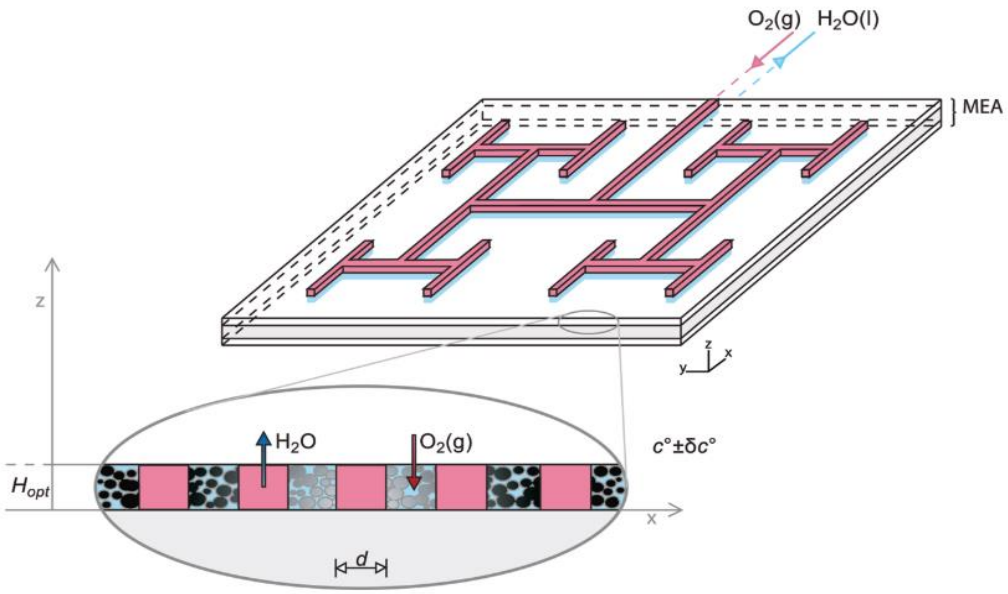

Figure 2: Hierarchical, fractal gas flow distributor for a polymer electrolyte membrane fuel cell (PEMFC). Figure adapted from [58]

Marquis' PhD thesis [59] and Trogadas et al. [36] developed a simulation and experimental validation study for lung-inspired PEMFCs, as shown in Fig. 3. Furthermore, finite element models in combination with two-phase agglomerate models, and numerical simulations of 3D hierarchical fractal flow-fields were studied by Trogadas et al. [36] and Cho et al. [60]. Here, the effects of hierarchical branching generations on the gas diffusion layer (GDL) thickness and the resulting PEMFC performance were explored. Through these numerical simulations, the ideal number of branching generations '*N'* required to deliver a diffusion dominated flow at the fractal outlets that is similar in magnitude to convection dominated flow at the inlet (Pé ~ 1) with minimal entropy generation was identified to be between *N* = 5 and *N* = 7 [36,60]. For fuel cells with larger electrode area (flow-field plates), larger N is required to deliver diffusion dominated flow at the outlets.

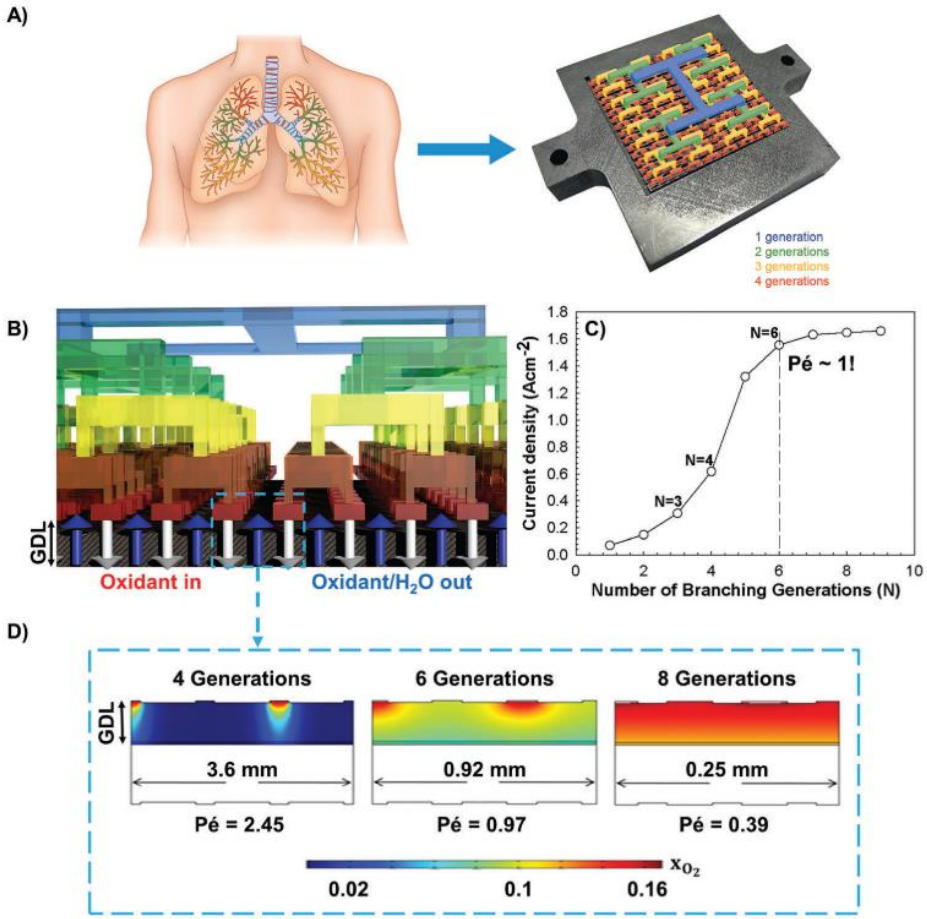

Figure 3: A) Lung-inspired PEMFC design inspired from airflow network inside lungs, (B) fractal flow structure design for PEMFC, (C) simulation results of current density with number of fractal generations and (D) simulation results of number of generations needed for matching convection and diffusion flow through outlets. Figure adapted from [36].

Experimental realisation of the modelling and simulation studies, as discussed above [36,60], were performed initially on a 10 cm^2 and later on a 25 cm^2 active MEA area lung-inspired PEMFCs, respectively. The cells had up to four fractal generations and were developed from laser sintering of stainless steel, as shown in Fig. 4. The lung-inspired flow-field PEMFCs indicated performance enhancement and low pressure drop values over conventional serpentine flow-

field PEMFCs at 50% and 75% reactant RH conditions as a result of uniform and homogeneous reactant distribution across the catalyst layer.

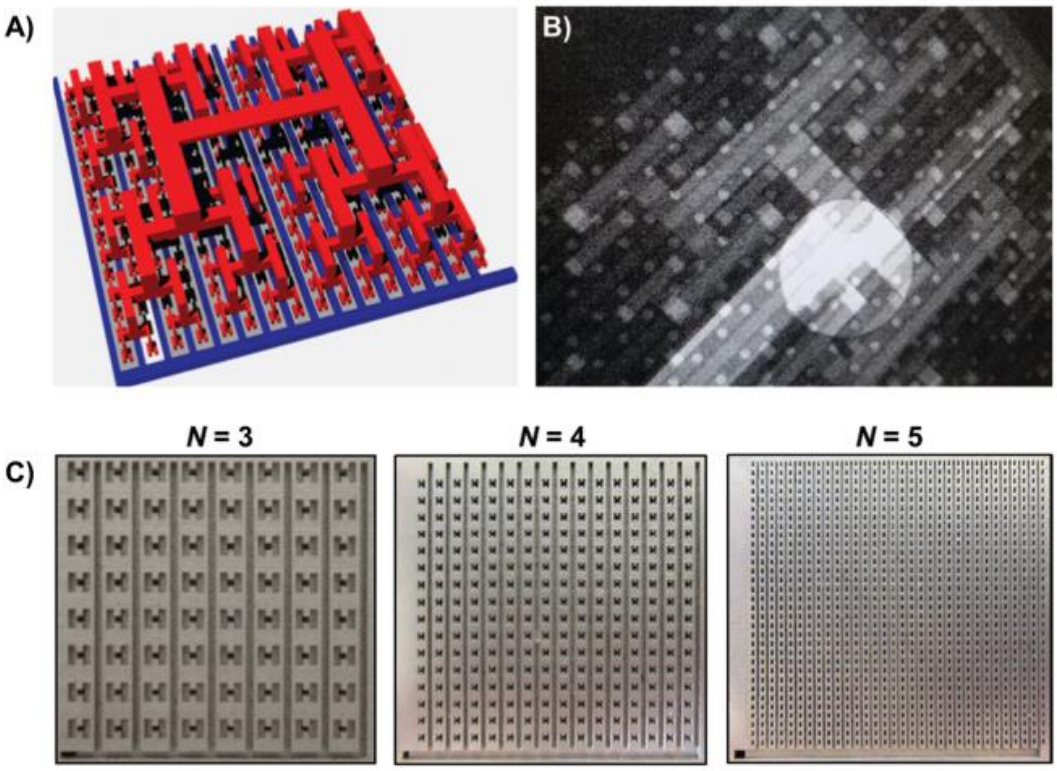

Figure 4: (A) 4-generation, 3D fractal network design, (B) X-ray radiography of fractal flow-field, (C) stainless steel based fractal flow-fields for different generations. Figure adapted from [61].

1.3. Perspective of this thesis

1.3.1. Printed circuit board (PCB) based layered lung-inspired PEMFCs

Previously, works by Marquis [59] and Trogadas, Cho et al. [36] applied the NICE approach to the analysis of lung-inspired, fractal flow-fields. Initial modelling and simulation studies were performed to optimise the distributor structure and identify the optimal number of fractal branching generations to achieve uniform reactant distribution. Further, laser sintering of stainless steel was used to construct the 3D flow-field structure, and it was found that, up to four generations, the fractal flow-field exhibited significant performance enhancement over conventional flow-field designs. However, Trogadas, Cho et al. [36] identified difficulties in water management at higher humidity (100% RH), using the laser sintered stainless steel plates, that resulted in performance degradation for higher numbers of generations. Furthermore, the weight (approximately 0.5 kg per flow-field), complexity, time and cost (~£600 - £800 per flow-field) involved in the flow-field fabrication (laser sintering of stainless steel) can hinder the use of such fractal structures in commercial fuel cells and stacks. In summary, while the benefits of a NICE approach to flow-field design are clear, a common concern is the high reactant humidity operations, cost and manufacturability of these complex 3D structures at scale.

Incorporating the membrane electrode assembly (MEA) within the layers of printed circuit boards (PCBs) has proven to be a promising means of PEMFC fabrication. Some key benefits of PCB-based fuel cell development are ease of manufacturability, durability, and adaptability, as well as the light weight and

cost-effectiveness [62–67]. However, to date, the PCB flow-fields have conformed to conventional ‘2D’ flow configurations.

In this thesis, the cost-effective PCB approach, and the hierarchical lung-inspired flow-field design are combined for the first time. A 3D fractal flow-field is constructed using a 2D planar multi-layered PCB approach [62–66]. The 3D lung-inspired flow-fields are fabricated on PCBs using a computer numeric control (CNC) technique. Furthermore, the development of different fractal flow-field configurations, utilising the PCB plate’s surfaces optimally, is presented. The structural integrity is established through X-ray scans to ascertain the accuracy in the layered assembly approach. Performance of the different flow-fields, tested over a range of experimental conditions and operating parameters, are presented in detail. Besides, polarisation, electrochemical impedance spectroscopy (EIS), degradation tests, electro-thermal mapping, and acoustic emission technique are utilised for diagnosing the performance of the different fractal flow-field PEMFCs.

Furthermore, the performance of PCB-based, lung-inspired flow-field PEMFCs is compared with the performance of PCB-based, conventional single-serpentine flow-field PEMFCs. Here, a single-serpentine flow-field is chosen for the comparison with the lung-inspired flow-field’s performance, because the serpentine pattern is known to provide the best PEMFC performance and effective water management and reactant distribution among the existing conventional flow-fields [10,24–26,65].

1.3.2. Advanced metrology of lung-inspired PEMFCs

In this thesis, different metrology is utilised to diagnose and characterise the performance of the various tested lung-inspired and conventional flow-field fuel cells.

X-ray computed tomography (CT) scanning based structural characterisation allows visualising the internal channel arrangement of the flow-fields, the alignment of individual layers, structural integrity, as well as the quality of the cell assembly.

Polarisation scans are performed under different reactant, temperature, stabilisation and degradation conditions, which establish the cell operating performance. Electrochemical impedance spectroscopy (EIS) measurements are conducted to evaluate the resistance contribution from various components of the cells. The EIS technique is instrumental in assessing the individual and cumulative contributions of reactant and operating conditions, and flow-field structure on the cell performance.

Galvanostatic and potentiostatic tests are performed to evaluate the influence of hydration conditions on cell performance stability, which is influenced by water generation and removal dynamics inside the PEMFC.

Current and temperature mapping metrology has been utilised to characterise the electro-thermal performance of a fractal flow-field, for the first time, as well as of conventional flow-fields. Electro-thermal mapping primarily investigates the role of the flow-field structure, under different reactant and operating conditions, on the hydration distribution inside the cell and it’s corresponding

impact of the fuel cell performance through surface current and temperature distributions.

Finally, acoustic emission (AE) analysis, a non-invasive and non-destructive diagnostic tool, is utilised to probe water formation and removal inside an operating fuel cell. Acoustic emission as a function of polarisation (AEfP), a first of its kind hydration diagnostic technique, is utilised to characterise the cell performance electro-acoustically. AEfP can identify the presence of liquid water in flow channels and correlate its formation and removal with the level of cell polarisation, reactant RH and consequent cell temperature. Furthermore, simultaneous acoustic activity from the cells during polarisation cycles and stability studies, and use of amplitude analysis for hydration quantification, allow the relative water management characteristics of the fuel cells to be compared.

2. Literature review

2.1. Polymer electrolyte membrane fuel cell (PEMFC) technology

2.1.1. Technology overview

PEMFC technology has several advantages, like low-temperature operations, quick start-up conditions, low-pressure operations and high power density [68]. PEMFCs operating on hydrogen are considered to be an ideal replacement for a wide range of power sources for many stationary, portable, built environment and transport applications due to the low-temperature operation, zero emissions at the point of use, high efficiency, high power density, and quick start-up [3–5]. The energy efficiency of a PEMFC can reach around 40% and this can increase to as high as 95% [69] when used as a combined heat and power (CHP) device [70].

For transport applications, where the PEMFCs are required to replace the internal combustion engines of cars, buses and other utility vehicles, the typical fuel cell power ranges from 20 kW to 250 kW. Some of the PEMFC powered vehicular applications include the Toyota Mirai, Honda FCX, Hyundai FCV, Nissan XTERRA and others in the passenger car segment. Daimler fuel cell buses, Mercedes – Benz Citaro fuel cell buses are among the examples used in the public transportation segment [71–73].

In the portable power range applications, PEMFCs with a power range of 5 – 50 W are utilised as microcells for powering laptops, mobiles, toys and other electronic applications ordinarily supported by battery technology [71].

For stationary applications, PEMFCs are utilised for commercial/residential use with the fuel cell systems supporting heat-power cogeneration requirements. Several PEM fuel cell systems as combined heat and power devices for

stationary applications are developed by Plug Power, Ballard systems and others [74–76].

2.1.2. PEMFC materials and components

The major materials and components in a PEMFC are – Membrane electrode assembly, flow-field plates, current collector plates and end compression plates. The individual PEMFC components are shown in Fig. 5 [77].

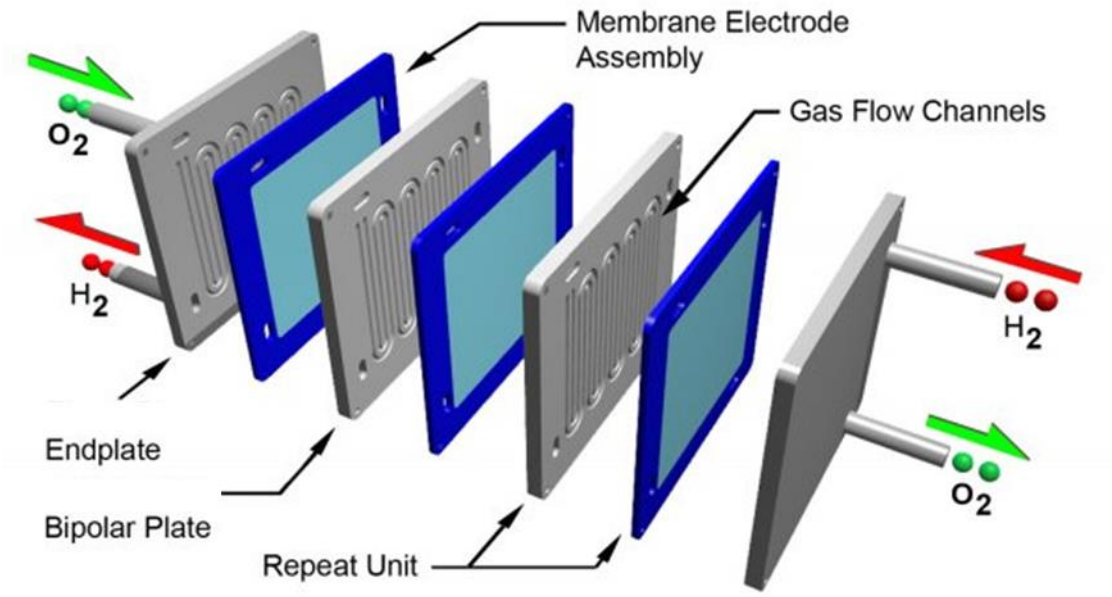

Figure 5: PEMFC assembly components. Figure adapted from [77]*.*

The membrane acts as an electrolyte in the PEMFC; it allows for selective conduction of protons, while separating reactants and being electrically insulating. Given the various operating conditions of PEMFCs, the membrane must endure temperature ranges between sub-freezing [78] and as high as 100 °C [79] and remain durable and stable in activity [80].

There are several possible candidates for proton-conducting membranes; however, their use depends on the operating conditions of the PEMFC. For

temperature below 80 °C, a per-fluorinated polymer electrolyte like Nafion® (DuPont) [81,82] is used as a membrane, while, at temperatures above 100 °C, sulfonated copolyimide ionomers and Hyflon® membranes are used [83,84].

The electrocatalyst is the other major component of a MEA in PEMFCs. The hydrogen oxidation reaction (HOR) and oxygen reduction reaction (ORR) occur at the respective electrocatalyst layers. The base material for the electrocatalysts are Pt-based, which show greater activity, stability and durability [85,86]. The overpotential for the ORR is much larger than that for the HOR; therefore, it contributes more to the reduction in PEMFC performance [87]. Thus, more Pt is used at the cathode than at the anode, due to the sluggish ORR kinetics [86]. Alternatives for Pt are other platinum group metals, including palladium, ruthenium, rhodium, iridium and osmium [88].

To reduce the amount of precious Pt used, they are supported with porous and conductive carbon surfaces with Pt coated or electrodeposited on the carbon surface. The use of a carbon support provides a high, active surface area, good electrical conductivity, stability and catalytic activity [7,89]. As carbon supports, highly conductive carbon blacks having a high surface area are used, such as Vulcan XC – 72R, Black Pearl 2000, Ketjen Black and Denka Black [90].

The gas diffusion layer (GDL) is primarily a porous material usually developed consisting of carbon fibre paper or carbon cloth support with macroporous and microporous layers. The typical pore size for the macroporous structure varies between 290 – 400 µm, for the microporous layer between 10 – 100 µm and the catalytic layer a few hundred nanometres, as shown in Fig. 6 [91]. The microporous layer consists of carbon black powder and a hydrophobic agent

that pushes the water away from the membrane to the flow-fields to avert flooding. It also facilitates the effective distribution of reactant gases at the membrane surface.

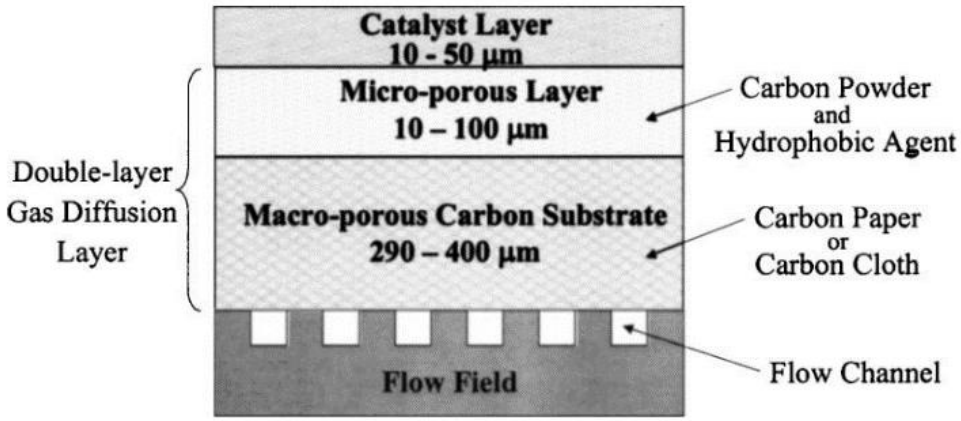

Figure 6: Schematic of a double-layer gas diffusion layer; the macroporous substrate is in contact with the flow-field and inlet gas, while the microporous layer is in contact with the catalyst layer. Figure adapted from [92].

The macroporous layer allows for the electrical contact between bipolar plates and electrode, as well as mechanical support between the flow-field and the microporous layer [93–95].

Bipolar plates are critical components in a PEMFC and have a multifunctional character, including distribution of reactants, conducting electrons from cell to cell, water removal from MEA, thermal management and providing mechanical compression [92]. Bipolar plates constitute a significant part of a PEMFC and its manufacturing costs [96]. Thus, for a real-time application, they must be of lightweight, cost-effective and easily manufactured materials. Furthermore, for any material to be considered as a good fit for bipolar material, it should possess good thermal conductivity (as high as possible), good electrical conductivity (resistance < 0.01 Ω cm^2), low hydrogen gas permeability (< 10^{-4}

cm^3 (STP) . cm . cm^{-2} . s^{-1} . $cmHg^{-1}$), low corrosion resistance (< 0.016 mA cm^{-2}), high compressive strength (> 1540 g cm^{-2}) and density (< 5 g cm^{-2}). Some major bipolar plate materials that satisfy the above material properties include graphite, sheet metal and polymer composites [9]. Fig. 7 identifies the different bipolar plates based on material classification [92].

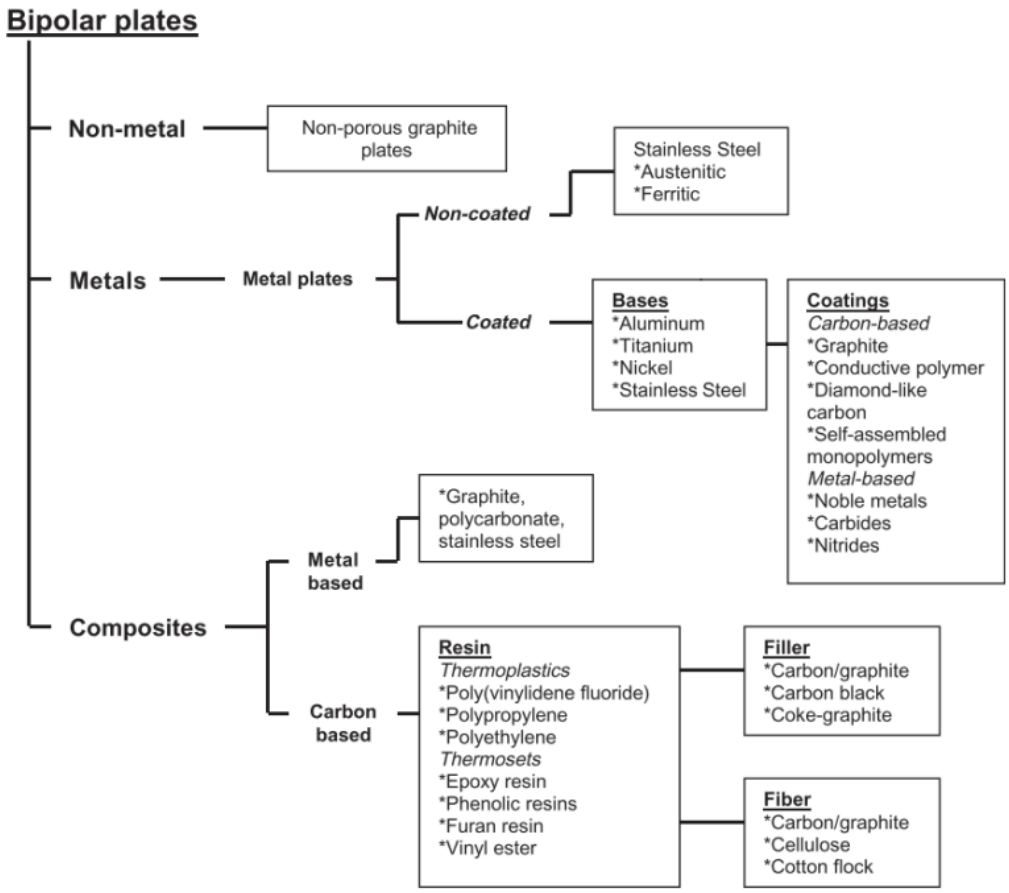

Figure 7: Classification of materials used as bipolar plates in PEMFC. Figure adapted from [91].

Apart from the materials discussed, printed circuit board (PCB) could also be used as a flow-field for PEMFCs: it is an effective material in terms of cost-effectiveness, ease of manufacturing, compressive strengths and durability. This planar material is also advantageous in terms of weight and volume constraints that make it an ideal replacement for existing bipolar plates [97].

2.2. Manufacturing methods

2.2.1. Conventional PEMFC flow-field overview

Flow-field plates (mono-polar or bi-polar plates) are a crucial component in PEMFCs, as they supply fuels, oxidant, and fuel hydrogen to their respective electrodes. They also remove water, collect current and provide mechanical support for components in the PEMFC. Other essential functionalities of a flow-field plate are:

- Separation of gases
- Providing an electrically conductive medium at the electrodes
- Even distribution of gases at the electrodes
- Structural support to fuel cell components
- Providing water and heat management

Design of a flow-field is crucial in delivering the functionalities discussed above effectively. If any of these functionalities fails, the performance of a PEMFC will be impacted significantly. A variety of flow-field designs are used in fuel cell research and industry:

- Pin-type flow-field
- Series-parallel flow-field
- Serpentine flow-field
- Interdigitated flow-field
- Metal sheet flow-field

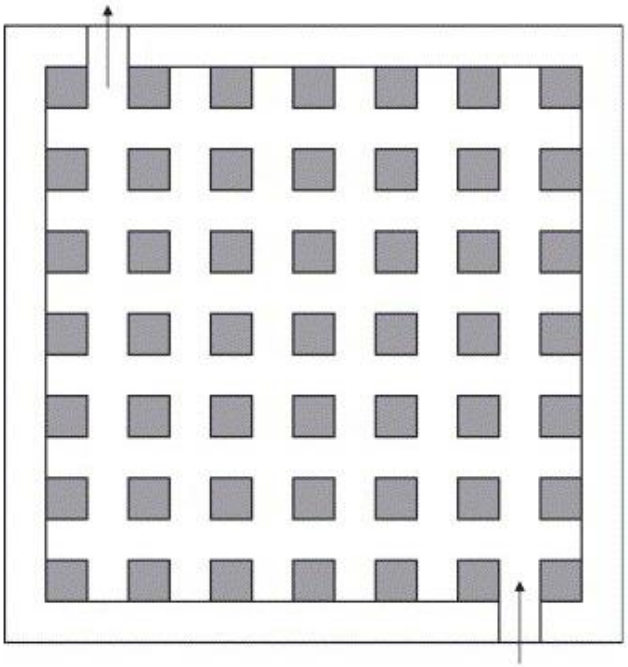

Figure 8: Pin-type flow-field arrangement for PEMFC. Figure adapted from [8].

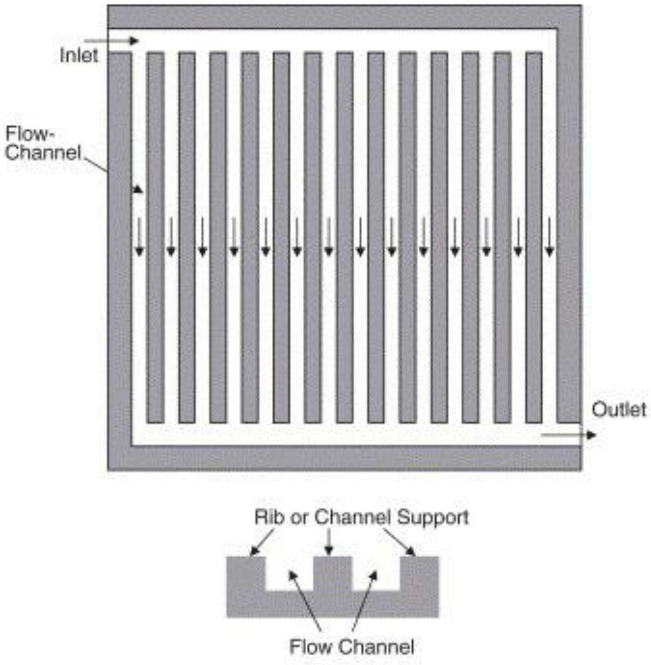

Figure 9: Straight/parallel flow-field arrangement for PEMFC. Figure adapted from [8].

The pin-type flow-field consists of a network of pins, either in circular or cubical shape and arranged in regular patterns. The reactant gases flow through the

intervening grooves, formed by the pins. The reactant flow through the pins follows the path of least resistance, thus resulting in reactant stagnation, uneven distribution and recirculation around the pins. A typical pin type flow-field example is shown in Fig. 8 [8]

A straight flow-field includes a series of parallel flow paths connecting the inlet and outlet headers, as shown in Fig. 9 [8]. Issues of pressure drop, uneven reactant distribution and improper water management are common in this type of flow-field design. The water formed in the flow channels accumulates at the bottom of the flow-field and requires an excess reactant gas purge to remove it. This accumulation results in a decrease in reactant usage efficiency and higher parasitic consumption in PEMFC operation [98].

A serpentine flow-field involves (a) single channel(s) travelling from the inlet to outlet of the reactant flow. The flow-field includes alternating regions of reactant flow and land, as shown in Fig. 10 [99]. This flow-field allows the reactant flow to traverse over the complete active area of the fuel cell. However, due to the long paths for the reactant to travel in this flow-field, severe concentration gradients occur between inlet and outlet. Also, the water generated accumulates in the flow path, thus requiring greater flow rates of oxidant to purge the excess water [100].

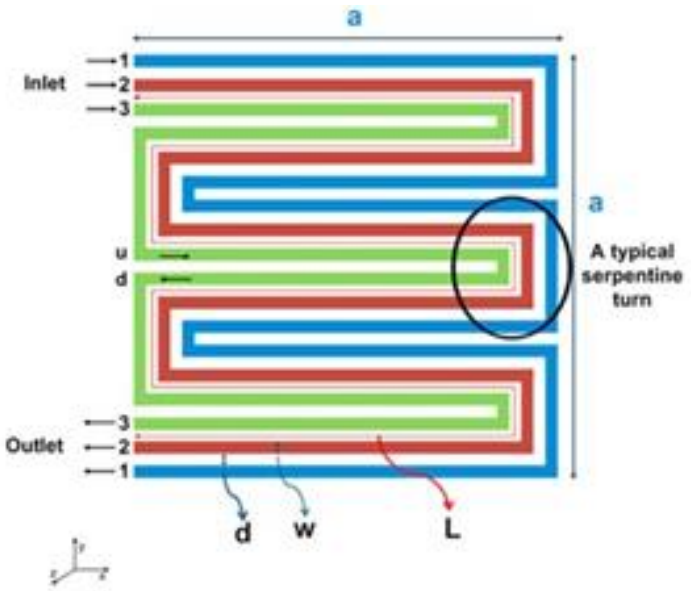

Figure 10: Serpentine flow-field configuration of a PEMFC. Figure adapted from [84].

An interdigitated flow-field provides convection to the gases normal to the electrode surface that allows for better mass transport and enhanced water removal capability from porous backing layers of the MEA. The flow channels are not continuous from inlet to outlet and are dead-ended, as shown in Fig. 11 [101].

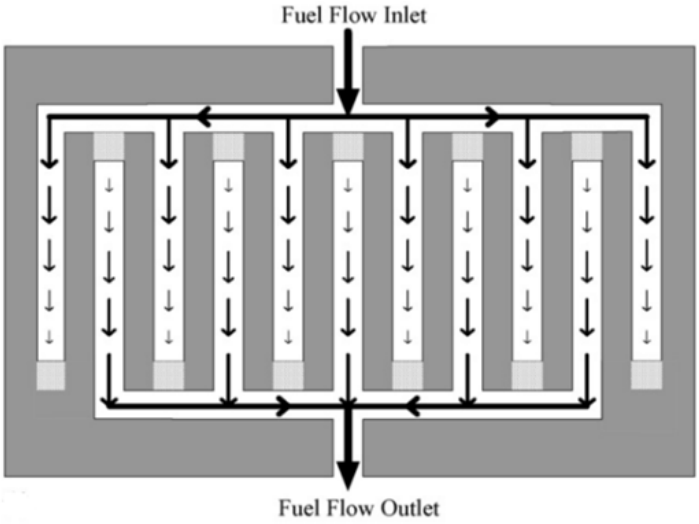

Figure 11: Interdigitated flow-field configuration of a PEMFC. Figure adapted from [86].

Dead-ended operation pressures the reactant flow through the porous backing layer, improving the fuel cell performance. However, large pressure losses occur on the oxidant side, requiring greater parasitic power for air compression and its drive-through [8].

Overall, the materials for use as flow-field plates should have good chemical stability, resistance to corrosion, electrical conductivity, gas impermeability, thermal conductivity, ease of manufacturability, weight and volume, and mechanical strength [9]. Non-porous graphite, coated metals and composite materials satisfy the criteria necessary for being ideal flow-field materials. The following sections will discuss in detail the different materials, satisfying the above criteria, conventionally used for developing fuel cells.

Graphite flow-field plates

Graphite primarily avoids the corrosion issue related to the low pH and humid operation of a PEMFC. It also shows good thermal and electrical conductivity, low density and ease of manufacturing. Flow-field designs, as shown in Fig. 12,

are developed on graphite plates using CNC machining. However, the porosity and brittle nature of graphite require the flow-field plates to be thick, increasing the weight and volume of the fuel cell.

Figure 12: Graphite flow-field (bi-polar) plates for PEMFC. Figure adapted from [165].

Metallic flow-field plates

Metallic flow-field plates have greater thermal and electrical conductivity, as shown in Fig. 13 [102]. They provide low gas permeability, are easy to manufacture and thin in dimensions. Metallic flow-field plate manufacturing options include CNC milling, foaming, die casting, etching, stamping and embossing. However, they pose corrosion issues, due to the low pH conditions inside a PEMFC, reducing the flow-field plate conductivity. Furthermore, the

metal ions leach out of the plates, damaging the MEA. Besides, the use of metals, like stainless steel, aluminium, titanium and chromium alloys increases the cost of a fuel cell.

Metallic flow-field can be manufactured from materials like titanium, chromium, stainless steel and niobium. Metallic flow-field can be made corrosion resistant

with coatings and can include reactant flow channels and cooling channels brazed together as a single plate. These flow-fields can also reduce the weight and volume of stacks compared to the carbon-based flow-fields. Also, the cost and complexity involved in manufacturing are some issues hindering the use of metallic flow-field on a wide range of fuel cell applications [103].

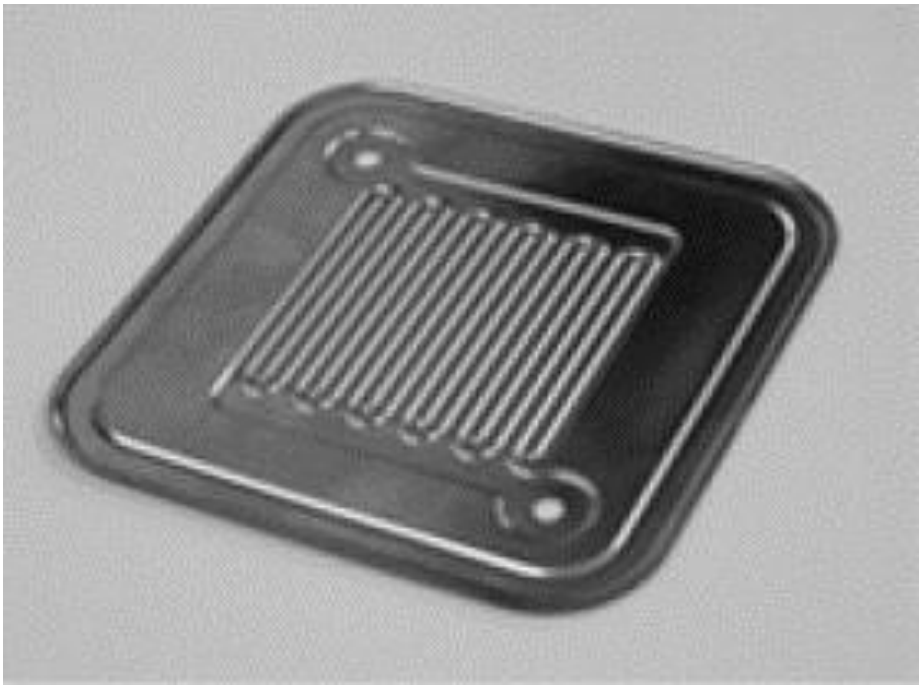

Figure 13: Metallic flow-field plate for PEMFC. Figure adapted from [102].

Composite flow-field plates

Composite flow-field plates are developed from dispersing conducting filler materials, like carbon or metal through an insulating polymer matrix, as shown in Fig. 14 [104], providing necessary thermal and electrical conductivity.

Metal-based polymer composite involves the addition of metallic components, like copper or aluminium to the composite materials, in developing flow-field plates [105]. Though it improves the thermal and electrical conductivity, issues of corrosion from the presence of metal could be significant. In addition, the conductivity differs between in-plane and through-plane directions of the flow-field.

Figure 14: Injection moulded graphite flow-field plate for PEMFC. Figure adapted from [104].

Thermosets or thermoplastics are the two types of polymers typically used in carbon-based polymer composite flow-field plates. Thermoplastics include polypropylene, polyethylene terephthalate, and polyvinyl fluoride, while

thermosets include vinyl esters, phenolic and epoxy resins. The filler carbons can be chosen from a wide range, like graphite, graphene, carbon black, carbon fibre and carbon nanotubes. Composite flow-field plates are mostly manufactured by methods like injection moulding and compression moulding.

Apart from the materials discussed, printed circuit boards (PCBs) can also be used as a flow-field for PEMFC; PCB has been a useful material in terms of cost-effectiveness, ease of manufacturing, compressive strengths and durability. This planar material is also advantageous in terms of weight and volume constraints that make it an ideal replacement for existing bipolar plates [97].

2.2.2. Printed circuit board (PCB) based PEMFC flow-field

The printed circuit board (PCB) is a well-known and extensively used material in the electronics and electrical industry. PCBs are made from FR4 composites (epoxy resin and glass fibre) and coated with a thin copper layer that acts as conductor. Such a conducting surface on a composite substrate makes it an ideal candidate for power generating applications, such as fuel cells.

The PCBs provide a wide scope in fuel cell development, especially for portable applications. They provide a range of advantages, like [62]:

- Lightweight composite materials
- Planar in nature
- Flexible
- Ease of manufacturing and low cost
- Low-temperature fabrication
- Low-volume stacks

The PCB material has low through-plane (0.29 W/m.K) and in-plane thermal (0.81 W/m.K) conductivities, high compressive strength (> 415 MPa), and low water absorption (<0.1 %) [107],

O'Hayre et al. [62] developed one of the first PCB hydrogen/oxygen based fuel cells, having a multi-cell voltage of 16V and a volumetric power density of 400 mW cm^{-3}. This study identified the possibility of using a PCB in developing portable PEMFCs with a maximum capacity of 1 kW. Schmitz et al. [106] developed air-breathing PEMFC using PCB technology with a 100 mW cm^{-2} power density and long-term operation for 1500 h. In addition, a Ni/Au coating

was suggested on the PCB substrate to avert corrosion occurring from fuel cell operating conditions. Obeisun et al. [64] studied the performance of a PCB fuel cell and simultaneously utilised thermal imaging to correlate the effect of PCB “bowing” with the lower temperatures observed. Schulze et al. [107] developed a bipolar plate using a PCB with segmented flow-fields. The segments were connected through resistances. This connection allowed for the measurement of the current density distribution on the flow-field of a PEMFC during its operation. Furthermore, the use of PCB in fuel cells has been mostly to study the current density distribution at the flow-field level and correlate with the PEMFC performance and other characterisations [63,108,109].

Other PCB-based fuel cell applications include water management in fuel cells with neutron imaging [65,110], understanding water management in capillaries-based PEMFC [66], cold start operation analysis on PCB PEMFC [63], use of PCB as current collector [111] and analysing the localised current density distribution [112,113].

2.3. PEMFC Metrology

Polarisation

A polarisation curve is considered to be a measure of fuel cell health. It is a plot between the voltage and current density developed in a PEMFC. Polarisation is a standard electrochemical technique to analyse the performance of a PEMFC.

A typical polarisation curve for a PEMFC is shown in Fig. 15 [114,115] and Fig. 16 [116]. The initial decrease in voltage from the equilibrium potential corresponds to losses occurring from activation polarisation. Furthermore, a linear region of voltage decrease is observed corresponding to the Ohmic losses, and, finally, the steep decrease in voltage following the Ohmic region corresponds to concentration polarisation losses.

Activation voltage losses occur to let the electrochemical reactions depart from the equilibrium conditions (OCV). The activation voltage losses correspond to both anode and cathode; however, a major contribution occurs from the cathode region, due to its sluggish kinetics of oxygen reduction reaction (ORR). Furthermore, Ohmic voltage losses arise due to the resistances developed from proton conductivity in electrolyte and electron conductivity through the electrode and other fuel cell components. Concentration voltage losses occur due to the mass transport limitations occurring from a high current density condition.

A polarisation curve provides the necessary information on the overall performance of a PEMFC. However, it cannot identify the performance contribution occurring from individual components within the cell. Furthermore, it is difficult to deduce the different dynamic mechanisms occurring inside the fuel cell and their influence on its performance.

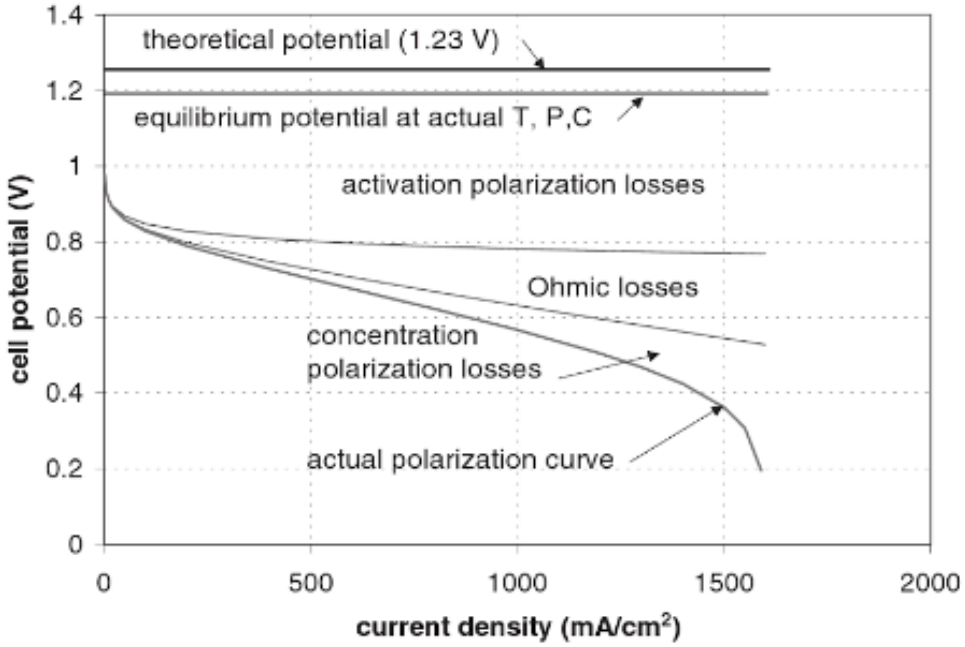

Figure 15: Polarisation curve of PEMFC with voltage losses. Figure adapted from [99,100].

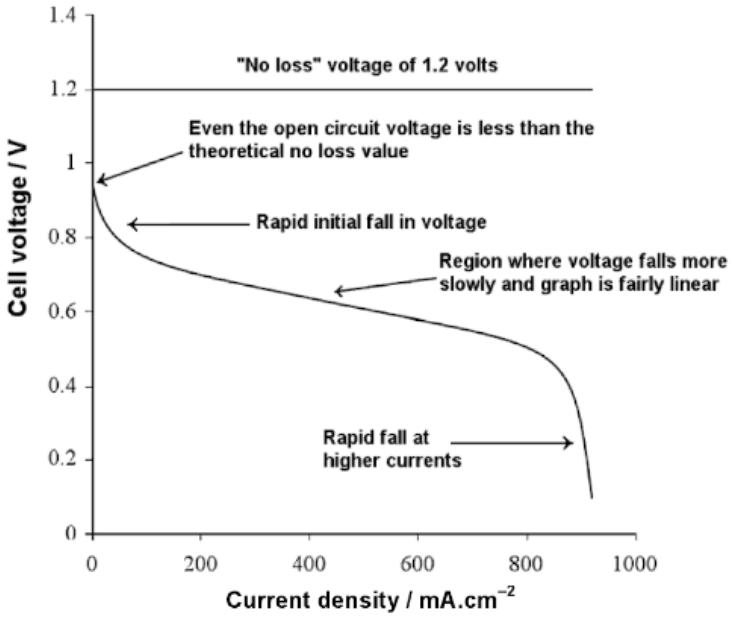

Figure 16: Polarisation curve with voltage fall analysis. Figure adapted from [101].

Polarisation is the most common electrochemical measurement method for analysing PEMFC performance. However, it is limited in terms of analysing the

underlying mechanisms, due to the overlap of different processes. Electrochemical impedance spectroscopy (EIS) is instrumental in overcoming the shortcomings in polarisation. EIS is a powerful characterisation technique to analyse the performance of PEMFCs [117] by understanding and analysing the inner workings for a PEMFC in steady-state and transient operating conditions.

Electrochemical impedance spectroscopy (EIS)

EIS involves the application of a small AC voltage or current perturbation. The resulting amplitude and phase of the signal is measured as a function of frequency. EIS for fuel cells is a non-invasive and effective performance characterisation and diagnostic tool [118,119]. EIS is instrumental in characterising diffusion losses [120], evaluating Ohmic resistances [121], evaluating MEA resistances [122,123] and studying ORR kinetics [124] in fuel cells.

Impedance data are conventionally presented either as Bode plots or as Nyquist plots. A Bode plot involves amplitude and phase of the impedance plotted as a function of frequency. The Nyquist plot involves the imaginary part and the real part of impedance plotted against each other. A typical Nyquist curve of the impedance spectra is shown in Fig. 17 [89,116] and the arc identified has the frequency increasing from right to left.

The equivalent circuit for the single arc in Fig. 17 is represented by the Randles circuit, a common fuel cell model used for electrochemical interfaces [125,126]. The R_{el}, R_{ct} and C_{dl} correspond to the electrolytic resistance, charge transfer resistance and double-layer capacitance, respectively [89,116].

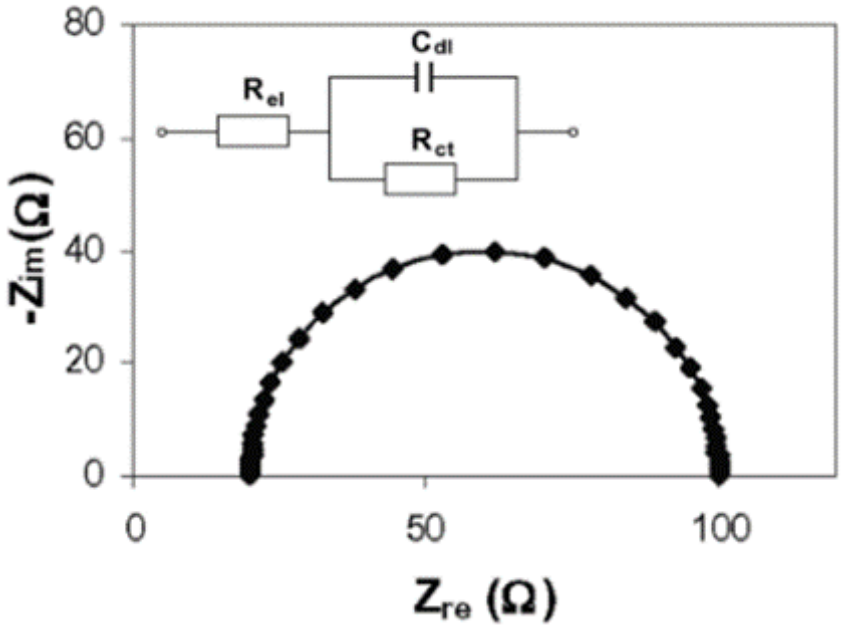

Figure 17: Simulated Nyquist curve over a frequency range of 0.1 Hz and 100 kHz with the Randles equivalent circuit. Figure adapted from [73].

Acoustic emission (AE) technique

Acoustic emission (AE) involves the generation of spontaneous elastic waves, due to the release of energy from a material or system undergoing mechanical perturbation [127]. The elastic waves then propagate through the material to be generated into detectable AE signals. AE-based monitoring and analysis is a non-invasive and non-destructive testing (NDT) process that has been instrumental in the study and characterisation of a wide range of applications, from small to industrial scales, such as medical diagnostics and therapeutics [128], and fatigue of metal plates [129]. AE-based analysis of electrochemical processes has been applied in studying corrosion, like cracking of stainless steel [130] and the structure of steel-reinforced concrete beams [131], in battery technology for the study of electrodes [132,133], lifetime evaluation of Li-ion batteries [134] and safety assessment tests [135], and in electrolysers for

performance analysis and as *in situ* diagnostic tool [136]. However, discrepancies in AE analysis can occur from the interference of elastic waves generated from the surrounding material and ambient conditions. Hence, to avoid such external disturbances, careful isolation of the target measurement is necessary, especially with a set of threshold acoustic conditions that will subtract the AE generated from the surrounding conditions [137].

In the field of fuel cells, AE has been utilised in understanding the thermophysical characteristics of a solid oxide fuel cell [138], the water uptake of Nafion® membrane and the impact of water content on the dimensional changes occurring in a membrane [139,140], and the performance diagnosis of a PEMFC under different operating conditions [137]. Legros et al. [137] performed AE-based characterisation of a PEMFC under different cell configurations and operating conditions. They identified that AE from a PEMFC is sensitive to the hydrodynamics of gas flow in the flow-field channels.

Electro-thermal mapping technique

Electro-thermal mapping involves the measurement of current and temperature distribution on the surface of fuel cells using a localised, segment-based measurement approach, as shown in Fig. 18. The electrochemical reactions occurring inside the cell result in the generation of electrical energy and by-product heat and water, whose quantity is dependent on the level of electrochemical reaction occurring inside the cell.

Current and temperature mapping have been instrumental for the *in situ* diagnosis and analysis of water management [141–143], reactant concentration and distribution [30,142,144], reactant physical conditions [145,146], flow

channel configurations [147], thermal management [148,149] and cell compression [150] on the performance of the cell.

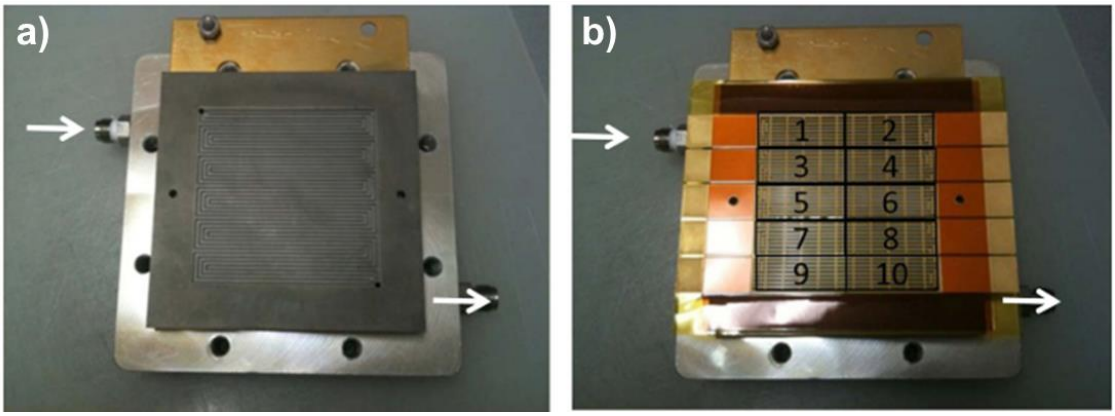

Figure 18: A photograph of the fuel cell bipolar plate: a) anode serpentine flow-field plate and b) segmented (1- 10) current distribution board anode serpentine flow-field plate. Figure adapted from [151].

Some of the current distribution measurement techniques include indirect correlations based on local values [152], use of magnetic effects and Hall sensors [153,154], a measure of local potential at the GDL and catalyst layer and segmented measurement [155]. The temperature distribution measurement techniques include thermocouple insertions [156], infrared imaging [149,157] and segmented measurement. Segmented measurements are identified as a popular technique, especially for combined current and temperature measurements, due to their ability to directly analyse a localised phenomenon, like reactant starvation and flooding inside the fuel cell [141,157,158]. Furthermore, PCB-based segment current collectors are widely used in the combined measurements of current and temperatures, due to their low-cost operation, usage flexibility during assembly and disassembly, easy implementation, and *in situ* measurement within the cell [144,148,159,160].

3. Methodology

3.1. NICE approach for the development of lung-inspired PEMFCs

Lung has the unique ability to bridge length scales, irrespective of size, while providing uniform distribution of oxygen into the blood cells with minimal thermodynamic losses. This is achieved through the narrowing fractal tree like bronchi structure transitioning into a more uniform channel architecture called acni.

Hierarchical transport networks and the unique structural characteristics of the lungs are utilised in the development of lung-inspired fractal flow-fields for PEMFCs in this study. The corresponding flow-field development methodology overview is summarised in Fig. 19.

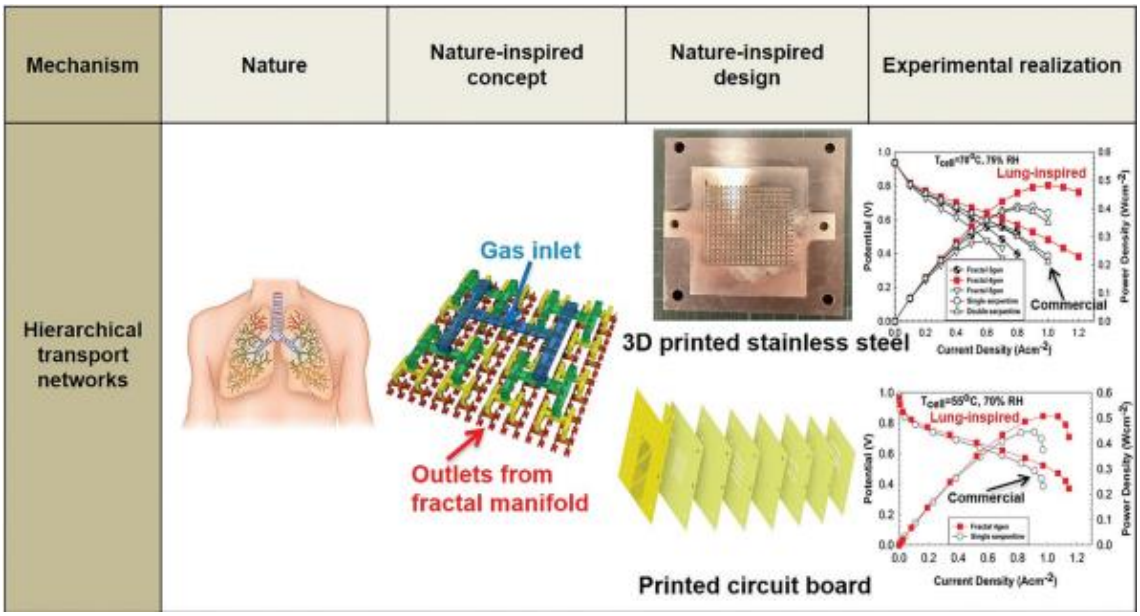

Figure 19: Schematic of the step-wise employment of NICE approach for the development of lung-inspired flow-fields for PEMFCs [161].

3.2. Design and conceptualisation of lung-inspired, fractal flow field

This thesis aims to develop a reactant supply system (cathode flow-field) for a PEMFC that can deliver the reactant gases to all regions of the MEA and remove the water uniformly, while keeping the PEMFC performance under optimal operating conditions. Furthermore, the flow-field should ensure optimal thermodynamic efficiency during operation.

The air transport mechanism in human lungs has a hierarchically organised, fractal structure, which has the ability to bridge length scales over 3-5 orders of magnitude. The fractal structure ensures a uniform distribution of oxygen throughout the volume of the lung. The human lung operates in two transport regimes: convection-dominated flow and diffusion-dominated transport. The upper part of the lungs consists of bronchi, with 14-16 self-similar generations of branches, which slow down the convection-dominated airflow to be compatible with the flow-through acinar airways, at the terminal bronchioles[162]. The acini contain 7-9 lower generations of more uniformly sized branches, which support diffusion dominated transport. In addition, the proportioning of the airways in the branching structure allows for the same entropy production in each branch, within both these regions, which minimises the overall entropy generation throughout its structure and leads to exceptional thermodynamic efficiency[163]. Furthermore, the transport of air inside the lungs through the fractal architecture obeys Murray's law, which states that the sum of the cubes of the diameter of the daughter branches is equal to the cube of the diameter of the parent branch:

$$D_p^3 = \sum_{i=1}^{n} D_i^3 \quad (4)$$

Where D_p is the diameter of the parent branch, and D_i is the diameter of a daughter branch. By obeying Murray's law, the overall global entropy generation in the flow structure is minimised.

The lung-inspired fractal flow field in this study comprises a tree with several generations of self-similarly repeated branches, inspired from the bronchial tree in lungs, spanning multiple length scales. In this study, the fractal geometry comprises of H-shaped, repeated units, as shown in Fig. 2, over 4 generations. The area-filling H-shaped units ensure uniform distribution of the reactants on the MEA region in a PEMFC, as will now be discussed.

The "H" shape from generation 1 develops into 4 smaller, similar "H's" at the ends of the initial H; this division is repeated from one generation to the next. The scale of each daughter H is half that of its parent H, implying that with each generation the distance between adjacent gas outlets in halved. With this, the fractal (similarity) dimension D [164] is evaluated by:

$$D = \frac{\log(n)}{\log(\frac{1}{s_f})} = \frac{\log(4)}{\log(\frac{1}{2})} = 2 \quad (5)$$

where n is the number of daughter shapes for a single parent shape, and s_f is the reciprocal of the size factor between daughter and parent. A fractal dimension D = 2 indicates that, for an infinite number of generations, the fractal structure is plane-filling. Thus, it can be concluded that the branching leads to 4^n outlets at the nth generation, with equal flow path length, and the structure remains planar in nature. This uniform, planar structure allows for uniform distribution of gases, due to the uniformity in the hydraulic path lengths from the gas inlet to the multiple outlets. Furthermore, the scaling of channel diameters

between the parent and daughter branches in the fractal structure is based on Murray's law, as given in equation (4) [165].

In addition, the fractal branching reduces the flow velocity, due to the net increase in total cross-sectional area over all the daughter branches at each generation. The gas transport thus transcends from a convective dominated flow at the entrance to include increasing contributions of diffusion at higher generations. In this study, the last generation meets the GDL of the fuel cell, where diffusion-dominated flow improves gas transport in this region [57,166].

The relationship between convective and diffusive flux is characterised by the Péclet (P_{e_L}) number [167,168], which is defined by:

$$P_{e_L} = LU/D_f \tag{6}$$

where L is the characteristic length (m), U is the flow velocity (m s^{-1}), and D_f is the diffusivity (m^2 s^{-1}). The flow velocity at the gas distributor and GDL interface is given by:

$$U = \frac{Q_i}{A_N 4^N} \tag{7}$$

$$A_N = \frac{\pi D_i^2}{4} \tag{8}$$

Where, Q_i is the volumetric flow rate through the gas inlet, N is the number of generations, and A_N the cross-sectional area at the end of the Nth generation as given in equation (8). It can be observed from equation (7) that the increase in cross-sectional area at the end of each generation results in a decrease in velocity U at that generation.

3.3. Experimental realisation and prototype development

The specialised manufacturing process methodology, using printed circuit board (PCB) technology, for realising the mathematical and conceptual designs in the development of lung-inspired flow-fields in Section 3.1 is discussed in this section.

3.3.1. Prepreg for multi-layer PCB bonding

Prepregs (pre-impregnated reinforcing fabrics) are used for the multi-layer PCB bonding in a hot press. A schematic of the hot press mechanism used for the assembly of planar PCB layers into flow-fields is given in Fig. 20.

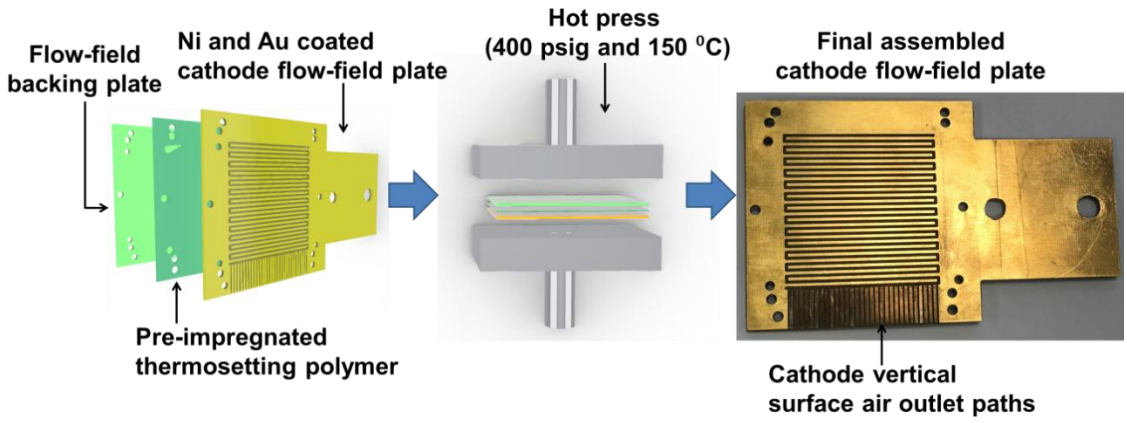

Figure 20: Schematic outline of layer-wise PCB based PEMFC flow-field assembly. The example presented here is of a 25 cm^2 cathode single-serpentine flow-field.

A hot press methodology is followed to achieve high-quality bonding between the PCB layers. It involves prepreg heating and melting, resin curing and a cooling-down cycle, as shown in Fig. 21 [89].

In the resin heating, melting and flowing region, the resin in the prepreg is heated initially to around 60 °C; then, compression is applied to allow the

prepreg to adjust between the PCB layers. The PCB plates with prepregs inserted between them are heated at a rate of 10 °C min^{-1} until a temperature of 140 °C is reached. During this heating phase, the resin becomes less viscous and reaches a minimum melt viscosity at which the resin flows between the PCB plates and sets at 140 °C.

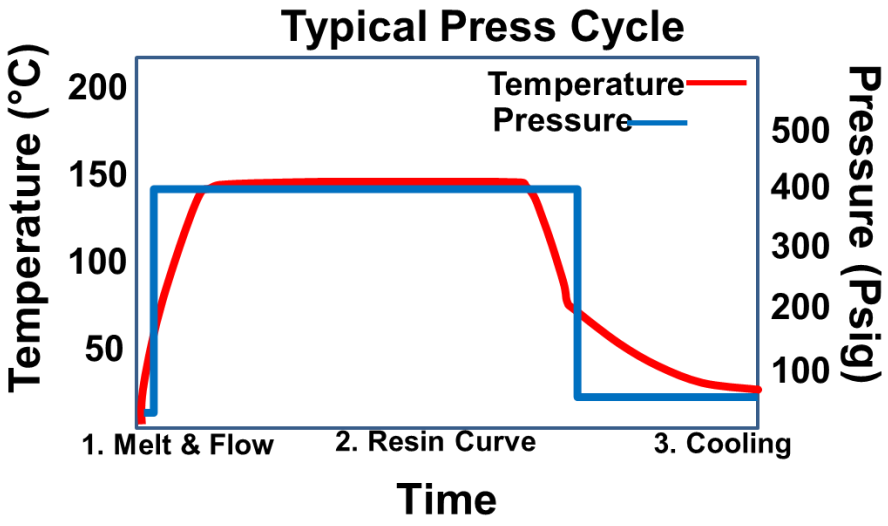

Figure 21: An example of press cycle for multi-layer PCB bonding. Figure adapted from [89]

Once the resin is well set, it continues to be heated for another 60 min. Finally, cooling of the pressed PCB plates is carried out at a rate equal to or larger than the heating rate. This cooling allows for the uniform bonding of the individual PCB layers into a fuel cell flow field [89].

3.3.2. Electroplating of PCB plates

Printed circuit board (PCB) plates used for fabricating the fractal and other relevant flow-fields in this thesis have a layer of copper coating on them. To avoid oxidation of Cu and further metallic degradation of the electrode materials due to Cu the PCB plates developed in this thesis are Ni and Au coated.

The Ni and Au coating mechanisms are as follows. The copper layer on the PCB plates is initially cleaned with a fine mesh paper to remove any sediments and dust on its surface. Later, large fragments on the surface of the copper PCB plate are removed through ultrasonic cleaning. Ultrasonication is followed by acidified peroxide cleaning for the removal of fine fragments. The peroxide solution retains the Cu, while removing the Cu^{+}/ Cu^{2+} species from the PCB surface.

Peroxide cleaning of the Cu PCB plate is based on Fenton's mechanism, as given below [169]:

$$Cu^{+} + H_2O \rightarrow Cu^{2+} + OH^{-} + OH^{\cdot} \quad (9)$$

$$Cu^{2+} + H_2O_2 \rightarrow Cu^{+} + H^{+} + OOH^{\cdot} \quad (10)$$

$$OH^{\cdot} + H_2O_2 \rightarrow H_2O + OOH^{\cdot} \quad (11)$$

$$OH^{\cdot} + Cu^{+} \rightarrow Cu^{2+} + OH^{-} \quad (12)$$

Fenton oxidation is capable of self-generating oxidants, as seen in the equations (9) – (12). Hydrogen peroxide acts as an reductant first and later as oxidant.

After the cleaning of the Cu layer on the PCB, Ni coating is performed before a Au layer is deposited on the Cu surface. Ni ensures that the solid-state diffusion of Au into the Cu layer is averted, especially at higher temperatures. It also prevents the exposure of less noble Cu to the MEA [97].

Ni electroplating is performed using 0.13 M $Ni(SO_3NH_2)_2$ solution at 4.3 mA cm^{-2} current density and between 3.0 – 3.5 V for 3 min. It is followed by Au

electroplating using 0.02 M $KAu(CN)_2$ solution at a current density of 2.4 mA cm^{-2} and between 3.5 – 3.7 V for 60 min, respectively.

3.3.3. Layer wise fractal flow field(s)

The fractal flow-field features are developed using the Rhinoceros 3D computer graphics and computer-aided design application software tool, version 6 (UCL educational license).

Rhinoceros software can be utilised on any existing system hardware, irrespective of the complexity, degree or size of the model. In addition, the software allows for several advanced features, like edit, analyse, model, render, animate, surfaces, curves, extrusions, solids, etc.

The working panel of Rhinoceros simulation software, as shown in Fig. 22, illustrates different views of the design (top, right, front and perspective) and individual layers (a - x) of the fractal flow-field, and others. The developed virtual designs in Rhinoceros software are converted into stereolithographic (.stl) files, which are used as input files for a computer connected to a computer numeric control (CNC) machine, which is used for converting the virtual designs into real objects through different fabrication methods.

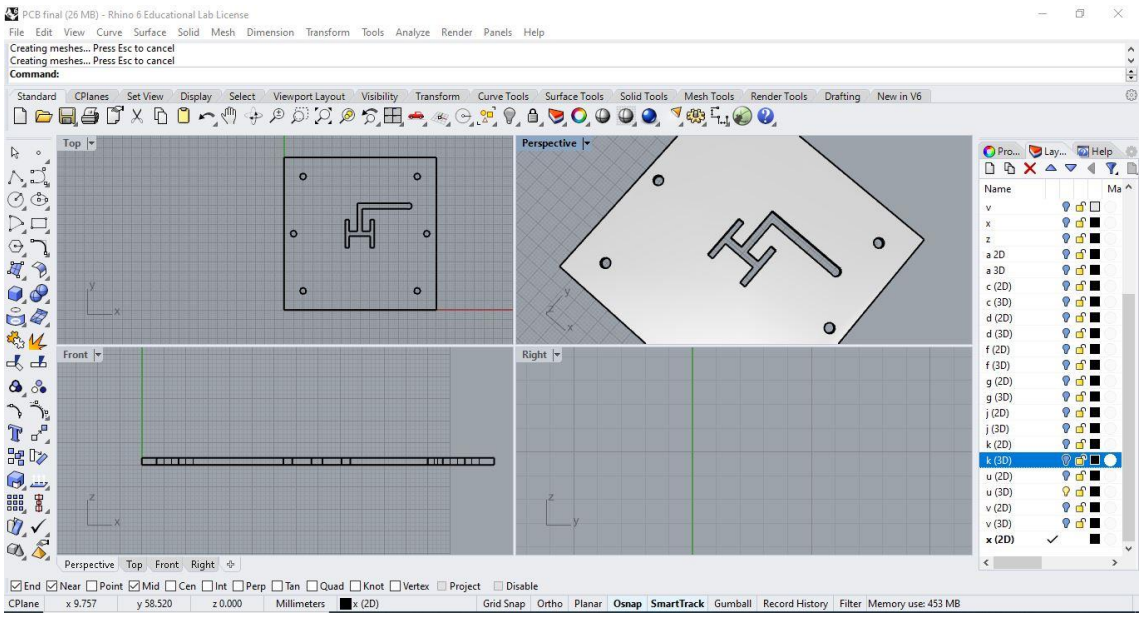

Figure 22: Simulation working panel of Rhinoceros software - Version 6.0. UCL educational license.

The following section illustrates the manufacturing methodology using the CNC technique in detail.

3.4. Manufacturing

Computer numeric control (CNC) machining

Computer numeric control (CNC) is a programmed manufacturing process, where a virtual design of an object is converted into a real one. A CNC fabrication process involves cutting or drilling of material into the desired object with the help of cylindrical tools and spindle holders. The milling process converts the computer program or design into Cartesian coordinates for precise manufacturing of objects from materials. A Roland MDX-40A CNC [170] machine is used to cut and drill the flow-field channel features of each PCB layer. A built-in software program for the CNC machine allows for the conversion of virtual designs to fit into the corresponding Cartesian coordinates for milling. The cutting tools used for the machining are 0.4 mm and 0.8 mm diameter tools having a flute length of 2.0 mm (DIXI Polytool, Switzerland) [171]. The schematic of a milling tool is given in Fig. 23. The corresponding cutting parameters for the tools used here are given in Table 1.

Figure 23: Schematic of the milling tool. Figure adapted from Dixi tools [171].

Table 1: CNC cutting parameters and milling tool choice for PCB layers development

	XY speed (mm/s)	Z speed (mm/s)	Spindle rotation	Cutting in amount (mm)	Path interval
0.4 mm Φ tool	1	1	15000	0.01	0.01
0.8 mm Φ tool	5	7	10800	0.1	0.05

3.5. Metrology

3.5.1. X-ray computed tomography (CT)

X-ray CT scan imaging is an imaging technique that operates non-destructively to construct the interior images of an object using a sufficient number of X-ray projections [172]. The CT scans generate 2D images of an object, called radiographs, and sequential 2D scan images that are utilised to develop a 3D volumetric representation of the sample, called tomograph. The 2D images are often referred to as “slices” composed of “voxels” or “volume elements”, similar to the pixels of a digital image. X-rays passing through a slice of the material get attenuated either by absorption or by scattering. The attenuation depends on the material type of object imaged and the energy of the X-rays used. The scan generates gray images of the object (radiograph and tomograph), and the observed gray levels in a scanned image depend on the level of X-ray attenuation offered by the material of the object being imaged. The intensity of attenuations for a monochromatic X-ray beam is based on Beer’s law, as given in equation (13):

$$I = I_o e^{-\mu x} \tag{13}$$

where I and I_0 are the final and initial X-ray intensities, μ is the material’s linear attenuation coefficient, and x is the X-ray path length.

The most common method of obtaining a CT scan image, especially for industrial applications, involves an X-ray beam source and a detector, with the sample for imaging placed between them on a rotating platform, as shown in Fig. 24.

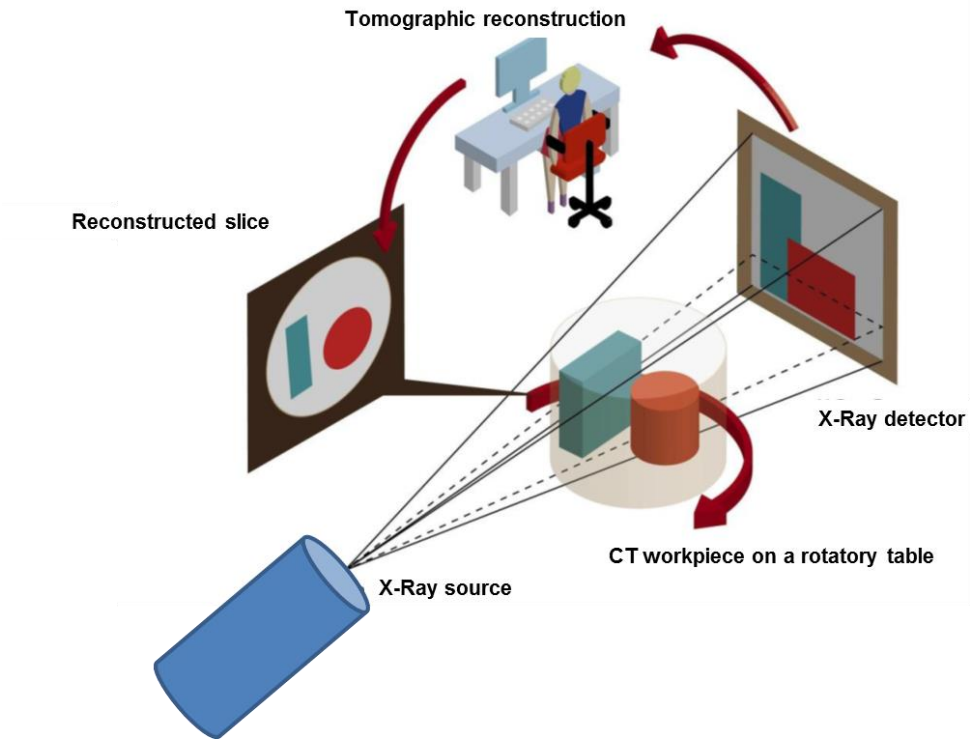

Figure 24: Schematic of cone beam scanner based X-ray CT scanning. Figure adapted from [173]

A cone beam is utilised for the tomographic imaging that allows for faster data acquisition in a single rotation. As the sample rotates (the rotation occurs on different angular orientations), the X-ray beam penetrates the sample and projects the 2D radiographs of the object on to the detector, as shown in Fig. 24. Several 2D radiographs are captured during the rotation of the sample and are processed through a software comprising of algorithms to generate a complete 3D reconstruction of the sample, called tomograph. A schematic example of the overall process of generating the tomograph of an object is shown in Fig. 25.

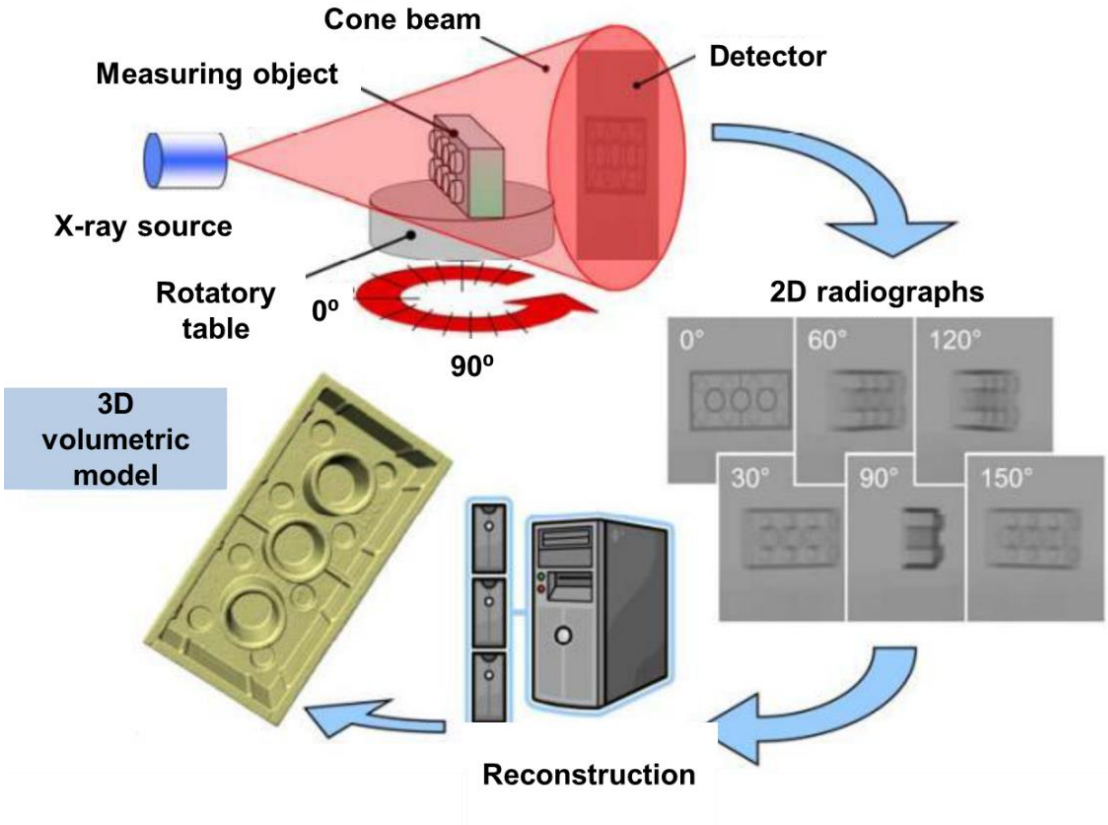

Figure 25: Schematic of X-ray CT reconstruction of an object. Figure adapted from [173].

3.5.2. Electrochemical impedance spectroscopy (EIS) (equivalent circuit)

Electrochemical impedance spectroscopy (EIS) is an effective and well-established technique for diagnosing the electrochemical performance of a fuel cell. In the EIS technique, first, a harmonic perturbation is imposed on the electrochemical system, and later the corresponding impedance from the system at a range of frequencies is measured. A frequency response analyser (FRA) and an electrical load are necessary for the EIS measurements, where a sinusoidal input generated from the FRA is fed via the load to the fuel cell. The response from the fuel cell is captured by the FRA, resulting in an impedance

spectrum. Furthermore, perturbations can be either by voltage/potentiostatic mode or by current/galvanostatic mode [174].

PEM fuel cells have complex mechanisms occurring inside them, and it is difficult to isolate and analyse these mechanisms based on the polarisation analysis alone. However, EIS has the capability to distinguish and identify the different processes, to a large extent, occurring inside a PEMFC. A typical EIS characterisation can identify, for instance, the reduction in cell performance and attribute that to membrane, charge transfer and mass transfer resistances developed in the cell, as shown in Fig. 26 [118].

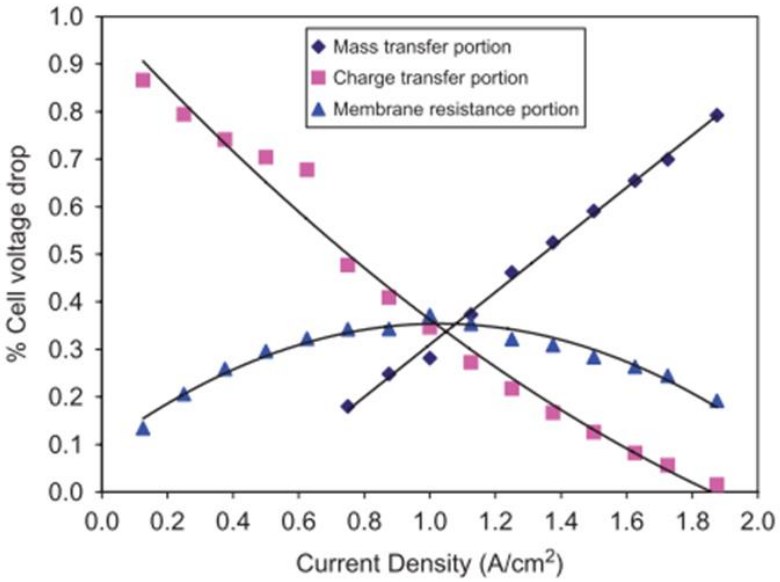

Figure 26: Percentage reduction in fuel cell performance (voltage) with respect to the mass transfer, charge transfer and membrane resistance. Figure adapted from [118]

EIS has several applications to PEM fuel cells and the most important of them include differentiating impedance contributions from different parameters in the fuel cell operation, like the membrane, electrode/catalyst, reactant distribution,

operating conditions and flow-field plates. It also has the ability to evaluate the individual contributions of the parameters to the overall cell performance.

Common EIS spectra, represented as Nyquist curves, for hydrogen and oxygen/air fuelled PEMFCs are shown in Fig. 27 [118]. Usually, two pronounced arcs appear in the EIS spectra, accounting for the charge transfer and the mass transfer processes in a PEMFC. The first arc to the left corresponds to the charge transfer process occurring at high frequencies and the second arc to the right corresponds to the mass transport process, occurring at low frequencies of the EIS measurement frequency range. The common frequency range for a PEMFC EIS measurement is between 10 mHz and 100 kHz [118].

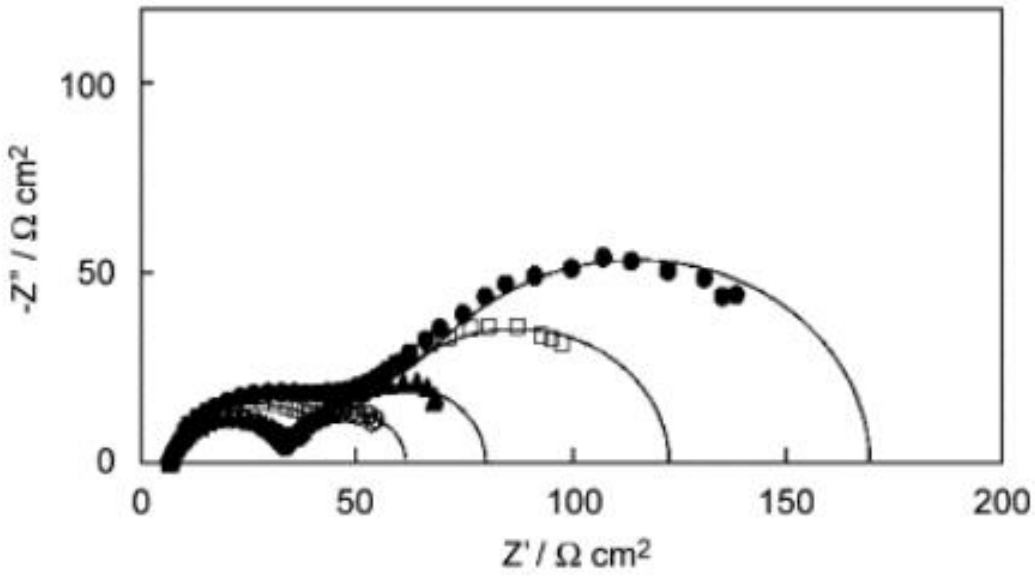

Figure 27: Nyquist curves for EIS measurements of a typical PEMFC with two distinctive arcs. EIS plot figure adapted from [175] [176]

The EIS spectra can be analysed with the help of measurement models, for instance, using equivalent circuits to identify the different resistances and capacitances developed in the cell. For a conventional EIS spectrum, as given in Fig. 27, the corresponding equivalent circuit is given in Fig. 28 [174].

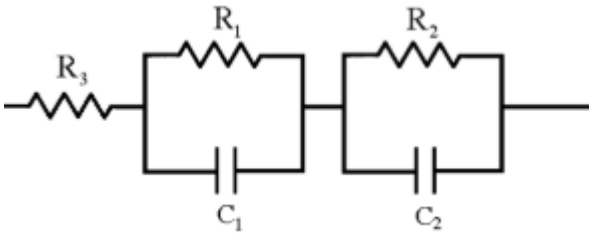

Figure 28: Equivalent circuit model for the EIS spectrum with two distinguishable arcs. Figure adapted from [174].

Each semicircle arc in Fig. 27 is modelled as a parallel combination of resistance and capacitor or constant phase element C_1 (CPE), as shown in Fig. 28. Typically, R_1, R_2 and R_3 in Fig. 28 correspond to charge transfer, mass transfer and Ohmic resistances, respectively.

A more detailed equivalent circuit model comprising of several resistance elements and a component-wise contribution to the overall resistance measurements is given in Fig. 29. It allows for detailed diagnostics and identification of the main degradation behaviours and their associated causes inside a PEMFC, as shown in Fig. 29 [177].

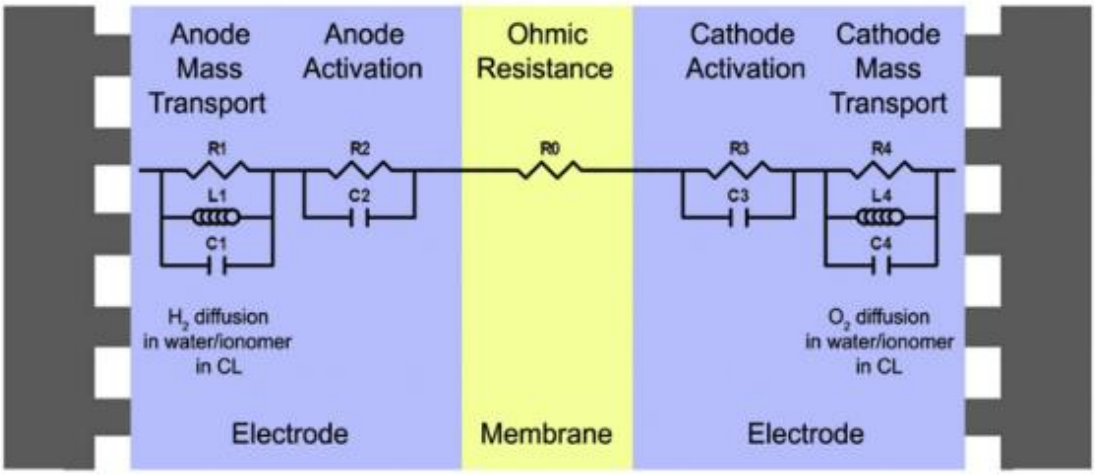

Figure 29: Detailed component-wise impedance contributions in a PEMFC. Figure adapted from [177].

Furthermore, the high frequency intercept of the first arc on the real axis of a Nyquist plot shown in Fig. 27 corresponds to the high frequency resistance (HFR) [178]. The HFR is a measure of the Ohmic resistance in the fuel cell that includes the membrane resistance together with the GDL, the bi-polar plate and the contact resistances. The HFR primarily reflects the membrane ionic resistivity levels, resulting from membrane hydration. In addition, the diameter of the first arc corresponds to the charge transfer resistances developed in the cell.

Under certain fuel cell operating conditions, a second arc appears in the Nyquist plots, as shown in Fig. 27 [118,179]. This arc corresponds to the low frequency arc and represents the impedance developed due to mass transport limitations. The mass transport limitations can occur from high current density operation, low reactant supply or flooding at the cathode [180]. The diameter of this arc corresponds to the resistances developed due to mass transport limitations.

3.5.3. Acoustic emission (AE)

Any material or system undergoing a mechanical perturbation releases energy that generates spontaneous elastic waves, which are called acoustic emissions (AE) [127]. The elastic waves then propagate through the material to be generated into detectable AE signals. A typical AE signal is given in Fig. 30. AE-based monitoring and analysis is a non-invasive and non-destructive testing (NDT) process that has been instrumental in the study and characterisation of a wide range of applications.

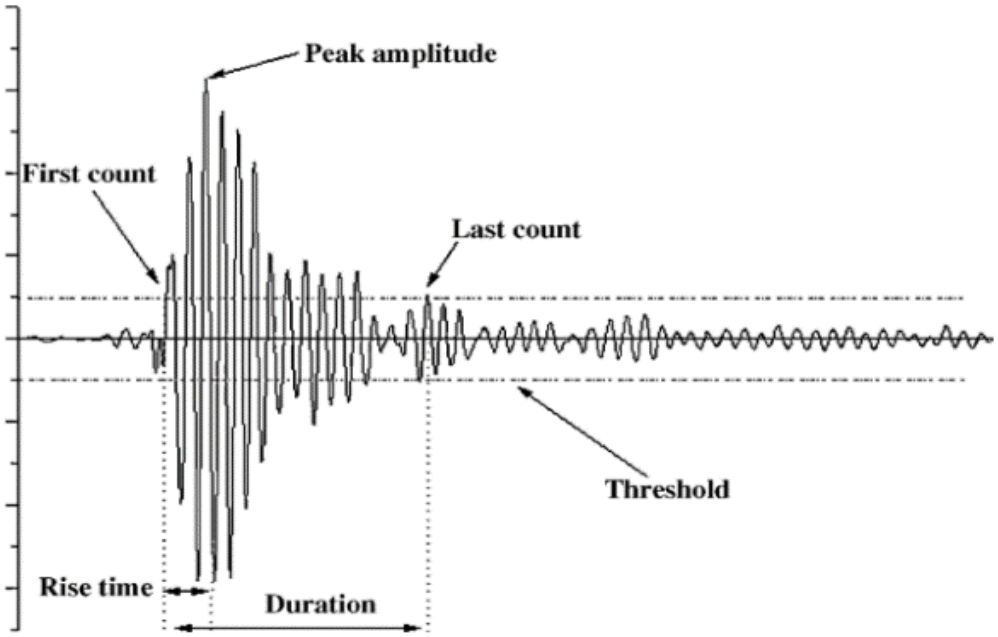

Figure 30: Five major parameters developing in any AE burst. Figure adapted from [120].

The five major AE parameters, having a universal character in any AE burst, as shown in Fig. 30, are: rise time – the time interval between first threshold crossing and the signal peak, counts – number of acoustic signals detected that have an amplitude greater than a threshold, duration – the period between first and last threshold crossings, and peak amplitude – highest voltage measured in a signal [137]. However, in this thesis, the peak amplitude of the AE signal burst is considered as the primary parameter for analysing the AE activity [137,139,140]. In addition, the number of acoustic hits over time, the average frequency of hits and the average amplitude of hits are recorded as supplementary information [136]. The sensitivity of the acoustic system is dependent on the background noise and undesired disturbances. Unwanted noise can interfere with acoustic recording and produce erroneous AE data.

Thus, a threshold amplitude, considering the experimental background noise, is identified in each of the cases studied and the AE events only beyond that threshold are recorded. A schematic outline of the AE generation mechanism from a PEMFC is shown in Fig. 31.

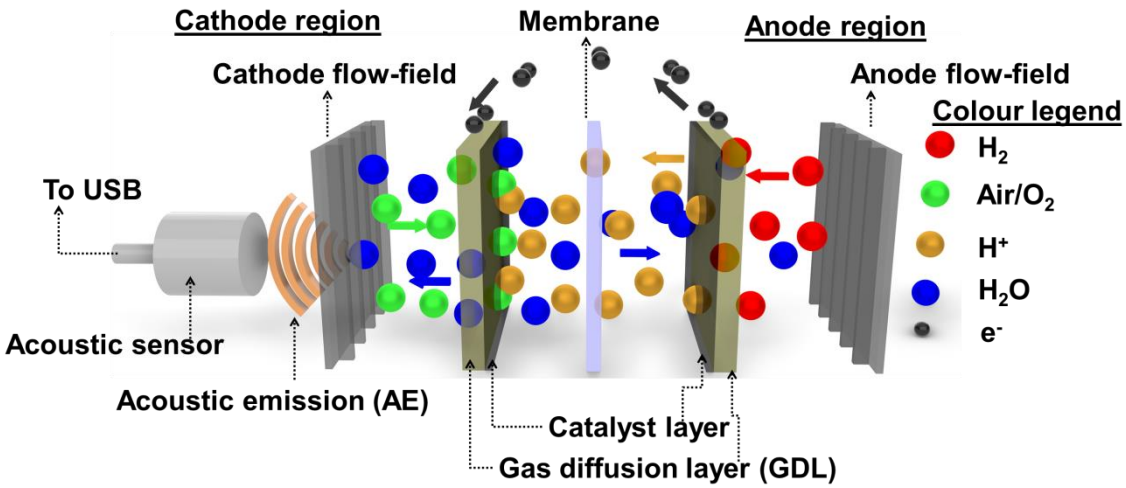

Figure 31: Schematic outline of acoustic emission (AE) generation mechanism inside a PEMFC

The measured AE is primarily presented as cumulated absolute AE energy, similar to that shown in Fig. 32 [137], developed during the PEMFC operation (AE energy recorded from the continuous AE events over time).

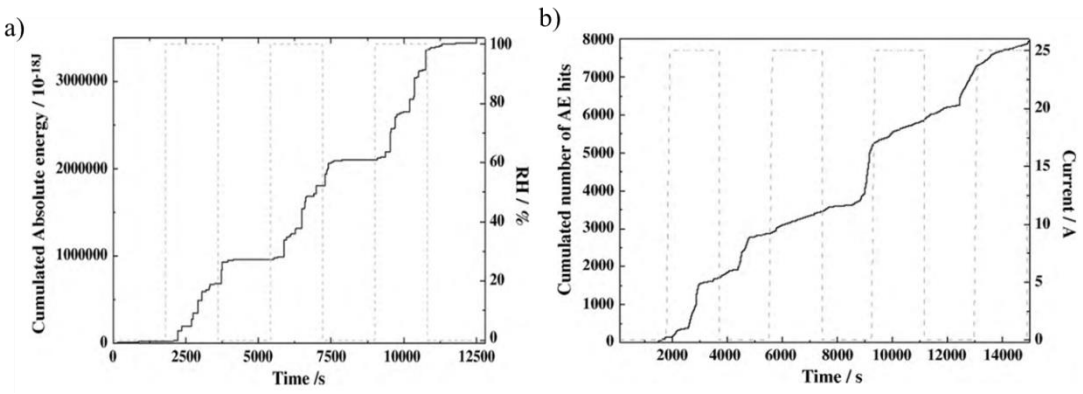

Figure 32: Cumulated acoustic emission (AE) energy developed from a PEMFC (a) with respect to reactant humidity and (b) with respect to the cell operating current. Figure adapted from [120].

Furthermore, in this thesis, a new technique called acoustic emission as a function of polarisation (AEfP) is developed for analysing the AE from a PEMFC. In the AEfP method, the AE activity from the PEMFC is measured in terms of simultaneous cumulative absolute AE energy (CAEE) hits generated, during operation, at discrete points on the polarisation curve. AEfP can identify the presence of liquid water in the flow channels and correlate its formation and removal with the level of cell polarisation, and consequent reactant humidities and internal temperatures [181].

3.5.4. Current - temperature mapping

An electro-thermal mapping and distribution device developed by S++ simulation services (Germany) is utilised in this thesis for electro-thermal performance evaluation of the developed PEMFCs. The mapping device is based on segmented PCB technology, as shown in Fig. 33.

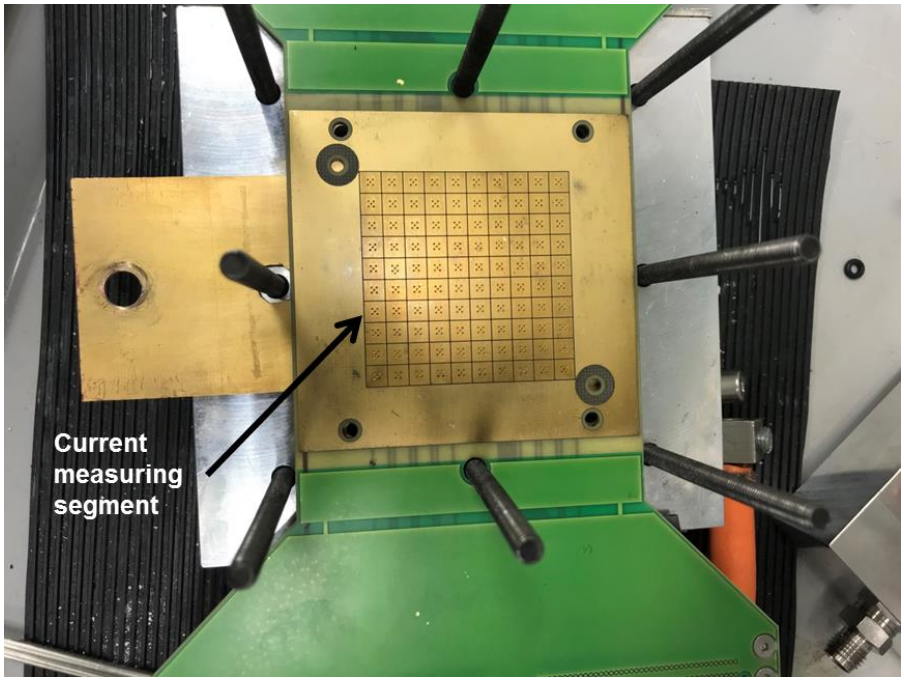

Figure 33: Segmented current and temperature distribution mapping plate from S++

The temperature distribution measurements are made using 5 x 5 “copper meanders” that have a temperature resistance coefficient of 3.9 x 10^{-3} K^{-1}. The meander is supplied with a small current and the corresponding voltage drop is measured, which is proportional to the temperature changes occurring.

The corresponding current distribution measurements are made using 10 x 10 shunt resistors, as shown in Fig. 33. The shunt resistors are made using an alloy that has a temperature coefficient less than copper that makes the resistors insensitive to changes occurring in temperatures. To avoid corrosion, the PCB plates in Fig. 33 are gold plated.

The current distribution measurement uses a low Ohmic shunt resistor. The shunt resistors are connected to a multiplexer that switches the signals to an

amplifier and to an analog-digital converter, as shown in Fig. 34. The output from the converter is fed via USB to a computer running CurrentView software. The fuel cells are run in galvanostatic mode with the mapping plates and any current applied to the cell is assumed to deliver constant voltage across the plate generating a distribution of local current density [148].

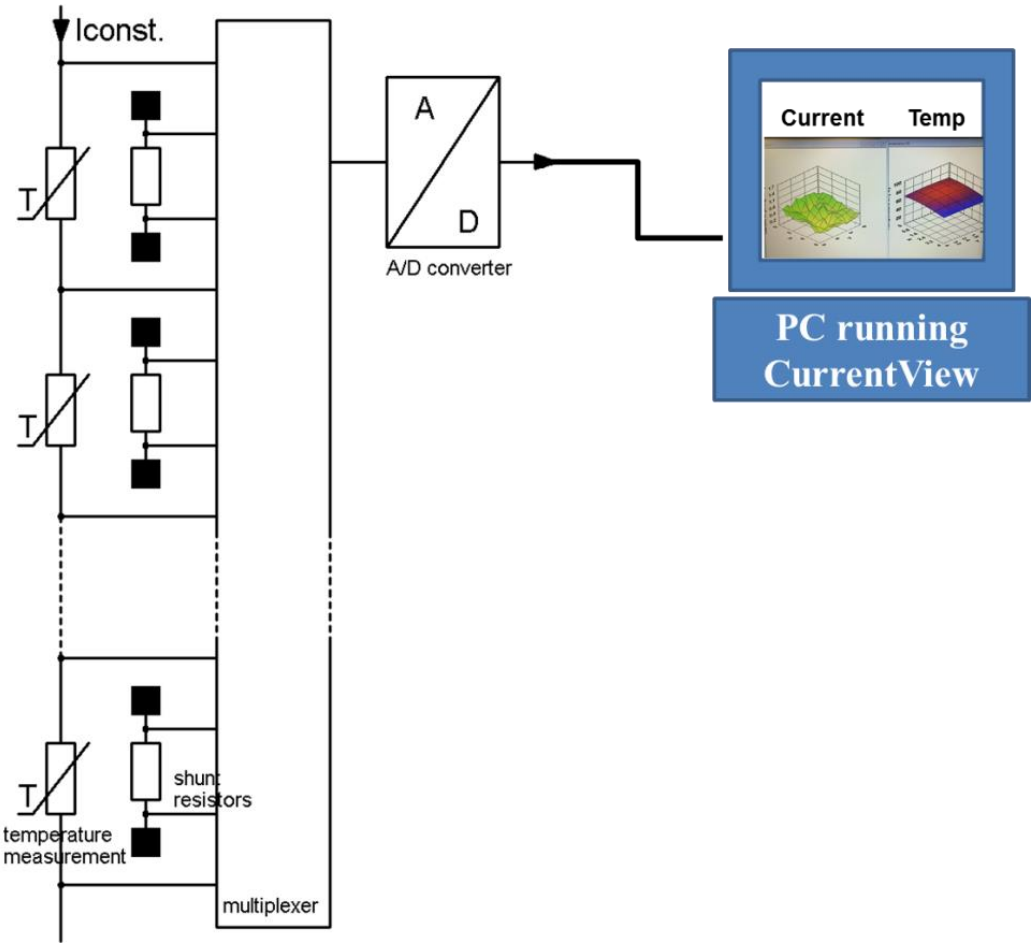

Figure 34: Schematic outline of current and temperature measurements using shunt resistors. Figure inspired from [148].

4. Development of layer-wise lung-inspired PEMFCs using planar PCB plates

4.1. Introduction

This chapter presents the design, development and fabrication of layer-wise, planar printed circuit board (PCB) based lung-inspired fractal cathode flow-fields studied in this thesis. Layer-wise PCB based assembly is identified as an easy to handle and cost-effective manufacturing approach to produce a lightweight and durable fractal flow-fields [182]. Here, the design of 3D hierarchical lung-inspired cathode fractal flow-fields using Rhinoceros computer graphics and computer-aided design application software models is discussed. A detailed methodology and approach for assembling the layers of PCB plates into their respective fractal flow-fields is presented. Furthermore, fabrication methods for realising the fractal flow-field features on layers of PCB plates using computer numeric control (CNC) technique are discussed. Besides, this chapter outlines the design, development and fabrication of other relevant PCB based flow-field plates tested in this thesis like cathode single-serpentine, anode single-serpentine, and graphite-based anode single-serpentine flow-fields, respectively. In addition, this chapter presents the X-ray CT scanning methodology and technique utilised for the characterisation and the structural analysis of the developed flow-fields. X-ray scans have been instrumental in observing the uniformity and alignment between individual PCB layers producing the fractal hierarchy of flow channels.

Sections of this chapter have been published or are under press in the following journal articles:

- **V.S. Bethapudi**, J. Hack, P. Trogadas, G. Hinds, P.R. Shearing, D.J.L. Brett and M.-O Coppens, Hydration state diagnosis in fractal flow-field based polymer electrolyte membrane fuel cells using acoustic emission analysis, Energy Convers. Manag. 2020; 220:113083.
- **V.S. Bethapudi**, M. Maier, G. Hinds, P.R. Shearing, D.J.L. Brett, M.O. Coppens, Acoustic emission as a function of polarisation: Diagnosis of polymer electrolyte fuel cell hydration state, Electrochem. Commun. 2019; 109: 106582.
- **V.S. Bethapudi,** J. Hack, P. Trogadas, J.I.S. Cho, L. Rasha, G. Hinds, P.R. Shearing, D.J.L. Brett, M.-O.Coppens, A lung-inspired printed circuit board polymer electrolyte fuel cell, Energy Convers. Manag. 2019; 202 :112198
- **V.S. Bethapudi,** G. Hinds, P.R. Shearing, D.J.L. Brett, M.-O. Coppens, Acoustic emission analysis of polymer electrolyte membrane fuel cells, 2020 ECS Trans. (98) 177.

4.2. Materials and experimental

4.2.1. Cathode flow-fields

One-way, lung-inspired cathode fractal flow-field

A 2D planar layer-wise approach was adopted for the development of a hierarchically structured 3D lung-inspired cathode fractal flow-field plate (or 1-way fractal), as shown in Fig 35 (a).

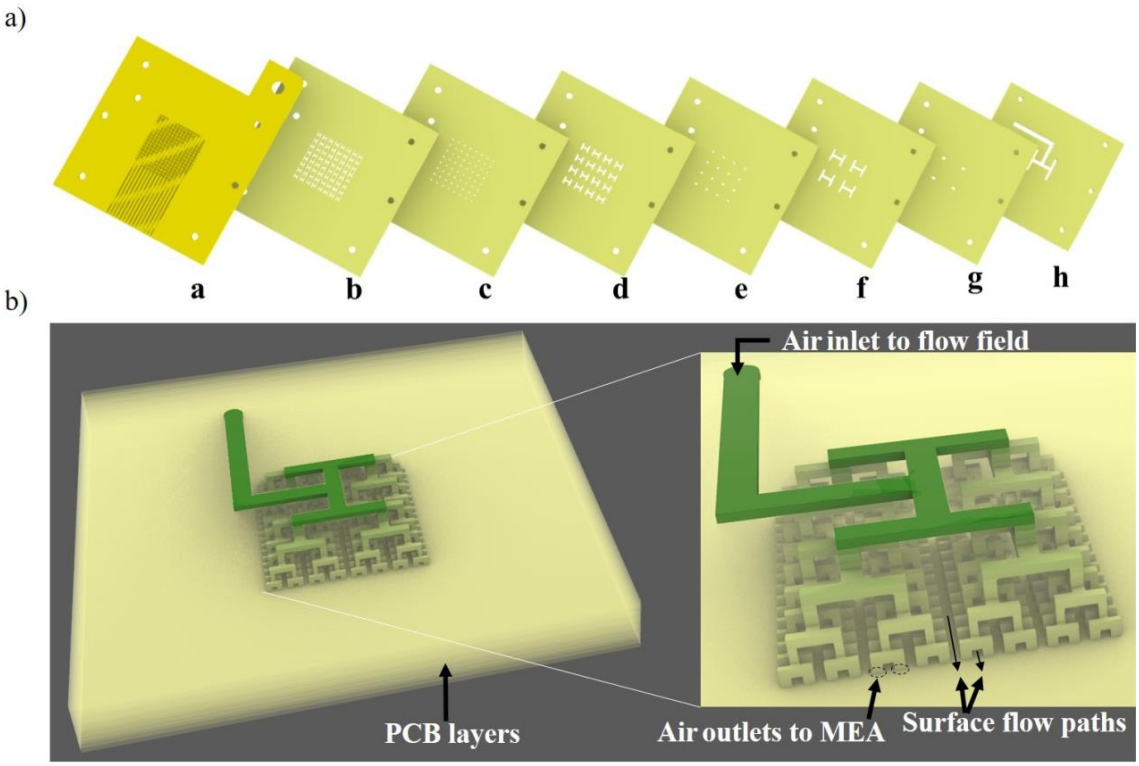

Figure 35: (a) PCB plates a-h comprising 2D planar individual layers of hierarchical fractal flow-field geometry. (b) Rhino model depicting the assembly of individual PCB layers, resulting in fractal flow-field geometry. Shown are the single air inlet, multiple air outlets to MEA level, and the surface flow paths for the cathode air and water outlets from the fuel cell.

Rhinoceros software, detailed in section 3.2.3 (UCL educational license) was used for the design and development of flow-field plates, as shown in Fig. 35. Here, “a” is a PCB plate coated with 38 µm of copper, which adjoins the membrane electrode assembly (MEA). Each of the plates “a-h” corresponds to a specific generation within the fractal geometry. Fig 35 (b) shows four generations of fractal flow, with airflow from a single inlet to 256 outlets (end of the 4^{th} generation) at the interface with the MEA. The total MEA active area covered by these 256 outlets is 6.25 cm^2.

Each of the 4^{th} generation outlets has a dimension of 400 µm × 800 µm with 1.18 mm spacing between adjacent outlets. Surface flow paths (0.5 mm wide and 1 mm deep) between these outlets, as seen in Fig. 36 (a), removed cathode air and excess water within the fuel cell (the previous study with laser sintered stainless steel lung-inspired plates adopted a dead-ended removal mechanism [36]).

A Roland-40 CNC machine (ROLAND, USA) was used to cut the channel features for each layer (fabrication methodology as in section 3.3). Fig. 36 (a) shows the fabricated individual PCB plates with channel features. Plate “a” was electroplated with Ni, followed by Au, and acted as the cathode current collector. The detailed methodology for the electroplating of Cu coated PCB plates has been given in section 3.2.2.

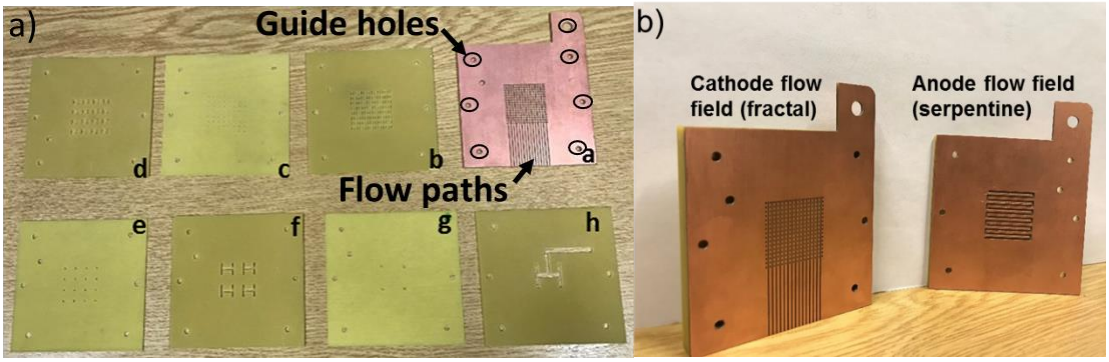

Figure 36: (a) Fabricated PCB plates with plate "a" Cu coated; (b) PCB plates assembled into a flow field with the first plate Au coated; this plate is also the current collecting plate. Cathode fractal flow-field plate dimensions – 80 mm x 80 mm x 9.6 mm (120 g in weight and a manufacturing cost of £30 per plate) and anode flow-field plate dimensions – 80 mm x 80 mm x 3.5 mm.

Plates “a-h” were assembled in a hot press at 140 °C under 400 psig compression for 1 hour. The corresponding hot press methodology has been given in section 3.2.1. Layers of prepreg (pre-impregnated polymer composite) thermosetting polymer sheets acted as adhesive between the PCB plates. The final assembled cathode fractal flow-field plate, having an overall thickness of 9.6 mm, is shown in Fig. 36 (b).

Two-way lung-inspired cathode fractal flow-field

A 2-way fractal flow-field was developed, as shown in Fig. 37, which has increased conductive contact area with convoluted and fractal means of water egress compared to the 1-way fractal flow-field or lung-inspired cathode fractal flow-field, which has less conductive contact area with direct means of water egress through the surface air outlets, as shown in Fig. 37.

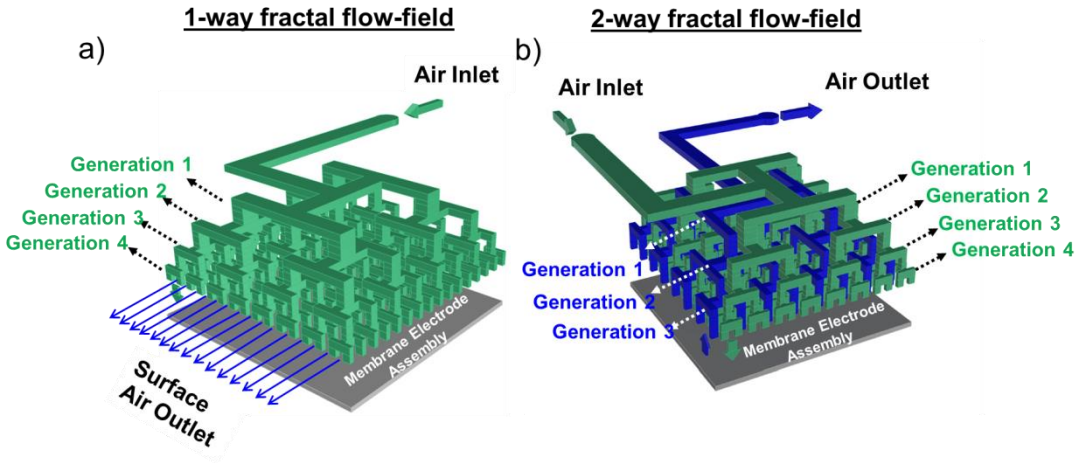

Figure 37: Design schematic of (a) 1-way fractal flow-field representing airflow inlet path (green) and (b) 2-way fractal flow-field representing airflow inlet path (green) and airflow outlet path (blue) at the cathode.

Similar to the 1-way fractal flow-field, as discussed above, the 2-way fractal flow-field was fabricated using 2D planar PCB plates and a layer-wise approach. Fig. 37 (a) presents the design schematic of a 1-way fractal flow-field; design and development of the 1-way fractal flow-field are already outlined above. Fig. 37 (b) presents the design schematic of the 2-way fractal flow-field, where the air distribution to the MEA (green) occurs via a four-generation fractal flow path, similar to that in the 1-way fractal flow-field (Fig. 37 (a)). However, the air removal from the MEA (blue) occurs via a three-generation fractal flow path, as shown in Fig. 37 (b). Here a fractal flow path to collect air from the MEA is used to increase the overall conductive flow-field area in contact with the MEA, compared to the 1-way fractal system, as seen in Fig. 37. Void spaces created by the air inlet flow path to the MEA (green), as shown in Fig. 37 (a), were utilised to develop the air removal path from the MEA (blue), as shown in Fig. 37 (b). For every four outlets at the end of the 4^{th} generation of air inlet points (green), it was possible to accommodate one entry point for the air outlet flow

path (blue), viz. a total of 4^3 = 64 inlets for the air outlet flow path (blue) from the MEA (Fig. 38).

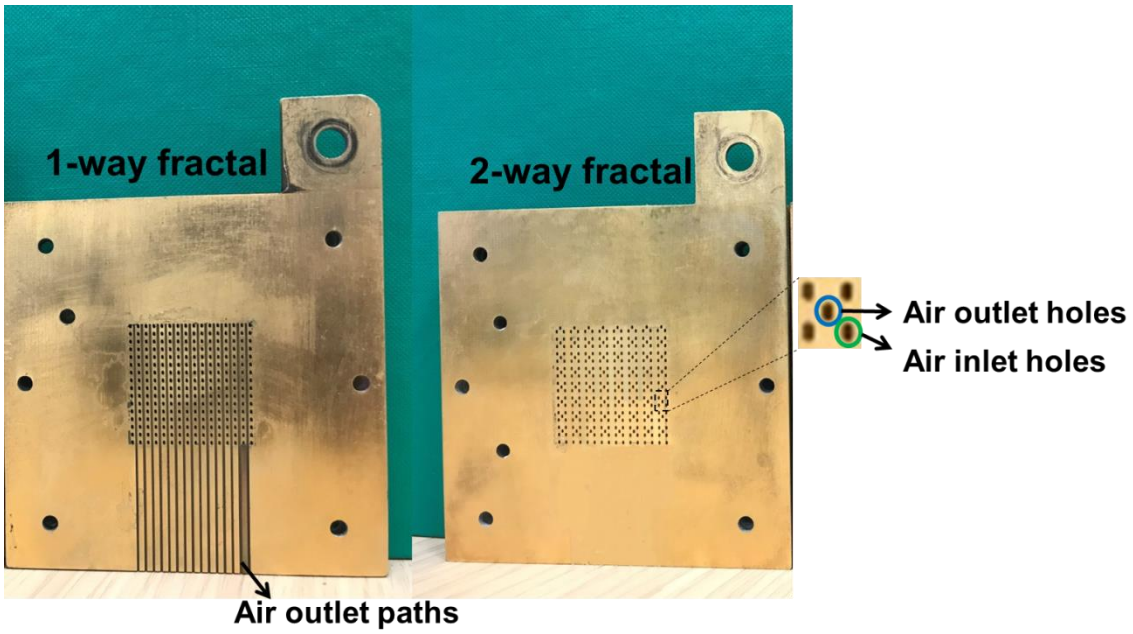

Figure 38: Final assembled cathode fractal flow-fields. Conductive flow-field area in contact with MEA (6.25 cm^2 in area) for 1-way fractal flow-field ≈ 3.375 mm^2 and for 2-way fractal flow-field ≈ 5.5 mm^2.

From 64 inlets to a single outlet, the air outlet flow path merges through three fractal generations, as shown in Fig. 37 (b). Furthermore, developing the air outlet flow path (blue) for the 2-way fractal within the hierarchical structure of the air inlet flow path (green) made it possible to maintain the same number of PCB plates to include both fractal flow-field concepts within a single design.

The fabrication of 2-way fractal flow-field features on the PCB plates was carried out according to the CNC methodology outlined in section 3.3. For the 2-way cathode fractal flow-fields, eight individual PCB plates (similar to the plates a-h in Figs. 35 (a) and 36 (a) of section 4.2.1) were machined that,

together, produced the branching flow paths when assembled. Five plates (a, b, d, f, h) were utilised to realise the four individual fractal generation features of the air inlet to the MEA flow path (green in Fig. 37 (a) and 37 (b)), and three plates (c, e and g) were utilised to create the interconnecting pathways between those four fractal generations. Furthermore, the fractal generations for the removal of air from the MEA in the 2-way fractal (blue in Fig. 37 (b)) were created in those plates (c, e, and g) that also include the three interconnecting pathways to introduce air to the cathode.

Similar to the 1-way fractal flow-field, the PCB plate adjoining the MEA for the 2-way cathode fractal flow-field has a 35 µm thick Cu-coated layer (all other seven PCB plates have no Cu coating) that was electroplated first with Ni and, subsequently, with Au; electroplating process is outlined in section 3.2.2. After electroplating, this Au coated PCB plate acted as the current collector for the respective cathode electrode of the 2-way fractal PEMFC.

The PCB plates, with prepreg thermosetting polymer sheets between them providing the necessary adhesion, were assembled into 2-way fractal flow-field using a hot press. The PCB plates were compressed under a pressure of 400 psig at 150 ˚C for 60 min (hot press methodology in section 3.2.1). After hot pressing, the overall dimensions of the 2-way cathode fractal flow-field plate was 80 mm × 80 mm × 9.6 mm. The final, assembled 1-way and 2-way fractal cathode flow-fields are shown in Fig. 38.

25 cm^2 cathode fractal flow-field

Similar to the 6.25 cm^2 cathode fractal flow-field, as discussed above in section 4.2.1, a 25 cm^2 cathode fractal flow-field was developed using 2D planar PCB plates and layer-wise assembly technique. Furthermore, the 25 cm^2 cathode fractal flow-field configuration was designed to accommodate the current and temperature mapping measurement setup (chapter 6), which had a predefined mapping sensor surface area.

The cathode fractal flow-field developed here has a 5-generation fractal structure. The airflow through this fractal flow-field structure occurs from a single inlet to 1024 outlets at electrode interface and covers an active MEA area of 25 cm^2. Each 5^{th} generation outlet has dimensions of 400 µm x 800 µm, with a spacing of 1.18 mm between adjacent outlets. Furthermore, a surface vertical flow path of 0.5 mm each in width and depth runs through this spacing. These vertical surface paths acted as the flow outlet paths for excess reactant air and water generated in the cathode region, making this flow-field an open-ended cathode fractal flow-field.

A total of 10 PCB plates were used to develop the 25 cm^2 fractal flow-field, as shown in Fig. 39. Six plates (1, 2, 4, 6, 8 and 10) accommodated the five fractal generations, and four plates (3, 5, 7, 9) acted as the interconnecting plates between generations (Fig. 39). Plate 1, which adjoins the MEA, was surface Au coated and acted as the cathode current collector for this flow-field, while the other plates (2-10) were plain PCB plates.

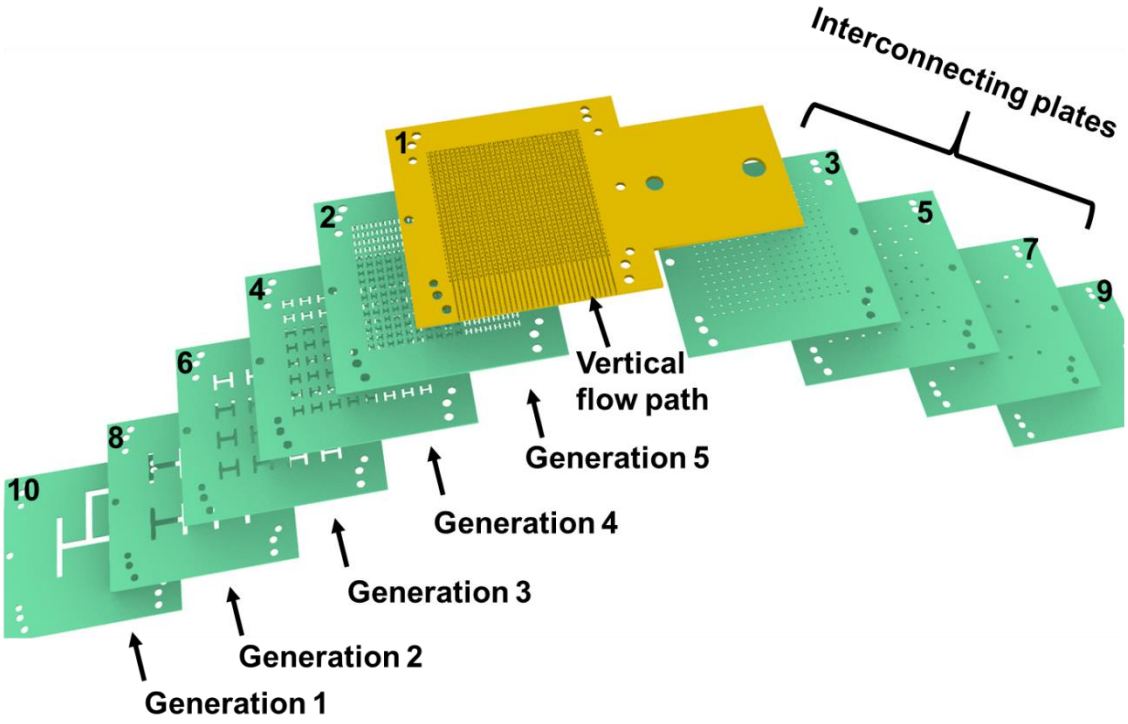

Figure 39: Schematic outline and order of 2D planar PCB plates (generations and interconnecting) used for the development of a 5th generation cathode fractal flow-field plate. Plate 1: Au coated; plate(s) 2 – 10: plain PCB plates.

The different flow-field features discussed above were fabricated using a Roland-40 CNC setup (ROLAND, USA). The fabrication methodology is outlined in section 3.3. In the 25 cm^2 cathode fractal flow-field, plate 1 had a 35 µm thick Cu coating that was Ni and Au electroplated. The corresponding electroplating methodology is outlined in section 3.2.2. Au electroplated plate 1 and plain plates 2 -10 were hot-press assembled under a pressure of 400 psig and 150 ^{0}C for 80 min, followed by a cooling phase of 120 min. Prepreg polymer materials were used for adhesion between the PCB plates. The final assembled dimensions of the cathode fractal flow-field, as shown in Fig. 40, after the hot press, were 80 mm x 80 mm x 7.25 mm.

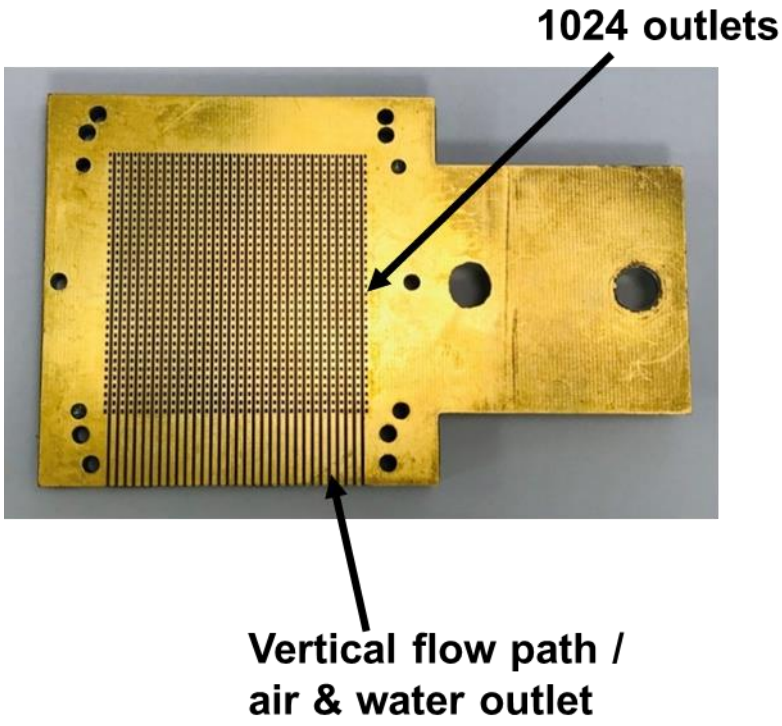

Figure 40: Final assembled cathode fractal flow-field with 25 cm^2 active MEA area – dimensions: 80 mm x 80 mm x 7.25 mm.

Cathode single-serpentine flow-field

A 6.25 cm^2 cathode single-serpentine flow-field was developed as the conventional flow-field for testing and performance comparison along with the 6.25 cm^2 cathode fractal flow-field PEMFCs developed in this study. A single-serpentine design was chosen over the forced-diffusion interdigitated design due to the overall better performance (stable output and better water regulation) identified with the serpentine flow channel PEMFC operation compared to other conventional (including interdigitated) designs [183]. The cathode single-serpentine flow-field presented here acted as the cathode current collector of the single-serpentine PEMFC and was developed using similar materials, dimensions and fabrication process to that of the cathode fractal flow-field plates, including Ni and Au electroplating.

The serpentine flow-field features of 1 mm^2 square channels with a depth of 1mm and covering an active MEA area of 6.25 cm^2 were cut on a PCB plate that had a thickness similar to plate “a” given in Figs. 35 and 36. In addition, a backing PCB plate was used as support to the cathode flow-field plate. The hot press methodology and conditions applied for the assembly of cathode single-serpentine flow-field were similar to those used for developing 1-way and 2-way fractal flow-fields. The overall dimension of the cathode single-serpentine flow-field after hot press assembly was 80 mm x 80 mm x 3.5 mm. However, the flow outlet from the cathode single-serpentine flow-field was from the surface via vertical channels of 0.5 mm width and 1 mm depth and with a spacing of 1.18 mm between adjacent channels, as shown in Fig. 41.

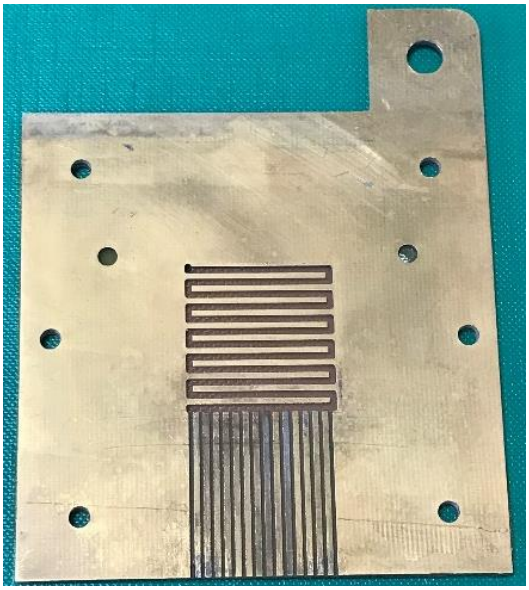

Figure 41: Cathode single-serpentine flow field with open-ended flow outlet arrangement. Cathode single-serpentine flow-field plate – dimensions: 80 mm x 80 mm x 3.5 mm.

Similar to the 6.25 cm^2 flow-field, a cathode single-serpentine flow-field covering an active MEA area of 25 cm^2 was developed using PCB plates, which was utilised for the conventional electrochemical performance evaluations (chapter

5) and the electro-thermal mapping/distribution measurements (chapter 6). The 25 cm^2 cathode flow-field, shown in Fig, 42, has a 1 mm^2 single-serpentine square channel with a depth of 1 mm and acted as the corresponding cathodic current collector. Furthermore, surface vertical flow paths of 0.5 mm in width and 1 mm in depth were provided, with a spacing of 1.18 mm between them, for the removal of excess reactant air and water generated in the cell. Similar to the 6.25 cm^2 plate, the 25 cm^2 cathode flow-field plate was Ni and Au coated and was hot pressed, along with a backing PCB plate (hot press methodology and conditions are outlined in sections 3.2.1 and 3.2.2, respectively). The final assembled cathode single-serpentine flow-field plate with 25 cm^2 active MEA area is given in Fig. 43, which has dimensions of 80 mm x 80 mm x 3.2 mm and weighs ~150 g.

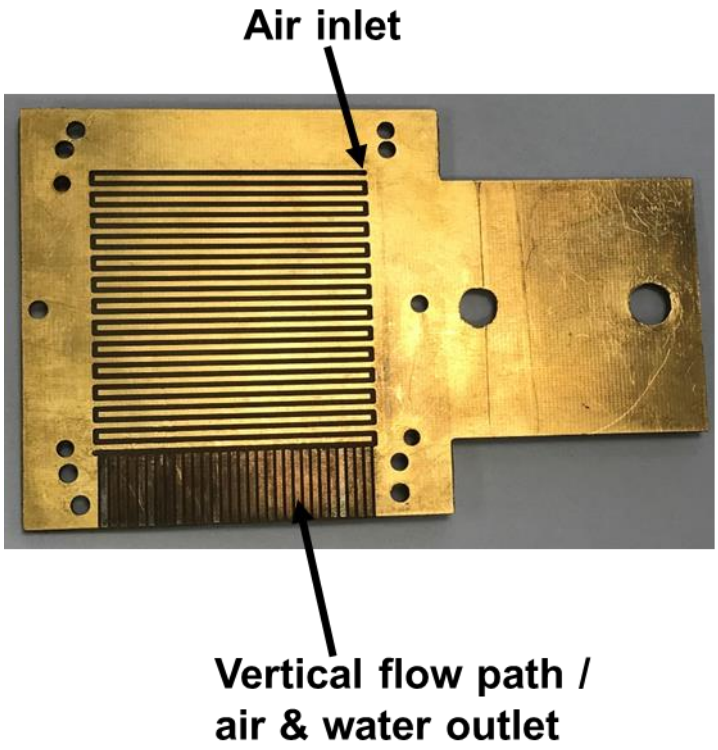

Figure 42: Final assembled cathode single-serpentine flow-field with 25 cm^2 active MEA area – dimensions: 80 mm x 80 mm x 3.2 mm.

4.2.2. Anode flow-fields

6.25 cm^2 anode single-serpentine flow-field

The corresponding anode flow-field plate used for testing with the 6.25 cm^2 based 1-way cathode fractal flow-field, 2-way cathode fractal flow-fields, and single-serpentine cathode flow-field, contained a single serpentine square channel, with a width, spacing and depth of 1 mm each; it had a single inlet and a single outlet. It also functioned as the respective anode current collector for the three PEMFCs tested. It was fabricated from a PCB plate of thickness similar to plate “a” in Figs. 35 and 36, with a backing plate as support to the anode flow-field plate. Ni and Au layers were electrodeposited on the anode flow-field plate. The electroplating process is described in section 3.2.2. The final assembled anode flow-field plate after hot-pressing (hot-press conditions similar to those outlined for the single-serpentine cathode in section 4.2.1) is shown in Fig. 43.

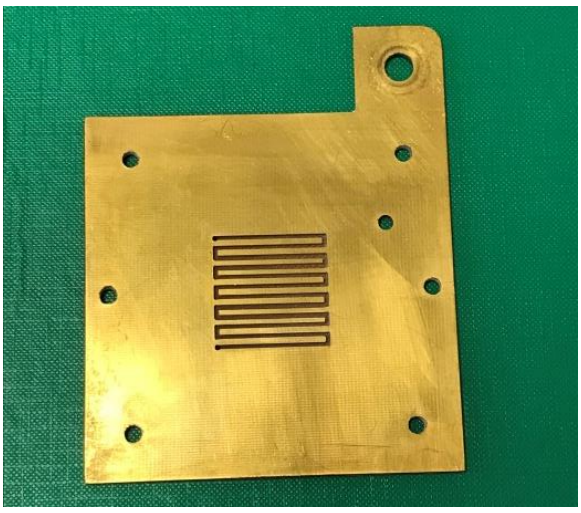

Figure 43: (a) Final assembled anode single-serpentine flow-field with 6.25 cm^2 effective MEA area – dimensions: 80 mm x 80 mm x 3.5 mm.

The overall dimensions of this cathode single-serpentine flow-field plate are 80 mm x 80 mm x 3.5 mm.

25 cm^2 anode single-serpentine flow-field

A 25 cm^2 anode single-serpentine flow-field, used for testing with the 25 cm^2 cathode fractal and cathode single-serpentine flow-fields was developed from a graphite plate of 3 mm in thickness, as shown in Fig. 44 (a). Here, graphite material was used as the anode flow-field material due to its conductive properties (electrical and thermal), which allowed for the current and temperature distribution measurements in the cells (chapter 5). The anode flow-field had a single-serpentine square channel with an area of 1 mm^2 and a depth of 1 mm. The dimensions of the final fabricated graphite-based anode single-serpentine flow-field were 80 mm x 80 mm x 3 mm and it weighed ~60 g.

The anodic current collector was developed from a 35 µm thick Cu coated PCB plate, having similar dimensions to the anode flow-field plate shown in Fig. 44 (a), is presented in Fig 44 (b). The Cu coated PCB plate was coated with Ni and Au layers, according to the electroplating process and methodology outlined in section 3.2.2.

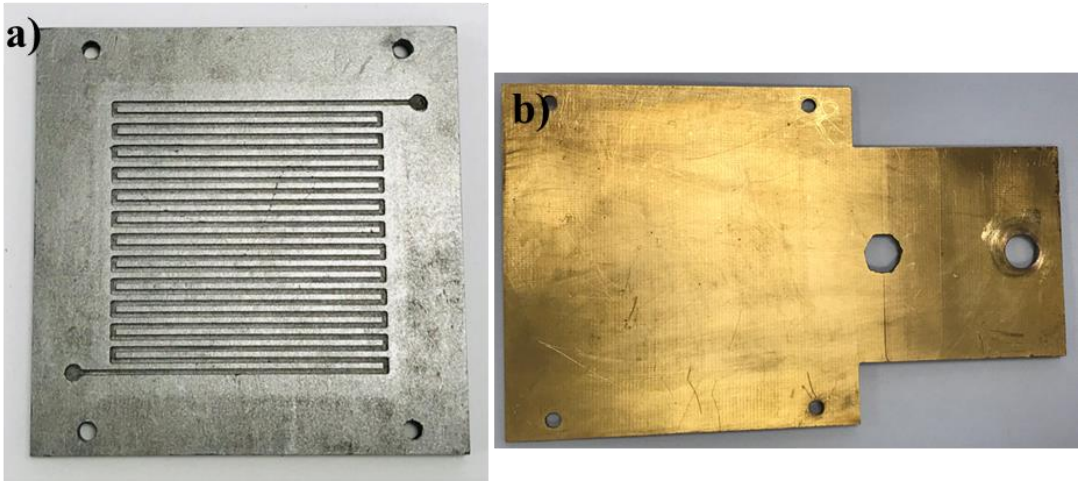

Figure 44: (a) Graphite anode single-serpentine flow-field – dimensions: 80 mm x 80 mm x 3 mm and (b) current collector Au coated PCB plate for graphite anode single-serpentine flow-field.

4.2.3. X-Ray Computed Tomography (X-ray CT)

An X-ray CT scan was performed on the cathode fractal flow-field plates developed, which are presented in section 4.2.1, using a Nikon 225 XT (Nikon Metrology, UK). The experimental setup used for the scan is shown in Fig. 45 (a).

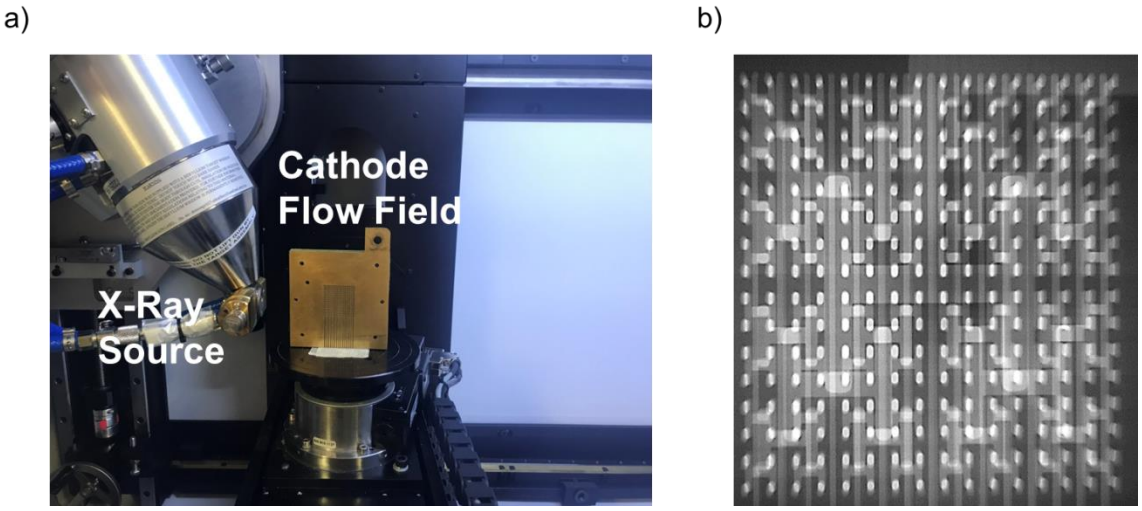

Figure 45: (a) Experimental setup for X-ray CT scanning, (b) radiograph of the region of interest (ROI) of the scanned lung-inspired flow-field.

The X-ray scan was performed using a beam voltage of 170 kV, a beam current of 240 µA and a scan rate of 1 frame per second. The region of interest (ROI) was chosen to be the lung-inspired flow-field, as shown in Fig. 45 (b), with a sample distance from the detector selected to ensure that the entire flow-field remained within the field-of-view (FOV) through the 360° of scanning (Fig. 45 (a)). The total acquisition time was 53 min with a collection of 3176 radiographs. A filtered back projection (FBP) reconstruction algorithm (using Nikon CT Pro 3D software – built-in software with Nikon 225 XT) was applied to the images to result in a three-dimensional dataset with a voxel size of 17 µm. Image analysis was done using Avizo (Thermo-Fischer Scientific, USA), by importing the

dataset into the software and analysing individual orthoslices in the three planes (xz, yz and xy).

4.3. Structural analysis

4.3.1. X-ray CT scan analysis of lung-inspired cathode fractal flow-field (1-way)

An X-ray CT scan of the lung-inspired flow-field (1-way), as shown in Fig. 46, visualises the internal channel arrangement of the flow-field and the alignment of individual layers, as well as the quality of the cell assembly. Fig. 46 (a) shows a volume rendering of the region scanned. This is a 3D representation of the entire sample. Fig. 46 (b) shows a virtual slice in the yz plane, displaying four fractal generations.

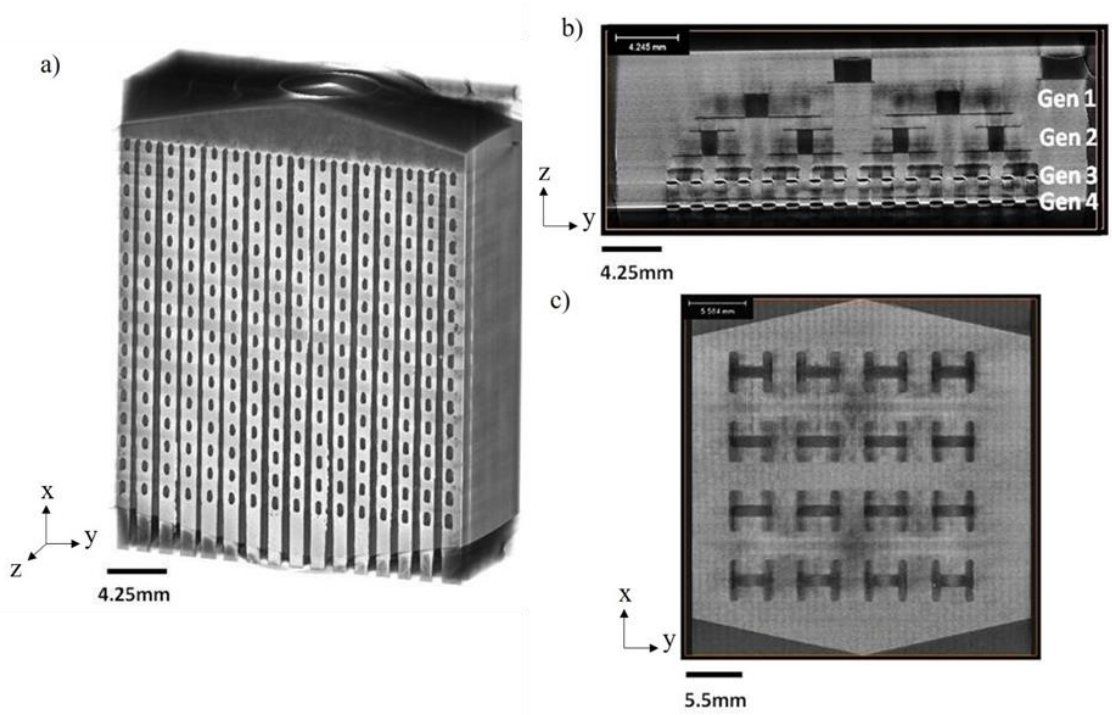

Figure 46: (a) Volume rendering of the scanned area of the lung-inspired flow-field and 3D track through video, (b) virtual slice in the yz plane showing the hierarchical fractal flow structure with four generations and (c) virtual slice in the xy plane showing the layout of channels at the 3rd generation outlets.

The layers are clearly visible and there is proper alignment between layers of the PCB without any overlapping channels. The dark grey regions, where the

attenuation is lower, correspond to the flow channels (voids) in the fractal geometry. In addition, Fig. 46 (c) shows the virtual slice of the 3rd generation fractal outlets from the front face, i.e. showing the entire flow-field. This further highlights that the outlet channels are unobscured with no misalignment.

4.3.2. X-ray CT scan analysis of lung-inspired cathode fractal flow-field (2-way)

In order to inspect the alignment of the hierarchical 2-way fractal flow-field designs and the integrity of each flow channel, X-ray CT was performed. Virtual slices from each dataset in the xy-plane for scans of the 1-way and 2-way fractal flow-fields are shown in Fig. 47 (a) and 47 (b), respectively. The X-ray attenuation in the flow channels (inlet and outlet) was lower, because they are empty, hence, these were observed as dark regions, while zones containing PCB material provided higher attenuation and were observed as bright regions.

Each H-shaped, dark region in Fig. 47 (a) is a segment of the flow inlet path on a PCB plate, corresponding to a specific generation in the 1-way fractal flow-field (schematically shown in Fig. 37 (a)) and the holes correspond to the interconnecting pathways on a PCB plate, between generations. Fig. 47 (a) also illustrates the order in which the individual PCB plates appear in the final assembly. It can be observed from the scans that all flow inlet path segments and holes, across four generations of the 1-way fractal flow-field, are clear of any distortion and misalignment. Further analysis on the 1-way fractal x-ray CT scans is given in section 4.3.1.

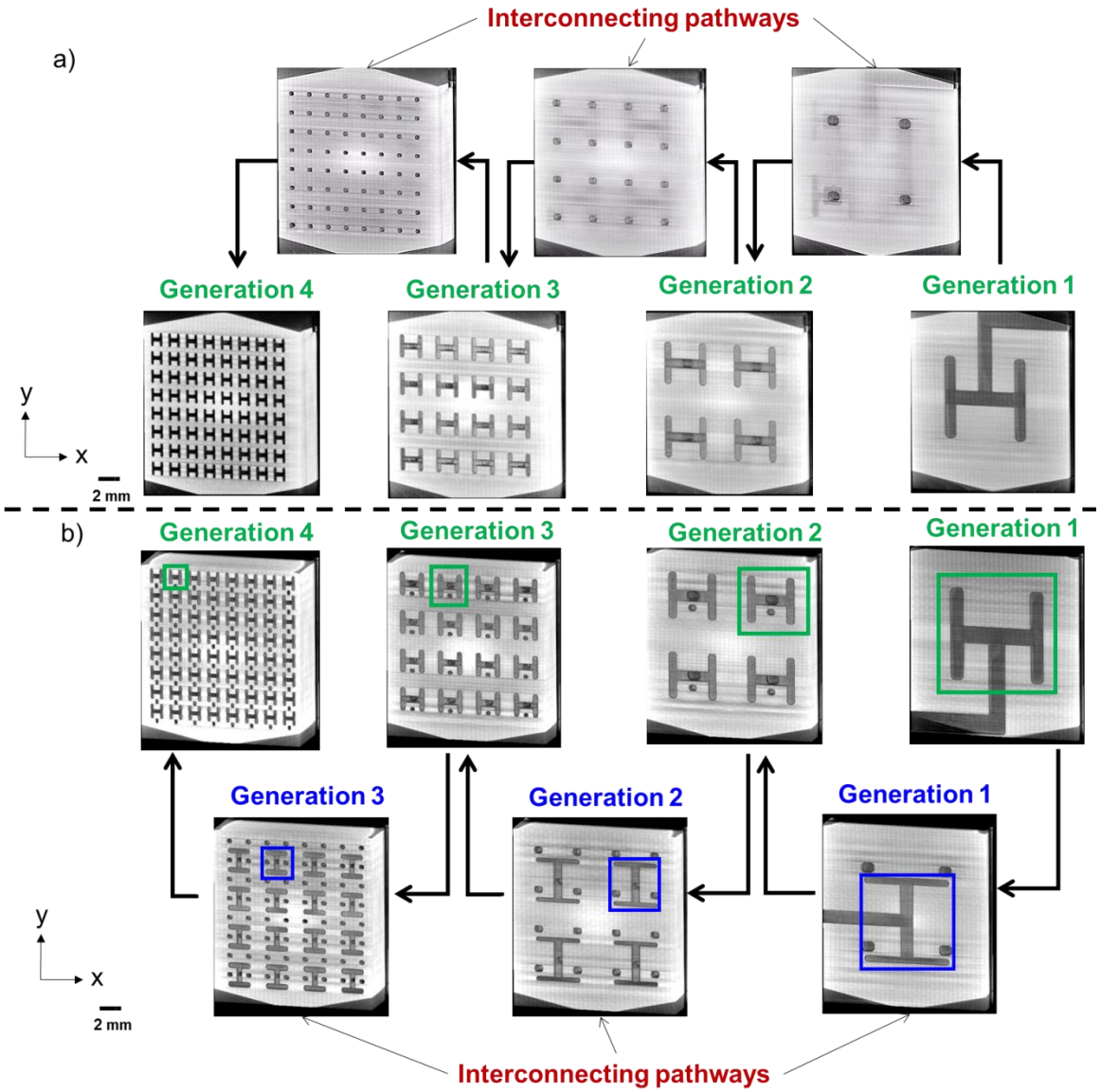

Figure 47: Virtual slices from the X-ray CT datasets in the xy-plane, showing (a) 1-way fractal and (b) 2-way fractal flow-fields. In the 2-way fractal flow-field the green box represents H-shaped fractal flow inlet paths and the blue box represents H-shaped fractal flow outlet paths.

The scan for the 2-way fractal flow-field, shown in Fig. 47 (b), represents H-shaped fractal inlet (green box) and fractal outlet (blue box) flow path segments (schematically shown in Fig. 37 (b)). The inlet flow paths for the 2-way fractal were similar to those in the 1-way fractal flow-field (Fig. 47 (a)). Furthermore, the fractal outlet flow paths were developed within the plates used for developing interconnecting flow paths for the 1-way fractal. This method of fabrication allowed for maintaining the same flow-field plate thickness for both 1-way fractal and 2-way fractal flow-fields (differences in flow-field thickness can alter the AE measured). Also, Fig. 47 (b) illustrates the order in which the inlet and the outlet flow paths of the 2-way fractal flow-field appear in the final assembly. The four generations of the fractal inlet (green) and three generations of the fractal outlet (blue box) can be clearly identified and are well aligned and unobstructed.

4.4. Conclusions

In this chapter, a first of its kind method of developing hierarchical, lung-inspired cathode fractal flow-fields has been presented. Layered 2D planar PCB plates are successfully utilised in realising the 3D hierarchical structures of lung-inspired cathode fractal flow-fields. This method of fabrication also reduces the cost, time, complexity, and weight of fractal flow-fields considerably, compared to the previous laser sintering of stainless-steel fractal flow-fields. Furthermore, fractal flow-fields having a greater conductive area (2-way), scaled-up electrode area (25 cm^2), and other relevant flow-fields (single-serpentine cathode and anode flow-fields) have been successfully developed using the layer-wise PCB approach.

X-ray CT scans of the flow-fields indicate well-aligned and properly assembled PCB layers, confirming the precision of the adopted method of manufacturing. The scans provide an unobtruded view of the complex flow path structures of the fractal flow-fields, especially the 2-way flow-field. Furthermore, features that are indicative of the quality of fabrication, like individual fractal generations and flow path continuity, are demonstrated via the scans.

In the following chapter, electrochemical performance testing of the different flow-field configurations developed in this chapter is presented. The performance evaluation and durability testing of the PEMFCs is achieved through polarisations, cell temperature analysis, impedance measurements and performance degradation tests.

5. Performance analysis of PCB lung-inspired PEMFCs using conventional metrology

5.1. Introduction

In this chapter, the electrochemical performance of lung-inspired flow-fields is measured in an operating PEMFC of 6.25 cm^2 (also called 1-way fractal) and 25 cm^2 effective electrode areas, respectively, over a range of reactant relative humidities. In addition, the fractal flow-field PEMFC performances are compared with those of the conventional flow-field PEMFC. Besides, electrochemical characterisations like polarisation, temperature profiles, degradation tests, and EIS are performed to diagnose the cell's operating performance.

In addition, this chapter presents the design, development and testing of a new 6.25 cm^2 fractal flow-field (also called 2-way fractal), for the first time, which has an increased contact area compared to the previous one [182]. The fractal flow-field with increased contact area has a convoluted water egress from the system, while the previous one with less contact area allows for a more direct means of water egress. Impacts of contact area and water removal mechanism, together and individually, on the performance of fractal PEMFCS are evaluated through polarisation measurements and other conventional characterisation techniques.

Further performance characterisation of the fuel cells developed in this chapter is carried out electro-thermally in chapter 6, for the 25 cm^2 case, and electro-acoustically in chapter 7, for the 6.25 cm^2 case, respectively.

Sections of this chapter have been published or are under press in the following journal articles:

- **V.S. Bethapudi**, J. Hack, P. Trogadas, G. Hinds, P.R. Shearing, D.J.L. Brett and M.-O Coppens, Hydration state diagnosis in fractal flow-field based polymer electrolyte membrane fuel cells using acoustic emission analysis, Energy Convers. Manag. 2020; 220:113083.
- **V.S. Bethapudi**, M. Maier, G. Hinds, P.R. Shearing, D.J.L. Brett, M.O. Coppens, Acoustic emission as a function of polarisation: Diagnosis of polymer electrolyte fuel cell hydration state, Electrochem. Commun. 2019; 109: 106582.
- **V.S. Bethapudi,** J. Hack, P. Trogadas, J.I.S. Cho, L. Rasha, G. Hinds, P.R. Shearing, D.J.L. Brett, M.-O.Coppens, A lung-inspired printed circuit board polymer electrolyte fuel cell, Energy Convers. Manag. 2019; 202 :112198.

5.2. Materials and experiments

5.2.1. Membrane electrode assembly (MEA) preparation

The MEAs with active areas of 6.25 cm^2 and 25 cm^2 were prepared by hot pressing of a Nafion 212® (DuPont, USA) membrane and HyPlat Pt catalyst (HyPlat, South Africa) coated gas diffusion electrodes at 150 °C for 3 min under an applied pressure of 400 psig. Both electrodes had a catalyst loading of 0.4 mg_{Pt} cm^{-2}. The Gas Diffusion Layer (GDL) used was Freudenberg H23C9, which is a carbon fibre paper with a total thickness of 210 µm, including a PTFE treated microporous layer (MPL). The overall thickness of the MEA after hot pressing was ~500 µm.

5.2.2. Fuel cell assembly and testing

6.25 cm^2 fractal PEMFC

The overall fuel cell assembly and the individual components involved in the testing of 6.25 cm^2 fuel cells, fractal (1-way and 2-way in Fig. 37 and 38) and conventional single-serpentine (Fig. 41) configurations, are shown in Fig. 48. The MEA was assembled between a pair of Tygaflor gaskets having a thickness of 250 µm each. The cell was heated at startup to 45 °C using cylindrical 75 W heating cartridges of 6.5 mm × 60 mm in dimensions (RS Components, UK).

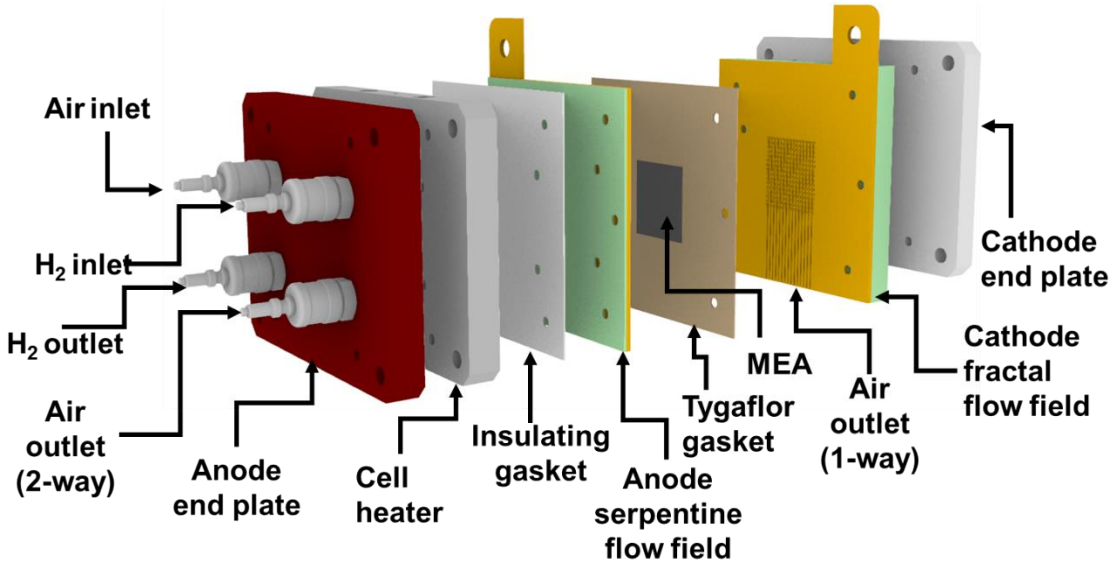

Figure 48: PEMFC components and assembly diagram for 6.25 cm^2 cell configurations. Cathode flow-fields tested: lung-inspired (1-way and 2-way) and single-serpentine.

A self-adhesive K-type thermocouple (OMEGA, UK) was attached to the anode flow-field to measure the cell surface temperature. The different thickness of single-serpentine and lung-inspired cathode flow fields may not provide an accurate representation of the local cell temperature for comparison. Hence, the surface temperature from the anode catalyst layer region was used as a representation of the local cell temperature, since identical anode flow fields (single-serpentine) were used for both the cathode flow fields tested, namely single-serpentine and lung-inspired. An insulating gasket was provided between the heating plate and flow-field plate to avoid electrical short-circuiting within the cell. Aluminium end-plates were used to provide overall compression to the assembly, with a torque of 1.2 Nm provided to the bolts running through them. Air inlet, hydrogen inlet and hydrogen outlet were provided from the manifolds on the anode end-plate. In contrast, air outlet was provided from the surface of

the cathode flow-field for 1-way fractal (Fig. 37 and 38) and single-serpentine (Fig. 41), and through fractal path way (Fig. 37 and 38 in and out of the manifold for the 2-way fractal, as in Fig. 48. The fuel cells were operated under ambient cooling, and no additional cooling channels or devices were present.

The fuel cell testing was carried out using a Scribner 850e fuel cell test station (Scribner Associates NC, USA). The test station could supply reactants at desired conditions, using temperature, humidity and mass flow controllers. The test station provided hydrogen at 99.995% purity under ambient temperature conditions. Hydrogen flow was maintained at 100 mL min^{-1} throughout, while the cathode airflow was fixed at a stoichiometry of 3.0 as defined at 0.6 A cm^{-2} [184]. The fuel cells were tested at three different cathode and anode reactant relative humidity (RH) levels: 40%, 70% and 100%.

25 cm^2 fractal PEMFC

For the 25 cm^2 PEMFC, the reactants, air and H_2, were supplied from the cathode region of the cell, as shown in Fig. 49. The air outlet for both the fractal cathode and the single-serpentine cathode containing cells occurred from the surface vertical flow paths into the ambient, as shown in Figs. 40 and 42, while the H_2 outlet occurred from a manifold, as shown in Fig. 49. The corresponding air and H_2 flows are represented by blue and red lines, respectively, as shown in Fig. 49. Necessary compression for the cell components, which was 1.4 Nm in this case, was provided using aluminium end plates (cathode and anode). The anodic end plate also acted as a heating device, which consisted of cylindrical 100 W heating cartridges of 10 mm × 40 mm in dimensions (RS Components, UK), providing the necessary startup temperature to the cells, which was 45 °C. The cell temperatures were measured using a K-type

thermocouple from the anode flow-field plate of the cells. Again, the anode region was chosen for cell surface temperature measurements, due to different cathode flow-field configurations used in the fuel cells tested. Like for the 6.25 cm^2 PEMFC, surface temperature measurements for flow-fields of varying thickness may not give an accurate representation of the local cell temperatures for comparison. The cells tested here were operated under ambient cooling conditions.

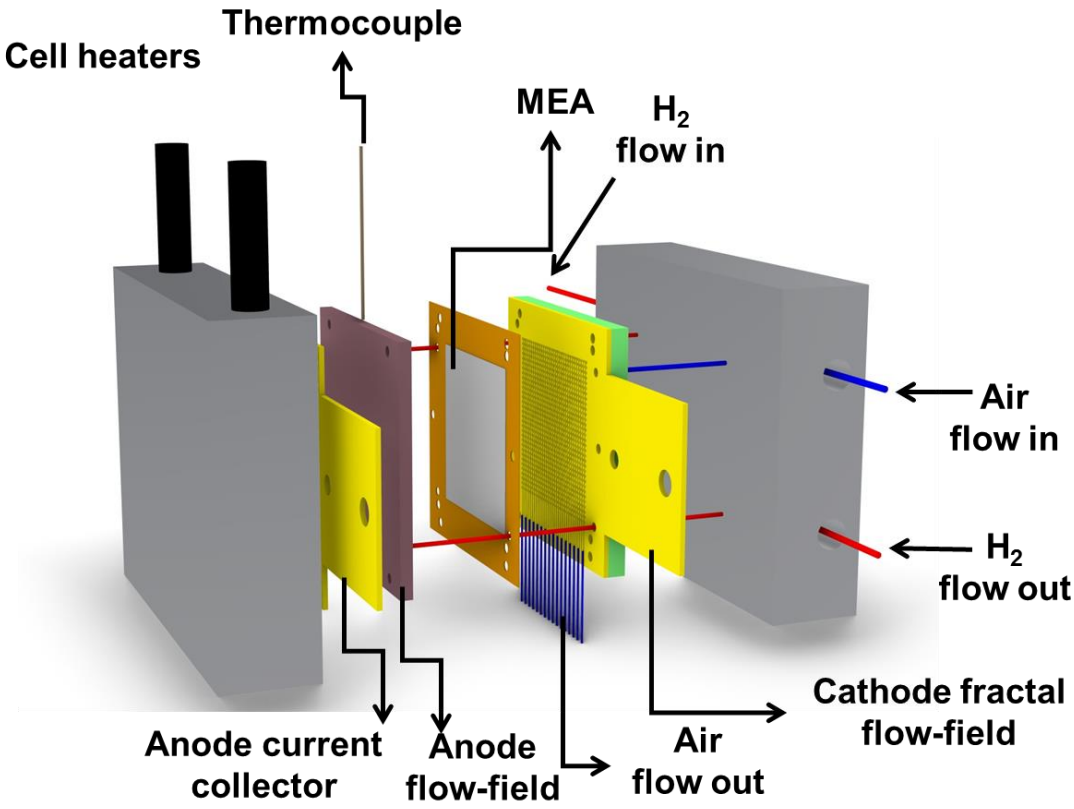

Figure 49: PEMFC components and assembly diagram for 25 cm^2 cell configuration

Similar to the 6.25 cm^2 active area fuel cell testing, a Scribner 850e fuel cell testing station (Scribner Associates NC, USA) was used for the testing of the 25 cm^2 active area fuel cells. The testing station supplied the reactants at desired conditions like temperature, humidity and flowrates. The fuel cells were supplied

with hydrogen of 99.995% purity at a constant flow rate of 200 mL min^{-1}, while the cathode airflow was maintained at a constant flow rate of 1500 mL min^{-1}.

5.2.3. Electrochemical impedance spectroscopy

Electrochemical impedance spectroscopy (EIS) measurements were performed using a Gamry Reference 3000 and Gamry Reference 30k Booster (Gamry Instruments, USA). EIS measurements on the fuel cells were performed in galvanostatic mode. The frequency range for analysis was 100 kHz to 0.1 Hz, with 10 points per decade, and AC modulation amplitude of 5% of the DC input signal. The electrochemical conditions discussed above were the same for all PEMFCs tested in this thesis.

5.3. Results, analysis and discussions

5.3.1. Performance analysis

6.25 cm^2 fractal PEMFC (1-way)

Polarisation curves were measured between open-circuit voltage (OCV) and 0.3 V, where each data point was recorded at 0.05 V intervals with 30 s hold [185] at each interval. Measurements were carried out at three different RH levels - 40% RH, 70% RH and 100% RH - for the single-serpentine and lung-inspired cathode flow-fields, as shown in Fig. 50.

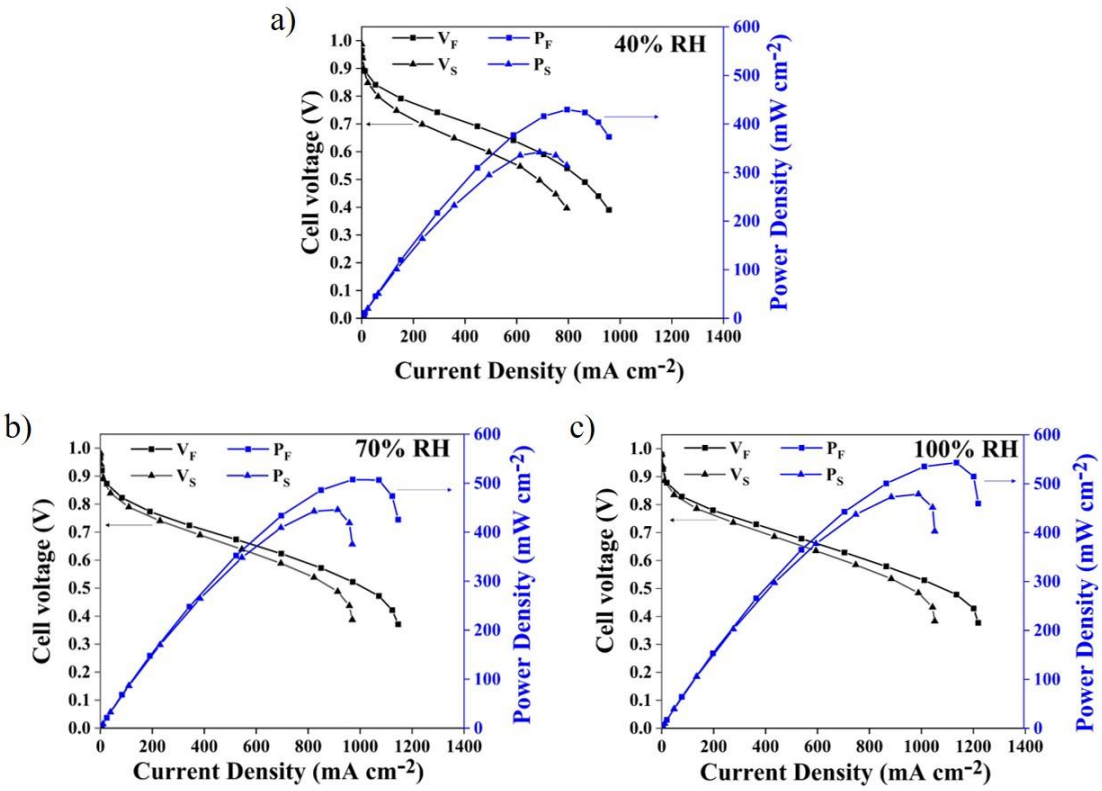

Figure 50: Polarisation curves at (a) 40% RH, (b) 70% RH and (c) 100% RH. (Legend: V_F – cell voltage with fractal flow-field; V_S – cell voltage with serpentine flow-field; P_F – power density with fractal flow-field; P_S – power density with serpentine flow-field).

The lung-inspired fuel cell shows better performance compared to the single-serpentine fuel cell under all conditions. The optimal performance current density, which was measured at 0.6 V [186] cell voltage and taken to be a trade-off between efficiency and power, at 40% RH, 70% RH and 100% RH with the single-serpentine cathode flow-field was: 510 mA cm^{-2}, 680 mA cm^{-2} and 700 mA cm^{-2}, respectively; with the lung-inspired flow-field it was appreciably higher, namely, 705 mA cm^{-2}, 760 mA cm^{-2} and 800 mA cm^{-2}, respectively. This corresponds to an increase in performance of 41%, 12% and 14% of the lung-inspired design over the single-serpentine fuel cell, at 40% RH, 70% RH and 100% RH, respectively.

The higher performance of the lung-inspired flow-field is attributed to its fractal geometry, with equal hydraulic path lengths between the inlet and all the outlets. This results in a transition from convective to diffusive airflow at the outlets, which distributes the reactants uniformly over the surface of the MEA [36]. The difference in performance between the lung-inspired and single-serpentine flow-fields decreases with increasing RH, particularly in the activation and Ohmic regions, which is attributed to the improved conductivity of the membrane [187,188]. It is likely that the higher velocity of air in the serpentine flow-field channels leads to excessive drying of the membrane at low RH, leading to reduced membrane conductivity and cell performance. However, the performance of the lung-inspired design in the mass transport limited regime is much better compared to the single-serpentine flow-field, irrespective of reactant RH.

It is clear that the lung-inspired flow-field performs better than the conventional serpentine flow-field at higher current density and is less subject to mass

transport issues, such as water flooding and reactant starvation [189,190]. Furthermore, the presence of vertical flow paths, as shown in Fig. 36 and Fig. 38, results in more effective water management compared to the previous dead-ended design [36], which flooded during operation at higher RH [36]. Severe mass transport limitations are evident in the cell with a single-serpentine flow-field compared to a lung-inspired flow-field at higher current density, between 900 mA cm^{-2} and 1100 mA cm^{-2}, where its performance reduces drastically [191], as seen in Figs. 50 (b) and 50 (c).

The increase in cell temperature with respect to current density, which was monitored during polarisation measurements, is shown in Fig. 51.

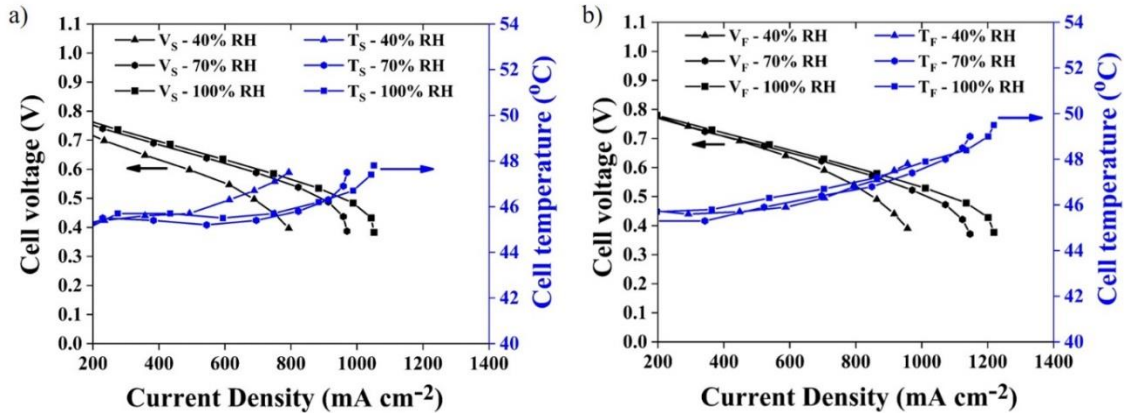

Figure 51: Cell temperature during polarisation curve measurements for (a) single-serpentine flow-field and (b) lung-inspired flow-field at 40% RH, 70% RH and 100% RH. (Legend: V_S – cell voltage with serpentine flow-field; V_F – cell voltage with fractal flow-field; T_S – serpentine flow-field temperature; T_F – fractal flow-field temperature).

At higher current density, there are mass transport limitations, and the cell temperature has a significant influence on the degree of liquid water saturation. Lower cell temperatures result in higher water retention at MEA level and a

corresponding decrease in current density, and *vice versa* [192,193]. From Fig. 51 it can be observed that, at a given current density, higher cell temperatures are reached for the single-serpentine flow-field at low reactant RH (40%), which can be attributed to membrane dehydration, while lower cell temperatures are reached for the single-serpentine flow-field (despite operating at lower potentials compared to the lung-inspired flow-field) at higher reactant RH (70% and 100%), which can be attributed to the occurrence of flooding in the cell.

Furthermore, it can be observed that the increase in cell temperature for the single-serpentine flow-field is initially slow and later rises rapidly beyond 500 mA cm^{-2} at 40% RH and beyond 800 mA cm^{-2} for 70% RH and 100% RH, whereas for the lung-inspired design it increases much more gradually throughout the accessible current density range. This may be due to a more uniform hydration of the MEA, arising from the use of the lung-inspired flow-field, compared to that using the single-serpentine flow-field, where a non-uniform temperature increase is caused by the presence of localised dry regions [194,195]. Furthermore, membrane resistance plays a crucial role in fuel cell performance, especially at low RH, and, hence, its effect is demonstrated in the next section.

Overall, the lung-inspired flow-field allows higher operating temperatures that result in superior performance compared to the single-serpentine flow-field.

25 cm² fractal PEMFC

Polarisation curves were measured between open-circuit voltage (OCV) and 0.3 V, where each data point was recorded at 0.05 V intervals with 30 s hold [185] at each interval. Measurements were carried out at three different RH levels - 40% RH, 70% RH and 100% RH - for the single-serpentine and lung-inspired cathode flow-fields, as shown in Fig. 52.

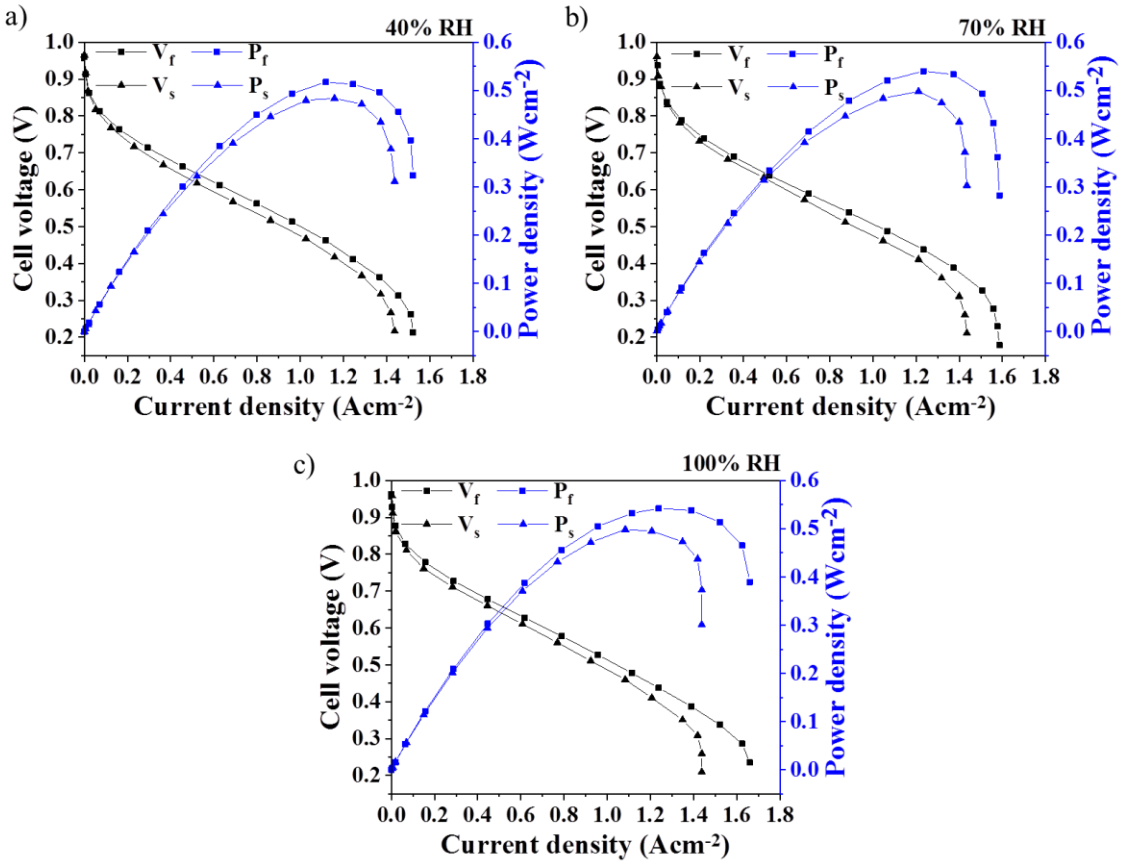

Figure 52: Polarisation curved for the fractal and single-serpentine cells at (a) 40% reactant RH conditions, (b) 70% reactant RH conditions and (c) 100% reactant RH conditions. Legend: V_f – voltage of fractal cell, V_s – voltage of single-serpentine cell, P_f – power density of fractal cell and P_s – power density of single-serpentine cell.

Polarisation performance of the fractal cell was better than that of the single-serpentine cell at different reactant conditions tested. For instance, at 0.6 V cell potential, which was considered to be a trade-off between efficiency and power [182], the corresponding current density output at 40%, 70% and 100% RH for the fractal cell was: 0.65 A cm^{-2}, 0.68 A cm^{-2} and 0.72 A cm^{-2}, respectively; for the single-serpentine cell, it was: 0.58 A cm^{-2}, 0.60 A cm^{-2}, and 0.64 A cm^{-2}, respectively. Furthermore, the limiting current densities at 40%, 70% and 100% RH for the fractal were 1.52 A cm^{-2}, 1.59 A cm^{-2} and 1.66 A cm^{-2} compared to 1.44 A cm^{-2}, 1.43 A cm^{-2} and 1.42 A cm^{-2} for the single-serpentine flow-field.

The overall enhanced performance of the fractal cell can be attributed to its fractal geometry based cathode flow-field structure, where a hierarchically structured flow channel with equal hydraulic path lengths, between inlet and outlet, allows for the transition of air flow from a convection dominated state at the inlet to a more diffusion dominated state at the outlets, resulting in uniform distribution of reactants on the MEA surface [36,58,182,196]. The effects of uniform reactant distribution at the cathode region of the MEA of the fractal cell can be identified from its better performance over the single-serpentine cell, especially in the high current density region between 1.2 A cm^{-2} and 1.6 A cm^{-2}, where mass transport limitations occurring from reduced oxygen concentration in the cell are predominant [197]. In addition to uniform reactant distribution, the presence of vertical flow paths in the fractal cell regulates the excess water away from the MEA more effectively, avoiding excess stagnation of liquid water within the system throughout [182]. In contrast, the single-serpentine cell delivers much lower performance in the mass transport region, particularly the performance degradation in this region increases with an increase in the

reactant RH, which can be attributed to the presence of mass transport issues like flooding and reactant (oxygen) starvation in the cell [182,191].

The increase in cell temperatures, measured during polarisation measurements, is given in Fig. 53.

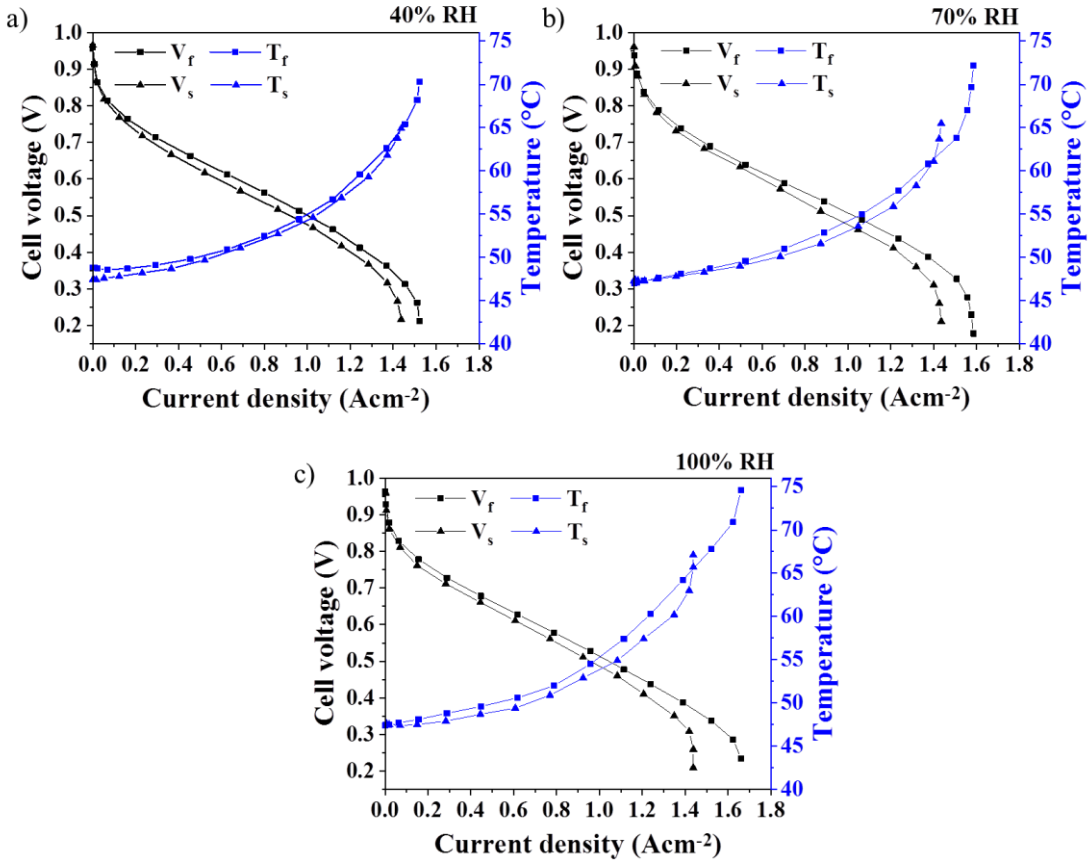

Figure 53: Cell temperature distributions measured using thermocouple on the surface of anode flow-field plate for the fractal and single-serpentine cells at (a) 40% reactant RH conditions, (b) 70% reactant RH conditions and (c) 100% reactant RH conditions. Legend: V_f – voltage of fractal cell, V_s – voltage of single-serpentine cell, T_f – temperature of fractal cell and T_s – temperature of single-serpentine cell.

The maximum cell temperatures attained (limiting current density) by the fractal and single-serpentine cells, at 40%, 70% and 100% RH, were 70.3 ºC, 72.2 ºC and 74.6 ºC, and 64.9 ºC, 65.5 ºC and 67.1 ºC respectively. The fractal cell

attained higher operating temperatures, especially in the high current density region, compared to the single-serpentine cell. Higher cell temperatures in the fractal cell may have resulted in lower levels of water saturation inside it, especially in the mass transport region, and better current density generated and *vice versa* [30]. Corresponding lower cell temperatures developed in the single-serpentine cell, despite operating at lower cell voltages, can be attributed to the presence of excess water saturation (flooding) inside the cell, which reduced its performance and *vice versa* [198].

Overall, the uniform reactant and water distribution occurring in the fractal cells allowed for the development of higher operating temperatures and better current densities compared to the single-serpentine cell[182].

6.25 cm^2 1-way and 2-way fractal PEMFC

Polarisation curves for the tested 1-way and 2-way fractal flow-field PEMFCs are presented in Fig. 54. At 70% RH conditions (Fig. 54 (a)), the polarisation performance of the 2-way fractal PEMFC was slightly better than that of the 1-way fractal PEMFC in the region between OCV and ~700 mA cm^{-2}. This can be attributed to the greater conductive contact area available between the MEA and the flow-field for the 2-way fractal flow-field (as seen in Figs. 37 and 38 of section 4.2.1). At current densities >700 mA cm^{-2} the performance of the 2-way fractal PEMFC decreased considerably with respect to the 1-way fractal flow-field, reaching a limiting current density of ~1200 mA cm^{-2}. In contrast, the performance of the 1-way fractal PEMFC remained stable throughout its operation and attained a higher limiting current density of ~1500 mA cm^{-2}. The performance reduction for the 2-way fractal PEMFC at higher current densities

can be attributed to flooding within the cell, due to inefficient water removal, impeding effective reactant (oxygen) transport to the electrode [20,31,199].

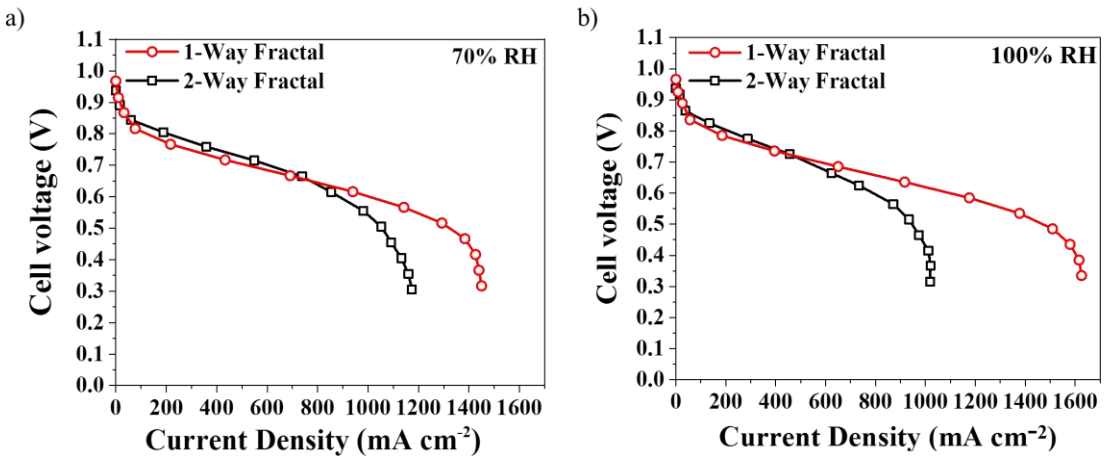

Figure 54: Polarisation curves at (a) 70% reactant RH and (b) 100% reactant RH; AEfP curves at (c) 70% reactant RH and (d) 100% reactant RH.

By controlling the air supply's RH, it is possible to control the amount of water within the system, for any given current density. For the 100% RH case, the corresponding polarisation performance is shown in Fig. 54 (b). As for the 70% RH case, the 2-way design performs slightly better at low current density, due to the greater contact surface area with the electrode. With increasing current density, a more significant decrease in cell performance is observed for the 2-way fractal PEMFC, compared to the 1-way fractal PEMFC, than for the 70% RH case. In addition, the limiting current density attained with the 2-way fractal design is ~1000 mA cm^{-2}, ~200 mA cm^{-2} less than that achieved for the 70% RH case. The marked decrease in the overall performance of the 2-way fractal PEMFC using highly humidified reactants (100% RH) can be attributed to exacerbated flooding in the cell. This is consistent with a higher rate of water condensation from the highly humid reactants, in addition to the water

generated from the electrochemical reaction with increasing current density [200,201].

In contrast, the performance of the 1-way fractal PEMFC increased with reactant RH [202], as a result of optimal rise in its membrane hydration, which increased the limiting current density attained from ~1400 mA cm^{-2} (70% RH) to ~1600 mA cm^{-2} (100% RH) [203].

Overall, the polarisation measurements confirm that the 2-way fractal PEMFC was significantly limited by flooding, whilst the 1-way fractal PEMFC was closer to optimal with respect to hydration. The surface flow channels (blue arrows in Fig. 37 (a)) of the cathode air outlet in the 1-way fractal flow-field allow effective water removal via a straight path, compared with the more tortuous cathode air outlet flow channels (blue arrows in Fig. 37 (b)) in the 2-way fractal flow-field, which are not effectively flushed and result in more liquid water stagnation and electrode flooding.

Cell temperatures measured simultaneously during polarisation for the fractal PEMFCs are presented in Fig.55. It can be observed that, at 70% RH (Fig. 55 (a)) and 100% RH (Fig. 55 (b)), the cell temperature profile for the 2-way fractal PEMFC is much less pronounced than that for the 1-way fractal PEMFC. Lower cell temperatures in the 2-way fractal PEMFC are a result of the cell flooding occurring during operation, where higher amounts of water retained by the flow-field reduce the cell temperature and lead to a corresponding decrease in current density, and *vice versa* [193]. For instance, the maximum temperature attained by the 2-way fractal PEMFC reduced from ~51.5 ºC at 70% RH to ~50.3 ºC at 100% RH; this drop in maximum cell temperature parallels a

reduction in limiting current density attained from ~1200 mA cm^{-2} (70% RH case) to ~1000 mA cm^{-2} (100% RH case).

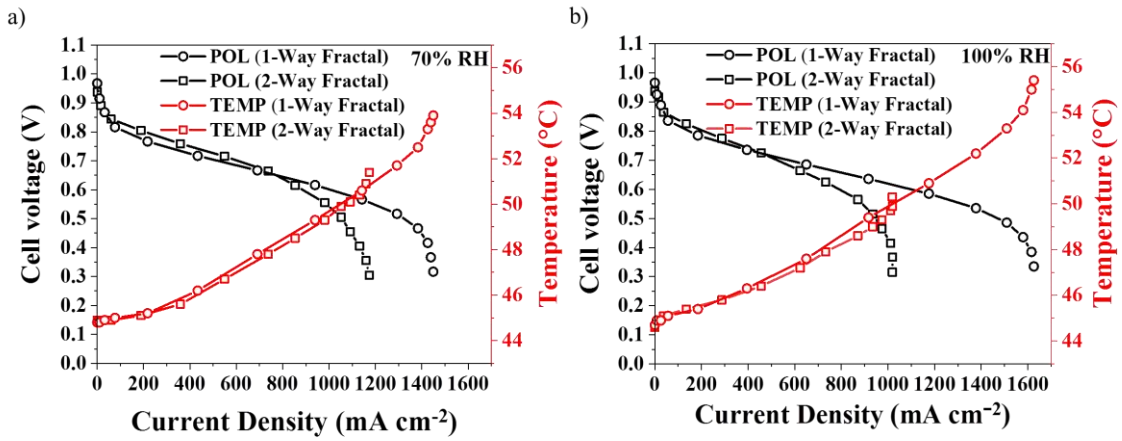

Figure 55: Temperature distribution for fractal PEMFCs measured simultaneously with polarisations at (a) 70% reactant RH and (b) 100% reactant RH. Legend: POL – Polarisation and TEMP – Temperature.

However, for the 1-way fractal PEMFC, the maximum cell temperatures attained at 70% RH and 100% RH were ~54 ºC and ~55.5 ºC, respectively. These temperatures were higher than those developed in the 2-way fractal PEMFC by ~2.5 ºC at 70% RH and ~5.2 ºC at 100% RH; an influence of the higher cell operating temperatures developed in the 1-way fractal PEMFC was reflected in the limiting current densities attained, which were ~1400 mA cm^{-2} at 70% RH and ~1600 mA cm^{-2} at 100% RH, respectively. Overall, higher operating temperatures, supported by an increase in hydration levels, enhanced the membrane conductivity of the 1-way fractal PEMFC and resulted in superior performance and *vice versa*, compared to the flooded lower-temperature operation of the 2-way fractal PEMFC [32,204].

5.3.2. Electrochemical characterisations

Electrochemical impedance spectroscopy (EIS) measurements for the PEMFCs tested here are based on the methodology discussed in section 3.5.2. The corresponding equivalent circuit used for modelling the EIS spectrum is given in Fig. 28 (refer section 3.5.2, pg.90).

6.25 cm^2 fractal PEMFC

EIS was performed between 0.1 Hz and 100 kHz for the single-serpentine and lung-inspired flow-fields over a range of current densities [125,205]. To obtain a stable measurement, the cells were held at the respective current density and reactant conditions constantly for 2 min before the corresponding EIS was performed. This hold ensured a uniform voltage development as a result of the equilibrium achieved between the reactant conditions, like temperature and humidity, and the cell operating conditions. The EIS spectra at 300 mA cm^{-2}, 600 mA cm^{-2} and 900 mA cm^{-2} are shown in Figs. 56 (a), (b) and (c).

At the lowest current density of 300 mA cm^{-2}, the charge transfer resistance observed for the lung-inspired and single-serpentine cells is almost identical under all humidity conditions tested (the corresponding equivalent circuit is given in the methodology section 3.5.2, Fig. 28). Corresponding charge transfer values are given in Table 2. Increasing the current density to 600 mA cm^{-2}, the charge transfer and mass transport resistances (R_{mt}) (equivalent circuit is depicted in Fig. 28 [206]) for the cell with lung-inspired flow-field (R_{mt} is 0.025 $\Omega.cm^2$ and 0.03 $\Omega.cm^2$ at 70% RH and 100% RH, respectively) are lower than those with the single-serpentine flow-field (R_{mt} is 0.042 $\Omega.cm^2$ and 0.044 $\Omega.cm^2$ at 70% RH

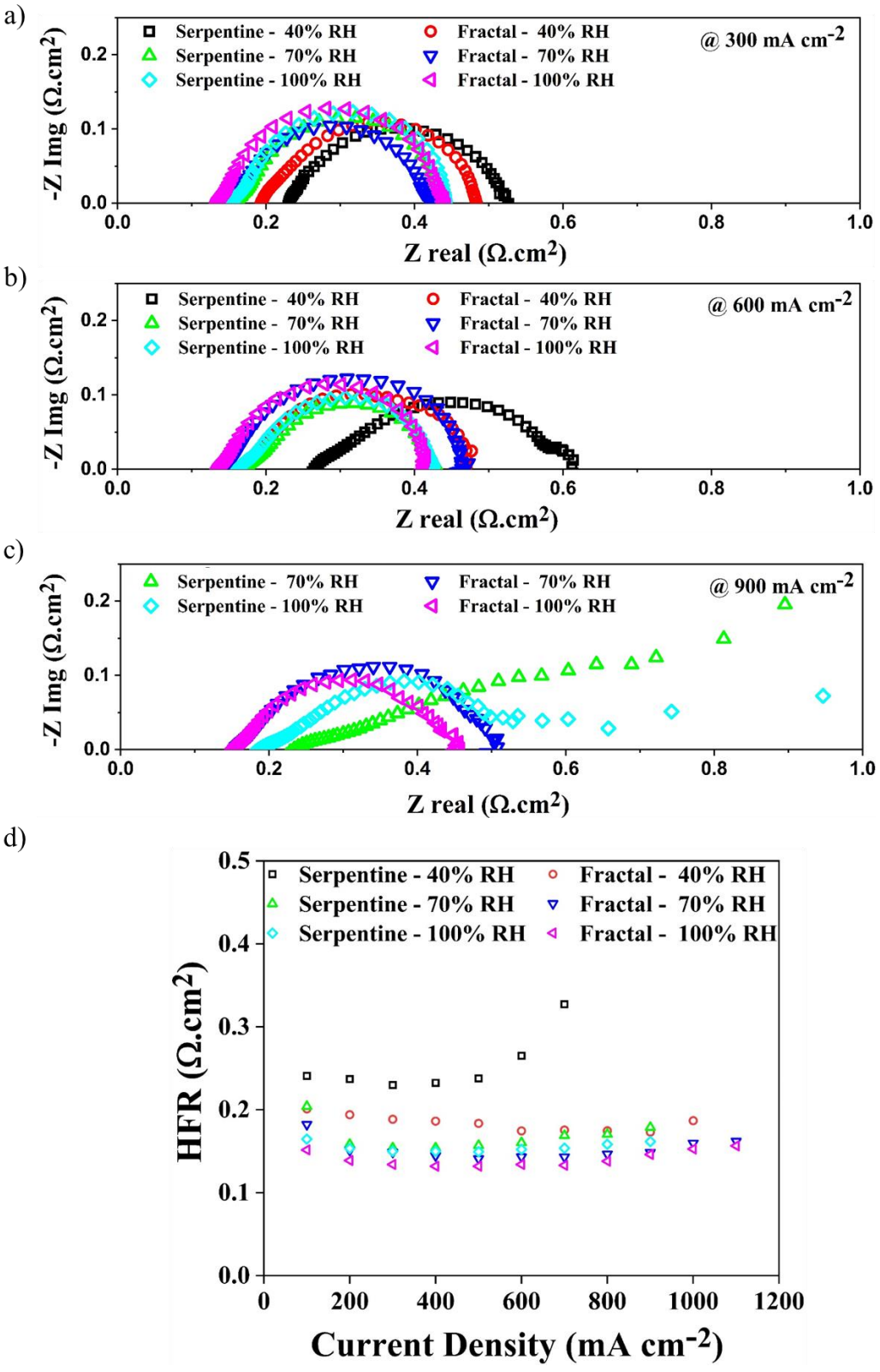

Figure 56: Electrochemical impedance spectra for single-serpentine and fractal flow-fields at (a) 300 mA cm^{-2}, (b) 600 mA cm^{-2} and (c) 900 mA cm^{-2}, at 40% RH, 70% RH and 100% RH. (d) HFR for single-serpentine and lung-inspired flow-fields at 40% RH, 70% RH and 100% RH.

and 100% RH, respectively). Finally, at 900 mA cm^{-2}, the cell with the single-serpentine flow-field has significantly higher charge transfer and mass transfer resistances (R_{mt} is 0.16 $\Omega.cm^2$ and 0.9 $\Omega.cm^2$ at 70% RH and 100% RH, respectively) compared to the lung-inspired flow-field (R_{mt} is 0.03 $\Omega.cm^2$ and 0.04 $\Omega.cm^2$ at 70% RH and 100% RH, respectively), implying that it is subject to excessive flow channel flooding (from water released out of the catalyst/gas diffusion layers) that results in much lower levels of oxygen concentration at the cathode [207].

Table 2: Charge transfer resistances measured based on equivalent circuit in reference [58] from electrochemical impedance spectroscopy for single-serpentine and lung-inspired flow fields at 300 mA cm^{-2} current density.

Charge transfer resistance Single-serpentine flow field			*Charge transfer resistance Lung-inspired flow field*		
40% RH	*70% RH*	*100% RH*	*40% RH*	*70% RH*	*100% RH*
0.283 $\Omega.cm^2$	*0.275 $\Omega.cm^2$*	*0.281 $\Omega.cm^2$*	*0.285 $\Omega.cm^2$*	*0.278 $\Omega.cm^2$*	*0.283 $\Omega.cm^2$*

In contrast, the cell with the lung-inspired flow-field shows a well-defined, stable and lower charge transport resistance with minimal or no mass transport/diffusive impedance. This demonstrates the ability of the lung-inspired design to distribute reactant gases and water uniformly over the MEA surface, maintaining a well-hydrated system, clear of any flooding in the flow path under a wider range of operating conditions. This is consistent with the improved performance in the mass transport region of the cell with the lung-inspired flow-field, as seen in Fig. 50.

The high frequency resistance (HFR), which is determined from the high-frequency intercept with the real axis of the Nyquist plots (obtained from the EIS measurements, as outlined in section 5.3.2) in Fig. 56, provides a measure of the Ohmic resistance and is predominantly attributed to the membrane hydration and its associated conductivity [177,208]. Fig. 56 (d) shows that at 70% RH and 100% RH the membrane resistance initially decreases, as water is produced in the electrochemical reaction, goes through a minimum, and then increases as the cell temperature increases, leading to membrane dehydration. This is well established behaviour [209] and common to both flow-field designs.

The generally higher resistance at low RH (40%) indicates a less uniformly hydrated membrane. Even so, the resistance of the cell with the lung-inspired flow-field design remains relatively stable over the operational range, while the membrane resistance of the serpentine flow-field is significantly higher and increases rapidly for current densities above 500 mA cm^{-2}. This steep increase can be attributed to the decrease of membrane conductivity as a result of membrane dehydration [64,180,210]. This suggests that the superior performance of the lung-inspired flow-field system at low RH can be attributed to the diffusion dominated, uniformly distributed and low velocity reactant flow occurring through the fractal structure [57,196] that minimises membrane dehydration while enabling higher temperature operation (Fig. 51 (b)).

25 cm^2 fractal PEMFC

EIS measurements were performed to understand the resistances developed within the tested 25 cm^2 cells. Fig. 57 (a) illustrates the high frequency resistance (HFR) or Ohmic resistance developed in the cells over a range of

operating conditions. The HFR was measured from the high frequency intercept of the Nyquist curves, obtained from the EIS measurements, with the real axis [121]. Corresponding Nyquist curves for the EIS measurements are given in Fig. 58.

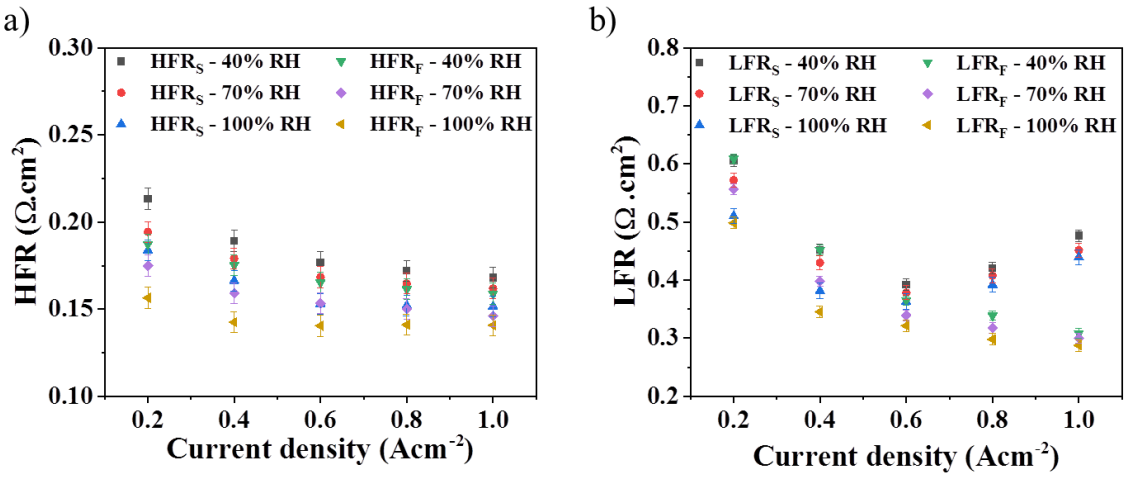

Figure 57: (a) High frequency resistance (HFR or Ohmic) for fractal and single-serpentine cells at 40%, 70% and 100% RH reactant conditions and (b) Low frequency resistance (LFR) or total resistance for fractal and single-serpentine cells at 40%, 70% and 100% RH reactant conditions. Legend - HFR_S – HFR of single-serpentine cell, HFR_F – HFR of fractal cell, LFR_S – LFR of single-serpentine cell, LFR_F – LFR of fractal cell.

From Fig. 57 (a), it can be observed that the HFR for the cells decreased with an increase in the reactant RH from 40% to 100%. Furthermore, the influence of reactant RH on HFR is predominantly evident in the low current density region (e.g. 0.2 A cm^{-2}), where the water contribution from electrochemical reactions is considerable less, with highly humid reactant RH resulting in lower HFR compared to the low reactant RH. However, the individual HFR and the difference between HFRs of the cells reduced gradually with an increase in the current density, irrespective of the reactant RH, as a result of improved membrane hydration occurring from water generated from improved

electrochemical reactions (current density). Overall, HFR analysis suggests that both the cells tested were sufficiently hydrated, especially in the high current density regions, resulting in uniform membrane conductivity.

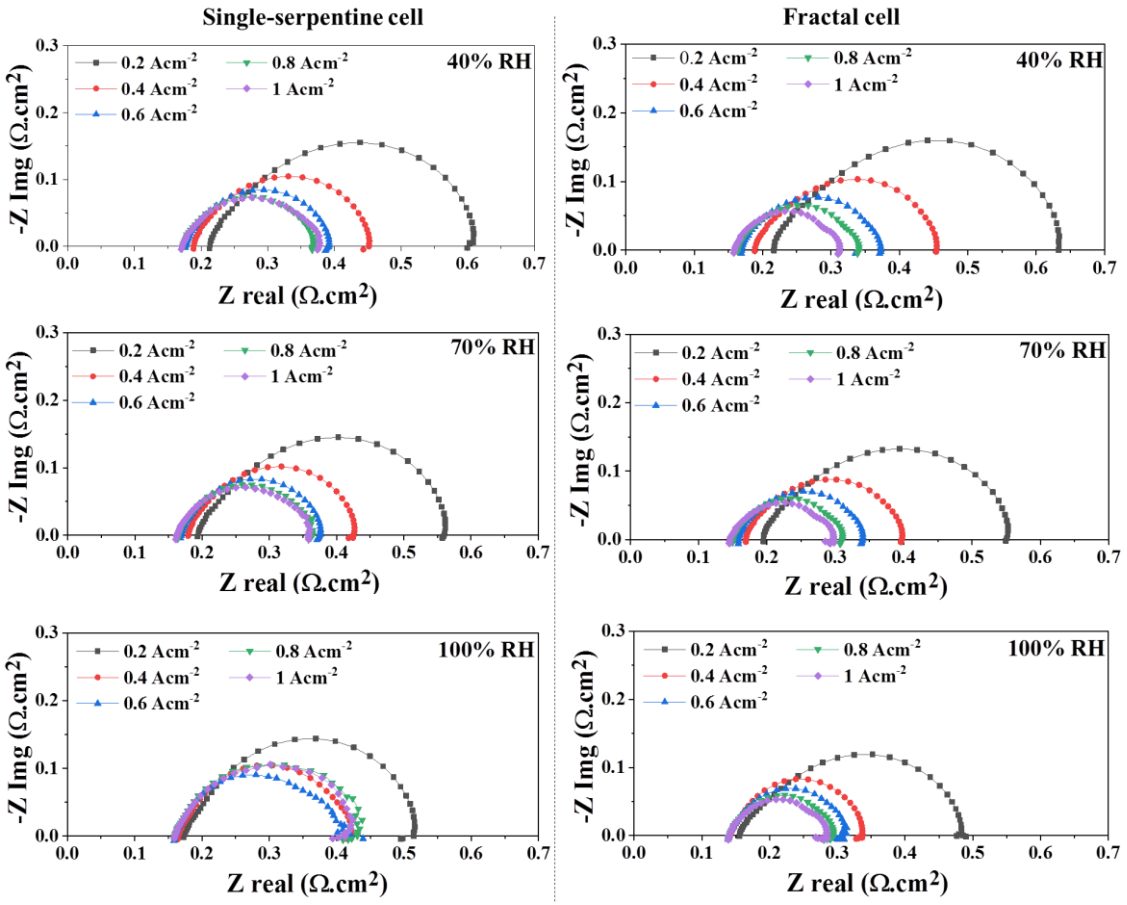

Figure 58: Electrochemical impedance spectroscopy (EIS) curves for single-serpentine and fractal cells at 40%, 70% and 100% reactant RH and 0.2 A cm^{-2}, 0.4 A cm^{-2}, 0.6 A cm^{-2}, 0.8 A cm^{-2} and 1 A cm^{-2} current density.

Low frequency resistance (LFR), as shown in Fig. 57 (b), was measured from the low frequency real axis intercept of the EIS measurements and corresponds to the total resistance developed in a cell [64]. An initial decrease in LFR, as seen in Fig. 57 (b), can be attributed to the transition of the cell from the activation to the Ohmic region of operation [206]; a gradual reduction in LFR for both cells was observed between 0.2 A cm^{-2} and 0.6 A cm^{-2}. The LFR, at 40%,

70% and 100% RH, for the single-serpentine and fractal cells, were almost similar, with 0.63 Ω.cm^2, 0.57 Ω.cm^2, 0.51 Ω.cm^2 and 0.65 Ω.cm^2, 0.55 Ω.cm^2, 0.49 Ω.cm^2 respectively at 0.2 A cm^{-2}, and with 0.39 Ω.cm^2, 0.37 Ω.cm^2, 0.36 Ω.cm^2 and 0.36 Ω.cm^2, 0.33 Ω.cm^2, 0.32 Ω.cm^2 respectively at 0.6 A cm^{-2}. It can be observed that, between 0.2 A cm^{-2} and 0.6 A cm^{-2}, the reduction in LFR was consistent with the reduction in HFR, as observed in Fig. 57 (a). However, with an increase in current density to 0.8 A cm^{-2} and further to 1 A cm^{-2}, a sudden rise in LFR for the single-serpentine cell was observed. This sudden growth in LFR for the single-serpentine cell, especially at higher operating currents, can be attributed to the increased charge and mass transport related resistances as a result of cell flooding and reactant starvation [211]. The corresponding charge transfer resistances (R_{ct}) and mass transfer resistances (R_{mt}) for the single-serpentine and fractal cells at 0.8 A cm^{-2} and 1 A cm^{-2} current densities are given in Table 3. In contrast, the LFR for the fractal cell continued to decrease throughout its operation, especially in the high current density region, where R_{ct} and R_{mt} of the fractal are lower than that of the single-serpentine, which can be attributed to the flooding-free, diffusion-dominated oxygen mass transport at its MEA surface [60].

Table 3: Charge transfer resistances and mass transfer resistances for single-serpentine cell and fractal cell at 0.8 A cm^{-2} and 1 A cm^{-2} for 40%, 70% and 100% RH reactant conditions.

		Single-serpentine			**Fractal**		
		40% RH	**70% RH**	**100% RH**	**40% RH**	**70% RH**	**100% RH**
R_{ct}($\Omega.cm^2$)	**@ 0.8 A cm^{-2}**	0.207	0.175	0.221	0.189	0.147	0.138
	@ 1 A cm^{-2}	0.194	0.172	0.225	0.188	0.136	0.123
R_{mt}($\Omega.cm^2$)	**@ 0.8 A cm^{-2}**	0.015	0.024	0.041	0.006	0.012	0.015
	@ 1 A cm^{-2}	0.016	0.024	0.046	0.008	0.015	0.016

6.25 cm^2 "1-way and 2-way" fractal PEMFC

High frequency resistance (HFR) values, presented in Fig. 60, were measured from the high-frequency, real-axis intercept of the Nyquist plot of the EIS measurements. For the fractal PEMFCs, the HFR was identified to be uniform, within 5-10% variation, between 200 mA cm^{-2} and 1000 mA cm^{-2}, as shown in Fig. 59. The relatively small difference in HFR for the fractal PEMFCs, over this current density range, indicates that the membrane was sufficiently hydrated throughout its operation, especially in the high current density region, where higher cell temperatures tend to dehydrate the membrane.

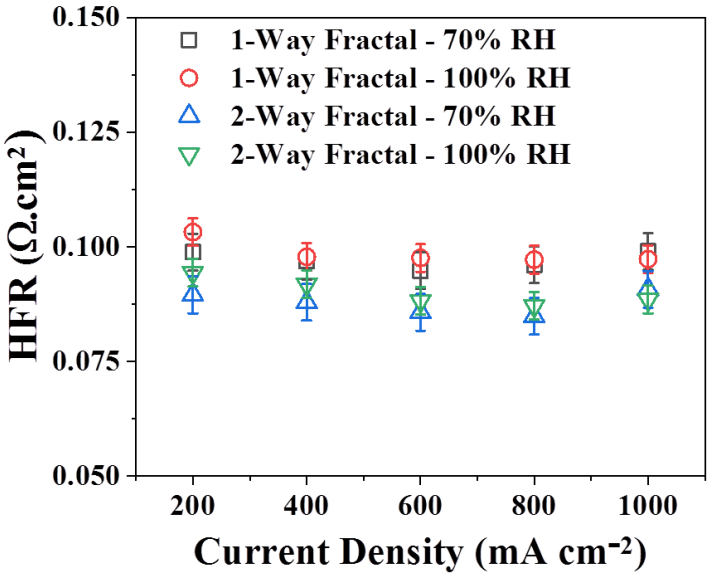

Figure 59: High frequency resistance (HFR) for the fractal PEMFCs tested at different reactant RH and current density conditions, all at T = 45 ˚C.

Furthermore, at a given experimental condition (reactant RH), the Ohmic resistance for the 2-way fractal PEMFC is observed to be lower than that of the 1-way fractal PEMFC. This may be attributed to the increased contact area between the flow-field and MEA in the 2-way fractal (section 4.2.1, Fig. 37), especially when all the other factors affecting the bulk resistance, like cell temperature, assembly torque, current density, reactant RH, etc., were constant [206]. Furthermore, the impact of reduced Ohmic resistance in the 2-way fractal PEMFC can be observed from its better performance at low current density (Figs.54 (a) and 54 (b)). Thus, the deterioration in cell performance observed for the 2-way fractal PEMFC can be ascribed to the reduced oxygen concentrations at the membrane surface, caused by excessive hydration or flooding in the electrode region [212].

The Nyquist curves for EIS measurements of 1-way and 2-way fractal PEMFCs at 70% and 100% reactant RH are presented in Figs. 61 (a) and 61 (b), respectively. The corresponding charge transfer (R_{ct}) and mass transfer (R_{mt}) resistances are given in Table 4 (the equivalent circuit used for modelling is given in Fig. 28).

At 70% RH, the corresponding R_{ct} for the 1-way and 2-way fractal PEMFCs are very similar at ~0.03 Ω cm^2, within a range of 10%, at 800 mA cm^{-2} and 1000 mA cm^{-2} current density conditions, as observed from Table 4. However, the mass transport resistances developed in the 2-way fractal PEMFC are much larger than those developed in the 1-way fractal PEMFC, which can be attributed to mass transfer related issues in the 2-way fractal flow-field [201,206,213].

Furthermore, at higher reactant humidity (100% RH), R_{ct} for the 1-way fractal PEMFC, at 800 mA cm^{-2} and 1000 mA cm^{-2}, was similar to that at 70% RH, while a slight increase in the R_{mt} was observed. However, in the 2-way fractal PEMFC, R_{ct} increased by 29% and 36% at 800 mA cm^{-2} and 1000 mA cm^{-2}, respectively. Such an increase in R_{ct} with reactant RH can be attributed to the presence of some unresolved mass transport component contained in the charge transfer resistance [206,213]. In addition, the corresponding R_{mt} for the 2-way fractal PEMFC at 800 mA cm^{-2} and 1000 mA cm^{-2} was 0.89 Ω cm^2 and 1.07 Ω cm^2, respectively. Such large R_{mt} values were developed at 100% RH due to the excessive water flooding of the cell, which was already evident at 70% RH at higher current densities [214,215]. This reflects the inability of the 2-way fractal flow field design to regulate excess water away from the flow-field region. However, throughout its operation, the 1-way fractal PEMFC maintained

uniform water distribution in the cell, which is reflected in lower resistance values.

Overall, the observations from the EIS measurements provide further support for the deductions made on the state of water distribution in the fractal flow-fields.

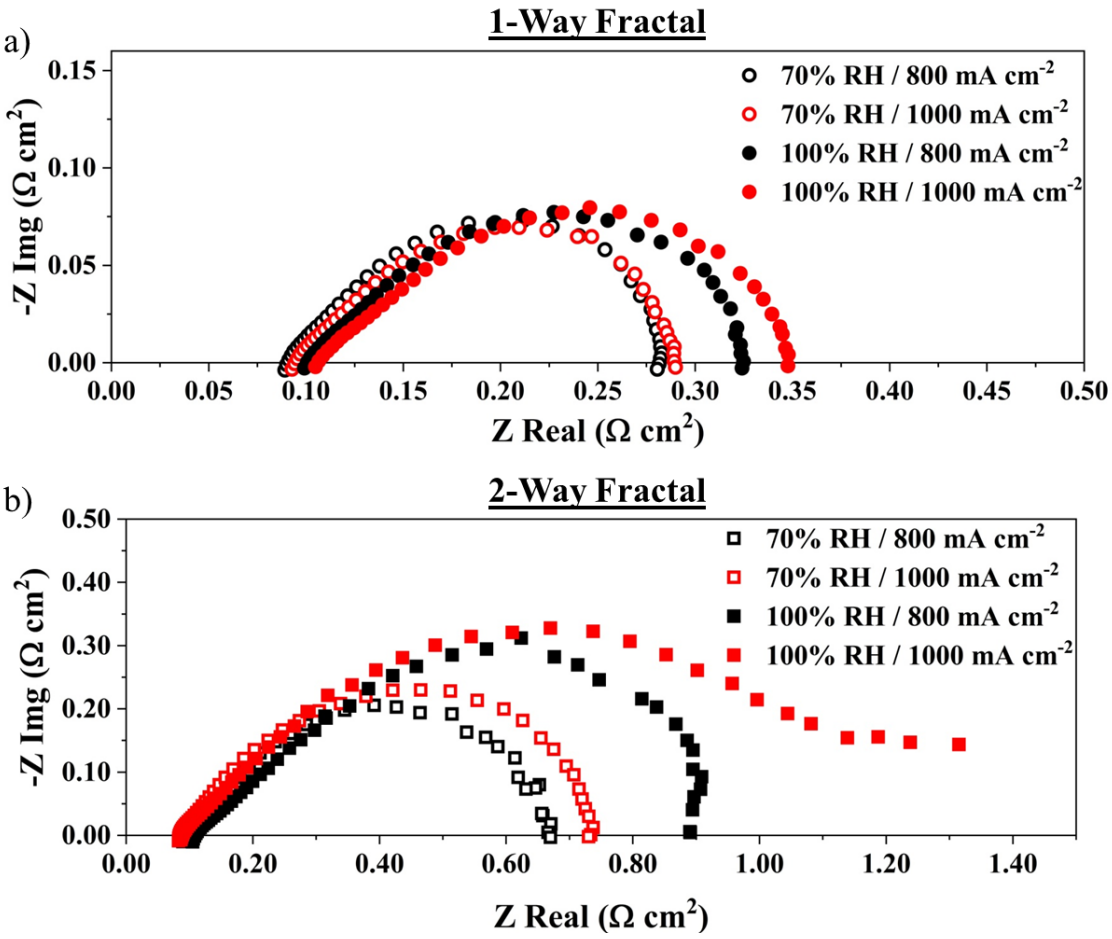

Figure 60: Nyquist curves for electrochemical impedance spectroscopy (EIS) measurements for 1-way and 2-way fractal PEMFCs at 800 mA cm^{-2} and 1000 mA cm^{-2} and at (a) 70% reactant RH and (b) 100% reactant RH, respectively.

Table 4: Charge transfer R_{ct} and mass transfer R_{mt} resistances for 1-way and 2-way fractal PEMFCs at 70% and 100% reactant RH and at 800 mA cm^{-2} and 1000 mA cm^{-2}.

Experimental condition	Current density (mA cm^{-2})	Charge transfer (R_{ct}) (Ω cm^2)	Mass transfer (R_{mt}) (Ω cm^2)
70% RH 1-way	800	0.03	0.15
	1000	0.03	0.16
100% RH 1-way	800	0.033	0.18
	1000	0.035	0.19
70% RH 2-way	800	0.031	0.55
	1000	0.033	0.62
100% RH 2-way	800	0.040	0.89
	1000	0.045	1.07

5.3.3. Operating stability

A galvanostatic test was performed to evaluate performance stability of the 6.25 cm^2 fractal PEMFC under both relatively dry and relatively humid conditions. Fig. 61 shows galvanostatic measurements at 40% RH (dry) and 70% RH (humid) conditions, where the current density is maintained at 700 mA cm^{-2} and 750 mA cm^{-2}, respectively. At 40% RH, the performance of the lung-inspired flow-field is more stable compared to that of the single-serpentine flow-field over the entire duration of the test; the cell voltage variation for the lung-inspired and single-serpentine flow-fields ranged within 4% and 8%, respectively, of their initial values. Furthermore, at 70% RH the cell voltage variation range for the lung-inspired flow-field decreased to 2%, while for the single-serpentine flow-field it was much higher at 12%.

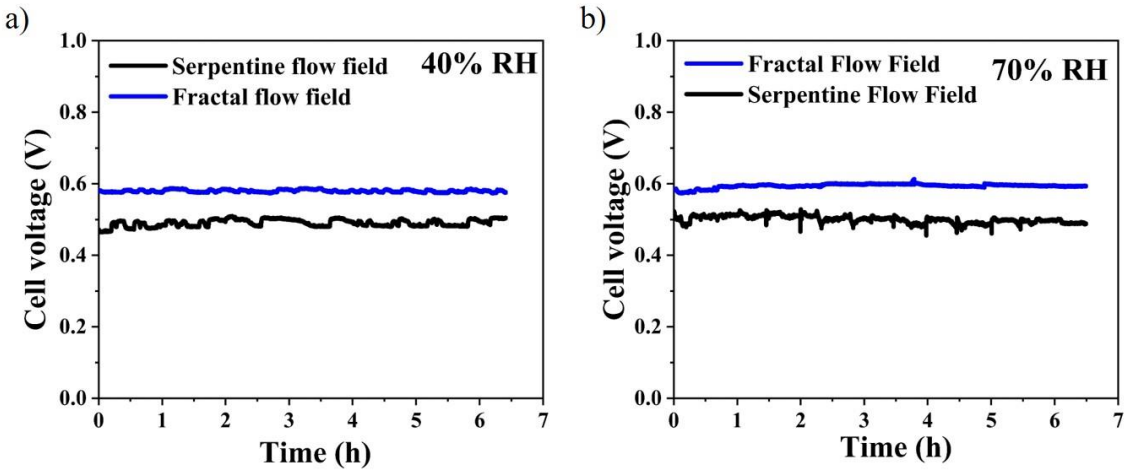

Figure 61: Cell voltage fluctuation over 6 h during galvanostatic tests at (a) 40% RH and 700 mA cm^{-2} and (b) 70% RH and 750 mA cm^{-2}.

Cell voltage fluctuations and erratic behaviour are related to liquid water accumulation in the gas distribution channels and its uneven removal [216,217]. Increase in water accumulation decreases the voltage, and *vice versa* [218]. The results in Fig. 61 provide further evidence of a more uniform water distribution and cell performance in the lung-inspired design, compared to the conventional single-serpentine design. The convection-dominated gas flow in the single-serpentine flow-field may have resulted in uneven levels of water saturation, creating regions of high and low water retention (flooding and drying) [35]. In addition, the single-serpentine flow-field could be subject to periodic localised flooding [126], suggested by the cell voltage fluctuations [219,220]. In previous work, the extent of the cell voltage fluctuations (peaks in Fig. 61 (a) and 60(b)) has been linked to the degree of flooding in a fuel cell [197], the degree of hydration of the membrane and its level of swelling [221]. Increasing RH from 40% to 70% increases the level of cell voltage fluctuations for the single-serpentine flow-field, indicative of greater flooding in channels at higher RH. However, the lung-inspired system remains stable when humidity

increases, which is consistent with more uniformity in water distribution. This is in line with the improved transport of reactants via lung-inspired flow-fields.

Furthermore, galvanostatic testing was performed on the 1-way and 2-way fractal PEMFCs, to compare the relative performance, by operating them at a constant current density of 1000 mA cm^{-2} and 70% reactant RH for a little over 3 h. The corresponding cell voltage fluctuation are presented in Fig. 62.

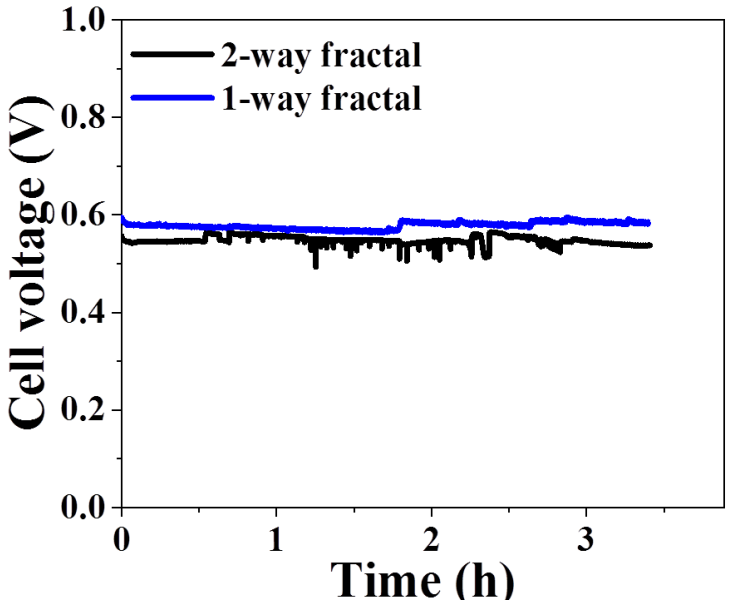

Figure 62: Cell voltage fluctuation over 3 h during galvanostatic tests at 70% RH and 600 mA cm^{-2} for 1-way and 2-way fractal PEMFCs.

As observed in the single-serpentine case previously, intermittent voltage fluctuations observed in the 2-way fractal PEMFC can be attributed to the flooding events occurring inside the cell [221]. In contrast, the cell voltage for the 1-way fractal PEMFC remains almost constant compared to the fluctuating cell voltage observed for the 2-way fractal PEMFC. This is due to more effective

water removal from the cell, resulting in less water retention at the flow-fields [181].

5.4. Conclusions

This chapter presented a study that is the first to combine a fractal, lung-inspired cathode flow-field with a low cost PCB-based manufacturing technique, via a layer-wise assembly approach. The PCB-based approach offers a cost-effective alternative to previously reported fabrication methods for such flow-fields, which employed selective laser sintering. This also opens up the possibility of easily scalable manufacturing of fractal flow structures for a range of other applications.

Initially, a 6.25 cm^2 lung-inspired flow-field (1-way) delivered enhanced performance compared to a conventional single-serpentine flow-field. Polarisation curves indicated a performance enhancement in lung-inspired flow-fields by 41%, 12% and 14% at 0.6V cell potential for 40%, 70% and 100% reactant humidity (RH) conditions, respectively. Higher operating temperatures by 2-3 ºC were observed in the lung-inspired flow-field that resulted in its superior performance over the single-serpentine flow-field.

In addition, the performance enhancement in the lung-inspired flow-field was particularly observed at high RH and high current density. Electrochemical impedance spectroscopy established that this is due to more uniform distribution of reactants and water management in the cell; the mass transfer resistances developed at 100% RH and higher current density (~900 mA cm^{-2}) were 0.04 $\Omega.cm^2$ for a lung-inspired flow-field and 0.9 $\Omega.cm^2$ for a single-serpentine flow-field. Galvanostatic tests on the flow-fields indicated a much more stable operation of lung-inspired PEMFC; voltage fluctuations at constant current hold for lung-inspired and single-serpentine flow-fields were observed to

be within, respectively, 2% and 12% of their initial values at relatively humid reactant conditions.

Similar to the 6.25 cm^2, a 25 cm^2 fractal fuel cell with 5 fractal generations delivered better performance, especially in high current density region of polarisation, compared to the conventional single-serpentine cell, at different reactant and operating conditions. The enhanced performance of the fractal cell was a result of higher cell temperatures of around 5 – 7 ºC developed in the fractal cell compared to the single-serpentine cell. Uniform and stable Ohmic resistances were measured for both cells, indicating a uniformly hydrated membrane condition throughout the operation. In addition, electrochemical impedance spectroscopy measurements showed stable and flooded operating conditions in the fractal and the single-serpentine cells, respectively.

This chapter also presented, for the first time, the design, development and testing of a new 2-way fractal flow-field that has an increased contact area, but a more convoluted water removal path, compared to the previously reported fractal 1-way flow-field. The influence of contact area and water removal mechanism on the performance delivered by the fractal PEMFCs was investigated. The acoustic emission technique was utilised to understand and diagnose water management inside both fractal PEMFCs.

The 2-way fractal PEMFC delivered better performance in the Ohmic region of operation: 0 - 700 mA cm^{-2} at 70% RH and 0 - 400 mA cm^{-2} at 100% RH. Beyond this, its performance degraded drastically, compared to the 1-way fractal PEMFC, as a result of severe cell flooding. Good correlation was

observed between complementary measurements of cell polarisation curves, cell temperature and cell voltage fluctuation during galvanostatic testing.

Further efforts are ongoing to address the design of the reactant flow outlet path in the 2-way fractal system by making it less convoluted, which should result in better overall performance, particularly in the mass transport limited region.

6. Performance diagnostics of lung-inspired PEMFCs using current and temperature mapping metrology

6.1. Introduction

Current and temperature mapping have been instrumental for the *in situ* diagnosis and analysis of various factors that affect the performance of fuel cells, such as water management [141–143], reactant concentration and distribution [30,142,144], reactant physical conditions [145,146], flow channel configurations [147], thermal management [148,149] and cell compression [150]. Some of the current distribution measurement techniques include indirect correlations based on local values [152], use of magnetic effects and Hall sensors [153,154], measurements of the local potential at the GDL and catalyst layers, and segmented measurement [155]. Temperature distribution measurement techniques include thermocouple insertions [156], infrared imaging [149,157] and segmented measurement. Segmented measurements are a popular technique, especially for combined current and temperature measurements, due to their ability to directly measure localised phenomena, like reactant starvation and flooding inside the fuel cell [141,157,158]. Furthermore, PCB-based segmented current collectors are widely used in the combined measurements of current and temperatures, due to their low cost operation, usage flexibility during assembly and disassembly, and easy implementation and *in situ* measurement within the cell [144,148,159,160].

Studies reported in section 5.3 on a 25 cm^2 fractal PEMFC saw a fractal cell performing better than a single-serpentine cell, as a result of improved reactant distribution and water management inside the cell, which influences the overall current and temperature generated in the cells; this was observed via a range of electrochemical characterisation techniques [36,56,182]. In this chapter, current and temperature mapping metrology are utilised, for the first time, to provide

crucial additional information that allows understanding the better performance of the fractal fuel cell compared to a conventional single-serpentine fuel cell. The mapping primarily investigates the role of reactant RH and operating conditions on the surface current and temperature distributions. Furthermore, localised conditions, like segment currents are investigated to analyse the influence of flow-field structure on the cell's overall performance.

Sections of this chapter have been published or are under press in the following journal articles:

- **V.S. Bethapudi**, J. Hack, P. Trogadas, G. Hinds, P.R. Shearing, D.J.L. Brett and M.-O Coppens, Hydration state diagnosis in fractal flow-field based polymer electrolyte membrane fuel cells using acoustic emission analysis, Energy Convers. Manag. 2020; 220:113083.
- **V.S. Bethapudi**, M. Maier, G. Hinds, P.R. Shearing, D.J.L. Brett, M.O. Coppens, Acoustic emission as a function of polarisation: Diagnosis of polymer electrolyte fuel cell hydration state, Electrochem. Commun. 2019; 109: 106582.
- **V.S. Bethapudi,** J. Hack, P. Trogadas, J.I.S. Cho, L. Rasha, G. Hinds, P.R. Shearing, D.J.L. Brett, M.-O.Coppens, A lung-inspired printed circuit board polymer electrolyte fuel cell, Energy Convers. Manag. 2019; 202 :112198.

6.2. Materials and experiments

6.2.1. Fuel cell assembly

The fuel cell components and their order of assembly are shown in Fig. 63. A current and temperature mapping plate (S++ Simulation Services, Germany), was sandwiched between the anode flow-field and anode current collector.

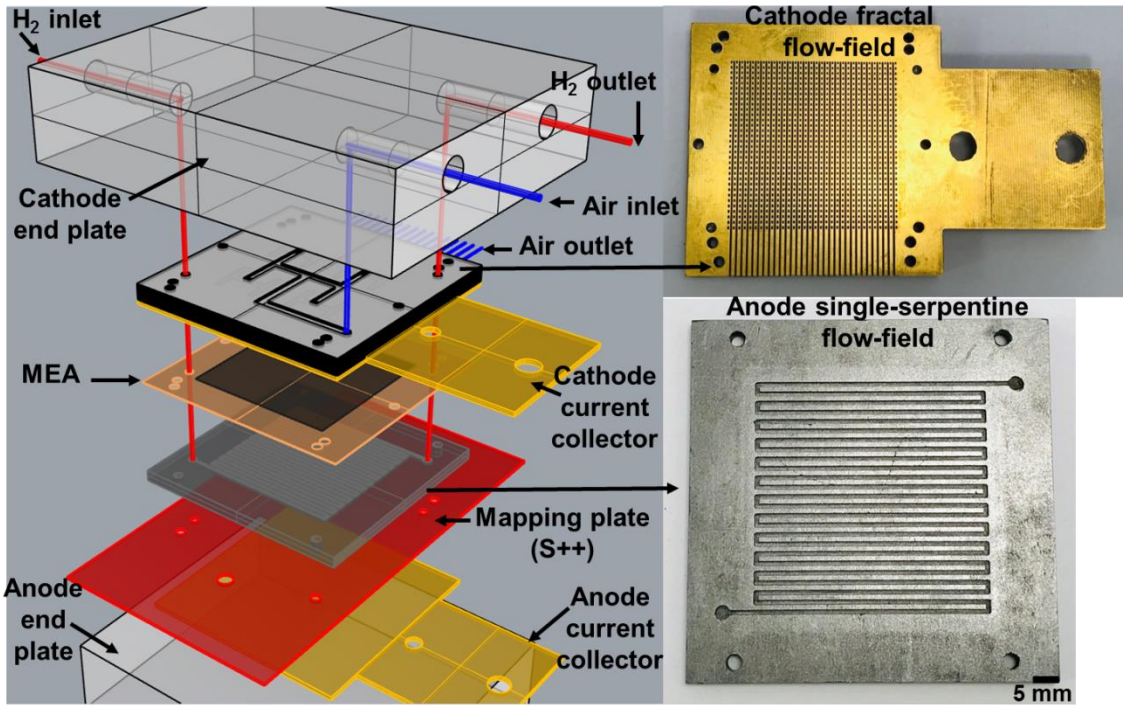

Figure 63: Assembly outline and primary components used in the PEMFCs tested.

The S++ plate consisted of an array of 10 x 10 integrated shunt resistors, with each resistor having an area of 5 x 5 mm^2 covering a total electrode area of 25 cm^2. The current measurements occurred in through plane mode. The voltage measurements occurred from the anode current collector that included the Ohmic resistance contribution from the mapping plate (S++). The surface temperature distribution measurement utilised an array of 5 x 5 temperature sensors. Current and temperature measurements were performed

simultaneously and their respective sensors were provisioned on the same sensor plate – a PCB-plate with gold coated contact segments. The S++ plate was connected to a computer via a USB interface that provided live displays of current and temperature contours, and data recording. The reactants, air and H_2, were supplied from the cathode region of the cell. The air outlets for both cells (fractal and single-serpentine cathode) occurred via surface vertical flow paths into the ambient, as in Figs. 49 and 64, while the H_2 outlet occurred from a manifold, as shown in Fig. 49. The corresponding air and H_2 flows are represented, respectively, by blue and red lines in Fig. 49. Necessary compression for the cell components, which was 1.4 Nm in this case, was provided using aluminium end plates at the cathode and anode.

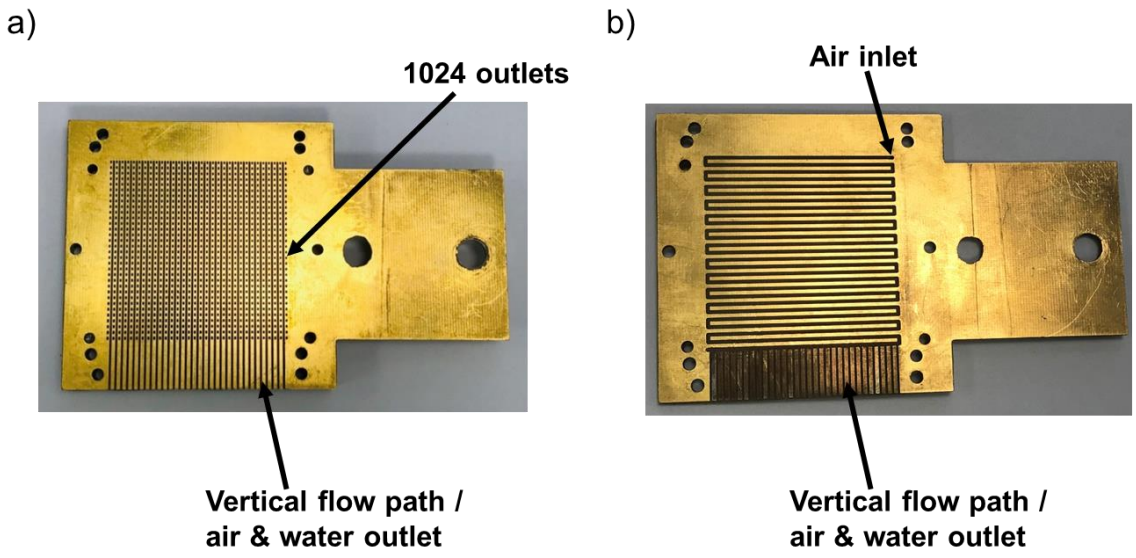

Figure 64: Final assembled (a) cathode fractal flow-field – 7.25 mm x 80 mm x 80 mm and (b) cathode single-serpentine flow-field – 3.2 mm x 80 mm x 80 mm.

The anodic end plate also acted as a heating device, providing the necessary start-up temperature to the cells, which was 45 °C. The cell temperatures were measured using a K-type thermocouple from the anode flow-field plate of the

cells. The anode region was chosen for cell temperature measurements, due to different cathode flow-fields used in the fuel cells tested, whose temperature measurements may not give an accurate representation of the local cell temperatures for comparison due to varying flow-field thicknesses. The cells operated under ambient cooling conditions.

6.3. Results, analysis and discussion

6.3.1. Current distribution analysis

The current and temperature mapping results presented in this section were obtained during polarisation experiments on the 25 cm^2 cell, as discussed in section 5.3.1, with the results shown in Figs. 52 and 53. Current distribution maps, in the anode region of the cells, at 40%, 70% and 100% reactant RH are presented in Figs. 65 – 67, where (a, d), (b, e) and (c, f) represent the current distribution maps at 0.8 V, 0.6 V and 0.4 V cell potentials, respectively.

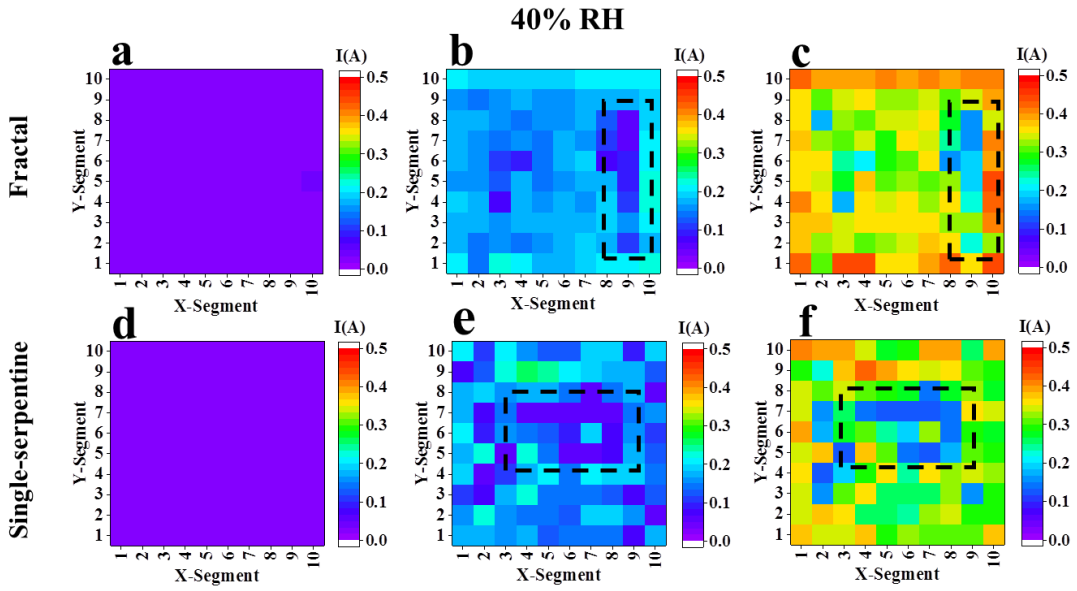

Figure 65: Current distribution for fractal (top) and single-serpentine (bottom) cells under 40% reactant RH and at (a, d) 0.8 V, (b, e) 0.6 V and (c, f) 0.4 V respectively.

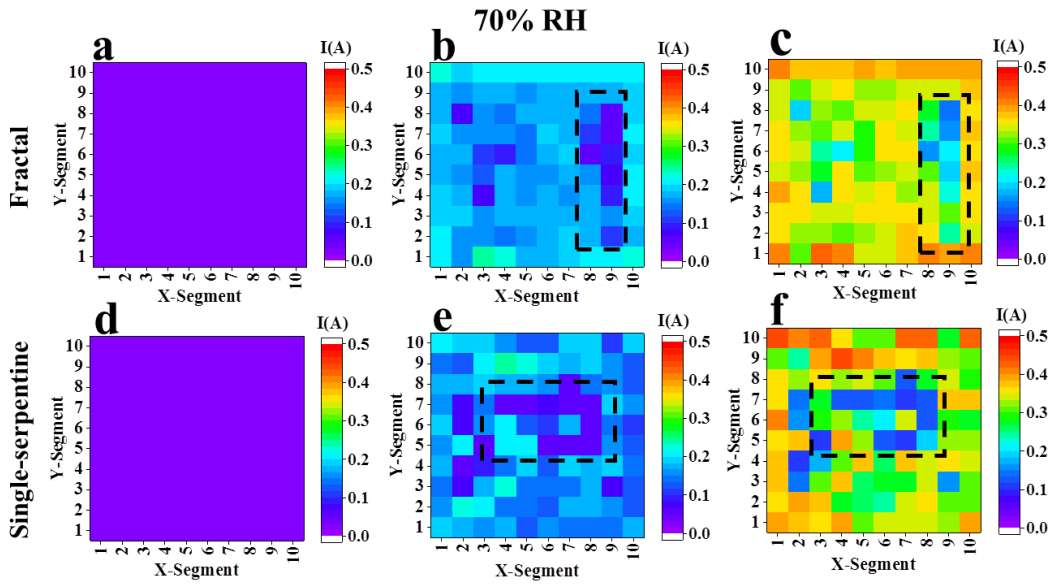

Figure 66: Current distribution for fractal (top) and single-serpentine (bottom) cells under 70% reactant RH and at (a, d) 0.8 V, (b, e) 0.6 V and (c, f) 0.4 V, respectively.

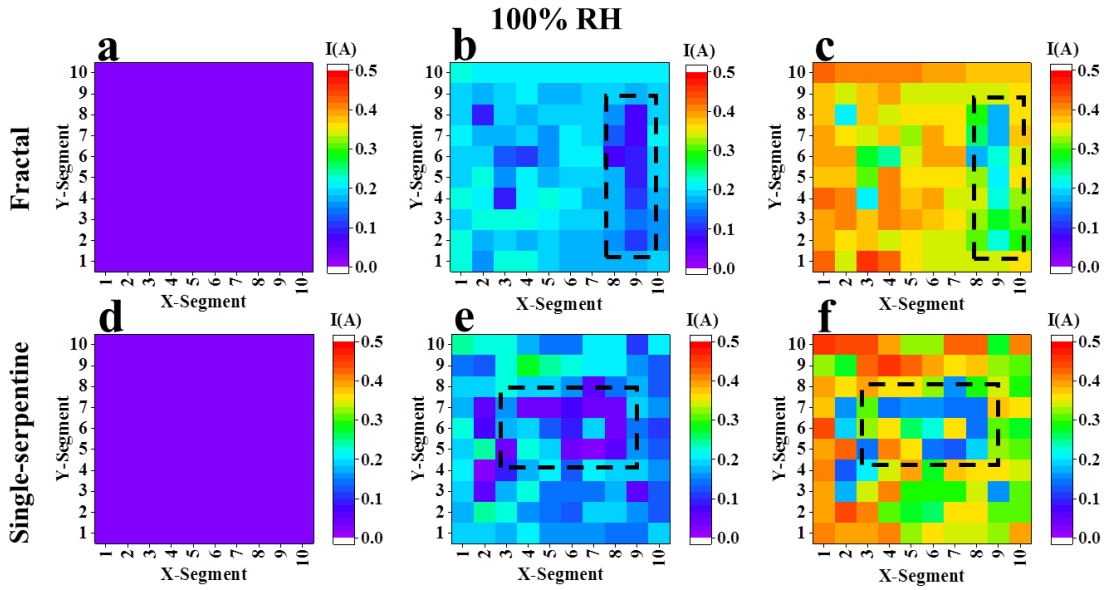

Figure 67: Current distribution for fractal (top) and single-serpentine (bottom) cells under 100% reactant RH and at (a, d) 0.8 V, (b, e) 0.6 V and (c, f) 0.4 V, respectively.

The maps are indexed through x-segments (1 – 10) and y-segments (1 – 10), as shown in Figs. 65 – 67, according to the 10 x 10 shunt resistors on the S++ plate.

A schematic representation of the cathode flow-fields, as covered under the current mapping segments, is given in Fig. 68. Furthermore, the mean of segment currents (MSC) and the corresponding standard deviation (STDEV) representing variations in segment currents from the MSC are given in Fig. 69.

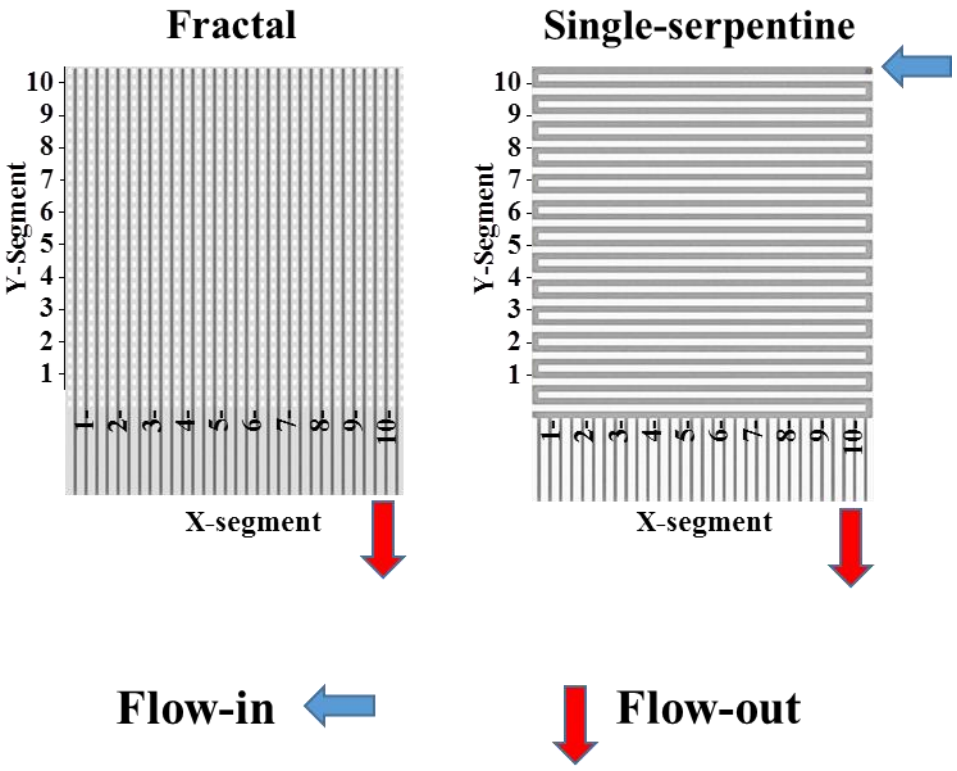

Figure 68: Schematic representation of the fractal and single-serpentine cathode flow-fields, covered under the current mapping segments. Could not depict flow-in for the fractal as it occurs from behind the plate.

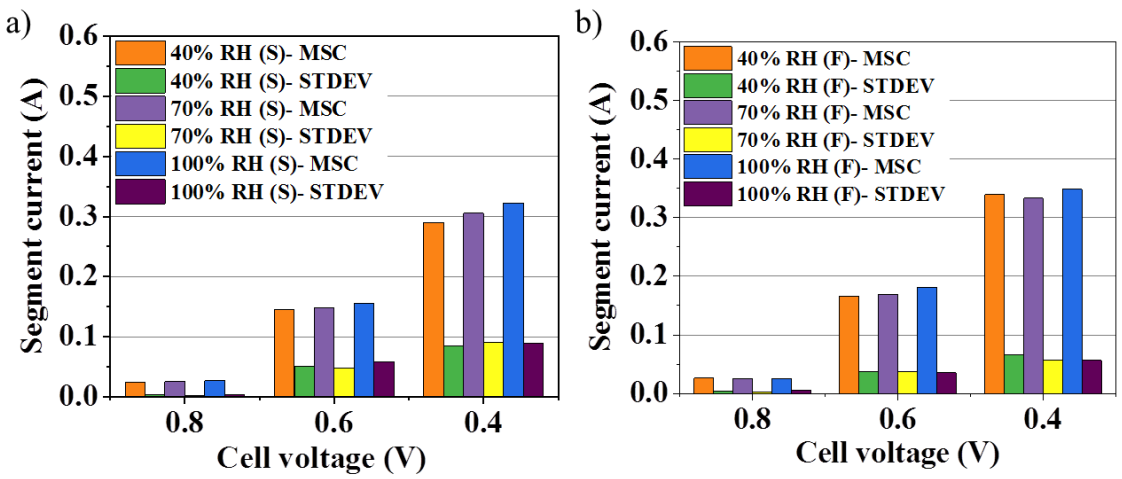

Figure 69: Mean of segment currents (MSC) and their corresponding standard deviation (STDEV) for (a) single-serpentine fuel cell and (b) fractal fuel cell, at 40%, 70% and 100% reactant RH respectively. Legend: S – single-serpentine, F – fractal.

At 0.8 V cell potential, it can be observed from the maps in Figs. 65 – 67 that, irrespective of the reactant RH condition, a similar current distribution, segment-wise and overall, is measured in single-serpentine and fractal cells. MSC and STDEV at 0.8 V for both cells are similar at ~0.025 A and ~0.003 A, respectively. This implies that the overall current distribution is uniform in both cells at low operating currents [146,222,223]. Such homogeneity in the current distribution, at higher cell voltages, can be attributed to negligible diffusion limitations, since the intrinsic rate of reaction and current are low as well, with minimal requirements on water management and reactant concentration [145,159]. Here, the observed similarities in current distribution between the cells corroborate with the polarisation performances observed in Fig. 52, where, at 0.8 V, each cell delivered an output of ~0.1 A cm^{-2} = (100 x 0.025 A)/25 cm^2.

At lower cell potentials of 0.6 V and 0.4 V, the MSC and STDEV for the fractal cell are observed to be larger and smaller, respectively, compared to those

observed for the single-serpentine cell, indicating higher currents (overall and segment-wise) with a more homogeneous distribution generated in the fractal cell. The specific influence of the cathode flow-field structure on the current distribution patterns observed in Figs. 65 – 67 can be evaluated in detail if the segment currents, which are a reflection of the electrochemical activity (and associated current) occurring in the cell regions covered by the segments, are analysed.

At 0.6 V and 0.4 V cell potentials, the current maps in Figs. 65 – 67 show that each cell develops regions with low and high local currents. However, the number of such regions varies, depending on the cathode flow-field type used (note again that a single-serpentine anode flow-field was used in both cases). In particular, the number of low current segments developed in a fractal cell is much lower than those developed in a single-serpentine cell under any condition. For instance, in the 40% RH case (Fig. 65), comparing the areas surrounded by a dashed line-, especially segments between (X9, Y4) – (X9, Y8) of the fractal cell and segments between (X2, Y3) – (X2, Y7), (X4, Y7) – (X8, Y7) and (X6, Y5) – (X8, Y5) of the single-serpentine cell consist of particularly low current regions, which correspond to segments delivering currents lower than the MSC. Similar trends in the low current segments are observed at 70% RH (Fig. 66) and 100% RH (Fig. 67), respectively.

It is widely observed in fuel cells that low currents result from either dehydrated or flooded conditions of the cell regions, while high cell currents occur only when the cell regions have balanced hydration [216,224,225]. Sufficient cell hydration, throughout the experimental conditions, was confirmed by the uniform and stable HFR measured, as shown in Fig. 57 (a) of section 5.3.2.

This rules out dehydration as a reason for the observed low currents [226]. Thus, the low current segments that developed should be attributed to reactant starvation, occurring due to the presence of localised flooding in the cell regions covered by these segments. Furthermore, the localised flooding in the cells is observed only at higher operating currents (corresponding to 0.6 V and 0.4 V cell potentials), irrespective of reactant RH, implying that the generation of water from electrochemical reactions contributes significantly to the observed flooding.

The single-serpentine cell developed more extended regions of localised flooding, seen as a prominent horizontal blue patch covering the segments (X4, Y7) – (X8, Y7) and (X6, Y5) – (X6, Y8) [227]. This patch of localised flooding, occurring at preferential regions of the cell, can be attributed to the presence of water droplets on the hydrophobic surface of the cathode GDL and channel interface, which was wicked away through the GDL pores into the channels [20,228]. Furthermore, channel flooding in the single-serpentine cell can be confirmed by the horizontal distribution of the very low current regions, which is consistent with the horizontal cathode flow channel arrangement for reactant supply and removal in the cell, as seen in Figs. 64 and 68 [157]. Comparatively, in the fractal cell, only minimal localised flooding is observed, with the only prominent low current region between (X9, Y4) – (X9, Y8), appearing as a vertical blue patch. The observed vertical distribution of very low currents is consistent with the vertical flow paths in a fractal cell for the removal of reactants and water (Figs. 64 and 68), where localised channel flooding could be expected. Furthermore, all other segments in either cell, with the exception of those in the low current regions, result in improved performance with

increased reactant RH, asserting the observed low current regions as a result of localised flooding only, which may have resulted in the local blocking of reactant supply to the MEA [142,229].

6.3.2. Segment current analysis

In the single-serpentine cell, more heterogeneous segment current distribution is observed. This is a typical current distribution pattern observed in serpentine based flow-fields, where non-uniform distribution of oxygen over the MEA region, due to flooding along the channel length, results in significant current distribution gradients [146,158,159,230]. However, relatively lower gradients with a more homogeneous current distribution between high (orange-red) and low (blue) current regions are observed in the fractal cell, as in Figs. 65 – 67, which may be attributed to the presence of more uniform concentration of oxygen at its MEA surface, as a result of diffusion controlled reactant (air) transport facilitated by a close spacing between the outlets, which are uniformly reached through a fractal branching hierarchy [36,58,182,196].

To evaluate the intensity of localised flooding in the cells, and their response to variations in reactant RH, based on the current distribution maps of the cells a sample low current (zone-α) and high current (zone-β) regions are identified and evaluated. In the fractal cell, low (zone α) and high (zone β) current regions are segments (X9, Y4) – (X9, Y8) and (X1, Y4) – (X1, Y8), respectively, as seen in Fig. 65 – 67. Fig. 70 depicts the local currents, segment-wise, in zones α and β.

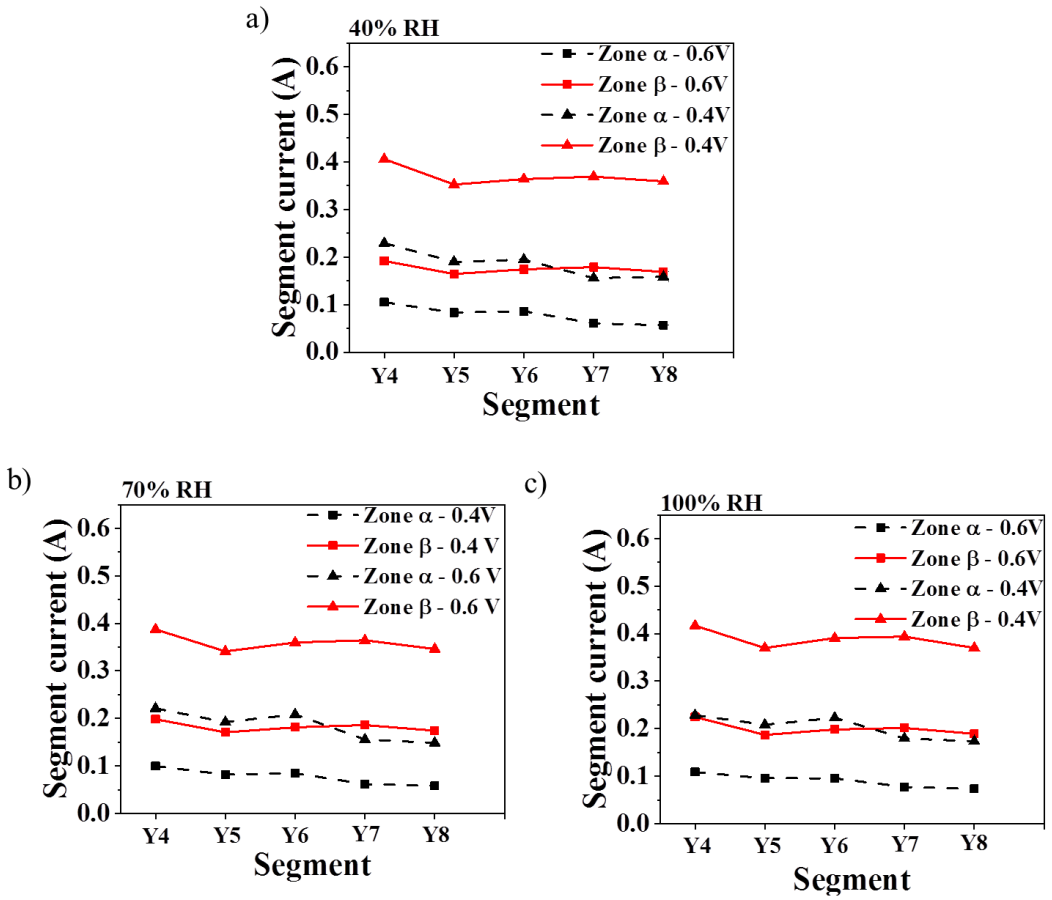

Figure 70: Regions of representative low and high local currents in a fractal cell at: (a) 40% reactant RH, (b) 70% reactant RH, and (c) 100% reactant RH. Low current region (zone α) = segments between (X9, Y4) and (X9, Y8) and high current region (zone β) = segments between (X1, Y4) and (X1, Y8).

The average difference between zone-β and zone-α segment currents at 0.6 V are 0.10 A at 40% RH, 0.10 A at 70% RH and 0.11 A at 100% RH; at 0.4 V, they are, respectively, 0.18 A at 40% RH, 0.17 A at 70% RH and 0.19 A at 100% RH. In other words, there is no statistically significant effect of the RH on these differences; however the average difference is higher at the higher potential, corresponding to the lower current density. This difference between

zone segment currents can be attributed to increased localised flooding in the low current segments that reduces the corresponding zone currents further.

Similarly, in the single-serpentine cell, zone-α and zone-β comprise of current segments in the (X4, Y7) – (X8, Y7) and (X4, Y9) – (X8, Y9) regions, respectively. The corresponding segment current distributions in these segments are given in Fig. 71.

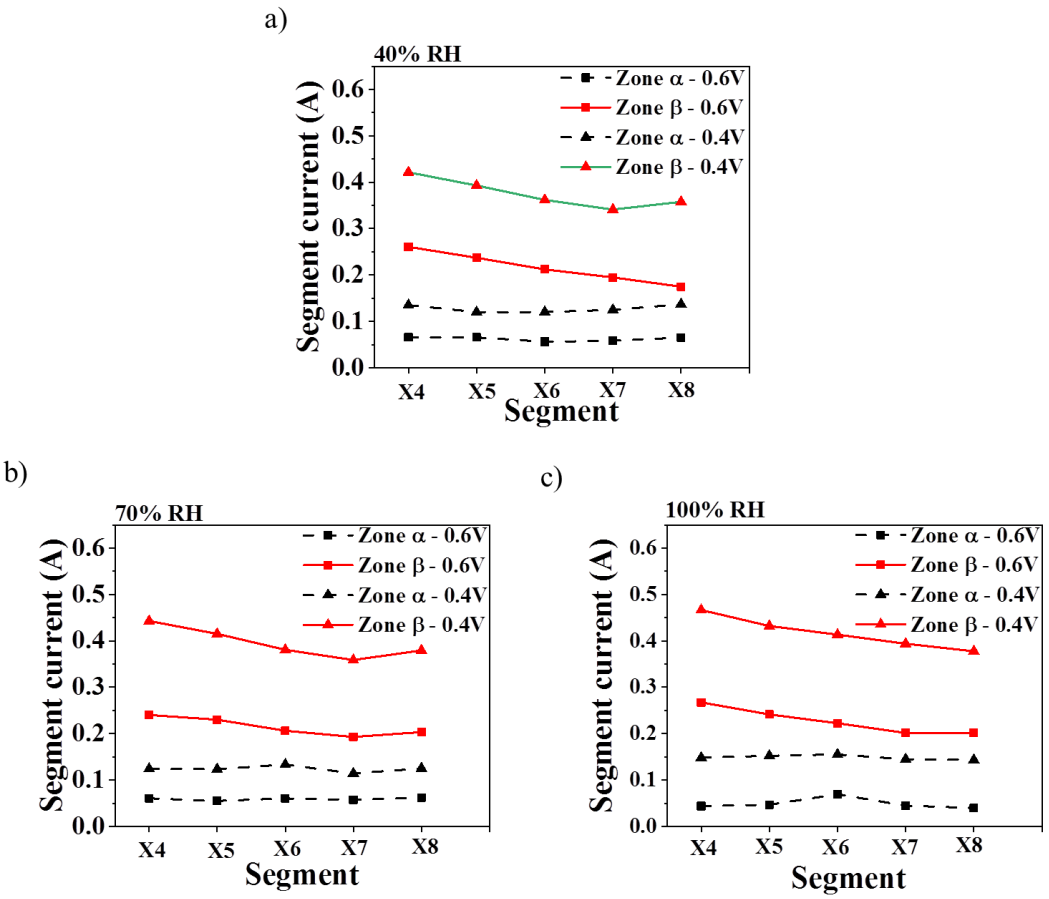

Figure 71: Regions of representative low and high local currents in a single-serpentine cell at (a) 40% reactant RH, (b) 70% reactant RH and (c) 100% reactant RH. Low current region (zone α) = segments between (X4, Y7) and (X8, Y7) and high current region (zone β) = segments between (X4, Y9) and (X8, Y9).

The average differences between the zone segment currents at 0.6 V are 0.15 A at 40% RH, 0.16 A at 70% RH and 0.18 A at 100% RH; at 0.4 V, these are, respectively, 0.25 A at 40% RH, 0.26 A at 70% RH and 0.27 A at 100% RH. Similar to the fractal cell, there is little variation with RH, but the difference between zone currents increases at lower cell voltages. However, it can be observed that, at any operating condition, the difference between zone currents for the single-serpentine cell is ~50% larger than that of the fractal cell. This can be attributed to ability of the fractal flow-field to uniformly distribute the reactants throughout the MEA region and flush the excess water out of the system, effectively maintaining better segment currents [182].

6.3.3. Surface temperature mapping

The corresponding anode surface temperature distributions, indicative of the local cell temperatures, for the fractal and the single-serpentine cells are given in Figs. 72 – 74. The core surface temperatures, measured at the centre of the anode surface, for the fractal cell at 0.6 V are 53.4 ºC (40% RH), 55.0 ºC (70% RH) and 56.1 ºC (100% RH) and at 0.4V are 64.6 ºC (40% RH), 66.1 ºC (70% RH) and 71.9 ºC (100% RH), respectively. Corresponding core cell temperatures for the single-serpentine cell at 0.6 V are 51.4 ºC (40% RH), 52.8 ºC (70% RH) and 54.5 ºC (100% RH) and at 0.4 V are 62.4 ºC (40% RH), 63.6 ºC (70% RH) and 65.4 ºC (100% RH), respectively.

Thus, the fractal cell develops much higher core temperatures compared to the single-serpentine cell, irrespective of reactant RH and cell operating voltage, corroborating the cell temperatures measured during polarisations, as in Fig. 53. Furthermore, the difference between the core and edge surface temperatures, as seen in Figs. 72 – 74, for both cells are similar: ~0.4-0.6 ºC at 0.8 V, ~1-2 ºC at 0.6 V and ~3-4 ºC at 0.4 V, irrespective of the reactant conditions, indicating overall higher surface temperature in the fractal cell. Furthermore, with continuous heat dissipation to the ambient along the edges, the temperature distributions developed as uniform gradients on the cell's surface with higher temperatures at the core and lower temperatures at the edges, respectively [160,231,232].

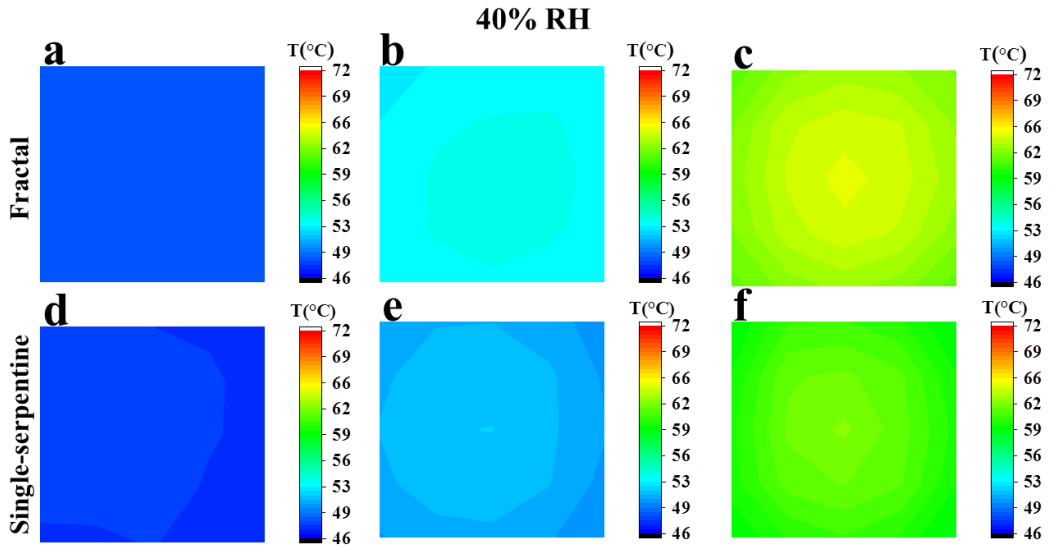

Figure 72: Anode surface temperatures for fractal and single-serpentine cells at 40% reactant RH and at (a, d) 0.8 V, (b, e) 0.6 V and (c, f) 0.4 V, respectively.

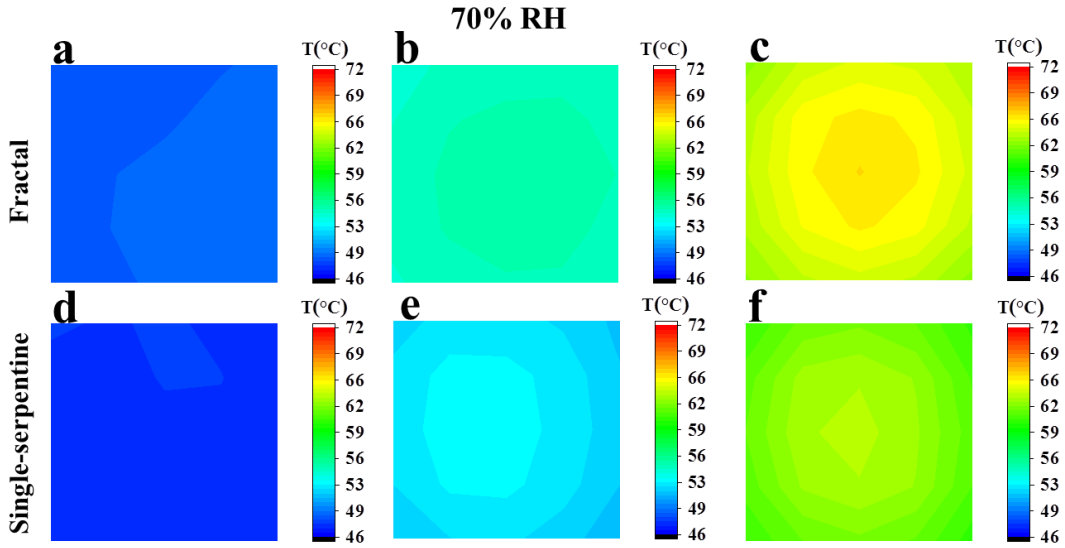

Figure 73: Anode surface temperatures for fractal and single-serpentine cells at 70% reactant RH and at (a, d) 0.8 V, (b, e) 0.6 V and (c, f) 0.4 V, respectively.

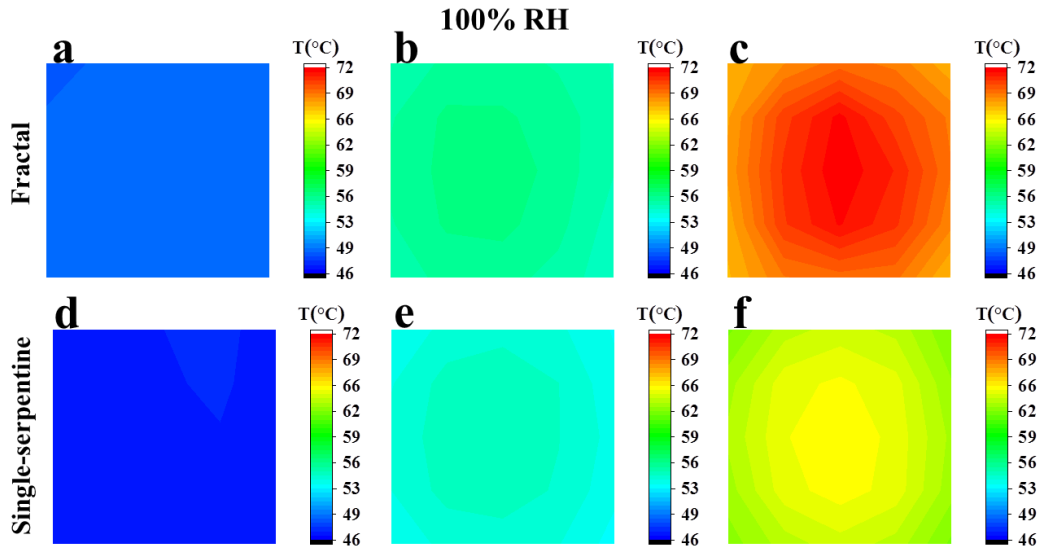

Figure 74: Anode surface temperatures for fractal and single-serpentine cells at 100% reactant RH and at (a, d) 0.8 V, (b, e) 0.6 V and (c, f) 0.4 V, respectively.

Overall, the higher surface temperatures measured in the fractal cell result in an increase in the ionic conductivity of the cell and its associated current density generated and *vice versa*. However, the lower temperatures measured in the single-serpentine cell, as a result of the localised flooding, decrease the current density generated from the cell [233].

6.4. Conclusions

This chapter has presented the first electro-thermal mapping metrology results to help analyse the performance of fractal flow-field based polymer electrolyte fuel cells. The study provides a relationship between the homogeneity the of reactant distribution and the surface distribution of the developed current and temperature. It also provides an understanding of localised flooding that occurs as a result of the flow-field configuration.

A more homogeneous current distribution was observed in the fractal cell, as a result of a more uniform reactant and water distribution, while a non-uniform current distribution was developed in the single-serpentine cell, as a result of flooded conditions. Furthermore, the more uniform reactant distribution in a fractal cell was reflected in the relatively smaller segment current gradients developed in it, compared to those developed in the single-serpentine cell. Uniform surface temperature gradients of ~1-2 ºC at 0.6 V and ~3-4 ºC at 0.4 V were observed for both cells; however, the fractal cell developed around 5-6 ºC higher surface temperatures, as a result of 100-200 mA cm^{-2} higher limiting current densities, compared to the single-serpentine cell.

Overall, the current and temperature mapping metrology ascertains the observed better performance of fractal cells, established by polarisation and other electrochemical characterisation techniques in section 5.3, because of a more homogeneous and uniformly distributed reactant and water distribution at the electrode surface.

7. Acoustic emission (AE) as a diagnostic and metrological tool for PEMFCs

7.1. Introduction

In this chapter, acoustic emission (AE) based performance characterisation of PEMFCs, as a hydration diagnostic tool, is established over a range of operating, reactant and flow-field conditions. Firstly, a conventional single-serpentine PEMFC was characterised under different operating conditions using AE measurements. The AE activity as a function of polarisation (AEfP) was determined across a range of humidities, temperatures and current densities. The electrochemical response was correlated with the acoustic response to deliver new insights into the water dynamics in an operational PEMFC and, importantly, provide a means of separating performance degradation due to dehydration from that of reactant starvation.

Subsequently, AEfP is explored further by focusing on the dynamic relationship between cell performance and its corresponding generated acoustic activity. The cell performance and the acoustic activity are determined under a time dependent parametrisation, which directly elucidates the influence of the extent of electrochemical reaction (water generated) on the AE generated inside the cell. In addition, cells are acoustically tested through consecutive forward and reverse polarisation scans, which is a way to explore the dynamic relationship between polarisation and acoustic emission. Correlations between the electrochemical performance and the generated AE are studied during galvanostatic and potentiostatic tests to bring out the synchronous relation between water dynamics and its resulting acoustic activity. Furthermore, cell temperatures, which depend on the extent of the electrochemical activity, are utilised to establish the measured acoustic activity as a direct reflection of

dynamic electrochemical reactions occurring inside the cell. Conventional electrochemical characterisations are performed to confirm the observations made by acoustic activity analysis.

Finally, the developed AEfP methodology is utilised in characterising the performance of the two fractal flow-fields introduced earlier (see section 4.2): one with increased contact area and convoluted water egress from the system (2-way), and the other one with less contact area and a more direct means of water egress from the system (1-way). Here, the impacts of contact area and water removal mechanism are evaluated, together and individually, on the performance of fractal PEMFCs, through the acoustic emission technique. The study primarily utilises the AEfP method to characterise the performance of the fractal PEMFCs, under different operating conditions, by diagnosing the hydration conditions inside the cells. The acoustic activity from the fractal PEMFCs during consecutive polarisation cycles and the quantification of the corresponding hydration levels developed inside the cell using amplitude analysis allow the relative water management characteristics of the two fractal flow-fields to be compared. Generic PEMFC performance characterisation, including polarisation measurements and galvanostatic tests, with simultaneous acoustic measurements are performed to further establish the correlations between cell design, performance and AE activity.

Sections of this chapter have been published or under press in the following journal articles:

- **V.S. Bethapudi**, J. Hack, P. Trogadas, G. Hinds, P.R. Shearing, D.J.L. Brett and M.-O Coppens, Hydration state diagnosis in fractal flow-field based polymer electrolyte membrane fuel cells using acoustic emission analysis, Energy Convers Manage 2020; 220:113083.
- **V.S. Bethapudi**, M. Maier, G. Hinds, P.R. Shearing, D.J.L. Brett, M.O. Coppens, Acoustic emission as a function of polarisation: Diagnosis of polymer electrolyte fuel cell hydration state, Electrochem. Commun. 109 (2019) 106582. doi:10.1016/j.elecom.2019.106582.
- **V.S. Bethapudi,** J. Hack, P. Trogadas, J.I.S. Cho, L. Rasha, G. Hinds, P.R. Shearing, D.J.L. Brett, M.-O.Coppens, A lung-inspired printed circuit board polymer electrolyte fuel cell, Energy Convers. Manag. 202 (2019) 112198.doi:10.1016/j.enconman.2019.112198.
- **V.S. Bethapudi,** G. Hinds, P.R. Shearing, D.J.L. Brett, M.-O. Coppens, Acoustic emission analysis of polymer electrolyte membrane fuel cells, 2020 ECS Trans. 98 177.

7.2. Materials and experiments

Acoustic activity from a fuel cell was measured using a piezoelectric acoustic sensor (transducer S9208; Mistras NDT, UK) attached to the cathode flow-field plate, as shown in Fig. 75.

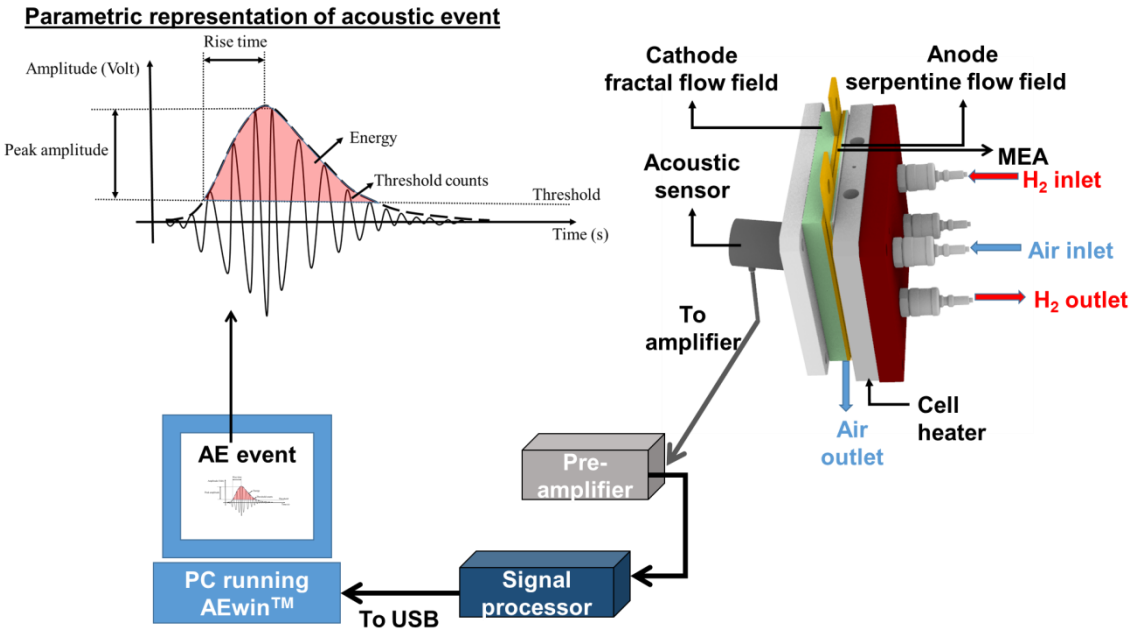

Figure 75: Schematic representation of AE testing with the parametric representation of an acoustic event for a single-serpentine flow-field PEMFC (adapted from [181]*).*

The sensor was connected to an in-line, low-power pre-amplifier, which filtered and pre-amplified the acoustic signal by 26 dB, followed by a single-channel AE digital signal processor. The signal processor was connected through a USB to a PC running AEwin™ (Physical Acoustics Corporation, USA) software, which performed data collection, processing and analysis. Furthermore, the software used for processing the acoustic signals measured an average of the acoustic hits generated over time and filtered out the hits below a threshold limit. The sensor had a resonant frequency of 500 kHz and an operating frequency range

of 200 kHz - 1000 kHz. The single-channel AE acquisition system had lower and upper analogue filters of 20 kHz and 1 MHz, respectively, and a fixed threshold value of 29 dB. This threshold was set, taking into account the background ‘noise’ during testing, and any signal beyond this threshold value was recorded as an ‘AE hit’ in terms of a voltage profile, as shown in Fig. 75.

The AE hit dataset primarily consisted of amplitude (dB), counts, duration (µs), rise time (µs) and absolute energy (aJ) [137,181]. In this study, the acoustic activity was presented as cumulative absolute acoustic emission energy (CAEE) [181] and peak amplitude (PA) measured from individual acoustic hits, measured over a specified time interval. The acoustic sensor was fastened against the cathode flow-field, using silicone grease for coupling.

7.3. Results, analysis and discussions

7.3.1. Acoustic emission as a function of polarisation (AEfP)

Electrochemical performance

Polarisation curves, Figs. 76 (a) and 76 (c), and the corresponding acoustic emission as a function of polarisation (AEfP) curves for a conventional single-serpentine fuel cell (further cell details in section 4.2), Figs. 76 (b) and 76 (d), were measured at reactant relative humidity (RH) levels of 40% RH, 70% RH and 100% RH, and at cell temperatures of 45 °C and 60 °C.

Considering points on the polarisation curves of equal current density as having the same rate of water generation (from the electrochemical reaction), RH as a measure of the water introduced to the cell from reactant flow, and temperature as a driving force for water to be removed from the cell, it is possible to analyse the AE results based on different cell hydration conditions.

At 45 °C cell temperature, a reduced cell performance was observed at 40% RH (Fig. 76 (a)), which can be attributed to the decreased membrane conductivity arising from insufficient hydration [234]. Increasing the reactant humidity to 70% RH, and then 100% RH, resulted in continually improved cell performance, predominantly observed in the Ohmic region and attributed to the improved membrane hydration [235].

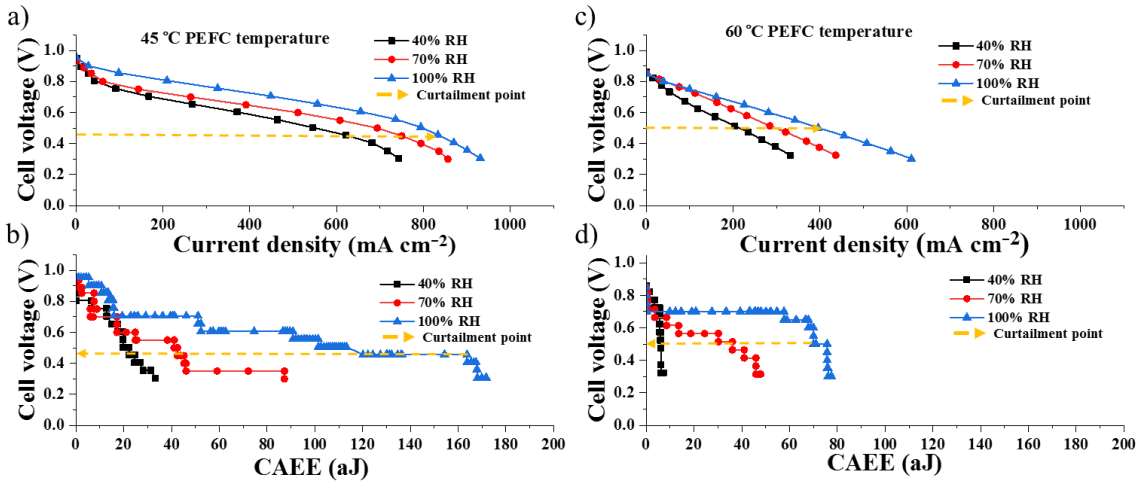

Figure 76: (a) Polarisation curve of PEMFC at 40%, 70% and 100% reactant RH – 45 °C cell temperature, (b) AEfP curve showing CAEE during polarisation – 45 °C cell temperature, (c) Polarisation curve of PEMFC at 40%, 70% and 100% reactant RH – 60 °C cell temperature and (d) AEfP curve showing CAEE during polarisation – 60 °C cell temperature. The data presented here correspond to a single-serpentine flow-field PEMFC.

Over the conventional activation region of the polarisation curve (low current density), the cumulative absolute AE energy (CAEE) for each RH was similar. However, at higher current densities, increased RH led to increased AE activity. At 40% RH the CAEE increase was gradual and steady over the entire current density range, whereas at the higher RH levels a significant increase in CAEE was observed in the Ohmic region, with the 100% case, which attained the highest current density, showing curtailment of AE activity above ~850 mA cm^{-2}.

Such incremental development in CAEE with current density is primarily attributed to increased water generation from the electrochemical reaction (reactant's RH and velocity remained constant throughout the test in each case). It is well known, from the likes of neutron imaging studies [65,209], that,

as current density increases, water initially builds up within the gas diffusion layer (GDL), primarily under the land regions, and then inhabits the flow channel itself. Release of liquid water into the channels, and particularly its impingement on channel walls at corners and switchbacks, is a source of AE. Higher RH tends to promote liquid water accumulation in the channels, which is consistent with the increasing CAEE observed in the Ohmic region with increasing RH (Fig. 76 (b)).

Although the cell was externally heated to 45 °C, the local temperature of the cathode will increase based on reaction conditions. As current density increases, cell heating occurs and acts to drive off water, removing liquid water from channels and the GDL and potentially dehydrating the membrane [185,236]. The curtailment of CAEE (~0.45V) and the corresponding current density of ~850 mA cm^{-2} at ~0.45V for the 100% RH condition is consistent with removal of liquid water from channels due to the dehydrating action of a higher cell temperature and current.

At a higher externally set temperature, 60 °C, the cell will be more prone to dehydration. The cell performance (Fig. 76 (c)) and acoustic polarisation (CAEE) (Fig. 76 (d)) of the PEMFC at all operating conditions decreased substantially (compared to 45 °C). At 40% RH, a very low level of CAEE was measured, as a result of the higher set temperature that dehydrated the cell considerably. This excessive dehydration reduced the membrane conductivity to a greater extent, such that the limiting current density delivered by the PEMFC dropped to 350 mA cm^{-2} at 60 °C (from 743 mA cm^{-2} at 45 °C).

Increasing the reactant RH to 70%, the cell performance improved, with an increase in CAEE observed over the entire polarisation range.

At 60 °C, the curtailment of CAEE is clearly observed for the 100% RH case during the transition from a ‘wet channel’ to ‘dry channel’ condition above ~400 mA cm^{-2}, as the local cathode temperature increases with current density. This transition is also evident for the 70% RH case from ~300 mA cm^{-2} on.

To express the relative changes in membrane hydration under different conditions, measurements of high frequency resistance (HFR), as given in Figs. 77 (a) and 77 (b), and EIS, as given in Fig. 77 (c), were carried out [64].

At 45 °C, there is a systematic difference in membrane resistance over the current range, with greater RH leading to lower membrane resistance, as expected. With increasing current density, there is a decrease in membrane resistance, as the membrane becomes increasingly hydrated, due to the generation of product water. However, for the poorly humidified 40% RH condition, the increase in cell temperature associated with higher current density leads to membrane dehydration. This results in a steep increase in resistance beyond 600 mA cm^{-2}. At this cell temperature, the 70% and 100% RH flow conditions are sufficient to adequately hydrate the membrane.

However, with an increase in set cell temperature to 60 °C, there is a rise in the HFR under all conditions, indicating a significant drop in membrane hydration. In addition, a significant increase in charge transport resistance (R_{ct}) is observed, as shown in Fig. 77 (c) (EIS performed at 400 mA cm^{-2} current density). The corresponding R_{ct} measured indicated almost a 50% higher value

at 60 °C compared to that measured at 45 °C, as presented in Table 5, indicating considerable membrane dehydration [206].

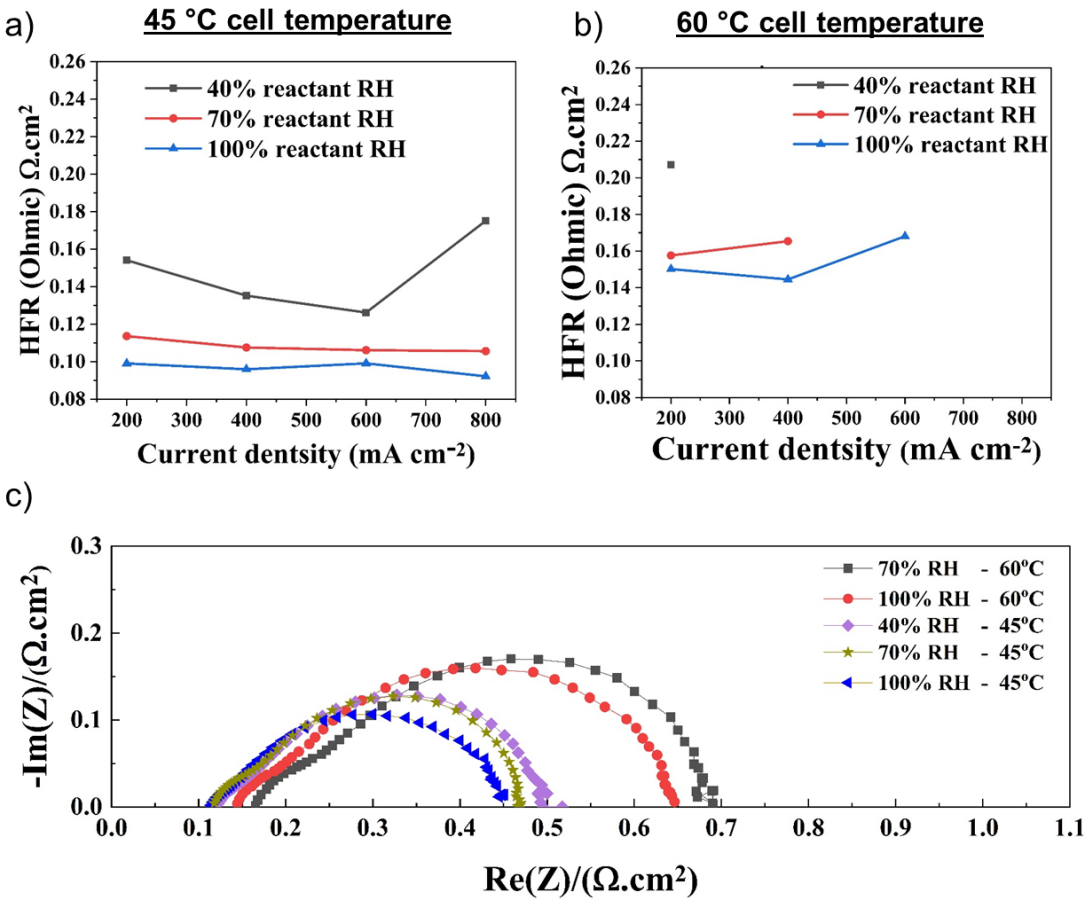

Figure 77: High frequency resistance, HFR (an average of 3 measurements and reproducible within 0.006 Ω.cm²) of the PEMFC tested at 40%, 70% and 100% RH at (a) 45 ℃ cell temperature and (b) 60 ℃ cell temperature, and (c) EIS measurements at 400 mA cm⁻² at 45 ℃ and 60 ℃ cell temperatures.

Table 5: Charge transfer (R_{ct}) resistances determined for PEMFC at 45 ℃ and 60 ℃ cell temperature and 400 mA cm^{-2} current density.

	45 °C cell set temperature			60 °C cell set temperature	
Reactants RH	**40%**	**70%**	**100%**	**70%**	**100%**
***R*$_{ct}$ (Ω.cm^2)**	0.39	0.35	0.34	0.53	0.5

Overall, membrane resistance rapidly increases with current density (and local temperature) and limits the ability of the cell to deliver higher currents. These results, from the membrane hydration perspective, are consistent with reduction in the liquid water volume, derived from acoustic measurements, and collectively describe the cell hydration over the polarisation range.

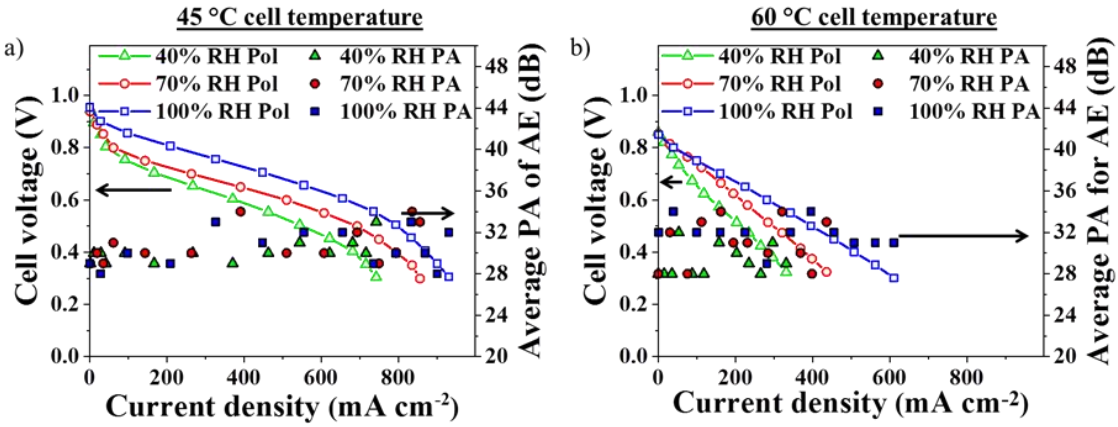

Figure 78: Average of the peak amplitude (PA) developed for the AE generated during cell polarisation, at (a) 45 ℃ and (b) 60 ℃ cell set temperatures. PA represents the intensity of AE generated as a result of water impacting the flow-field. Legend: RH – relative humidity; Pol – polarisation; PA – peak amplitude.

It has been identified that acoustic activity from PEMFCs can be utilised to establish the hydration conditions inside the fuel cell, as reported in [181,237]. Physical impact events created by the release of water into flow-fields result in the generation of AE and the corresponding intensity of such impacts is measured by the amplitude (dB) of AE signals detected. Furthermore, peak amplitude (PA) corresponds to the largest of the amplitudes detected in an AE signal, above a threshold value, which defines the overall energy of the AE signal [137,181]. It can be observed from Fig. 78 that, irrespective of cell conditions, the average PA of the AE signals measured during the polarizations was between 28-35 dB, indicating a fixed impact range from liquid water release into flow-fields. Such a confined amplitude range is consistent with the measured AE signal being associated with water impacts occurring specifically in the flow-fields [137,181], which have a fixed physical dimension defining their magnitude. Furthermore, the amount of liquid water generated inside the cell can be evaluated from the peak counts in an AE signal, which reflects the number of times a PA associated with water impacts has been detected. It can be observed from Figs. 79 (a – c) and 78 (d – f) that the counts increased with an increase in the reactant RH, irrespective of cell temperature, which can be attributed to the greater amount of liquid water generated inside the cell from condensation [137,181]. In addition, it can be observed from Fig. 79 (a – c) that the counts tended to increase with current density, which is due to increased water generation from the electrochemical reaction. However, the counts decreased significantly when the cell set temperature was increased to 60 °C, as shown in Fig. 79 (d – f), as a result of the lower amounts of liquid water

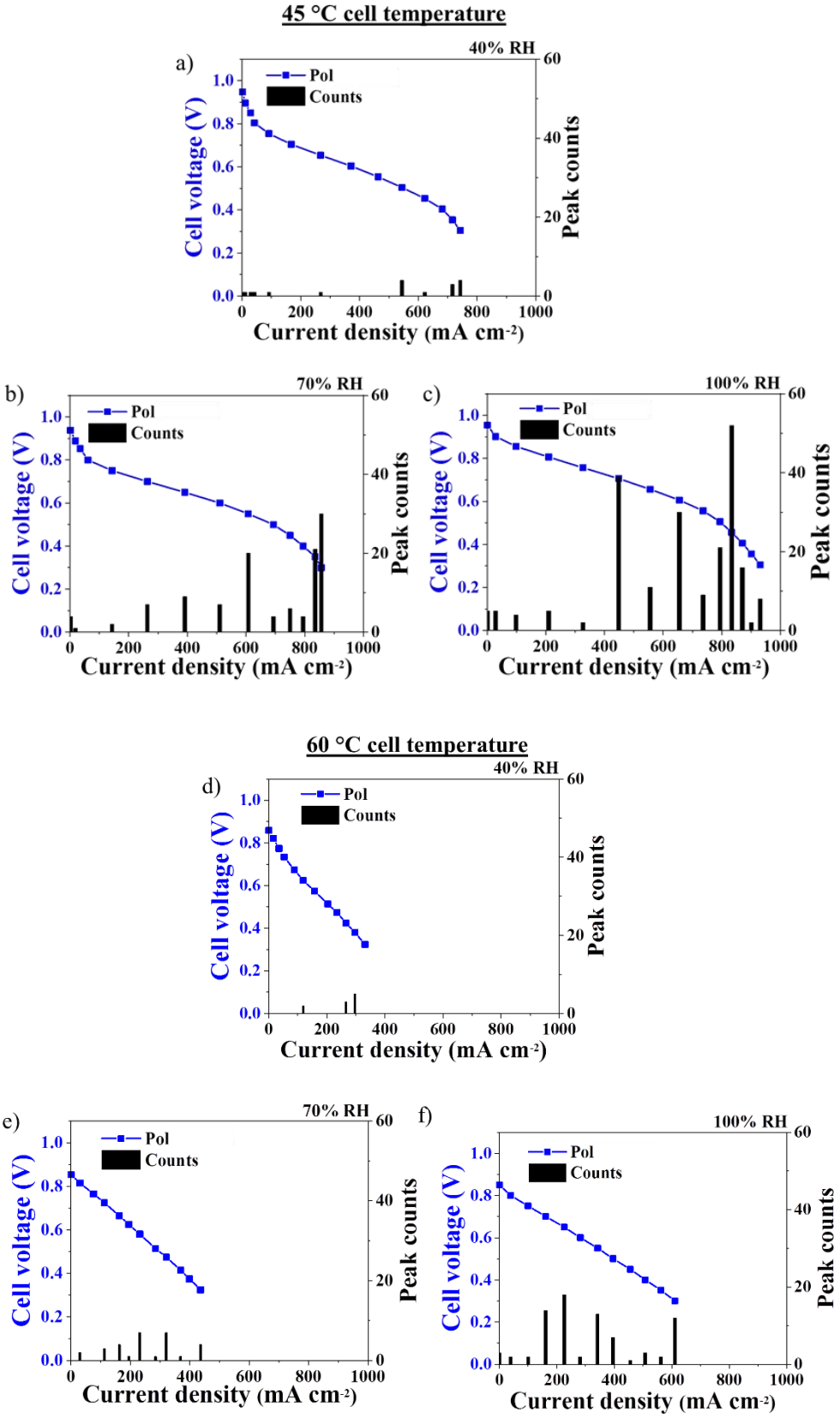

Figure 79: Peak counts – a measure of the number of peak amplitudes (PAs) generated – during cell polarisation for a cell set temperature of 45 ℃ at (a) 40% RH, (b) 70% RH, (c) 100% RH. Legend: Pol – polarisation.

released into the flow-field, due to the reduced rate of condensation at the higher temperature. Furthermore, the increase in counts with current density at 60 °C, as shown in Figs. 79 (d – f), was less marked than that at 45 °C, which can be attributed to the lower rate of electrochemical reactions (current density and associated water generated) occurring at corresponding points of polarization at elevated temperatures. The observed increase in counts with reactant RH can be attributed to the increased humidity carried by reactants, similar to that seen in Fig. 79 (a – c).

Besides, the corresponding cell temperature evolution during polarisation as a function of reactant RH and cell set temperature is shown in Fig. 80.

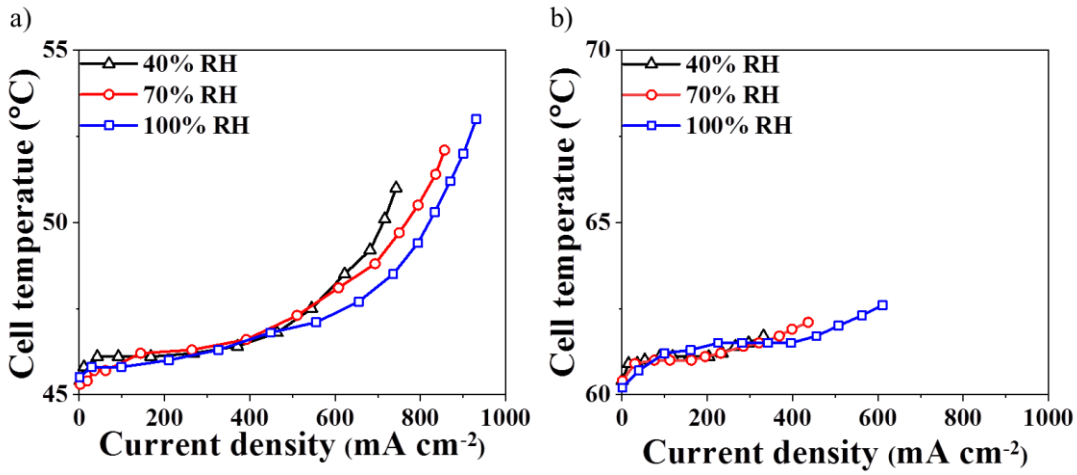

Figure 80: Cell temperatures developed during polarisation at 40%, 70% and 100% reactant RH conditions and at (a) 45 °C and (b) 60 °C cell set temperature.

Higher cell set temperatures resulted in a decrease in OCV, as seen in Fig. 80 (refer Figs. 76 and 79 for polarisation data), which may be due to the reduced mass fractions of hydrogen and oxygen or hydrogen crossover due to membrane dehydration occurring at elevated temperatures [238]. Furthermore,

it can be observed that at 45 °C cell set temperature, the maximum cell temperatures attained at 40% RH, 70% RH and 100% RH conditions were ~51 °C, ~52 °C and ~53 °C, respectively, and the corresponding limiting current densities were ~740 mA cm^{-2}, ~860 mA cm^{-2} and ~930 mA cm^{-2}, respectively, while at 60 °C set temperature the maximum cell temperatures attained at 40% RH, 70% RH and 100% RH conditions were ~61 °C, ~62 °C and ~63 °C, respectively, and the corresponding limiting current densities were ~330 mA cm^{-2}, ~440 mA cm^{-2} and ~610 mA cm^{-2}, respectively. The current density determines both the increase in cell temperature and the amount of water generated. A similar temperature rise was observed for cell set temperatures of 45 °C and 60 °C, when comparing points at the same current density, as seen in Figs. 79 (a – c) and 79 (d – f). However, the maximum rise in cell temperature of ~1 – 3 °C at 60 °C, as opposed to ~6 – 8 °C at 45 °C, can be attributed to the reduced performance (maximum current density) delivered by the cell at 60 °C, which also resulted in lower amounts of water generated, as shown in Fig. 79 (d – f).

Cell start-up and current hold

A galvanostatic test was performed on the PEMFC at a current density of 600 mA cm^{-2} and a cell temperature of 45 °C to examine initial start-up of the cell and dynamic performance over time. The corresponding CAEE is given in Fig. 81. Over the initial 0 – 25 s, the rate of CAEE increase for each of the RH conditions is similar and can be attributed to an equilibration phase, where flow, temperature and humidification factors stabilise, and the membrane hydrates (expands), as reported by Legros et al. [137].

Following the initial stabilisation period, the CAEE for the 40% RH case reaches a plateau, indicating dry-channel operation. On the other hand, the profiles for 70% and 100% RH exhibit an extended initial stabilisation phase of ~50 s, corresponding to more extensive hydration of the gases compared to the 40% RH case. Then follow periods of relative inactivity (plateaus), which can last upwards of 100 s, with relatively short intermittent periods of significant acoustic activity. This observation is consistent with the 'flushing' events commonly seen in PEMFC operation [221,239].

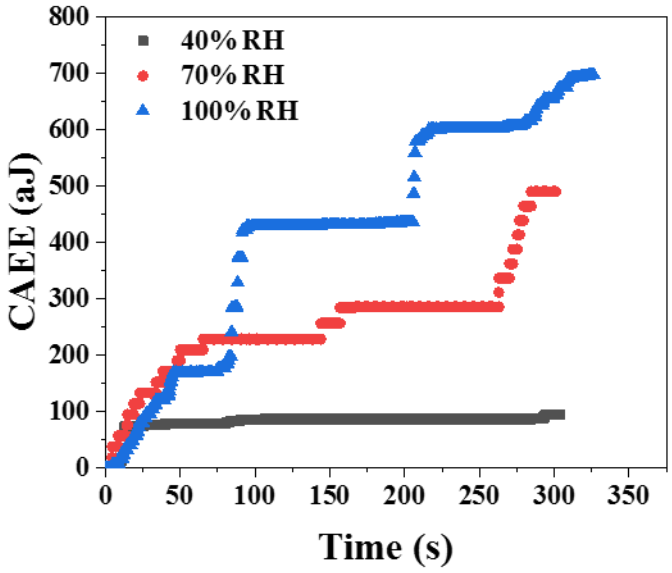

Figure 81: CAEE response during galvanostatic test at 600 mA cm^{-2}, at 45 ℃.

As observed by the likes of dimensional change and neutron imaging measurements [65,221], as well as those generally experienced in fuel cell testing, water is typically expelled from a fuel cell sporadically during 'flushing' events. As water builds in the channels of a fuel cell, it will typically initially exist as sessile droplets [209,236]. Periodically, droplets detach as they grow and eventually become entrained in the reactant gas flow. These droplets can then act to dislodge other droplets, resulting in an 'avalanche' effect with resulting

emission of sudden spurts of water from the cell. Neutron imaging has also identified the ‘snaking’ effect of water that becomes dislodged and coalesces into a ‘long train’ water droplet that makes its way through a cell with a similar sudden ejection of water [209].

The corresponding PA and peak counts as a function of time during the current hold are shown in Figs. 82 (a) and 82 (b), respectively. Fig. 82 (a) shows that, at each tested reactant RH, the PA between 0–25 s reached peaks up to 50 dB, which is higher than the aforementioned steady-state range of about 28-35 dB. This can be attributed to the cell stabilisation period before a steady-state develops that is determined by the reactant flowrate, temperature and humidity [137].

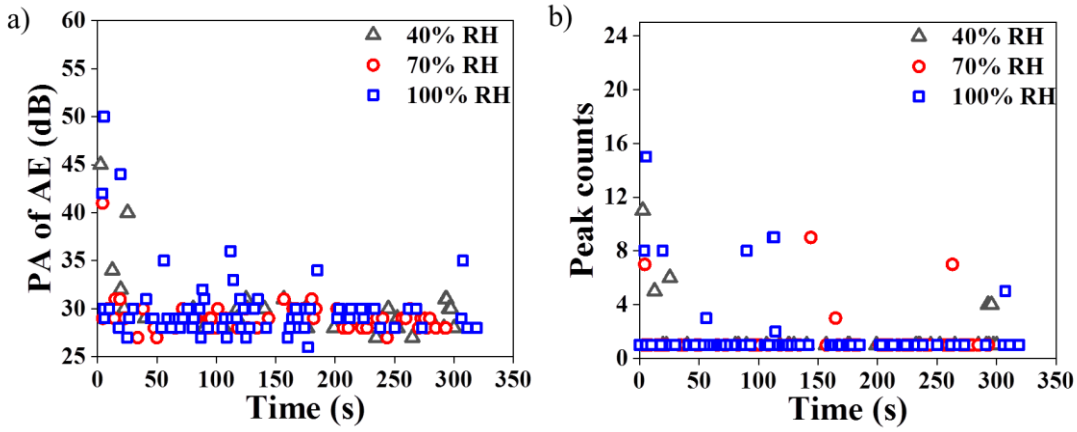

Figure 82: (a) Peak amplitude (PA) of acoustic emission (AE) and (b) peak counts developed during galvanostatic tests on the PEMFC at 45 ℃ set cell temperature and 600 mA cm^{-2} for ~300 s.

Beyond 50 s, the observed PA for all conditions again ranged between 28 – 35 dB, confirming the impact generation occurring from water release into the flow-fields, similar to that shown in Fig. 78. However, under 100% RH conditions, intermittent large PA values were detected, which can be attributed to excess

hydration and its associated water condensation and release into the cell, resulting in flushing events. Flushing events occur when water droplets generated inside a PEMFC and released into the flow-fields coalesce as large droplets and are eventually expelled from the fuel cell, resulting in large AE [181]. Furthermore, the peak counts during current hold, as shown in Fig. 82 (b), indicate an initial spike in the initial, 0 – 25 s period, which can be attributed to stabilisation, similar to what was observed in Fig. 82 (a) for the PA values. In addition, the counts measured increased with an increase in the reactant RH. However, at 40% RH, the number of peak counts was considerably lower, which can be attributed to less water generation inside the cell at this low RH. At higher reactant RH, the hydration levels improved inside the cell, which was reflected in better cell performance and increased water generation from electrochemical reaction, as in Fig. 78 (a), resulting in more counts.

7.3.2. Time based AE analysis

In this section, acoustic activity from a PEMFC as a dynamic response to the electrochemical activity occurring inside the cell is studied based on a time-dependent performance evaluation. A range of dynamic electrochemical measurement conditions are performed to probe the synchronous relationship between the measured acoustic emission (AE) and the electrochemical performance.

Polarisation stabilisation based AE analysis

The influence of the polarisation voltage stabilisation time on the performance of a PEMFC and its associated AE generated at three different stabilisation conditions – 10 s, 60 s and 120 s per voltage point (V_{pt}) – is shown in Fig. 83.

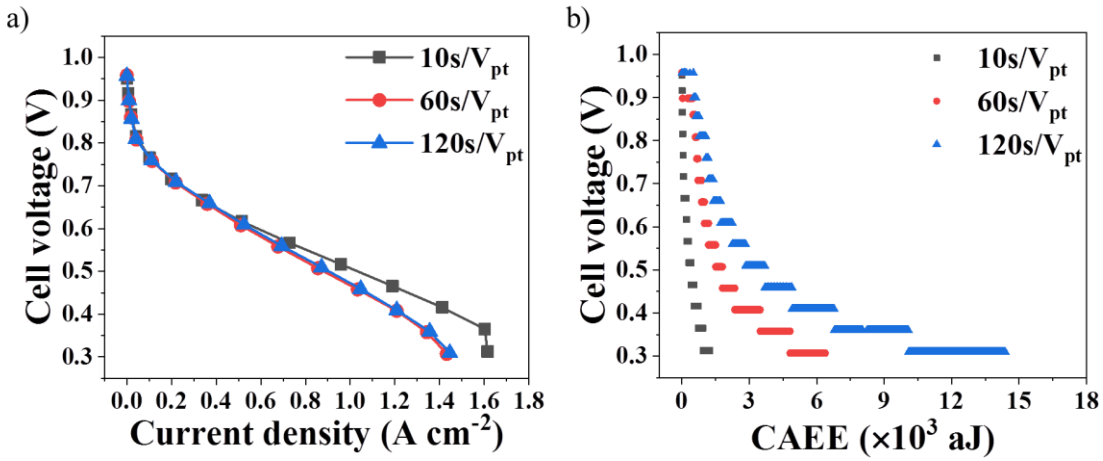

Figure 83: (a) Polarisation curves and (b) simultaneous acoustic emission as a function of polarisation (AEfP) curves, at 10 s, 60 s and 120 s voltage stabilisation durations, respectively.

It can be observed from Fig. 83 (a) that, with increased current density and especially between OCV and 0.6 V (Ohmic region of operation), the performance of the cell remained similar, irrespective of the stabilisation

conditions. However, decreasing the voltage further resulted in a continuous decrease of the cell performance for 60 s/V_{pt} and 120 s/V_{pt} compared to 10 s/V_{pt}. The longer the voltage hold, the longer the electrochemical reaction can occur, with associated water generation [197]. Thus, the observed decrease in cell performance at lower cell voltages for longer durations of 60 s and 120 s can be attributed to mass transport limitations that could be induced by flooding occurring inside the cell, as a result of excess water generation and retention with time [240,241]. Furthermore, the overall cell polarisation at 60 s and 120 s conditions remained similar, as seen in Fig. 83 (a), indicating that the impact of the level of cell flooding on the cell performance did not become worse between 60 s and 120 s.

Cell flooding can be identified from the corresponding acoustic emission as a function of polarisation (AEfP) curves, which reflect the acoustic emission (AE) energy measured from the impacts of water generation and release into the flow-fields, as shown in Fig. 83 (b) [181]. It can be observed from Fig. 83 (b) that the cumulative absolute acoustic emission energy (CAEE) measured from the cells increased as the cell voltage decreased, which can be attributed to the increased extent of the electrochemical reactions and associated water generation inside the cell [137,140,181]. In addition, with rising voltage hold duration, the corresponding CAEE measured increased as well, as a result of additional water generation with voltage hold time [241]. The overall CAEE measured was the lowest at 10 s/V_{pt}, namely ~1500 aJ, which delivered optimal performance, compared to the 60 s and 120 s conditions; hydration levels generated inside the cell at 10 s/V_{pt} optimally hydrated the membrane, which resulted in its better performance. However, the overall CAEE generated for the

60 s and 120 s conditions was ~6500 aJ and ~14500 aJ, respectively, and such excessive acoustic activity can be attributed to water flooding occurring inside the cell, especially in the mass transport region of operation. Furthermore, the CAEE measured at each voltage point on the polarisations increased considerably when moving from 60 s/V_{pt} to and 120 s/V_{pt}. For instance, at 0.4 V, the corresponding CAEE was ~1150 aJ and ~1900 aJ, respectively. However, this difference did not further impact the polarisation performance of the cell, which and can be attributed to similar membrane hydration saturation, while the excess CAEE measured at 120 s/V_{pt} was a result of the excess AE from the greater amounts of water released into the flow-field [181,241].

Electrochemical impedance spectroscopy measurements

Electrochemical impedance spectroscopy (EIS) measurements on the same PEMFC were performed to diagnose the cell performance in the high current density operating region. Here, EIS was performed at 0.8 A cm^{-2} (20 A), 1 A cm^{-2} (25 A) and 1.2 A cm^{-2} (30 A). The corresponding EIS spectra and resistances developed in the PEMFC are given in Fig. 84 and Table 6, respectively (corresponding equivalent circuit use for modelling the EIS data is given in section 3.5, Fig. 28).

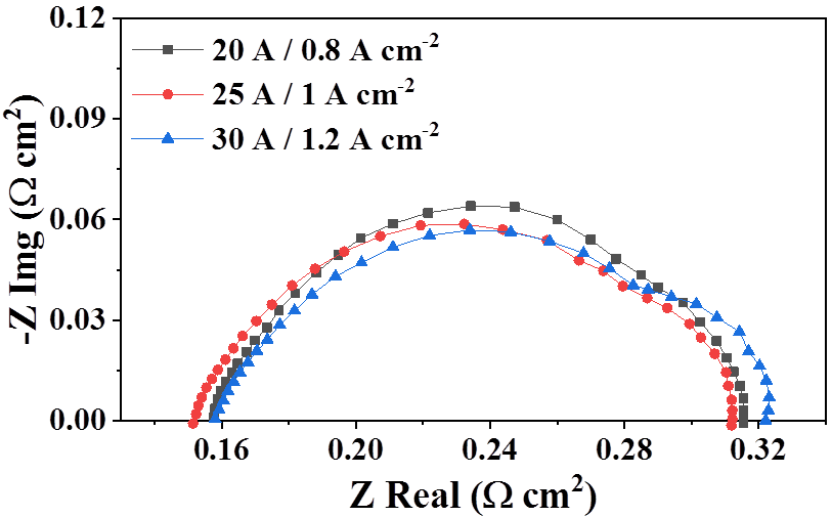

Figure 84: Electrochemical impedance spectroscopy measurements at 20 A (0.8 A cm^{-2}), 25 A (1 A cm^{-2}) and 30 A (1.2 A cm^{-2}) current conditions, respectively.

Table 6: Resistances developed in the PEMFC at 0.8 A cm^{-2}, 1 A cm^{-2} and 1.2 A cm^{-2} current densities.

	Resistance Ω.cm^2		
Load	**HFR**	**R_{ct}**	**R_{mt}**
20 A / 0.8 A cm^{-2}	0.158	0.285	0.025
20 A / 1 A cm^{-2}	0.154	0.283	0.033
20 A / 1.2 A cm^{-2}	0.158	0.281	0.040

It can be observed from Table 6 that with an increase in the current density from 0.8 A cm^{-2} to 1 A cm^{-2} , R_{mt} increased by 32 %, and further increasing the current density to 1.2 A cm^{-2}, R_{mt} increased by 60 % and 21 % over the R_{mt} at 0.8 A cm^{-2} and 1 A cm^{-2}, respectively. Furthermore, the change in R_{ct} over the current density range was marginal and in the range of 0.7 % to 1.4 %. Such stable R_{ct} and large increase in R_{mt}, in the high current density region,

establishes the susceptibility of the PEMFC to mass transport related issues like flooding at higher currents [207], and with an increase in voltage hold duration in this region the mass transfer issues further exacerbate, as confirmed by the polarisations and the AEfP results shown in Fig. 83.

Forward and reverse polarisations

To evaluate the dynamic relationship between electrochemical activity and acoustic activity generated in a PEMFC, forward and reverse polarisation scans were performed, as shown in Fig. 85 (a), at 60 s/V_{pt}. The corresponding acoustic activity during the scans is represented in Fig. 85 (b).

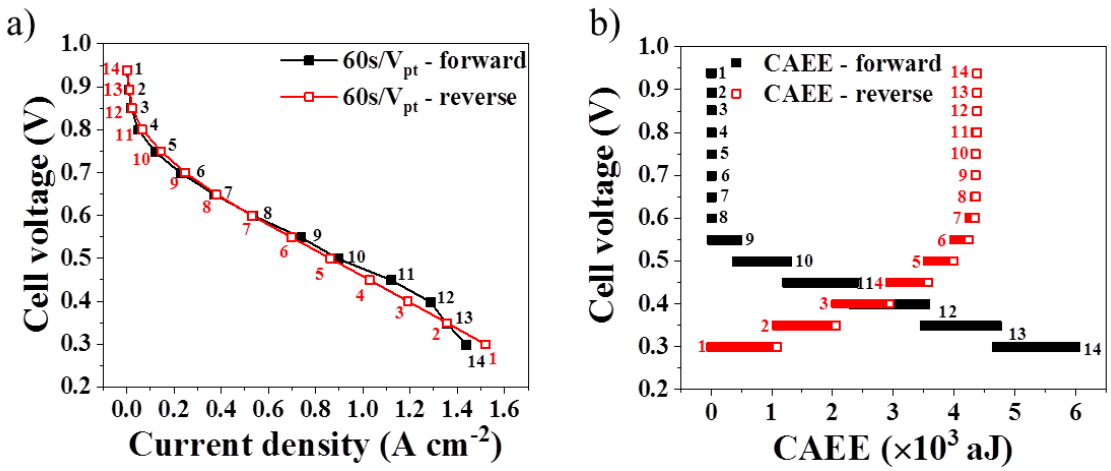

Figure 85: (a) Forward (black solid square) and reverse (red open square) polarisation curves and (b) cumulative absolute acoustic emission energy (CAEE) measured during forward and reverse polarisation scans at 60 s per voltage point (V_{pt}) stabilisation duration.

The forward scan was run between OCV and 0.3 V, while the reverse scan was run between 0.3 V and OCV, respectively. It can be observed from Fig. 85 (a) that the polarisation performance during forward and reverse scans was similar with only marginal differences observed in the high current density region. Such

similarity in forward and reverse polarisation curves indicates an optimal stabilisation condition for the PEMFC, to reach steady state operation, at each voltage point [242]. Furthermore, the similarity in polarisation performance was established by the near identical high frequency resistances (Ohmic resistance) generated, which establish the level of membrane hydration and its associated conductivity, as shown in Fig. 86 [243].

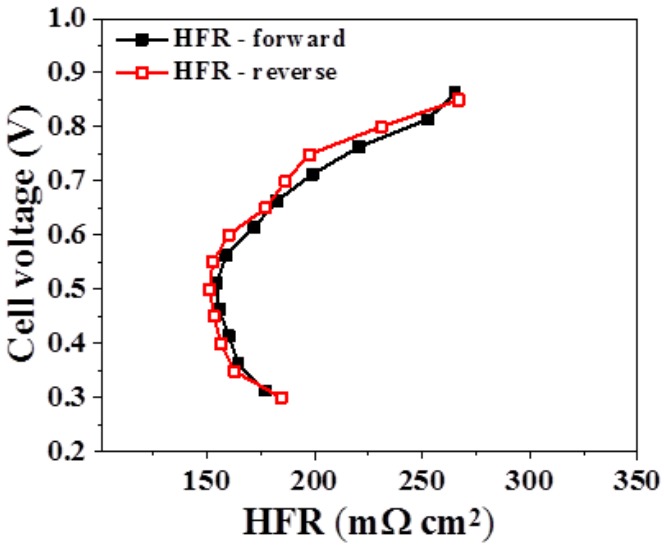

Figure 86: High frequency resistance (HFR or Ohmic resistance) for forward and reverse polarisation scans, respectively.

The corresponding CAAE measured during polarisations is shown in Fig. 85 (b). It can be observed that for both forward and reverse scans, there was similar acoustic activity measured between OCV and 0.6 V voltage points, which establish the measured AE as a dynamic response to the level of polarisation (electrochemical reaction) in the cell. In addition, the measured AE was minimal in this voltage region and can be attributed to the low levels of electrochemical reaction and corresponding water generated in the cell. However, between 0.6 V and 0.3 V cell voltages, there was considerable acoustic activity measured

from the PEMFC, because of the increased electrochemical activity and associated water generation at higher current densities.

It can be observed from Fig. 85 (b) that the net CAEE measured between 0.6 – 0.3 V for the reverse scan was ~18 – 25 % less than that measured for the forward scan. During a reverse scan, the initially high currents require a greater uptake of water by the membrane to maintain sufficient hydration and its associated conductivity. With a further decrease in current density the level of water generated in the gas diffusion layer gradually reduces and this promotes re-absorption of existing water in the cell into the GDL [244,245]. This additional utilisation of water generated in the cell by the GDL during reverse scan may have resulted in comparatively lower levels of water released into the flow-field and associated AE measured compared to the forward scan, where the continuous electrochemical activity resulted in saturation of water in the GDL. Furthermore, the additional utilisation of water during the reverse scan can be established from the HFR, as given in Fig. 86 [239]. HFR is an index for the level of water uptake by a membrane and its associated conductivity [243]. The observed similar hydration conditions (HFR) for both scans imply that during the reverse scan the utilisation of generated water may have occurred to offset the additional hydration requirements, resulting in reduced water released into the flow-field and the associated AE measured.

Potentiostatic tests

The AE response to dynamic electrochemical conditions inside the PEMFC are studied under voltage hold conditions, as shown in Fig. 87. Voltage hold conditions under three regions of PEMFC operation, namely, activation (0.8 V),

Ohmic (0.6 V) and concentration polarisation (0.4 V) regions, were considered. Under each voltage condition, the cell was held for 900 s at a particular voltage (gradient profile) followed by an OCV hold for 300 s (flat profile).

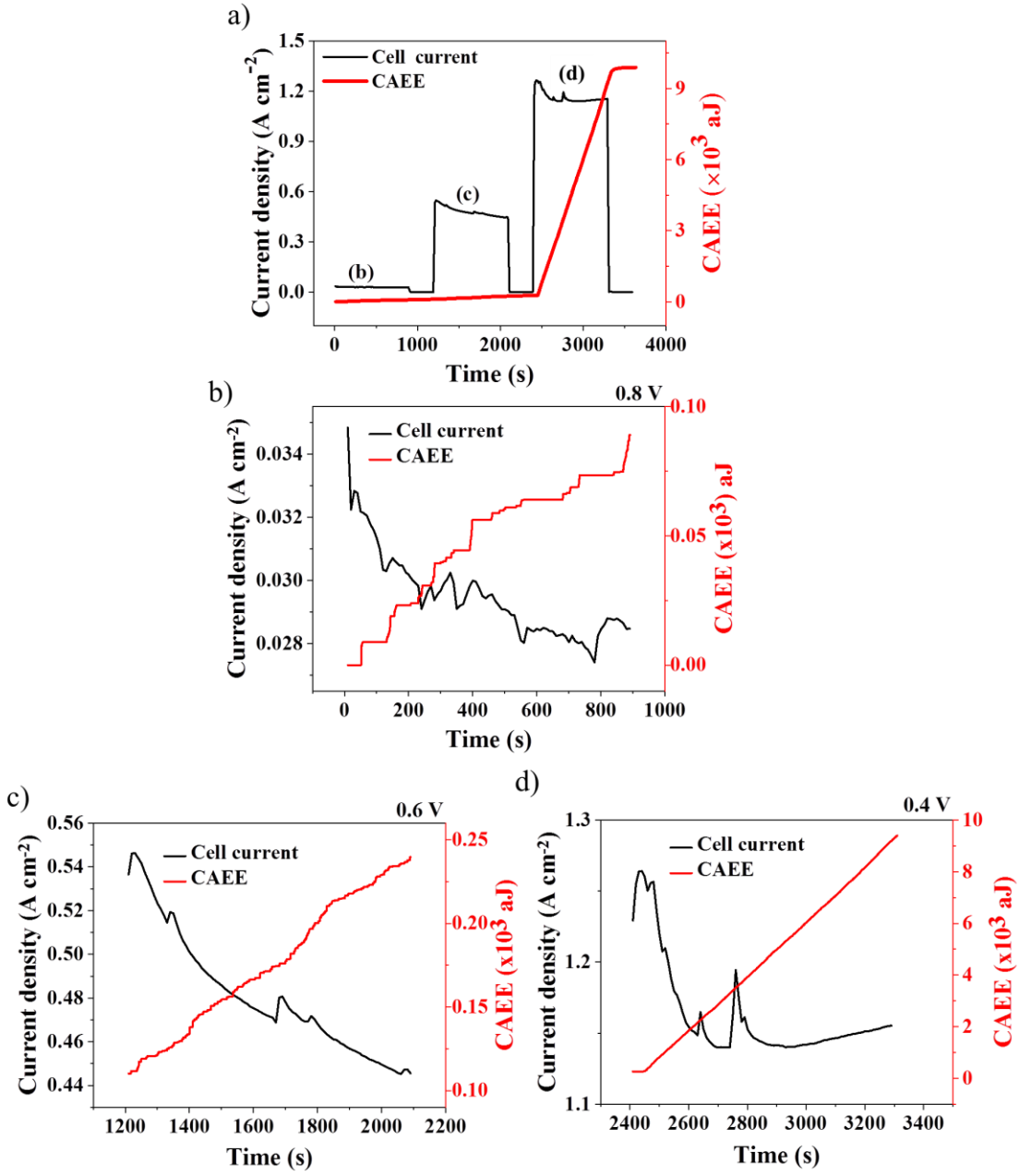

Figure 87: (a) Overall current density distribution and cumulative absolute acoustic emission energy (CAEE) at 0.8 V, 0.6 V and 0.4 V voltage hold conditions, respectively; specific current density distribution and CAEE at (b) 0.8 V, (c) 0.6 V and (d) 0.4 V voltage hold conditions, respectively.

It can be observed from Fig. 87 (b) that, at 0.8 V hold, the current density decreased from 0.035 A cm^{-2} to 0.028 A cm^{-2} with periodic “spikes” observed in the current density profile, which are commonly referred to as “flushing events” in a PEMFC [181]. Flushing events occur when the water in a flow-field builds up continuously, reducing the apparent cell performance, and eventually resulting in sudden ejection of water through the flow-field out of the cell followed by a spontaneous increase in the cell performance [245]. Here, such sudden spurts of water inside the cell resulted in AE, as presented in Figs. 87 (a) [137,181]. It can be observed from Fig. 87 (b) that the AE response is synchronous with the current density distribution, with step increase and plateau regions in AE corresponding to spikes and stable regions in current density distribution, respectively [137].

Similarly, at 0.6 V hold conditions, as in Fig. 87 (c), the current density decreased from 0.55 A cm^{-2} to 0.44 A cm^{-2}, which can be attributed to gradual water stagnation inside the cell that obstructed the active sites of the catalyst layer, resulting in performance degradation [246]. However, the current density profile is less synchronous with CAEE, which is no longer a discrete step-wise pattern, as shown in Fig. 87 (b). This is due to the continuous water generation as a result of increased electrochemical reactions (current density) over 0.8 V conditions that resulted in sustained AE generation. Further reducing the cell voltage to 0.4 V hold, as in Fig. 87 (d), the current density reduced from 1.25 A cm^{-2} to 1.15 A cm^{-2} and the corresponding increase in CAEE was much larger and sustained compared to the previous two voltage holds, which can be attributed to greater amounts of water generated as a result of a higher current density in the cell.

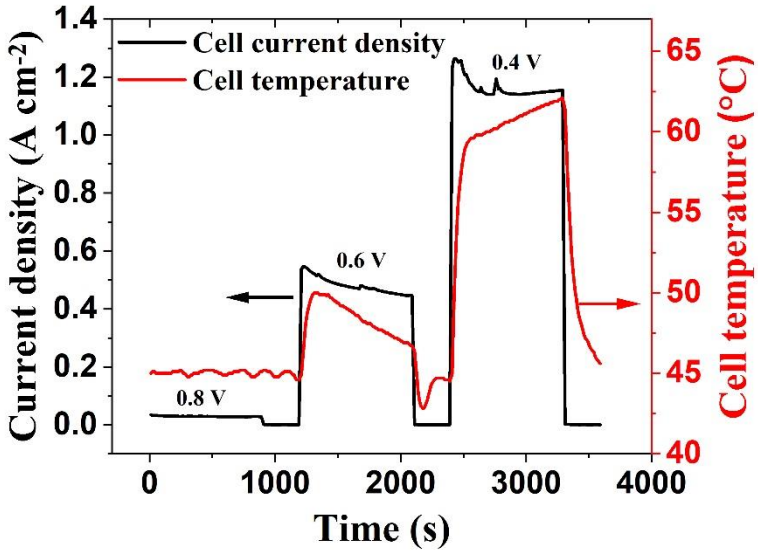

Figure 88: Cell temperatures and current density distribution measured during 0.8 V, 0.6 V and 0.4 V voltage hold conditions.

In addition to the water generated, the cell temperature developed is another variable that is dependent on the extent of the electrochemical reactions occurring inside a cell. The cell temperatures developed during potential hold conditions are given in Fig. 88. At lower current densities (corresponding to a potential of 0.8 V), the extent of electrochemical reaction is minimal, which results in lower cell temperatures, as shown in Fig. 88, similar to the CAEE in Fig. 87. With an increase in current density (corresponding to a lower potential of 0.6 V or 0.4 V), the level of electrochemical reaction occurring in the cell increases significantly and this impacts the cell temperature too. Furthermore, the decreasing and increasing trends in cell temperatures observed at 0.6 V and 0.4 V can be correlated with the corresponding current density (electrochemical reaction) trends, as seen in Fig. 88. Overall, the observed semblance between cell temperature and CAEE profiles confirms the measured

AE to be a dynamic response to the level of electrochemical reaction, similar to the cell temperature.

Galvanostatic tests

A current hold measurement is performed to probe the effect of cell performance on the generated CAEE, specifically at higher current densities, where mass transport limitations are prominent (Table 4). Constant current hold tests are presented in Fig. 89 for two different current densities, namely 1 A cm^{-2} (25 A) and 1.2 A cm^{-2} (30 A).

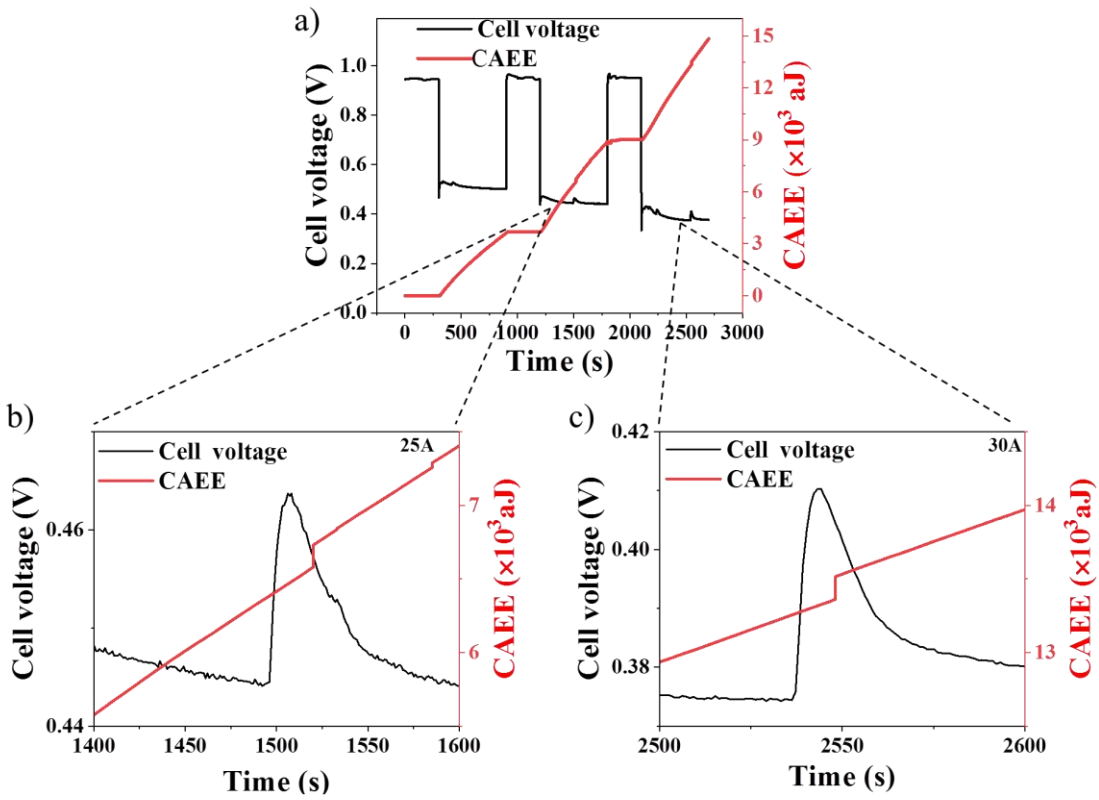

Figure 89: (a) Overall voltage evolution and cumulative absolute acoustic emission energy (CAEE) at 20 A (0.8 A cm^{-2}), 25 A (1 A cm^{-2}) and 30 A (1.2 A cm^{-2}) current hold conditions, respectively; specific voltage evolution and CAEE at (b) 25 A (1 A cm^{-2}) and (c) 30 A (1.2 A cm^{-2}) current hold conditions, respectively.

At each current density, the cell was held for 600 s, followed by an OCV hold for 300 s, respectively. It can be observed from Fig. 89 (a) that, at each current density, there is a stabilisation phase, identified by the initial spike(s) in cell voltage, where an equilibrium operation state is achieved among several factors, like reactant concentration, current density, cell temperature, reactant humidity, membrane water content and GDL properties [242].

Fig. 89 (a) shows that, during OCV conditions, no acoustic activity (CAEE) (plateau regions) is detected, implying that the measured CAEE during the cell operation is primarily contributed by the water generated from electrochemical reactions. Under the current regions tested, there is a constant increase in the CAEE, which can be attributed to the continuous generation of water as a result of a greater extent of the electrochemical reactions occurring at large currents. For instance, at 25 A (Fig. 89 (b)) and 30 A (Fig. 89 (c)), a voltage peak is observed at 1500 s and 2550 s, respectively. Such peaks occur due to the sudden release of built-up water, as a flushing event, from inside the cell [221]. Such flushing events provide improved catalytic area for the electrochemical reactions, resulting in improved cell performance. Corroboratively, a peak in CAEE is observed after the onset of such voltage peaks, as seen in Figs. 89 (b) and 88 (c), and can be attributed to the sudden AE generated from the flushing events occurring inside the cell [181].

Similar to the potentiostatic tests, the cell temperature profiles developed during the current hold conditions corroborate the generated CAEE, as shown in Fig. 90; higher and lower cell temperature profiles correspond to increasing and flat plateau regions in CAEE profiles, during current hold and OCV conditions, respectively. In addition, increased currents (electrochemical reactions) result in

simultaneous increases in cell temperature and acoustic activity; the CAEE and cell temperature range developed during 20 A, 25 A and 30 A conditions were 3622 aJ at 45 – 50 °C, 5061 aJ at 45 – 54 °C and 5839 aJ at 45 – 58 °C, respectively. Overall, the potentiostatic tests further establish the AE measured to be a dynamic response to electrochemical reactions occurring inside the cell.

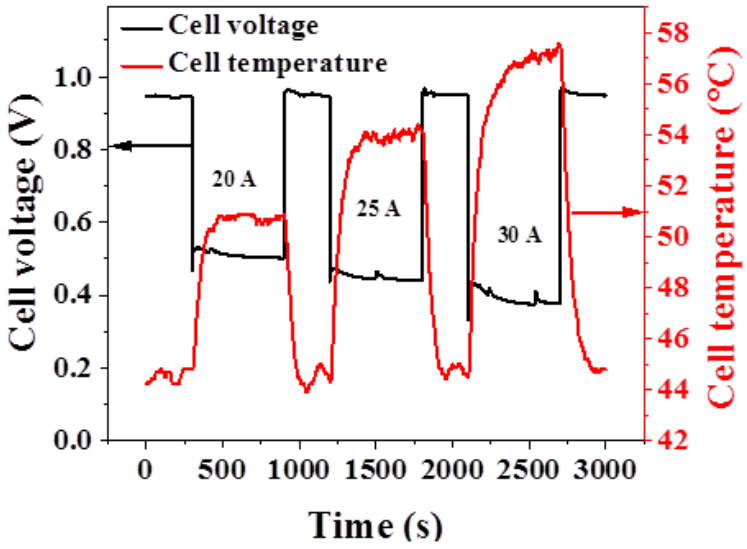

Figure 90: Cell temperatures and voltages measured during 20 A (0.8 A cm^{-2}), 25 A (1 A cm^{-2}) and 30 A (1.2 A cm^{-2}) current hold conditions.

7.3.3. AE based performance characterisation of fractal PEMFCs

AEfP measurements on 1-way and 2-way fractal PEMFCs

Polarisation and AEfP curves for the fractal flow-field (1-way and 2-way) PEMFCs tested are presented in Fig. 91. The corresponding polarisation and electrochemical performances in Fig. 91 (a) and 91 (b) were discussed in detail in section 5.3. Here, the performance of fractal (1-way and 2-way) PEMFCs is characterised utilising the AEfP methodology, discussed in section 3.4.

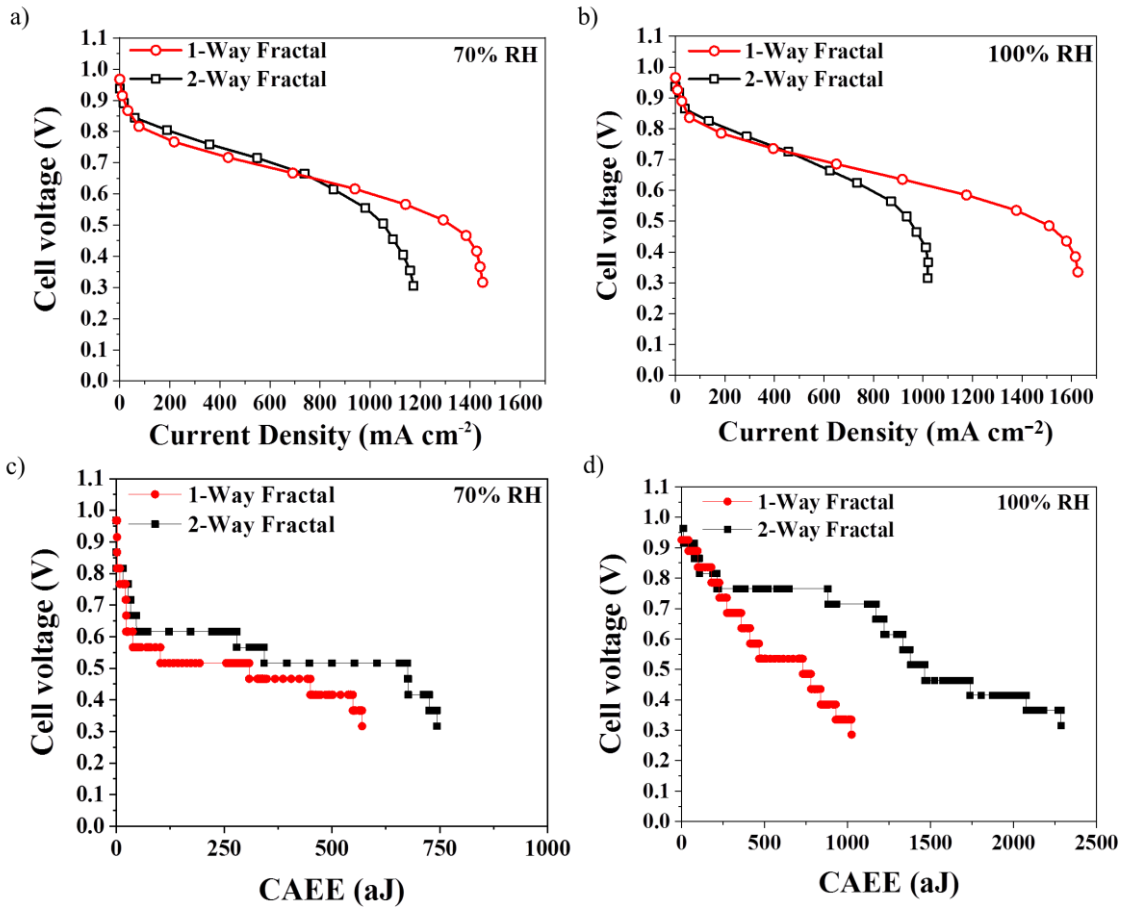

Figure 91: Polarisation curves at (a) 70% reactant RH and (b) 100% reactant RH; AEfP curves at (c) 70% reactant RH and (d) 100% reactant RH.

Observing the acoustic activity for the 70% RH case, as shown in Fig. 91 (c), between OCV and ~0.65 V (~700 mA cm^{-2}) the increase in CAEE for both fractal PEMFCs is similar, implying similar amounts of liquid water in the flow-fields [181]. Similar liquid water levels are maintained in the flow-field for each system; the superior performance of the 2-way fractal PEMFC at lower current density is attributed to the greater land-electrode surface area, which reduces the Ohmic resistance of the system (Fig. 91 (a)). However, above 800 mA cm^{-2} (~0.6 V) the increase in CAEE for the 2-way fractal PEMFC is much larger than that for the 1-way fractal PEMFC, implying greater liquid water activity with the 2-way design. This results in electrode flooding and degradation of cell performance, as seen in Fig. 91 (a). The lower CAEE observed for the 1-way fractal PEMFC, as seen in Fig. 91 (c), implies less extensive flooding and results in more sustained polarisation performance to higher current density. Note that the point in the AEfP profile at which the CAEE increases sharply is ~0.6 V for the 1-way design and ~0.5 V for 2-way design, which corresponds with the 'roll-off' in polarisation for each. This, once again, confirms that the mass transport limitation effect is predominantly a liquid water based phenomenon for this system.

Increasing the reactant RH to 100%, the polarisation performance of the 2-way fractal decreases significantly with an increase in the current density. It has been established by polarisation and electrochemical characterisations in section 5.3 that the observed decrease in performance of the 2-way fractal PEMFC can be attributed to the exacerbated flooding occurring within the cell. This is consistent with the higher rate of water generation as a result of

improved reactant humidity and water generation from electrochemical reactions.

Corroborating evidence for exacerbated flooding inside the 2-way fractal flow-field was provided by the AEfP measurements: Fig. 91 (d) indicates that at 100% RH the abrupt increase in CAEE for the 2-way fractal PEMFC occurs at a much lower current density (~400 mA cm^{-2}) compared to the 70% RH case (~800 mA cm^{-2}). Furthermore, the magnitude of the CAEE observed with the 2-way fractal PEMFC during polarisation increased significantly with RH, from ~750 aJ at 70% RH to ~2250 aJ at 100% RH at the limiting current density. These observations are consistent with the increase in performance drop and the decrease in limiting current density indicated by the electrochemical measurements, as in section 5.3.2.

In contrast, the performance of the 1-way fractal PEMFC increased with reactant RH [202]. The increase in CAEE (from ~600 aJ at 70% RH to ~1000 aJ at 100% RH) with humidity may reflect an optimal rise in the membrane hydration and its associated conductivity occurring due to improved generation and distribution of water at the electrodes, which increased the limiting current density attained from ~1400 mA cm^{-2} (70% RH) to ~1600 mA cm^{-2} (100% RH) [203].

Overall, the polarisation and AEfP measurements confirm that the 2-way fractal PEMFC was significantly limited by flooding, whilst the 1-way fractal PEMFC was closer to optimal with respect to hydration. The surface flow channels (blue arrows in Fig. 37 (a)) of the cathode air outlet in the 1-way fractal flow-field allow effective water removal via a straight path, compared with the more tortuous

cathode air outlet flow channels (blue arrows in Fig. 37 (b)) in the 2-way fractal flow-field, which are not effectively flushed and result in more liquid water stagnation and associated acoustic activity generation resulting in electrode flooding.

Current density cycling

The influence of reactant RH and current density (electrochemical reaction) on the increase of CAEE over time for the fractal PEMFCs was evaluated under current density cycling (successive polarisation) and is presented in Fig. 92. Each cycle in Fig. 92 is a representation of the current density generated over time, which was 420 s per cycle, as measured during a single polarisation cycle. The current density was measured for the polarisation conditions outlined in section 5.2.2. In addition, a 30 s rest time was employed between consecutive cycles.

At 70% RH, a stepwise increase in CAEE was observed in the fractal PEMFCs for each current density cycle, as shown in Fig. 92 (a). The CAEE increase in the 1-way fractal PEMFC happens in discrete steps, with no observed activity between cycles. The inter-cycle region is essentially an “OCV – low current” region between two consecutive cycles, with minimal electrochemical activity and its associated water generation, resulting in zero or insignificant acoustic activity. The presence of such discrete CAEE steps during operation of the 1-way fractal PEMFC suggests the following: (i) water generation in the 1-way fractal flow-field is consistent with the electrochemical activity occurring inside the cell and (ii) the 1-way fractal flow-field is very efficient at flushing water out of the cell, as noted in section 5.3. However, the CAEE increase in the 2-way

fractal PEMFC occurred continuously, even between cycles, which can be attributed to the constant generation of acoustic activity resulting from liquid water stagnation and flooding in the flow-field, even when no electrochemical reaction is occurring.

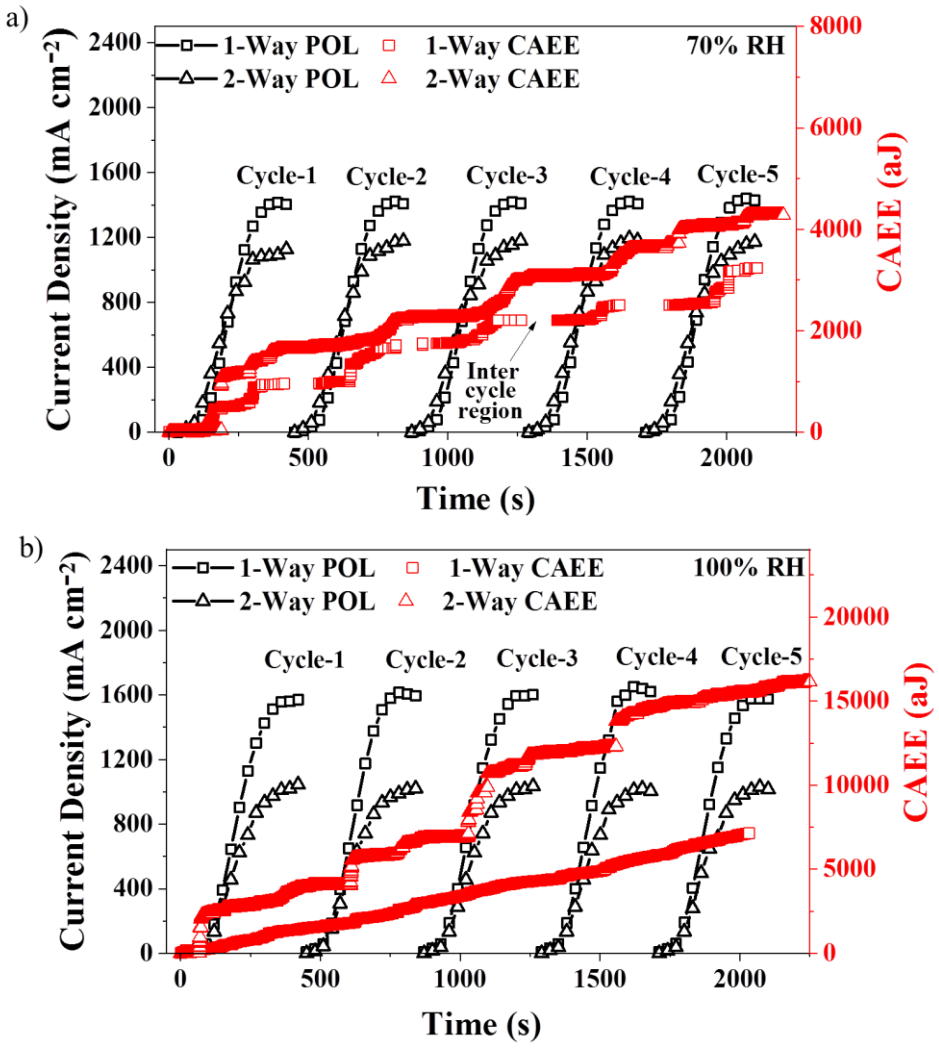

Figure 92:Successive cycling (five consecutive polarisations) of 1-way and 2-way fractal PEMFCs between OCV and limiting current density with simultaneous acoustic emission (CAEE) measurements at (a) 70% reactant RH and (b) 100% reactant RH.

Overall, at the end of five consecutive current cycles, the 2-way fractal PEMFC delivered lower performance with a relatively higher CAEE generated (~4400 aJ), as a result of flooding, compared to the 1-way fractal PEMFC, which delivered consistently better performance with lower CAEE generated (~3300 aJ). With an increase in reactant humidity to 100% RH, the CAEE for both fractal PEMFCs, as shown in Fig. 92 (b), grows continuously in relatively smaller and larger steps for the 1-way and 2-way fractal PEMFCs, respectively. This continuous increase in CAEE, including between cycles, can be attributed to the constant accumulation of water in the flow-fields due to condensation of water in the high-humidity cathode environment (100% RH), in addition to the water generated from electrochemical reaction. Condensation in a high-humidity environment at the cathode can be confirmed from the presence of CAEE in the inter-cycle region (Fig. 92 (b)) for the 1-way fractal PEMFC, which was absent at 70% RH (Fig. 92 (a)).

The total CAEE generated after 5 cycles for the 1-way fractal and 2-way fractal PEMFCs at 100% RH was ~7000 aJ and ~16500 aJ, respectively. Thus, the total CAEE increased by 2.3 times and 4 times for 1-way and 2-way fractal PEMFCs, respectively, when the reactant RH increased from 70% RH to 100% RH. This further supports excessive flooding at 100% RH, consistent with a lower cell performance (Figs. 54) and temperature (Fig. 55).

Cell voltage fluctuation

Galvanostatic testing was performed on the fractal PEMFCs by operating them at a constant current density of 1000 mA cm^{-2} and 70% reactant RH for a little over three hours (~12000 s). The corresponding cell voltage fluctuation and

CAEE measured over time are presented in Fig. 93. Up until 2500 s, there is a continuous increase in CAEE for both fractal PEMFCs and the corresponding cell voltage remains almost constant in this region. This can be identified as the stabilisation phase in fractal PEMFC operation, where reactants, humidification and liquid water within the cell are developing into a steady state condition [137,181].

In the ~2500 s to ~4000 s region, the CAEE increase for the 2-way fractal PEMFC is greater than that observed for the 1-way fractal PEMFC. Increased acoustic activity in the 2-way fractal PEMFC can be attributed to increased flooding events occuring inside the cell, which leads to intermittent fluctuations in the cell voltage, as shown in Fig. 93 [221]. The number and magnitude of fluctuations and spikes in the cell voltage is a measure of the non-uniformity of water distribution inside the cell [218,247]. Furthermore, the CAEE for the 2-way fractal PEMFC continues to steadily increase between ~4000 s and ~9000 s, with a corresponding increase in both the number and magnitude of the cell voltage fluctuations and spikes. After ~9000 s, the cell voltage starts to drop continuously, instead of fluctuating, in the 2-way fractal PEMFC, and the corresponding CAEE increases in larger steps. Such large-step increase in CAEE occurs due to the more significant water retention in the 2-way fractal PEMFC, which continuously floods the cell and reduces its voltage [35].

In contrast, the cell voltage for the 1-way fractal PEMFC remains almost constant, with minor increases in CAEE beyond 3000 s, compared to the fluctuating cell voltage observed for the 2-way fractal PEMFC. This is due to

more effective water removal from the cell, resulting in less water retention at the flow-fields and associated generated acoustic activity [181].

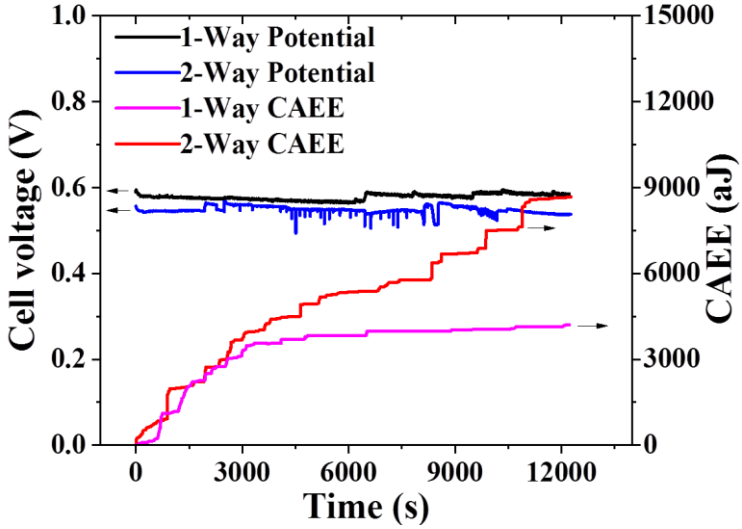

Figure 93: Cell voltage fluctuations at current hold (1000 mA cm^{-2}) for fractal PEMFCs with simultaneous CAEE measurements at 70% reactant RH.

Acoustic peak amplitude analysis

A detailed analysis of the peak amplitudes of the acoustic hits generated during current density cycling studies and quantification of the water generation in the cells is presented in this section.

Peak amplitude (PA) analysis during current density cycling measurements was performed to help quantify the amount of water generated inside the fractal PEMFCs, as shown in Fig. 94.

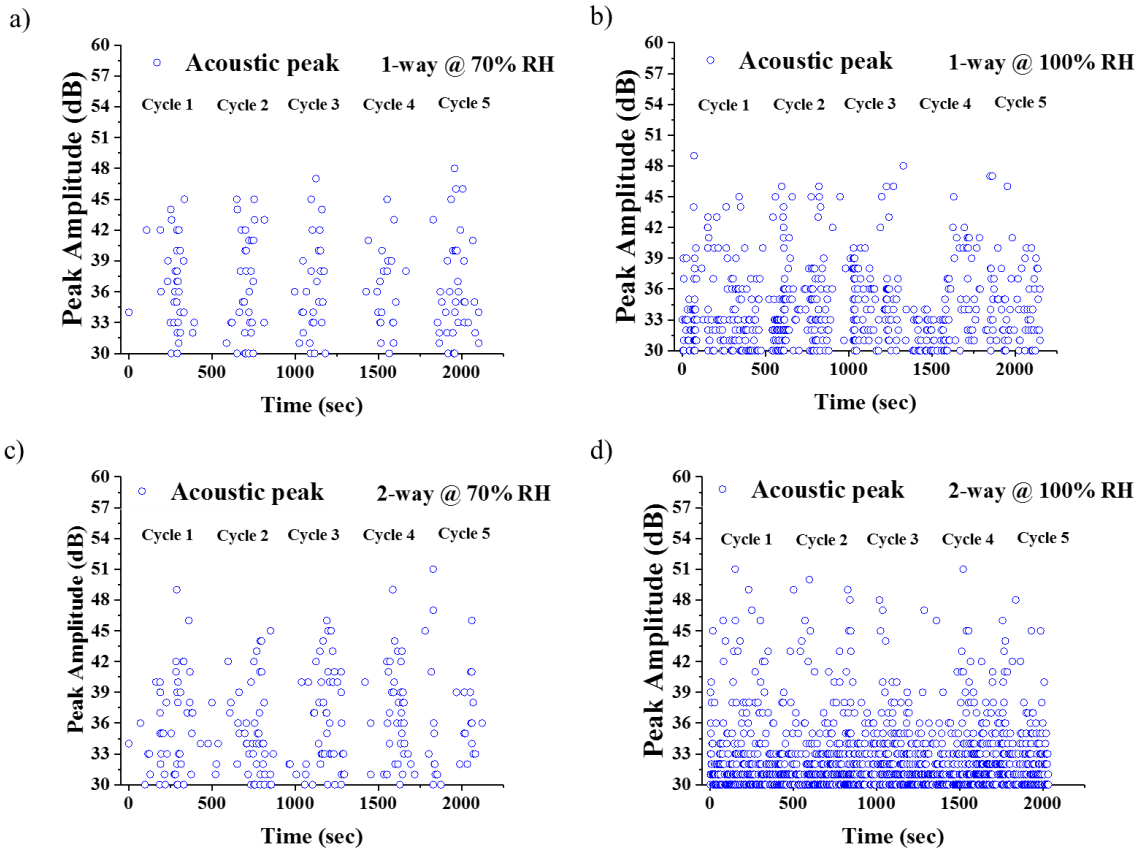

Figure 94: Peak amplitude (PA) analysis for the acoustic peaks (AE events) developed during current density cycling measurements for (a) 1-way fractal PEMFC at 70% RH, (b) 1-way fractal PEMFC at 100% RH, (c) 2-way fractal PEMFC at 70% RH and (d) 2-way fractal PEMFC at 100% RH.

PA is a measure of the maximum amplitude (dB) observed in a generated acoustic signal (an AE event is described in Fig. 75). In a PEMFC, an AE event is generated whenever liquid water impacts the flow-field, and the corresponding PA developed reflects the intensity with which such an impact occurs [181]. Fig. 94 illustrates the PAs measured, having an intensity of 30 dB and above (29 dB was the threshold amplitude for this study considering the background noise during measurement), over time for 1-way and 2-way fractal PEMFC operation during current density cycling (Fig. 92), at 70% and 100% reactant RH.

From Fig. 94 (a – d), it can be observed that the PA of signals developed during acoustic measurements on all the cells tested, at different operating conditions, ranged between 30 dB - 51 dB. However, the number of PAs developed (NPAD) varied with the kind of flow-field tested and the reactant conditions used. A fixed amplitude range for the PA generated, irrespective of flow-field configuration and testing conditions, indicates a fixed intensity range with which the water generation impacts the flow-field, while the overall NPAD corresponds to the number of such impacts (proportion) occurring inside the cells.

For the 1-way fractal PEMFC, at 70% RH (Fig. 94 (a)), the NPAD develops in five discrete cycles, corresponding to the 5 cycles generated in current density cycling measurements (Fig. 92 (a)). Furthermore, the NPAD during each cycle is similar, with an average NPAD of ~30 per cycle (Fig. 95), implying similar levels of water generation in each cycle.

Compared to the 70% RH case, at 100% RH the NPAD becomes less discrete (i.e., five individual cycles cannot be identified) and are greater in number (Fig. 94 (b)), with an average NPAD of ~125 per cycle (Fig. 95). Such continuous and increased NPAD detected, occurring at similar intensity (amplitude), indicates increased levels of liquid water (hydration) at 100% RH (compared to the 70% RH case).

For the 2-way fractal PEMFC, the NPAD are observed to be more continuous and larger in quantity compared to the 1-way fractal PEMFC, as seen in Figs. 94 (c) and 94 (d), with an average NPAD of ~55 per cycle at 70% RH, and ~300 per cycle at 100% RH, as seen in Fig. 95. Such a large number of impacts, at uniform intensity, occurring in the 2-way fractal PEMFC are a result of greater

amounts of liquid water generated and retained at the flow-field, resulting in flooding (70% RH) and exacerbated flooding (100% RH) in the cell. The PA analysis further establishes the inefficiency of the 2-way fractal design in removing excess water generated inside the cell.

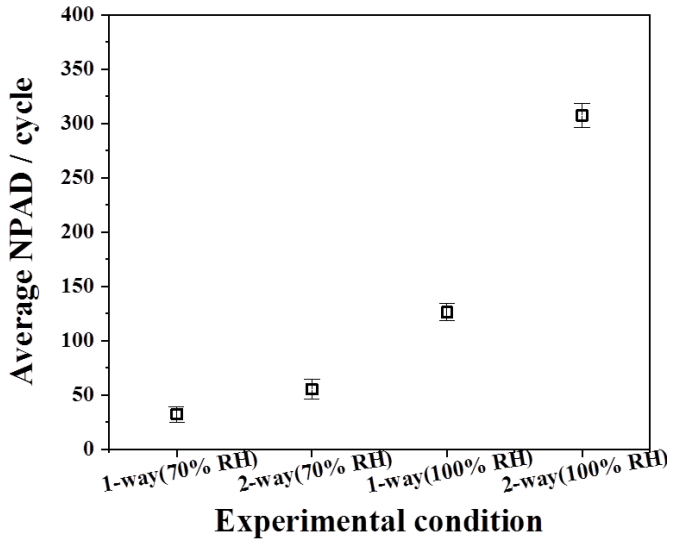

Figure 95: Average of the number of peak amplitudes developed (NPAD) for the 1-way and 2-way fractal PEMFCs at 70% and 100% reactant RH.

7.4. Conclusions

This chapter discussed the use of the acoustic emission technique as a hydration diagnostic tool to understand and diagnose water management inside conventional and fractal PEMFCs. The performance diagnosis of a conventional single-serpentine PEMFC under different experimental conditions, utilising the AE analysis, identified a strong correlation between PEMFC performance and the simultaneously generated acoustic activity. The measured AE activity was able to indicate the cumulative and discrete effects of reactant humidity and operating conditions on the performance of the PEMFC. Membrane dehydration was identified for PEMFC operation at 40% reactant RH by polarisation and electrochemical characterisations. Corroboratively, lower AE activity was measured during these operational conditions, indicating membrane dehydration under low reactant humidity conditions. However, under higher reactant humidity conditions the PEMFC performance improved with a simultaneous increase in the AE activity measured, confirming the influence of PEMFC operation on AE activity. Increasing the cell temperature by 15 °C exacerbated the membrane dehydration, which was reflected in a severe drop in cell performance and acoustic signal. Furthermore, the dependency of the AE activity on PEMFC operating performance was also confirmed by the high-frequency and charge transfer resistance determined from EIS.

Furthermore, the acoustic activity measured from a PEMFC as a dynamic response to the electrochemical activity occurring inside the cell under various operating and measurement conditions is established. The AE and electrochemical performance measured were identified to either corroborate

each other or be synchronous, depending on the type of measurement performed. The cell polarisation performance decreased by 16% in the limiting current density region with an increase in voltage stabilisation duration from 10 s to 60 s, as a result of flooding. Corroboratively, flooding was established by the measured AE, which was ~1500 aJ, ~6500 aJ and ~14500 aJ of CAEE at 10 s, 60 s and 120 s stabilisation durations, respectively. In addition, the robustness of PEMFC operation and the corresponding AE's dynamic response were established by forward and reverse polarisation scans. Flushing events were observed in galvanostatic and potentiostatic tests and corroborated via the measured AE, as spikes in current and voltage evolutions, synchronous with the peaks in CAEE. Furthermore, a correlation was observed between the generated cell temperatures, which reflect the extent of electrochemical activity, and the AE energy measured at different operating conditions.

Finally, the established AEfP metrology was used to characterise the performance of fractal PEMFCs by evaluating the hydration conditions inside them. AEfP was performed by probing the water dynamics inside two different fractal flow-field based PEMFCs, namely, 1-way and 2-way fractal PMEFCs, and measuring the corresponding acoustic activity generated from them. AEfP was performed on the fractal PEMFCs under relatively humid (70% RH) and fully humidified (100% RH) reactant relative humidity (RH) conditions. Presence of flooding in the 2-way fractal PEMFC, compared to the 1-way fractal PEMFC, under different operating conditions, was established by the relatively greater acoustic activity generated from it. Corroborating and correlating evidence of flooding in the 2-way fractal flow-field operations, under the different conditions

tested, was provided by its polarisation curves, impedance measurements and galvanostatic (current hold) measurements.

8. Summary and recommendations

8.1. Summary of the thesis

Recent work has shown that taking a nature-inspired approach in developing fuel cell flow-field plates can result in better performing PEMFCs. However, previous manufacturing methods and materials used for developing fractal, lung-inspired flow-fields are quite complex, and there are limitations to the cell performance under certain operating conditions. This thesis has aimed to address the limitations associated with the development of lung-inspired fuel cells, improving their operating performance under all testing conditions and providing a cost-effective and less complex fabrication method to realise the fractal flow-fields. Besides, advanced metrology has been utilised to evaluate the water management inside the fuel cell and its associated performance.

The methodology of developing PEMFCs with a lung-inspired fractal cathode flow-field, inspired from the air transport mechanism inside the lungs, is discussed in detail in chapter 4. A layer-wise, PCB-based technique has been identified as an effective method in terms of cost, complexity, scalability and ease of manufacture for developing the fractal flow-field structures, compared to the previous approach, which used additive manufacturing, based on the selective laser sintering of stainless steel. Here, three different configurations of the fractal flow-field are presented, namely, a 6.25 cm^2 1-way flow-field (having a 4-generation fractal air in-flow and an open-ended air out-flow), a 6.25 cm^2 2-way flow-field (having a 4 generation fractal air in-flow and 3-generation fractal air out-flow), and a 25 cm^2 1-way flow-field (having a 5-generation fractal air in-flow and open-ended air out-flow), respectively. The purpose of developing a 2-way flow-field is to evaluate the performance a fractal flow-field that has a greater conductive area compared to the 1-way flow-field. X-ray CT scans are

utilised to evaluate the quality of alignment of individual layers and the overall hierarchical structure of the flow path. Besides, the CT scans have been instrumental in providing an unobtruded view of the fractal structures, especially for the more complex 2-way fractal flow-field, where the incoming and outcoming flow features of the 2-way fractal flow-field are cut on the same number of PCB plates used for cutting 1-way fractal flow-field features.

Furthermore, the performance of PEMFCs with fractal cathode flow-fields is evaluated utilising different electrochemical methods and characterisations, which are reported in chapter 5. Polarisation studies establish that the fractal cell (1-way) performs better than the conventional single-serpentine cell at a range of operating and reactant conditions. This is attributed to the improved reactant air and water distribution at the electrode level as a result of diffusion-dominated transport occurring from the outlets of the fractal flow structure (the convective flow has been reduced to a Péclet number close to 1). Similarly, the better performance of the fractal flow-field cells over the conventional cells is observed even for scaled-up electrode areas, using fractal scaling, which keeps the final feature sizes of the hierarchical structure constant. Besides, the observed performance enhancements in the fractal cell are ascertained by the findings from conventional electrochemical characterisations and degradation tests, respectively. In addition, the 2-way cell initially delivered better performance in the Ohmic region of operation, as a result of the improved conductive electrode area available. However, its performance degraded considerably in the mass transfer limited region, with respect to the 1-way cell, as a result of cell flooding occurring in the complex in-out fractal flow path. Overall, chapters 4 and 5 introduce the design and development of PEMFCs

with a fractal flow-field, having different configurations, using a PCB-based approach, and they test their respective performance utilising conventional electrochemical metrology.

In chapter 6, electro-thermal mapping (local current density and temperature) is used for the first time to characterise the performance of a polymer electrolyte membrane fuel cell (PEMFC) having fractal cathode flow-fields, which are inspired by the air transport mechanism inside lungs. A comparison is made between fractal flow-field based PEMFCs, demonstrated previously to deliver enhanced mass transport performance, with conventional flow-field based PEMFC. The performance characterisation of fractal and single-serpentine flow-field PEMFCs is carried out by analysing the surface distribution of currents and temperatures developed in the cells at different reactant relative humidity (RH) and cell potential conditions. A relationship is developed between segment currents and surface temperatures, and reactant and cell operating conditions, respectively. Fractal cells performed better and resulted in more homogeneous current distributions compared to a single-serpentine flow-field, which developed non-uniform current distributions due to cell flooding. Temperature distributions indicate higher and lower surface cell temperatures in fractal and single-serpentine cells, respectively, supporting the observed cell performances. In addition, resistances measured from the electrochemical impedance spectroscopy characterisation of cells, as described in chapter 5, establish uniform and flooded operating conditions in the fractal and single-serpentine cells, respectively.

Acoustic emission (AE) analysis, a non-invasive and non-destructive diagnostic tool, is utilised to probe water formation and removal inside an operating fuel cell. This is presented in chapter 7. In the acoustic emission as a function of polarisation (AEfP) method, AE activity from the PEMFC is measured in terms of cumulative absolute AE energy (CAEE) hits during operation at discrete points on the polarisation curve. AEfP can identify the presence of liquid water in flow channels and correlate its formation and removal with the level of cell polarisation, and consequent internal temperature. Correlation between acoustic activity and water generation, supply and removal, is achieved by varying the current (polarisation), cathode air feed relative humidity (RH) and cell temperature, respectively. Features such as initial membrane hydration, liquid water formation, 'flushing' and the transition from 'wet-channel' to 'dry-channel' operation are identified using AE analysis, thereby providing a powerful and easy to implement diagnostic for PEFCs. Besides, AEfP is used to characterise the performance of fractal PEMFCs by evaluating the hydration conditions inside them. This is achieved by probing the water dynamics inside the fractal flow-field based PEMFCs discussed in chapters 4 and 5. AEfP is performed on the fractal PEMFCs under relatively humid (70% RH) and fully humidified (100% RH) reactant relative humidity (RH) conditions. Flooding in the 2-way fractal PEMFC, as opposed to the 1-way fractal PEMFC, is demonstrated under different operating conditions by the relatively higher acoustic activity it generates. Corroborating evidence of flooding in the 2-way fractal flow-field under different conditions is provided by its polarisation curves, impedance tests and galvanostatic (current hold) measurements. Overall, the

AE-based water management metrology has been instrumental in the direct hydration diagnostics inside the fuel cells.

In summary, this thesis has outlined a cost-effective and easy fabrication method to develop lung-inspired fractal flow-fields, using PCB plates. Besides, the study demonstrates that the design considerations associated with PCB-based fractal flow-field allows it to deliver better performance compared to the previous stainless steel fractal flow-field, and the conventional single-serpentine flow-field. Finally, advanced metrological studies, first-of-their-kind diagnostic approaches, like electro-thermal mapping and acoustic emission analysis, have been instrumental in the detailed understanding of the performance dynamics of fractal cells.

8.2. Further work and research scope

Nature-inspired fuel cells

The methodology presented in chapter 4 for developing cost-effective lung-inspired flow-fields using PCB technology can be utilised to develop further fractal generations with higher resolutions (down to ~50 µm). This can be achieved by utilising advanced CNC machining tools or high-power laser systems. A 50 µm can accommodate a fuel cell electrode area 100 cm^2 and have 6 generations of fractal flow path, which would bring the Pé $\rightarrow$1. Besides, scale-up through higher fractal generations can result in the development of better performing and larger electrode area nature-inspired fuel cells compared to the existing cells [36,60,182]. In addition, different conventional flow-field configurations, apart from those tested here, like multiple serpentine, parallel, interdigitated and others can be developed and tested along with the lung-inspired cells. Such an exercise will provide greater data points that establish the performance of lung-inspired cells, as discussed in chapter 5, against a range of conventional fuel cell flow-fields.

The 2-way fractal flow-field is discussed in chapters 4 and 5 on this thesis has an improved electrode contact area compared to the previously developed, 1-way fractal flow-fields [36,182,237]. Operational limitations are observed in the 2-way fractal cell due to its convoluted and complex water removal mechanism [237]. However, a direct water egress mechanism from the flow-field surface, similar to that present in 1-way fractal configuration, could be developed that will specifically enhance the 2-way fractal cell performance in the mass transport operating region.

A stand-alone fuel cell, without the metallic end plates for compression, can be developed by hot-pressing together the PCB-based, lung-inspired cathode and conventional anode flow-field plates, with an MEA sandwiched between them. This opens the possibility of developing a first-of-its-kind fractal fuel cell stack without the need for heavy and passive cell components that typically reduce the gravimetric energy density of the fuel cells. However, the cell compression conditions should be addressed with critical care, as the unit cell hot press assembly using PCB plates is an irreversible process.

Nature-inspired surface modifications [66], which are identified to provide improved water management inside the fuel cells, can be integrated with the fractal flow-fields developed in chapter 5 that result in further improvements in reactant and water distribution inside the fuel cells and their associated performance.

Advanced metrology for performance analysis of fuel cells

The experiments outlined in chapter 5, which establish the electrochemical performance of the cells developed in chapter 4, could be expanded further by testing under different operating and testing conditions, like varying environmental conditions, electrode properties, and without GDL (electrode coated membranes). This will establish the reactant flow advantages occurring from the fractal flow-field structure and their associated impact on the cell performance.

In this thesis, the EIS measurements are limited to a maximum 30 A cell current, owing to the limitations posed by the EIS experimental setups available in the laboratory for this study. However, use of impedance measurement

setups that can probe the cells at higher currents (>30 A) are critical to understand the cell behaviour in the mass transport region of operation, especially at limiting current conditions.

The cells in this study are tested on automated testing facilities (Scribner fuel cell testing stations) that provide well calibrated reactant and operating conditions. However, it is necessary to also study the cells under manually varied operating parameters and conditions that are typical during high power fuel cells and stacks testing operation, especially during emergency shutdown conditions, which impacts the cell performances considerably due to sudden reduction in reactant supply/distribution.

Degradation tests performed in this thesis are dependent on the reactant humidity, which acts as a prime parameter influencing the hydration distribution inside the cells. However, the scope of degradation tests performed in chapter 5 can be further improved by testing the cells at different temperatures, which are also instrumental in influencing the hydration distribution inside the fuel cell.

Electro-thermal mapping results discussed in chapter 6 have been performed on 25 cm^2 effective electrode area fuel cells. The mapping studies could be expanded to a 100 cm^2 effective electrode area; the corresponding mapping device is commercially available. A 100 cm^2 electrode area fractal fuel cell can be developed by either using a 6^{th} generation hierarchical flow-field structure or an array of four 5^{th} generation hierarchical flow-field structures. The hydration distribution conditions and the associated cell performance established by the mapping studies should then be validated using visual characterisation techniques, like x-ray imaging and neutron imaging that provide direct hydration

diagnostics inside fuel cells. Besides, simultaneous imaging with mapping can be instrumental in quantifying the water generation inside the cells and its influence on the localised and overall current and temperature distribution.

Acoustic emission based fuel cell diagnostics

In chapter 7, acoustic emission (AE) based hydration diagnostics of fuel cells is presented. The AE based water management tool and its corresponding performance diagnostics is validated against the conventional electrochemical characterisations like polarisations, EIS measurements, and degradation tests. However, validation by utilising direct water diagnostic techniques like x-ray imaging and neutron imaging can be instrumental in establishing the AE based water management tool as an effective direct hydration tool. Besides, such an exercise can also establish the AE based water management tool as a cost-effective, non-destructive and portable direct hydration metrology compared to the existing imaging techniques. In addition, the AE metrology in combination with the electro-thermal mapping, as discussed in chapter 6, can provide a much deeper understanding of the localised effects of hydration distribution on the overall cell performance. In chapter 6 it is identified that the water generation and removal in the flow-fields can influence the segment current development and distribution, and such hydration dynamics can influence the AE generated from the cells.

Furthermore, in this study AE from the fuel cells is measured from a single point on the surface of the fuel cell; this highlighted the cell hydration conditions and its associated performance. A single-point AE measurement is identified to be effective for the small electrode area fuel cells, as reported in this thesis.

However, while measuring AE from larger electrode area fuel cells, single-point measurements result in significant signal attenuations and, subsequently, result in improper hydration diagnostics of the fuel cells. To overcome such attenuations, multiple AE sensors could be utilised to cover the overall effective surface area of larger fuel cells.

9. Nomenclature

English letters

A_N	*Cross sectional area at N^{th} generation, m^2*
C_{dl}	*Double layer capacitance, F*
D	*Fractal dimension, -*
$\mathcal{D}$	*Diffusivity, $m^2\ s^{-1}$*
D_p	*Diameter of parent branch, m*
D_i	*Diameter of daughter branch, m*
I	*Current, A*
L	*Characteristic length, m*
N	*Number of generations, -*
P_{e_L}	*Péclet number, -*
Q_i	*Volumetric flow rate, $m^3\ s^{-1}$*
R_{ct}	*Charge transfer resistance, Ω*
R_{mt}	*Mass transfer resistance, Ω*
R_{el}	*Electrode resistance, Ω*
R_Ω	*Ohmic resistance, Ω*
S_f	*Reciprocal of size factor between daughter and parent shapes, -*
U	*Flow velocity, $m\ s^{-1}$*
V	*Potential, V*
W_s	*Warburg impedance, $\Omega.cm^2$*
Z'/Z_{re}	*Real part of impedance, $\Omega.cm^2$*
Z''/Z_{im}	*Imaginary part of impedance, $\Omega.cm^2$*

Greek letters

α_{air}	*Air stoichiometry*
Δ	*Enthalpy, kJ/kg*
n	*Number of daughter shapes*
T	*Torque, Nm*
ω	*Angular frequency, Hz*
Φ	*Diameter, m*

Superscripts/Subscripts/Acronyms

AC	*Alternating current*
AE	*Acoustic emission*
CAEE	*Cumulated absolute acoustic emission energy*
CPE	*Constant phase element*
CHP	*Combined heat and power*
CNC	*Computer numeric control*
CT	*Computed tomography*
DC	*Direct current*
DI	*Deionised*
EIS	*Electrochemical impedance spectroscopy*
FBP	*Filter back projection*
FF	*Flow fields*
FOV	*Field of view*
FPS	*Frames per second*
GDL	*Gas diffusion layer*
HFR	*High frequency resistance*

HOR	*Hydrogen oxidation reaction*
LFR	*Low frequency resistance*
MEA	*Membrane electrode assembly*
MSC	*Mean segment current*
OCV	*Open circuit voltage*
ORR	*Oxygen reduction reaction*
PAC	*Physical acoustic corporation*
PC	*Personal computer*
PCB	*Printed circuit board*
PEMFC	*Polymer electrolyte Membrane fuel cell*
POL	*Polarisation*
RH	*Relative humidity*
ROI	*Region of interest*
SHE	*Standard hydrogen electrode*
STDEV	*Standard deviation*
USB	*Universal serial bus*

10. References

[1] F. Barbir, T.N. Veziroğlu, H.J. Plass, Environmental damage due to fossil fuels use, Int. J. Hydrogen Energy. 15 (1990) 739–749. https://doi.org/10.1016/0360-3199(90)90005-J.

[2] G. Nicoletti, N. Arcuri, G. Nicoletti, R. Bruno, A technical and environmental comparison between hydrogen and some fossil fuels, Energy Convers. Manag. 89 (2015) 205–213. https://doi.org/10.1016/j.enconman.2014.09.057.

[3] T. Elmer, M. Worall, S. Wu, S.B. Riffat, Fuel cell technology for domestic built environment applications: State of-the-art review, Renew. Sustain. Energy Rev. 42 (2015) 913–931. https://doi.org/10.1016/j.rser.2014.10.080.

[4] T. Wilberforce, A. Alaswad, A. Palumbo, M. Dassisti, A.G. Olabi, Advances in stationary and portable fuel cell applications, Int. J. Hydrogen Energy. 41 (2016) 16509–16522. https://doi.org/10.1016/j.ijhydene.2016.02.057.

[5] A. Alaswad, A. Baroutaji, H. Achour, J. Carton, A. Al Makky, A.G. Olabi, Developments in fuel cell technologies in the transport sector, Int. J. Hydrogen Energy. 41 (2016) 16499–16508. https://doi.org/10.1016/j.ijhydene.2016.03.164.

[6] S. Litster, G. Mclean, PEM fuel cell electrodes, 130 (2004) 61–76. https://doi.org/10.1016/j.jpowsour.2003.12.055.

[7] J. Larminie, A. Dicks, Fuel Cell Systems Explained, John Wiley & Sons Ltd., Chichester, England, 2000.

[8] X. Li, I. Sabir, Review of bipolar plates in PEM fuel cells: Flow-field designs, Int. J. Hydrogen Energy. 30 (2005) 359–371. https://doi.org/10.1016/j.ijhydene.2004.09.019.

[9] V. Mehta, J.S. Cooper, Review and analysis of PEM fuel cell design and manufacturing, J. Power Sources. 114 (2003) 32–53. https://doi.org/10.1016/S0378-7753(02)00542-6.

[10] A.P. Manso, F.F. Marzo, J. Barranco, X. Garikano, M. Garmendia Mujika, Influence of geometric parameters of the flow fields on the performance of a PEM fuel cell. A review, Int. J. Hydrogen Energy. 37 (2012) 15256–15287. https://doi.org/10.1016/j.ijhydene.2012.07.076.

[11] J. Wang, Theory and practice of flow field designs for fuel cell scaling-up: A critical review, Appl. Energy. 157 (2015) 640–663. https://doi.org/10.1016/j.apenergy.2015.01.032.

[12] J.P. Kloess, X. Wang, J. Liu, Z. Shi, L. Guessous, Investigation of bio-inspired flow channel designs for bipolar plates in proton exchange membrane fuel cells, J. Power Sources. 188 (2009) 132–140. https://doi.org/10.1016/j.jpowsour.2008.11.123.

[13] A. Arvay, J. French, J.C. Wang, X.H. Peng, A.M. Kannan, Nature inspired flow field designs for proton exchange membrane fuel cell, Int. J. Hydrogen Energy. 38 (2013) 3717–3726. https://doi.org/10.1016/j.ijhydene.2012.12.149.

[14] N. Guo, M.C. Leu, U.O. Koylu, Bio-inspired flow field designs for polymer electrolyte membrane fuel cells, Int. J. Hydrogen Energy. 39 (2014) 21185–21195. https://doi.org/10.1016/j.ijhydene.2014.10.069.

[15] Wood DL, Yi JS, Nguyen TV. Effect of direct liquid water injection and inter- digitated flow field on the performance of proton exchange membrane fuel cells. Electrochim Acta 1998;43:3795–809. https://doi.org/10.1016/S0013-4686(98) 00139-X.

[16] T. Van Nguyen, M.W. Knobbe, A liquid water management strategy for PEM fuel cell stacks, J. Power Sources.114 (2003) 70–79.

[17] P.J. Hamilton, B.G. Pollet, Polymer electrolyte membrane fuel cell (PEMFC) flow field plate: Design, materials and characterisation, Fuel Cells. 10 (2010) 489–509. https://doi.org/10.1002/fuce.201000033.

[18] S. Subramaniam, G. Rajaram, K. Palaniswamy, Comparison of perforated and serpentine fl ow fi elds on the performance of proton exchange membrane fuel cell, J. Energy Inst. 90 (2017) 363–371. https://doi.org/10.1016/j.joei.2016.04.006.

[19] A. Iranzo, P. Boillat, J. Biesdorf, A. Salva, Investigation of the liquid water distributions in a 50 cm 2 PEM fuel cell : Effects of reactants relative humidity , current density , and cathode stoichiometry, Energy. 82 (2015) 914–921. https://doi.org/10.1016/j.energy.2015.01.101.

[20] D. Spernjak, A.K. Prasad, S.G. Advani, Experimental investigation of liquid water formation and transport in a transparent single-serpentine PEM fuel cell, J. Power Sources.170 (2007) 334–344. https://doi.org/10.1016/j.jpowsour.2007.04.020.

[21] J.P. Owejan, T.A. Trabold, D.L. Jacobson, D.R. Baker, D.S. Hussey, M. Arif, In situ investigation of water transport in an operating PEM fuel cell using neutron radiography : Part 2 – Transient water accumulation in an interdigitated cathode flow field, Int J Heat Mass Transf 49 (2006) 4721–4731. https://doi.org/10.1016/j.ijheatmasstransfer.2006.07.004.

[22] Z. Wang, Y. Zeng, S. Sun, Z. Shao, B. Yi, Improvement of PEMFC water management by employing water transport plate as bipolar plate, Int. J. Hydrogen Energy. 42 (2017) 21922–21929. https://doi.org/10.1016/j.ijhydene.2017.07.052.

[23] W. Schmittinger, A. Vahidi, A review of the main parameters influencing long-term performance and durability of PEM fuel cells, J. Power Sources. 180 (2008) 1–14. https://doi.org/10.1016/j.jpowsour.2008.01.070.

[24] J.P. Feser, A.K. Prasad, S.G. Advani, On the relative influence of convection in serpentine flow fields of PEM fuel cells, J. Power Sources. 161 (2006) 404–412. https://doi.org/10.1016/j.jpowsour.2006.04.129.

[25] D.H. Jeon, S. Greenway, S.Ã. Shimpalee, J.W. Van Zee, The effect of serpentine flow-field designs on PEM fuel cell performance, Int. J. Hydrogen Energy. 33 (2008) 1052–1066. https://doi.org/10.1016/j.ijhydene.2007.11.015.

[26] X.D. Wang, Y.Y. Duan, W.M. Yan, Novel serpentine-baffle flow field design for proton exchange membrane fuel cells, J. Power Sources. 173 (2007) 210–221. https://doi.org/10.1016/j.jpowsour.2007.08.037.

[27] K.S. Choi, H.M. Kim, S.M. Moon, An experimental study on the enhancement of the water balance, electrochemical reaction and power density of the polymer electrolyte fuel cell by under-rib convection, Electrochem. Commun. 13 (2011) 1387–1390. https://doi.org/10.1016/j.elecom.2011.08.015.

[28] J.H. Nam, K.J. Lee, S. Sohn, C.J. Kim, Multi-pass serpentine flow-fields to enhance under-rib convection in polymer electrolyte membrane fuel cells: Design and geometrical characterization, J. Power Sources. 188 (2009) 14–23. https://doi.org/10.1016/j.jpowsour.2008.11.093.

[29] R. Taccani, N. Zuliani, Effect of flow field design on performances of high temperature PEM fuel cells: Experimental analysis, Int. J. Hydrogen Energy. 36 (2011) 10282–10287. https://doi.org/10.1016/j.ijhydene.2010.10.026.

[30] D. Natarajan, T. Van Nguyen, Three-dimensional effects of liquid water flooding in the cathode of a PEM fuel cell, J. Power Sources. 115 (2003) 66–80. https://doi.org/10.1016/S0378-7753(02)00624-9.

[31] A. Su, F.B. Weng, C.Y. Hsu, Y.M. Chen, Studies on flooding in PEM fuel cell cathode channels, Int. J. Hydrogen Energy. 31 (2006) 1031–1039. https://doi.org/10.1016/j.ijhydene.2005.12.019.

[32] L. Wang, A. Husar, T. Zhou, H. Liu, A parametric study of PEM fuel cell performances, Int J Hydrogen Energy. 28 (2003) 1263–1272. https://doi.org/10.1016/S0360-3199(02)00284-7.

[33] X. Li, I. Sabir, J. Park, A flow channel design procedure for PEM fuel cells with effective water removal, J. Power Sources. 163 (2007) 933–942. https://doi.org/10.1016/j.jpowsour.2006.10.015.

[34] W. Sun, B.A. Peppley, K. Karan, Modeling the influence of GDL and flow-field plate parameters on the reaction distribution in the PEMFC cathode catalyst layer, J. Power Sources.144 (2005) 42–53. https://doi.org/10.1016/j.jpowsour.2004.11.035.

[35] K. Tüber, D. Pócza, C. Hebling, Visualization of water buildup in the cathode of a transparent PEM fuel cell, J. Power Sources. 124 (2003) 403–414. https://doi.org/10.1016/S0378-7753(03)00797-3.

[36] P. Trogadas, J.I.S. Cho, T.P. Neville, J. Marquis, B. Wu, D.J.L. Brett, M.O. Coppens, A lung-inspired approach to scalable and robust fuel cell design, Energy Environ. Sci. 11 (2018) 136–143. https://doi.org/10.1039/c7ee02161e.

[37] M.-O. Coppens, Multiscale nature inspired chemical engineering. In Multiscale Methods—Bridging the Scales in Science and Engineering. Edited by Fish J. Oxford: Oxford University Press; 2009:536-560. https://doi.org/10.1093/acprof:oso/9780199233854.003.0016

[38] M.O. Coppens, A nature-inspired approach to reactor and catalysis engineering, Curr. Opin. Chem. Eng. 1 (2012) 281–289. https://doi.org/10.1016/j.coche.2012.03.002.

[39] A. Krogh, On the Mechanism of the Gas-Exchange in the Lungs 1, Skand. Arch. Physiol. 23 (1910) 248–278. https://doi.org/10.1111/j.1748-1716.1910.tb00601.x.

[40] Meinzer FC, Clearwater MJ, Goldstein G. Water transport in trees: current per- spectives, new insights and some controversies. Environ Exp Bot 2001;45:239–62. https://doi.org/10.1016/S0098-8472(01)00074-0.

[41] Z. Smalko, An impact of thermodynamic processes in human bodies on performance reliability of individuals, J. Konbin. 27 (2015) 5–22. https://doi.org/10.2478/jok-2013-0101.

[42] E.R. Weibel, Fractal geometry: a design principle for living organisms., Am. J. Physiol. 261 (1991) L361-9. https://doi.org/10.1152/ajplung.1991.261.6.L361.

[43] M.O. Coppens, Scaling-up and -down in a nature-inspired way, Ind. Eng. Chem. Res. 44 (2005) 5011–5019. https://doi.org/10.1021/ie0490482.

[44] M. Asadzade, A. Shamloo, Design and simulation of a novel bipolar plate based on lung-shaped bio-inspired fl ow pattern for PEM fuel cell, Int. J. Energy Res. (2017) 1730–1739. https://doi.org/10.1002/er.

[45] R. Roshandel, F. Arbabi, G.K. Moghaddam, Simulation of an innovative flow-field design based on a bio inspired pattern for PEM fuel cells, Renew. Energy. 41 (2012) 86–95. https://doi.org/10.1016/j.renene.2011.10.008.

[46] K. Wu, V. Francia, M.O. Coppens, Dynamic viscoplastic granular flows: A persistent challenge in gas-solid fluidization, Powder Technol. 365 (2020) 172–185. https://doi.org/10.1016/j.powtec.2019.04.053.

[47] P. Trogadas, M.O. Coppens, Nature-inspired chemical engineering: A new design methodology for sustainability, Elsevier Inc., 2019. https://doi.org/10.1016/B978-0-12-814681-1.00002-3.

[48] A.S. Perera, M.O. Coppens, Re-designing materials for biomedical applications: From biomimicry to nature-inspired chemical engineering, Philos. Trans. R. Soc. A Math. Phys. Eng. Sci. 377 (2019). https://doi.org/10.1098/rsta.2018.0268.

[49] P. Trans, R.S. Lond, Systematic technology transfer from biology to engineering Receive free email alerts when new articles cite this article - sign up in the box at the top, Phil. Trans. R. Soc. Lond. A (2002) 36 159– 173. https://doi.org/10.1098/rsta.2001.0923.

[50] S.S. Latthe, C. Terashima, K. Nakata, A. Fujishima, Superhydrophobic surfaces developed by mimicking hierarchical surface morphology of lotus leaf, Molecules. 19 (2014) 4256–4283. https://doi.org/10.3390/molecules19044256.

[51] A.S. Perera, M.O. Coppens, Re-designing materials for biomedical applications: From biomimicry to nature-inspired chemical engineering, Philos. Trans. R. Soc. A Math. Phys. Eng. Sci. 377 (2019). https://doi.org/10.1098/rsta.2018.0268.

[52] M.M. Sundaram, G.K. Ananthasuresh, Gustave Eiffel and his optimal structures, Resonance. 14 (2009) 849–865. https://doi.org/10.1007/s12045-009-0081-x.

[53] P. Trogadas, M.M. Nigra, M.O. Coppens, Nature-inspired optimization of hierarchical porous media for catalytic and separation processes, New J. Chem. 40 (2016) 4016–4026. https://doi.org/10.1039/c5nj03406j.

[54] K. Wu, L. de Martín, L. Mazzei, M.O. Coppens, Pattern formation in fluidized beds as a tool for model validation: A two-fluid model based study, Powder Technol. 295 (2016) 35–42. https://doi.org/10.1016/j.powtec.2016.03.011.

[55] M.M. Lynch, J. Liu, M. Nigra, M.O. Coppens, Chaperonin-Inspired pH Protection by Mesoporous Silica SBA-15 on Myoglobin and Lysozyme, Langmuir. 32 (2016) 9604–9610. https://doi.org/10.1021/acs.langmuir.6b02832.

[56] J.I.S. Cho, T.P. Neville, P. Trogadas, Q. Meyer, Y. Wu, R. Ziesche, P. Boillat, M. Cochet, V. Manzi-Orezzoli, P. Shearing, D.J.L. Brett, M.-O. Coppens, Visualization of Liquid Water in a Lung-Inspired Flow-Field based Polymer Electrolyte Membrane Fuel Cell via Neutron Radiography, Energy. 170 (2018) 14–21. https://doi.org/10.1016/J.ENERGY.2018.12.143.

[57] P. Trogadas, V. Ramani, P. Strasser, T.F. Fuller, M.O. Coppens, Hierarchically Structured Nanomaterials for Electrochemical Energy Conversion, Angew. Chemie - Int. Ed. 55 (2016) 122–148. https://doi.org/10.1002/anie.201506394.

[58] S. Kjelstrup, M.O. Coppens, J.G. Pharoah, P. Pfeifer, Nature-inspired energy-and material-efficient design of a polymer electrolyte membrane fuel cell, Energy and Fuels. 24 (2010) 5097–5108. https://doi.org/10.1021/ef100610w.

[59] J. Marquis, PhD thesis, Rensselaer Polytechnic Institute, Troy, NY; 2013.

[60] J.I.S. Cho, J. Marquis, P. Trogadas, T.P. Neville, D.J.L. Brett, M.O. Coppens, Optimizing the Architecture of Lung-Inspired Fuel Cells, Chem. Eng. Sci. (2019) 115375. https://doi.org/10.1016/j.ces.2019.115375.

[61] Trogadas P, Cho JIS, Neville TP, Marquis J, Wu B, Brett DJL, et al. A lung-inspired approach to scalable and robust fuel cell design. Energy Environ Sci 2018;11:136–43. https://doi.org/10.1039/c7ee02161e.

[62] R. O'Hayre, D. Braithwaite, W. Hermann, S.J. Lee, T. Fabian, S.W. Cha, Y. Saito, F.B. Prinz, Development of portable fuel cell arrays with printed-circuit technology, J. Power Sources. 124 (2003) 459–472. https://doi.org/10.1016/S0378-7753(03)00802-4.

[63] R. Lin, Y. Weng, X. Lin, F. Xiong, Rapid cold start of proton exchange membrane fuel cells by the printed circuit board technology, Int. J. Hydrogen Energy. 39 (2014) 18369–18378. https://doi.org/10.1016/j.ijhydene.2014.09.065.

[64] O.A. Obeisun, Q. Meyer, J. Robinson, C.W. Gibbs, A.R. Kucernak, P.R. Shearing, D.J.L. Brett, Development of open-cathode polymer electrolyte fuel cells using printed circuit board flow-field plates: Flow geometry characterisation, Int. J. Hydrogen Energy. 39 (2014) 18326–18336. https://doi.org/10.1016/j.ijhydene.2014.08.106.

[65] Y. Wu, J.I.S. Cho, T.P. Neville, Q. Meyer, R. Ziesche, P. Boillat, M. Cochet, P.R. Shearing, D.J.L. Brett, Effect of serpentine flow- fi eld design on the water management of polymer electrolyte fuel cells : An in-operando neutron radiography study, J. Power Sources. 399 (2018) 254–263. https://doi.org/10.1016/j.jpowsour.2018.07.085.

[66] J.I.S. Cho, T.P. Neville, P. Trogadas, J. Bailey, P. Shearing, D.J.L. Brett, M.O. Coppens, Capillaries for water management in polymer electrolyte membrane fuel cells, Int. J. Hydrogen Energy. 43 (2018) 21949–21958. https://doi.org/10.1016/j.ijhydene.2018.10.030.

[67] E. Engebretsen, J.B. Robinson, O. Obeisun, T. Mason, D. Finegan, G. Hinds, P.R. Shearing, D.J.L. Brett, Electro-thermal impedance spectroscopy applied to an open-cathode polymer electrolyte fuel cell, J. Power Sources. 302 (2016) 210–214. https://doi.org/10.1016/j.jpowsour.2015.10.047.

[68] A. Kirubakaran, S. Jain, R.K. Nema, A review on fuel cell technologies and power electronic interface, Renew. Sustain. Energy Rev. 13 (2009) 2430–2440. https://doi.org/10.1016/j.rser.2009.04.004.

[69] P.E. Dodds, I. Staffell, A.D. Hawkes, F. Li, P. Grünewald, W. McDowall, P. Ekins, Hydrogen and fuel cell technologies for heating: A review, Int. J. Hydrogen Energy. 40 (2015) 2065–2083. https://doi.org/10.1016/j.ijhydene.2014.11.059.

[70] K.B. Prater, Polymer electrolyte fuel cells: a review of recent developments, J. Power Sources. 51 (1994) 129–144. https://doi.org/10.1016/0378-7753(94)01934-7.

[71] Y. Wang, K.S. Chen, J. Mishler, S. Chan, X. Cordobes, A review of polymer electrolyte membrane fuel cells : Technology , applications , and needs on fundamental research, Appl. Energy. 88 (2011) 981–1007. https://doi.org/10.1016/j.apenergy.2010.09.030.

[72] B.D. Mcnicol, D.A.J. Rand, K.R. Williams, Fuel cells for road transportation purposes — yes or no ?, J. Power Sources. 100 (2001) 47– 59.

[73] K. Haraldsson, A. Folkesson, P. Alvfors, Fuel cell buses in the Stockholm CUTE project — First experiences from a climate perspective, 145 (2005) 620–631. https://doi.org/10.1016/j.jpowsour.2004.12.081.

[74] A.S. Feitelberg, J. Stathopoulos, Z. Qi, C. Smith, J.F. Elter, Reliability of Plug Power GenSys Short communication fuel cell systems, J. Power Sources. 147 (2005) 203–207. https://doi.org/10.1016/j.jpowsour.2005.01.012.

[75] C. Wang, Z. Mao, F. Bao, X. Li, X. Xie, Development and performance of 5 kw proton exchange membrane fuel cell stationary power system, Int. J. Hydrogen Energy. 30 (2005) 1031–1034. https://doi.org/10.1016/j.ijhydene.2004.11.010.

[76] J.J. Hwang, M.L. Zou, Development of a proton exchange membrane fuel cell cogeneration system, J. Power Sources.195 (2010) 2579–2585. https://doi.org/10.1016/j.jpowsour.2009.10.087.

[77] http://www.ballard.com/.

[78] Q. Yan, H. Toghiani, Y.W. Lee, K. Liang, H. Causey, Effect of sub-freezing temperatures on a PEM fuel cell performance, startup and fuel cell components, J. Power Sources. 160 (2006) 1242–1250. https://doi.org/10.1016/j.jpowsour.2006.02.075.

[79] Q. Li, R. He, J.O. Jensen, N.J. Bjerrum, Approaches and Recent Development of Polymer Electrolyte Membranes for Fuel Cells Operating above 100 °C, Chem. Mater. 15 (2003) 4896–4915. https://doi.org/10.1021/cm0310519.

[80] S. Zhang, X. Yuan, H. Wang, W. Mérida, H. Zhu, J. Shen, S. Wu, J. Zhang, A review of accelerated stress tests of MEA durability in PEM fuel cells, Int. J. Hydrogen Energy. 34 (2009) 388–404. https://doi.org/10.1016/j.ijhydene.2008.10.012.

[81] O. Savadogo, Emerging membranes for electrochemical systems: Part II. High temperature composite membranes for polymer electrolyte fuel cell (PEFC) applications, J. Power Sources. 127 (2004) 135–161. https://doi.org/10.1016/j.jpowsour.2003.09.043.

[82] S. Banerjee, D.E. Curtin, Nafion® perfluorinated membranes in fuel cells, J. Fluor. Chem. 125 (2004) 1211–1216. https://doi.org/10.1016/j.jfluchem.2004.05.018.

[83] K. Miyatake, M. Watanabe, Emerging membrane materials for high temperature polymer electrolyte fuel cells: durable hydrocarbon ionomers, J. Mater. Chem. 16 (2006) 4465. https://doi.org/10.1039/b612153e.

[84] L. Zhang, S.R. Chae, Z. Hendren, J.S. Park, M.R. Wiesner, Recent advances in proton exchange membranes for fuel cell applications, Chem. Eng. J. 204–205 (2012) 87–97. https://doi.org/10.1016/j.cej.2012.07.103.

[85] J.K. Nørskov, J. Rossmeisl, A. Logadottir, L. Lindqvist, J.R. Kitchin, T. Bligaard, H. Jónsson, Origin of the overpotential for oxygen reduction at a fuel-cell cathode, J. Phys. Chem. B. 108 (2004) 17886–17892. https://doi.org/10.1021/jp047349j.

[86] S. Sui, X. Wang, X. Zhou, Y. Su, S. Riffat, C. jun Liu, A comprehensive review of Pt electrocatalysts for the oxygen reduction reaction: Nanostructure, activity, mechanism and carbon support in PEM fuel cells, J. Mater. Chem. A. 5 (2017) 1808–1825. https://doi.org/10.1039/C6TA08580F.

[87] T. Toda, Enhancement of the Electroreduction of Oxygen on Pt Alloys with Fe, Ni, and Co, J. Electrochem. Soc. 146 (2002) 3750. https://doi.org/10.1149/1.1392544.

[88] C.J. Yang, An impending platinum crisis and its implications for the future of the automobile, Energy Policy. 37 (2009) 1805–1808. https://doi.org/10.1016/j.enpol.2009.01.019.

[89] I.U. Dedigama, PhD thesis,Unviersity College London, London, 2014.

[90] S. Sharma, B.G. Pollet, Support materials for PEMFC and DMFC electrocatalysts - A review, J. Power Sources. 208 (2012) 96–119. https://doi.org/10.1016/j.jpowsour.2012.02.011.

[91] M. Han, J.H. Xu, S.H. Chan, S.P. Jiang, Characterization of gas diffusion layers for PEMFC, Electrochim. Acta. 53 (2008) 5361–5367. https://doi.org/10.1016/j.electacta.2008.02.057.

[92] A. Hermann, T. Chaudhuri, P. Spagnol, Bipolar plates for PEM fuel cells: A review, Int. J. Hydrogen Energy. 30 (2005) 1297–1302. https://doi.org/10.1016/j.ijhydene.2005.04.016.

[93] M. Neergat, A.K. Shukla, Effect of diffusion-layer morphology on the performance of solid-polymer-electrolyte direct methanol fuel cells, J. Power Sources. 104 (2002) 289–294. https://doi.org/10.1016/S0378-7753(01)00877-1.

[94] L.R. Jordan, A.K. Shukla, T. Behrsing, N.R. Avery, B.C. Muddle, M. Forsyth, Diffusion layer parameters influencing optimal fuel cell performance, J. Power Sources. 86 (2000) 250–254. https://doi.org/10.1016/S0378-7753(99)00489-9.

[95] H. Meng, C.-Y. Wang, Electron Transport in PEFCs, J. Electrochem. Soc. 151 (2004) A358. https://doi.org/10.1149/1.1641036.

[96] H. Tsuchiya, O. Kobayashi, Mass production cost of PEM fuel cell by learning curve, Int. J. Hydrogen Energy. 29 (2004) 985–990. https://doi.org/10.1016/j.ijhydene.2003.10.011.

[97] A. Schmitz, S. Wagner, R. Hahn, H. Uzun, C. Hebling, Stability of planar PEMFC in Printed Circuit Board technology, J. Power Sources. 127 (2004) 197–205. https://doi.org/10.1016/j.jpowsour.2003.09.023.

[98] J. Wang, H. Wang, Discrete approach for flow field designs of parallel channel configurations in fuel cells, Int. J. Hydrogen Energy. 37 (2012) 10881–10897. https://doi.org/10.1016/j.ijhydene.2012.04.034.

[99] A. Ghanbarian, M.J. Kermani, J. Scholta, M. Abdollahzadeh, Polymer electrolyte membrane fuel cell flow field design criteria – Application to parallel serpentine flow patterns, Energy Convers. Manag. 166 (2018) 281–296. https://doi.org/10.1016/j.enconman.2018.04.018.

[100] K.S. Choi, H.M. Kim, S.M. Moon, Numerical studies on the geometrical characterization of serpentine flow-field for efficient PEMFC, Int. J. Hydrogen Energy. 36 (2011) 1613–1627. https://doi.org/10.1016/j.ijhydene.2010.10.073.

[101] W.M. Yan, C.Y. Chen, S.C. Mei, C.Y. Soong, F. Chen, Effects of operating conditions on cell performance of PEM fuel cells with conventional or interdigitated flow field, J. Power Sources. 162 (2006) 1157–1164. https://doi.org/10.1016/j.jpowsour.2006.07.044.

[102] T. Matsuura, M. Kato, M. Hori, Study on metallic bipolar plate for proton exchange membrane fuel cell, J. Power Sources. 161 (2006) 74–78. https://doi.org/10.1016/j.jpowsour.2006.04.064.

[103] H. Tawfik, Y. Hung, D. Mahajan, Metal bipolar plates for PEM fuel cell-A review, J. Power Sources. 163 (2007) 755–767. https://doi.org/10.1016/j.jpowsour.2006.09.088.

[104] A. Müller, P. Kauranen, A. Von Ganski, B. Hell, Injection moulding of graphite composite bipolar plates, J. Power Sources. 154 (2006) 467–471. https://doi.org/10.1016/j.jpowsour.2005.10.096.

[105] J.K. Kuo, C.K. Chen, A novel Nylon-6-S316L fiber compound material for injection molded PEM fuel cell bipolar plates, J. Power Sources. 162 (2006) 207–214. https://doi.org/10.1016/j.jpowsour.2006.06.034.

[106] D. Ruffing, B. Kovacic, S. Demetriou, E.F. Domino, Naloxone enhancement of DMT and LSD-25 induced suppression of food-rewarded bar pressing behavior in the rat, Psychopharmacology (Berl). 62 (1979) 207–210. https://doi.org/10.1016/S0378-7753(03)00080-6.

[107] M. Schulze, E. Gülzow, S. Schönbauer, T. Knöri, R. Reissner, Segmented cells as tool for development of fuel cells and error prevention/prediagnostic in fuel cell stacks, J. Power Sources. 173 (2007) 19–27. https://doi.org/10.1016/j.jpowsour.2007.03.055.

[108] L.C. Pérez, L. Brandão, J.M. Sousa, A. Mendes, Segmented polymer electrolyte membrane fuel cells-A review, Renew. Sustain. Energy Rev. 15 (2011) 169–185. https://doi.org/10.1016/j.rser.2010.08.024.

[109] P.C. Ghosh, T. Wüster, H. Dohle, N. Kimiaie, J. Mergel, D. Stolten, In situ approach for current distribution measurement in fuel cells, J. Power Sources. 154 (2006) 184–191. https://doi.org/10.1016/j.jpowsour.2005.03.219.

[110] E. Coz, J. Théry, P. Boillat, V. Faucheux, D. Alincant, P. Capron, G. Gébel, Water management in a planar air-breathing fuel cell array using operando neutron imaging, J. Power Sources. 331 (2016) 535–543. https://doi.org/10.1016/j.jpowsour.2016.09.041.

[111] J.W. Guo, X.F. Xie, J.H. Wang, Y.M. Shang, Effect of current collector corrosion made from printed circuit board (PCB) on the degradation of self-breathing direct methanol fuel cell stack, Electrochim. Acta. 53 (2008) 3056–3064. https://doi.org/10.1016/j.electacta.2007.11.044.

[112] S.J.C. Cleghorn, C.R. Derouin, M.S. Wilson, S. Gottesfeld, A Printed Circuit Board approach to measuring current distribution in a fuel cell, J. Appl. Electrochem. 28 (1998) 663–672. https://doi.org/10.1023/A:1003206513954.

[113] R. Eckl, R. Grinzinger, W. Lehnert, Current distribution mapping in polymer electrolyte fuel cells - A finite element analysis of measurement uncertainty imposed by lateral currents, J. Power Sources. 154 (2006) 171–179. https://doi.org/10.1016/j.jpowsour.2005.04.004.

[114] F. Barbir, PEM Fuel Cells, in: N. Sammes (Ed.), Fuel Cell Technol. Reach. Towar. Commer., Springer London, London, 2006: pp. 27–51. https://doi.org/10.1007/1-84628-207-1_2.

[115] F. Barbir Frano ; Barbir, PEM Fuel Cells: Theory and Practice, Elsevier Science, 2005.

[116] Xiao-Zi Yuan, Electrochemical impedance spectroscopy in PEM fuel cells : fundamentals and applications, Springer, London, 2009.

[117] S. Asghari, A. Mokmeli, M. Samavati, Study of PEM fuel cell performance by electrochemical impedance spectroscopy, Int. J. Hydrogen Energy. 35 (2010) 9283–9290. https://doi.org/10.1016/j.ijhydene.2010.03.069.

[118] X. Yuan, H. Wang, J. Colin Sun, J. Zhang, AC impedance technique in PEM fuel cell diagnosis-A review, Int. J. Hydrogen Energy. 32 (2007) 4365–4380. https://doi.org/10.1016/j.ijhydene.2007.05.036.

[119] S.M. Rezaei Niya, M. Hoorfar, Study of proton exchange membrane fuel cells using electrochemical impedance spectroscopy technique - A review, J. Power Sources. 240 (2013) 281–293. https://doi.org/10.1016/j.jpowsour.2013.04.011.

[120] M. Eikerling, A.A. Kornyshev, Electrochemical impedance of the cathode catalyst layer in polymer electrolyte fuel cells, J. Electroanal. Chem. 475 (1999) 107–123. https://doi.org/10.1016/S0022-0728(99)00335-6.

[121] K.R. Cooper, M. Smith, Electrical test methods for on-line fuel cell ohmic resistance measurement, J. Power Sources. 160 (2006) 1088–1095. https://doi.org/10.1016/j.jpowsour.2006.02.086.

[122] T. Romero-Castañón, L.G. Arriaga, U. Cano-Castillo, Impedance spectroscopy as a tool in the evaluation of MEA's, J. Power Sources. 118 (2003) 179–182. https://doi.org/10.1016/S0378-7753(03)00085-5.

[123] F. Lufrano, P. Staiti, M. Minutoli, Evaluation of nafion based double layer capacitors by electrochemical impedance spectroscopy, J. Power Sources. 124 (2003) 314–320. https://doi.org/10.1016/S0378-7753(03)00589-5.

[124] O. Antoine, Y. Bultel, R. Durand, Oxygen reduction reaction kinetics and mechanism on platinum nanoparticles inside Nafion®, J. Electroanal. Chem. 499 (2001) 85–94. https://doi.org/10.1016/S0022-0728(00)00492-7.

[125] C. Brunetto, A. Moschetto, G. Tina, PEM fuel cell testing by electrochemical impedance spectroscopy, Electr. Power Syst. Res. 79 (2009) 17–26. https://doi.org/10.1016/j.epsr.2008.05.012.

[126] N. Fouquet, C. Doulet, C. Nouillant, G. Dauphin-Tanguy, B. Ould-Bouamama, Model based PEM fuel cell state-of-health monitoring via ac impedance measurements, J. Power Sources. 159 (2006) 905–913. https://doi.org/10.1016/j.jpowsour.2005.11.035.

[127] F.T. Man, Real-Time Testing of Automatic Overload Control Systems in a Laboratory Environment, IEEE Trans. Commun. 21 (1973) 1027–1031. https://doi.org/10.1109/TCOM.1973.1091787.

[128] J. Kiselev, B. Ziegler, H.J. Schwalbe, R.P. Franke, U. Wolf, Detection of osteoarthritis using acoustic emission analysis R, Med. Eng. Phys. 65 (2019) 57–60. https://doi.org/10.1016/j.medengphy.2019.01.002.

[129] D.G. Aggelis, E.Z. Kordatos, T.E. Matikas, Acoustic emission for fatigue damage characterization in metal plates, Mech. Res. Commun. 38 (2011) 106–110. https://doi.org/10.1016/j.mechrescom.2011.01.011.

[130] Z. Zhang, X. Wu, J. Tan, In-situ monitoring of stress corrosion cracking of 304 stainless steel in high-temperature water by analyzing acoustic emission waveform, Corros. Sci. 146 (2019) 90–98. https://doi.org/10.1016/j.corsci.2018.10.022.

[131] A. Zaki, H.K. Chai, A. Behnia, D.G. Aggelis, J.Y. Tan, Z. Ibrahim, Monitoring fracture of steel corroded reinforced concrete members under flexure by acoustic emission technique, Constr. Build. Mater. 136 (2017) 609–618. https://doi.org/10.1016/j.conbuildmat.2016.11.079.

[132] Q. Lemarié, F. Alloin, P.X. Thivel, H. Idrissi, L. Roué, Study of sulfur-based electrodes by operando acoustic emission, Electrochim. Acta. 299 (2019) 415–422. https://doi.org/10.1016/j.electacta.2019.01.019.

[133] J.B. Robinson, M. Maier, G. Alster, T. Compton, D.J.L. Brett, P.R. Shearing, Spatially resolved ultrasound diagnostics of Li-ion battery electrodes, Phys. Chem. Chem. Phys. 21 (2019) 6354–6361. https://doi.org/10.1039/c8cp07098a.

[134] N. Beganovic, D. Söffker, Estimation of remaining useful lifetime of lithium-ion battery based on acoustic emission measurements, J. Energy Resour. Technol. Trans. ASME. 141 (2019) 1–10. https://doi.org/10.1115/1.4042234.

[135] L. Oca, N. Guillet, R. Tessard, U. Iraola, Lithium-ion capacitor safety assessment under electrical abuse tests based on ultrasound characterization and cell opening, J. Energy Storage. 23 (2019) 29–36. https://doi.org/10.1016/j.est.2019.02.033.

[136] M. Maier, Q. Meyer, J. Majasan, C. Tan, I. Dedigama, J. Robinson, J. Dodwell, Y. Wu, L. Castanheira, G. Hinds, P.R. Shearing, D.J.L. Brett, Operando flow regime diagnosis using acoustic emission in a polymer electrolyte membrane water electrolyser, J. Power Sources. 424 (2019) 138–149. https://doi.org/10.1016/j.jpowsour.2019.03.061.

[137] B. Legros, P.X. Thivel, Y. Bultel, M. Boinet, R.P. Nogueira, Acoustic emission: Towards a real-time diagnosis technique for Proton exchange membrane fuel cell operation, J. Power Sources. 195 (2010) 8124–8133. https://doi.org/10.1016/j.jpowsour.2010.07.045.

[138] J. Malzbender, R.W. Steinbrech, Advanced measurement techniques to characterize thermo-mechanical aspects of solid oxide fuel cells, J. Power Sources. 173 (2007) 60–67. https://doi.org/10.1016/j.jpowsour.2007.07.072.

[139] B. Legros, R.P. Nogueira, P.-X. Thivel, Y. Bultel, M. Boinet, Electrochemical Impedance and Acoustic Emission Survey of Water Desorption in Nafion Membranes, Electrochem. Solid-State Lett. 12 (2009) B116. https://doi.org/10.1149/1.3131728.

[140] B. Legros, P.X. Thivel, F. Druart, Y. Bultel, R. Nogueira, Diagnosis and Modelling of Proton- Exchange-Membrane Fuel Cell via and Acoustic-Emission Measurements, Electromotion. (2009) 1–6. https://doi.org/10.1109/ELECTROMOTION.2009.5259133.

[141] D.G. Strickland, S. Litster, J.G. Santiago, Current distribution in polymer electrolyte membrane fuel cell with active water management, J. Power Sources. 174 (2007) 272–281. https://doi.org/10.1016/j.jpowsour.2007.08.059.

[142] M. Rahimi-Esbo, A.A. Ranjbar, A. Ramiar, E. Alizadeh, M. Aghaee, Improving PEM fuel cell performance and effective water removal by using a novel gas flow field, Int. J. Hydrogen Energy. 41 (2016) 3023–3037. https://doi.org/10.1016/j.ijhydene.2015.11.001.

[143] N. Rajalakshmi, M. Raja, K.S. Dhathathreyan, Evaluation of current distribution in a proton exchange membrane fuel cell by segmented cell approach, J. Power Sources. 112 (2002) 331–336. https://doi.org/10.1016/S0378-7753(02)00352-X.

[144] M. Belhadj, A. Aquino, J. Heng, S. Kmiotek, S. Raël, C. Bonnet, F. Lapicque, Current density distributions in polymer electrolyte fuel cells: A tool for characterisation of gas distribution in the cell and its state of health, Chem. Eng. Sci. 185 (2018) 18–25. https://doi.org/10.1016/j.ces.2018.03.055.

[145] Q. Zhang, R. Lin, L. Técher, X. Cui, Experimental study of variable operating parameters effects on overall PEMFC performance and spatial performance distribution, Energy. 115 (2016) 550–560. https://doi.org/10.1016/j.energy.2016.08.086.

[146] Y. Yu, X.Z. Yuan, H. Li, E. Gu, H. Wang, G. Wang, M. Pan, Current mapping of a proton exchange membrane fuel cell with a segmented current collector during the gas starvation and shutdown processes, Int. J. Hydrogen Energy. 37 (2012) 15288–15300. https://doi.org/10.1016/j.ijhydene.2012.07.023.

[147] Y. Vazifeshenas, K. Sedighi, M. Shakeri, Numerical investigation of a novel compound flow-field for PEMFC performance improvement, Int. J. Hydrogen Energy. 40 (2015) 15032–15039. https://doi.org/10.1016/j.ijhydene.2015.08.077.

[148] Q. Meyer, K. Ronaszegi, J.B. Robinson, M. Noorkami, O. Curnick, S. Ashton, A. Danelyan, T. Reisch, P. Adcock, R. Kraume, P.R. Shearing, D.J.L. Brett, Combined current and temperature mapping in an air-cooled, open-cathode polymer electrolyte fuel cell under steady-state and dynamic conditions, J. Power Sources. 297 (2015) 315–322. https://doi.org/10.1016/j.jpowsour.2015.07.069.

[149] B.D. Gould, R. Ramamurti, C.R. Osland, K.E. Swider-Lyons, Assessing fuel-cell coolant flow fields with numerical models and infrared thermography, Int. J. Hydrogen Energy. 39 (2014) 14061–14070. https://doi.org/10.1016/j.ijhydene.2014.07.018.

[150] R. Vijayakumar, T. Ramkumar, S. Maheswari, P. Sridhar, S. Pitchumani, Current and clamping pressure distribution studies on the scale up issues in direct methanol fuel cells, Electrochim. Acta. 90 (2013) 274–282. https://doi.org/10.1016/j.electacta.2012.11.129.

[151] V. Lilavivat, S. Shimpalee, J.W. Van Zee, H. Xu, C.K. Mittelsteadt, Current Distribution Mapping for PEMFCs, Electrochim. Acta. 174 (2015) 1253–1260. https://doi.org/10.1016/j.electacta.2015.06.081.

[152] M. Wilkinson, M. Blanco, E. Gu, J.J. Martin, D.P. Wilkinson, J.J. Zhang, H. Wang, In Situ Experimental Technique for Measurement of Temperature and Current Distribution in Proton Exchange Membrane Fuel Cells, Electrochem. Solid-State Lett. 9 (2006) A507. https://doi.org/10.1149/1.2338769.

[153] C. Wieser, A. Helmbold, E. Gülzow, New technique for two-dimensional current distribution measurements in electrochemical cells, J. Appl. Electrochem. 30 (2000) 803–807. https://doi.org/10.1023/A:1004047412066.

[154] A. Hakenjos, C. Hebling, Spatially resolved measurement of PEM fuel cells, J. Power Sources. 145 (2005) 307–311. https://doi.org/10.1016/j.jpowsour.2005.01.075.

[155] S.A. Freunberger, M. Reum, J. Evertz, A. Wokaun, F.N. Büchi, Measuring the current distribution in PEFCs with sub-millimeter resolution, J. Electrochem. Soc. 153 (2006) 2158–2165. https://doi.org/10.1149/1.2345591.

[156] G. Zhang, L. Guo, L. Ma, H. Liu, Simultaneous measurement of current and temperature distributions in a proton exchange membrane fuel cell, J. Power Sources. 195 (2010) 3597–3604. https://doi.org/10.1016/j.jpowsour.2009.12.016.

[157] A. Hakenjos, H. Muenter, U. Wittstadt, C. Hebling, A PEM fuel cell for combined measurement of current and temperature distribution, and flow field flooding, J. Power Sources. 131 (2004) 213–216. https://doi.org/10.1016/j.jpowsour.2003.11.081.

[158] S.S. Hsieh, Y.J. Huang, Measurements of current and water distribution for a micro-PEM fuel cell with different flow fields, J. Power Sources. 183 (2008) 193–204. https://doi.org/10.1016/j.jpowsour.2008.04.065.

[159] I. Alaefour, G. Karimi, K. Jiao, X. Li, Measurement of current distribution in a proton exchange membrane fuel cell with various flow arrangements - A parametric study, Appl. Energy. 93 (2012) 80–89. https://doi.org/10.1016/j.apenergy.2011.05.033.

[160] C. Minnaar, F. De Beer, D. Bessarabov, Current Density Distribution of Electrolyzer Flow Fields: In Situ Current Mapping and Neutron Radiography, Energy & Fuels. 34 (2019) 1014–1023. https://doi.org/10.1021/acs.energyfuels.9b03814.

[161] P. Trogadas, M.O. Coppens, Nature-inspired electrocatalysts and devices for energy conversion, Chem. Soc. Rev. 49 (2020) 3107–3141. https://doi.org/10.1039/c8cs00797g.

[162] P. Gehr, H. Erni, Morphometric estimation of pulmonary diffusion capacity in two horse lungs, Respir. Physiol. 41 (1980) 199–210. https://doi.org/10.1016/0034-5687(80)90052-3.

[163] S. Gheorghiu, M.O. Coppens, Optimal Bimodal Pore Networks for Heterogeneous Catalysis, AIChE J. 50 (2004) 812–820. https://doi.org/10.1002/aic.10076.

[164] B.H. Kaye, A Random Walk Through Fractal Dimensions, Wiley-VCH Verlag GmbH, Weinheim, Germany, 2007.

[165] C.D. Murray, The Physiological Principle of Minimum Work: II. Oxygen Exchange in Capillaries, Proc. Natl. Acad. Sci. 12 (2006) 299–304. https://doi.org/10.1073/pnas.12.5.299.

[166] S. Kjelstrup, M.O. Coppens, J.G. Pharoah, P. Pfeifer, Nature-inspired energy-and material-efficient design of a polymer electrolyte membrane fuel cell, Energy and Fuels. 24 (2010) 5097–5108. https://doi.org/10.1021/ef100610w.

[167] P.W. Dierickx, D.S. De Wachter, F. De Somer, G. Van Nooten, P.R. Verdonck, Mass transfer characteristics of artificial lungs, ASAIO J. 47 (2001) 628–633. https://doi.org/10.1097/00002480-200111000-00012.

[168] B. Sapoval, M. Filoche, E.R. Weibel, Smaller is better--but not too small: A physical scale for the design of the mammalian pulmonary acinus, Proc. Natl. Acad. Sci. 99 (2002) 10411–10416. https://doi.org/10.1073/pnas.122352499.

[169] E.W. Hoppe, A. Seifert, C.E. Aalseth, P.P. Bachelor, A.R. Day, D.J. Edwards, T.W. Hossbach, K.E. Litke, J.I. McIntyre, H.S. Miley, S.M. Schulte, J.E. Smart, G.A. Warren, Cleaning and passivation of copper surfaces to remove surface radioactivity and prevent oxide formation, Nucl. Instruments Methods Phys. Res. Sect. A Accel. Spectrometers, Detect. Assoc. Equip. 579 (2007) 486–489. https://doi.org/10.1016/j.nima.2007.04.101.

[170] https://www.rolanddg.co.uk/

[171] http://www.dixipolytool.ch/en/

[172] G. Wang, H. Yu, B. De Man, An outlook on x-ray CT research and development, Med. Phys. 35 (2008) 1051–1064. https://doi.org/10.1118/1.2836950.

[173] Sun W , Brown S B and Leach R K, An overview of industrial X-ray computed tomography, National Physical Laboratory Report, NPL, UK, (2012).

[174] S. Mohammad, R. Niya, M. Hoorfar, Study of proton exchange membrane fuel cells using electrochemical impedance spectroscopy technique e A review, J. Power Sources. 240 (2013) 281–293. https://doi.org/10.1016/j.jpowsour.2013.04.011.

[175] Z. Xie, S. Holdcroft, Polarization-dependent mass transport parameters for orr in perfluorosulfonic acid ionomer membranes: An EIS study using microelectrodes, J. Electroanal. Chem. 568 (2004) 247–260. https://doi.org/10.1016/j.jelechem.2004.01.019.

[176] M. Ciureanu, R. Roberge, Electrochemical impedance study of PEM fuel cells. Experimental diagnostics and modeling of air cathodes, J. Phys. Chem. B. 105 (2002) 3531–3539. https://doi.org/10.1021/jp003273p.

[177] I. Pivac, D. Bezmalinović, F. Barbir, Catalyst degradation diagnostics of proton exchange membrane fuel cells using electrochemical impedance spectroscopy, Int. J. Hydrogen Energy. 43 (2018) 13512–13520. https://doi.org/10.1016/j.ijhydene.2018.05.095.

[178] P. Kurzweil, H.J. Fischle, A new monitoring method for electrochemical aggregates by impedance spectroscopy, J. Power Sources. 127 (2004) 331–340. https://doi.org/10.1016/j.jpowsour.2003.09.030.

[179] J. Wu, X.Z. Yuan, H. Wang, M. Blanco, J.J. Martin, J. Zhang, Diagnostic tools in PEM fuel cell research: Part I Electrochemical techniques, Int. J. Hydrogen Energy. 33 (2008) 1735–1746. https://doi.org/10.1016/j.ijhydene.2008.01.013.

[180] T.J.P. Freire, E.R. Gonzalez, Effect of membrane characteristics and humidification conditions on the impedance response of polymer electrolyte fuel cells, J. Electroanal. Chem. 503 (2001) 57–68. https://doi.org/10.1016/S0022-0728(01)00364-3.

[181] V.S. Bethapudi, M. Maier, G. Hinds, P.R. Shearing, D.J.L. Brett, M.O. Coppens, Acoustic emission as a function of polarisation: Diagnosis of polymer electrolyte fuel cell hydration state, Electrochem. Commun. 109 (2019) 106582. https://doi.org/10.1016/j.elecom.2019.106582.

[182] V.S. Bethapudi, J. Hack, P. Trogadas, J.I.S. Cho, L. Rasha, G. Hinds, P.R. Shearing, D.J.L. Brett, M.-O. Coppens, A lung-inspired printed circuit board polymer electrolyte fuel cell, Energy Convers. Manag. 202 (2019) 112198. https://doi.org/10.1016/j.enconman.2019.112198.

[183] D. Spernjak, A.K. Prasad, S.G. Advani, In situ comparison of water content and dynamics in parallel, single-serpentine, and interdigitated flow fields of polymer electrolyte membrane fuel cells, J. Power Sources. 195 (2010) 3553–3568. https://doi.org/10.1016/j.jpowsour.2009.12.031.

[184] A. Kazim, Exergy analysis of a PEM fuel cell at variable operating conditions, Energy Convers. Manag. 45 (2004) 1949–1961. https://doi.org/10.1016/j.enconman.2003.09.030.

[185] Q. Meyer, S. Ashton, P. Boillat, M. Cochet, E. Engebretsen, D.P. Finegan, X. Lu, J.J. Bailey, N. Mansor, R. Abdulaziz, O.O. Taiwo, R. Jervis, S. Torija, P. Benson, S. Foster, P. Adcock, P.R. Shearing, D.J.L. Brett, Electrochimica Acta Effect of gas diffusion layer properties on water distribution across air-cooled , open-cathode polymer electrolyte fuel cells : A combined ex-situ X-ray tomography and in-operando neutron imaging study, Electrochim. Acta. 211 (2016) 478–487. https://doi.org/10.1016/j.electacta.2016.06.068.

[186] U.S. Department of Energy, Fuel Cells Section, Multi-Year Res. Dev. Demonstr. Plan. 2015 (2015) 1–58.

[187] Y. Sone, Proton Conductivity of Nafion 117 as Measured by a Four-Electrode AC Impedance Method, J. Electrochem. Soc. 143 (1996) 1254. https://doi.org/10.1149/1.1836625.

[188] H. Al-Zeyoudi, A.P. Sasmito, T. Shamim, Performance evaluation of an open-cathode PEM fuel cell stack under ambient conditions: Case study of United Arab Emirates, Energy Convers. Manag. 105 (2015) 798–809. https://doi.org/10.1016/j.enconman.2015.07.082.

[189] D. Kramer, J. Zhang, R. Shimoi, E. Lehmann, A. Wokaun, K. Shinohara, G.G. Scherer, In situ diagnostic of two-phase flow phenomena in polymer electrolyte fuel cells by neutron imaging: Part A. Experimental, data treatment, and quantification, Electrochim. Acta. 50 (2005) 2603–2614. https://doi.org/10.1016/j.electacta.2004.11.005.

[190] Y.H. Park, J.A. Caton, Development of a PEM stack and performance analysis including the effects of water content in the membrane and cooling method, J. Power Sources. 179 (2008) 584–591. https://doi.org/10.1016/j.jpowsour.2008.01.050.

[191] K. Nishida, T. Murakami, S. Tsushima, S. Hirai, Measurement of liquid water content in cathode gas diffusion electrode of polymer electrolyte fuel cell, J. Power Sources. 195 (2010) 3365–3373. https://doi.org/10.1016/j.jpowsour.2009.12.073.

[192] L. You, H. Liu, A two-phase flow and transport model for the cathode of PEM fuel cells, Int. J. Heat Mass Transf. 45 (2002) 2277–2287. https://doi.org/10.1016/S0017-9310(01)00322-2.

[193] C. Song, Y. Tang, J.L. Zhang, J. Zhang, H. Wang, J. Shen, S. McDermid, J. Li, P. Kozak, PEM fuel cell reaction kinetics in the temperature range of 23-120 °C, Electrochim. Acta. 52 (2007) 2552–2561. https://doi.org/10.1016/j.electacta.2006.09.008.

[194] Q. Meyer, K. Ronaszegi, G. Pei-June, O. Curnick, S. Ashton, T. Reisch, P. Adcock, P.R. Shearing, D.J.L. Brett, Optimisation of air cooled, open-cathode fuel cells: Current of lowest resistance and electro-thermal performance mapping, J. Power Sources. 291 (2015) 261–269. https://doi.org/10.1016/j.jpowsour.2015.04.101.

[195] M. V. Williams, H.R. Kunz, J.M. Fenton, Operation of Nafion®-based PEM fuel cells with no external humidification: Influence of operating conditions and gas diffusion layers, J. Power Sources. 135 (2004) 122–134. https://doi.org/10.1016/j.jpowsour.2004.04.010.

[196] S. Gheorghiu, S. Kjelstrup, P. Pfeifer3, M.-O. Coppens, Is the Lung an Optimal Gas Exchanger?, in: G.A. Losa, D. Merlini, T.F. Nonnenmacher, E.R. Weibel (Eds.), Fractals Biol. Med., Birkhäuser Basel, Basel, 2006: pp. 31–42. https://doi.org/10.1007/3-7643-7412-8_3.

[197] H. Li, Y. Tang, Z. Wang, Z. Shi, S. Wu, D. Song, J. Zhang, K. Fatih, J. Zhang, H. Wang, Z. Liu, R. Abouatallah, A. Mazza, A review of water flooding issues in the proton exchange membrane fuel cell, J. Power Sources. 178 (2008) 103–117. https://doi.org/10.1016/j.jpowsour.2007.12.068.

[198] G. Karimi, F. Jafarpour, X. Li, Characterization of flooding and two-phase flow in polymer electrolyte membrane fuel cell stacks, J. Power Sources. 187 (2009) 156–164. https://doi.org/10.1016/j.jpowsour.2008.10.108.

[199] Y.G. Yoon, W.Y. Lee, G.G. Park, T.H. Yang, C.S. Kim, Effects of channel and rib widths of flow field plates on the performance of a PEMFC, Int. J. Hydrogen Energy. 30 (2005) 1363–1366. https://doi.org/10.1016/j.ijhydene.2005.04.008.

[200] P. Deevanhxay, T. Sasabe, S. Tsushima, S. Hirai, Effect of liquid water distribution in gas diffusion media with and without microporous layer on PEM fuel cell performance, Electrochem. Commun. 34 (2013) 239–241. https://doi.org/10.1016/j.elecom.2013.07.001.

[201] M.A. Rubio, A. Urquia, S. Dormido, Diagnosis of performance degradation phenomena in PEM fuel cells, Int. J. Hydrogen Energy. 35 (2010) 2586–2590. https://doi.org/10.1016/j.ijhydene.2009.03.054.

[202] H. Xu, H.R. Kunz, J.M. Fenton, Analysis of proton exchange membrane fuel cell polarization losses at elevated temperature 120 °C and reduced relative humidity, Electrochim. Acta. 52 (2007) 3525–3533. https://doi.org/10.1016/j.electacta.2006.10.015.

[203] D.H. Jeon, K.N. Kim, S.M. Baek, J.H. Nam, The effect of relative humidity of the cathode on the performance and the uniformity of PEM fuel cells, Int. J. Hydrogen Energy. 36 (2011) 12499–12511. https://doi.org/10.1016/j.ijhydene.2011.06.136.

[204] X. Liu, H. Guo, F. Ye, C.F. Ma, Flow dynamic characteristics in flow field of proton exchange membrane fuel cells, Int. J. Hydrogen Energy. 33 (2008) 1040–1051. https://doi.org/10.1016/j.ijhydene.2007.11.018.

[205] P.M. Gomadam, J.W. Weidner, Analysis of electrochemical impedance spectroscopy in proton exchange membrane fuel cells, Int. J. Energy Res. 29 (2005) 1133–1151. https://doi.org/10.1002/er.1144.

[206] S. Asghari, A. Mokmeli, M. Samavati, Study of PEM fuel cell performance by electrochemical impedance spectroscopy, Int. J. Hydrogen Energy. 35 (2010) 9283–9290. https://doi.org/10.1016/j.ijhydene.2010.03.069.

[207] H.D. Ham, Influence of the water content on the kinetics of counter-ion transport in pefiuorosulphonic membranes, J. Electroanal. Chem. 287 (1998) 43–59.

[208] H.D. Ham, Influence of the water content on the kinetics of counter-ion transport in pefiuorosulphonic membranes, J. Electroanal. Chem. 287 (1998) 43–59.

[209] Y. Wu, J.I.S. Cho, T.P. Neville, Q. Meyer, R. Zeische, P. Boillat, M. Cochet, P.R. Shearing, D.J.L. Brett, Effect of serpentine flow-field design on the water management of polymer electrolyte fuel cells: An in-operando neutron radiography study, J. Power Sources. 399 (2018) 254–263. https://doi.org/10.1016/j.jpowsour.2018.07.085.

[210] Q. Yan, H. Toghiani, J. Wu, Investigation of water transport through membrane in a PEM fuel cell by water balance experiments, J. Power Sources. 158 (2006) 316–325. https://doi.org/10.1016/j.jpowsour.2005.09.013.

[211] R. O'Hayre, T. Fabian, S. Litster, F.B. Prinz, J.G. Santiago, Engineering model of a passive planar air breathing fuel cell cathode, J. Power Sources. 167 (2007) 118–129. https://doi.org/10.1016/j.jpowsour.2007.01.073.

[212] D. Candusso, D. Hissel, A. Hernandez, A. Aslanides, A review on PEM voltage degradation associated with water management : Impacts , influent factors and characterization, J. Power Sources.183 (2008) 260–274. https://doi.org/10.1016/j.jpowsour.2008.04.037.

[213] X. Yuan, J.C. Sun, M. Blanco, H. Wang, J. Zhang, D.P. Wilkinson, AC impedance diagnosis of a 500 W PEM fuel cell stack. Part I: Stack impedance, J. Power Sources. 161 (2006) 920–928. https://doi.org/10.1016/j.jpowsour.2006.05.003.

[214] N. Ge, R. Banerjee, D. Muirhead, J. Lee, H. Liu, P. Shrestha, A.K.C. Wong, J. Jankovic, M. Tam, D. Susac, J. Stumper, A. Bazylak, Membrane dehydration with increasing current density at high inlet gas relative humidity in polymer electrolyte membrane fuel cells, J. Power Sources. 422 (2019) 163–174. https://doi.org/10.1016/j.jpowsour.2019.03.001.

[215] S. Shimpalee, U. Beuscher, J.W. Van Zee, Analysis of GDL flooding effects on PEMFC performance, Electrochim. Acta. 52 (2007) 6748–6754. https://doi.org/10.1016/j.electacta.2007.04.115.

[216] F. Barbir, H. Gorgun, X. Wang, Relationship between pressure drop and cell resistance as a diagnostic tool for PEM fuel cells, J. Power Sources. 141 (2005) 96–101. https://doi.org/10.1016/j.jpowsour.2004.08.055.

[217] Y. Shao, L. Xu, J. Li, Z. Hu, C. Fang, J. Hu, D. Guo, M. Ouyang, Hysteresis of output voltage and liquid water transport in gas diffusion layer of polymer electrolyte fuel cells, Energy Convers. Manag. 185 (2019) 169–182. https://doi.org/10.1016/j.enconman.2019.01.084.

[218] J.R. Atkins, S.C. Savett, S.E. Creager, Large-scale current fluctuations in PEM fuel cells operating with reduced feed stream humidification, J. Power Sources. 128 (2004) 201–207. https://doi.org/10.1016/j.jpowsour.2003.09.067.

[219] J.-M. Le Canut, R.M. Abouatallah, D.A. Harrington, Detection of Membrane Drying, Fuel Cell Flooding, and Anode Catalyst Poisoning on PEMFC Stacks by Electrochemical Impedance Spectroscopy, J. Electrochem. Soc. 153 (2006) A857. https://doi.org/10.1149/1.2179200.

[220] Y. Wang, L. Yue, S. Wang, New design of a cathode fl ow- fi eld with a sub-channel to improve the polymer electrolyte membrane fuel cell performance, J. Power Sources. 344 (2017) 32–38. https://doi.org/10.1016/j.jpowsour.2017.01.075.

[221] T.P. Neville, D.J.L. Brett, J. Millichamp, S. Simons, T.J. Mason, P.R. Shearing, A study of the effect of water management and electrode flooding on the dimensional change of polymer electrolyte fuel cells, J. Power Sources. 242 (2013) 70–77. https://doi.org/10.1016/j.jpowsour.2013.05.045.

[222] R. O'Hayre, T. Fabian, S. Litster, F.B. Prinz, J.G. Santiago, Engineering model of a passive planar air breathing fuel cell cathode, J. Power Sources. 167 (2007) 118–129. https://doi.org/10.1016/j.jpowsour.2007.01.073.

[223] D.J.L. Brett, S. Atkins, N.P. Brandon, V. Vesovic, N. Vasileiadis, A. Kucernak, Localized impedance measurements along a single channel of a solid polymer fuel cell, Electrochem. Solid-State Lett. 6 (2003) 110–113. https://doi.org/10.1149/1.1557034.

[224] H. Sun, G. Zhang, L.J. Guo, S. Dehua, H. Liu, Effects of humidification temperatures on local current characteristics in a PEM fuel cell, J. Power Sources. 168 (2007) 400–407. https://doi.org/10.1016/j.jpowsour.2007.03.022.

[225] J. Stumper, M. Löhr, S. Hamada, Diagnostic tools for liquid water in PEM fuel cells, J. Power Sources. 143 (2005) 150–157. https://doi.org/10.1016/j.jpowsour.2004.11.036.

[226] J.M. Le Canut, R. Latham, W. Mérida, D.A. Harrington, Impedance study of membrane dehydration and compression in proton exchange membrane fuel cells, J. Power Sources. 192 (2009) 457–466. https://doi.org/10.1016/j.jpowsour.2009.03.027.

[227] T. Sousa, D.S. Falcão, A.M.F.R. Pinto, C.M. Rangel, Advances in Hydrogen Energy Technologies : Oportunities and Challenges in a Hydrogen Economy Current density distribution mapping in polymer electrolyte membrane fuel cell Advances in Hydrogen Energy Technologies : Oportunities and Challenges in a Hydroge, Eco Community. (2011) 1–6.

[228] P.K. Sinha, C.Y. Wang, Pore-network modeling of liquid water transport in gas diffusion layer of a polymer electrolyte fuel cell, Electrochim. Acta. 52 (2007) 7936–7945. https://doi.org/10.1016/j.electacta.2007.06.061.

[229] I.S. Hussaini, C.Y. Wang, Visualization and quantification of cathode channel flooding in PEM fuel cells, J. Power Sources. 187 (2009) 444–451. https://doi.org/10.1016/j.jpowsour.2008.11.030.

[230] M. Wilkinson, M. Blanco, E. Gu, J.J. Martin, D.P. Wilkinson, J.J. Zhang, H. Wang, In situ experimental technique for measurement of temperature and current distribution in proton exchange membrane fuel cells, Electrochem. Solid-State Lett. 9 (2006) 507–511. https://doi.org/10.1149/1.2338769.

[231] C.Y. Wen, Y.S. Lin, C.H. Lu, Performance of a proton exchange membrane fuel cell stack with thermally conductive pyrolytic graphite sheets for thermal management, J. Power Sources. 189 (2009) 1100–1105. https://doi.org/10.1016/j.jpowsour.2008.12.103.

[232] L. Luo, Q. Jian, B. Huang, Z. Huang, J. Zhao, S. Cao, Experimental study on temperature characteristics of an air-cooled proton exchange membrane fuel cell stack, Renew. Energy. 143 (2019) 1067–1078. https://doi.org/10.1016/j.renene.2019.05.085.

[233] D.N. Ozen, B. Timurkutluk, K. Altinisik, Effects of operation temperature and reactant gas humidity levels on performance of PEM fuel cells, Renew. Sustain. Energy Rev. 59 (2016) 1298–1306. https://doi.org/10.1016/j.rser.2016.01.040.

[234] F.B. Weng, B.S. Jou, C.W. Li, A. Su, S.H. Chan, The effect of low humidity on the uniformity and stability of segmented PEM fuel cells, J. Power Sources. 181 (2008) 251–258. https://doi.org/10.1016/j.jpowsour.2007.12.078.

[235] Y. Song, H. Xu, Y. Wei, H.R. Kunz, L.J. Bonville, J.M. Fenton, Dependence of high-temperature PEM fuel cell performance on Nafion ® content, J. Power Sources. 154 (2006) 138–144. https://doi.org/10.1016/j.jpowsour.2005.04.001.

[236] Y. Wu, Q. Meyer, F. Liu, L. Rasha, J.I.S. Cho, T.P. Neville, J. Millichamp, R. Ziesche, N. Kardjilov, P. Boillat, H. Markötter, I. Manke, M. Cochet, P. Shearing, D.J.L. Brett, Investigation of water generation and accumulation in polymer electrolyte fuel cells using hydro-electrochemical impedance imaging, J. Power Sources. 414 (2019) 272–277. https://doi.org/10.1016/j.jpowsour.2019.01.003.

[237] V.S. Bethapudi, J. Hack, P. Trogadas, G. Hinds, P.R. Shearing, D.J.L. Brett, Hydration state diagnosis in fractal flow-field based polymer electrolyte membrane fuel cells using acoustic emission analysis, Energy Convers. Manag. 220 (2020) 113083. https://doi.org/10.1016/j.enconman.2020.113083.

[238] J. Zhang, Y. Tang, C. Song, J. Zhang, H. Wang, Short communication PEM fuel cell open circuit voltage (OCV) in the temperature range of 23 °C to 120 °C, J. Power Sources.163 (2006) 532–537. https://doi.org/10.1016/j.jpowsour.2006.09.026.

[239] A. Iranzo, A. Salva, P. Boillat, J. Biesdorf, E. Tapia, F. Rosa, Water build-up and evolution during the start-up of a PEMFC: Visualization by means of Neutron Imaging, Int. J. Hydrogen Energy. 42 (2017) 13839–13849. https://doi.org/10.1016/j.ijhydene.2016.11.076.

[240] X. Radiography, J. Hinebaugh, J. Electrochem, F. Soc, Visualizing Liquid Water Evolution in a PEM Fuel Cell Using Synchrotron Visualizing Liquid Water Evolution in a PEM Fuel Cell Using Synchrotron X-ray Radiography, (2012). https://doi.org/10.1149/2.054212jes.

[241] S. Litster, D. Sinton, N. Djilali, Ex situ visualization of liquid water transport in PEM fuel cell gas diffusion layers, J. Power Sources. 154 (2006) 95–105. https://doi.org/10.1016/j.jpowsour.2005.03.199.

[242] T. Fabian, J.D. Posner, R. O'Hayre, S.W. Cha, J.K. Eaton, F.B. Prinz, J.G. Santiago, The role of ambient conditions on the performance of a planar, air-breathing hydrogen PEM fuel cell, J. Power Sources. 161 (2006) 168–182. https://doi.org/10.1016/j.jpowsour.2006.03.054.

[243] M. Breitwieser, R. Moroni, J. Schock, M. Schulz, B. Schillinger, ScienceDirect Water management in novel direct membrane deposition fuel cells under low humidification, Int. J. Hydrogen Energy. 41 (2016) 11412–11417. https://doi.org/10.1016/j.ijhydene.2016.05.018.

[244] C. Zhang, Z. Liu, W. Zhou, S.H. Chan, Y. Wang, Dynamic performance of a high-temperature PEM fuel cell - An experimental study, Energy. 90 (2015) 1949–1955. https://doi.org/10.1016/j.energy.2015.07.026.

[245] D.A. McKay, J.B. Siegel, W. Ott, A.G. Stefanopoulou, Parameterization and prediction of temporal fuel cell voltage behavior during flooding and drying conditions, J. Power Sources. 178 (2008) 207–222. https://doi.org/10.1016/j.jpowsour.2007.12.031.

[246] A.J. Real, A. Arce, C. Bordons, Development and experimental validation of a PEM fuel cell dynamic model, J. Power Sources. 173 (2007) 310–324. https://doi.org/10.1016/j.jpowsour.2007.04.066.

[247] Y. Yang, X. Zhang, L. Guo, H. Liu, Mechanisms of voltage spikes and mitigation strategies for proton exchange membrane fuel cells with dead-ended anode under pressure swing operation, Int. J. Hydrogen Energy. 42 (2017) 28578–28587. https://doi.org/10.1016/j.ijhydene.2017.09.103.